Coupled Halogen-Sulfur-Aerosol Modelling in a 3D Chemical Transport Model

Thomas James Breider

Submitted in accordance with the requirements for the degree of
Doctor of Philosophy

University of Leeds
School of Earth and Environment
September 2010

Declaration of Authorship

The candidate confirms that the work submitted is his own, except where work which has formed part of jointly-authored publications has been included. The contribution of the candidate and the other authors to this work has been explicitly indicated below. The candidate confirms that appropriate credit has been given within the thesis where reference has been made to the work of others.

The publication Breider et al., (2010), *Impact of BrO on dimethylsulfide in the remote marine boundary layer*, Geophysical Research letters, 37, L02807, doi:10.1029/2009GL040868, 2010, was jointly-authored with Professor M. P. Chipperfield, Dr N. A. D. Richards, Professor K. S. Carslaw, Dr G. W. Mann and Dr D. V. Spracklen. This work forms part of Chapter 4. The text of the publication was written by the candidate with scientific comments from Professor M. P. Chipperfield and Professor K. S. Carslaw. Dr N. A. D. Richards, Dr G. W. Mann and Dr D. V. Spracklen provided modelling support. The model simulations, analysis and generation of figures were also performed by the candidate.

The publication Schmidt et al., (2010) *The impact of the 17831784 AD Laki eruption on global aerosol formation processes and cloud condensation nuclei*, Atmospheric Chemistry and Physics, 10, 6025-6041, doi:10.5194/acp-10-6025-2010 was jointly-authored by A. Schmidt, Professor K. S. Carslaw, Dr G. W. Mann, Professor M. Wilson, T. J. Breider, Dr S. J. Pickering, and T. Thordarson. T. J. Breider developed part of the coupled chemistry and aerosol model used in the study.

This copy has been supplied on the understanding that it is copyright material and that no quotation from the thesis may be published without proper acknowledgement.

The right of Thomas James Breider to be identified as Author of this work has been asserted by him in accordance with the Copyright, Designs and Patents Act 1988.

© 2010 The University of Leeds and Thomas James Breider.

Acknowledgements

Firstly I wish to express my sincere thanks to my two supervisors, Martyn Chipperfield and Ken Carslaw for their help and guidance during the last 4 years.

For support with computational and modelling issues I would like to thank Steven Pickering, Nigel Richards, Graham Mann, Dominick Spracklen and Steve Arnold.

I also wish to acknowledge the people who have provided data; Anoop Mahajan, Yoko Yokouchi and James Lee.

I would like to thank the Surface-Ocean Lower Atmosphere Study (SOLAS) community and the many scientists I have met at meetings and conferences, who have inspired and kept me motivated during this work. Also thanks to the Natural Environment Research Council (NERC) for financial assistance during my PhD.

Now thankyou to all the people who I have met in ICAS during my PhD, many legends that I will remember forever; Helen, McWoody, Girthman, the PM, P.Smith, G-lad, Luis, Tim, Lars, Rosey, Nig, Arwin and Big Baz, Benny, Anja and Kai. Thanks to my mates from my home shire, Creepy, Drifter, YT, Harv and Wellsy for providing endless laughter whenever I ventured back home.

I wish to thank my Mum and Dad and family for their support.

Finally I wish to dedicate this work to my dog Dylan, who like me loved science and running and chocolate.

Abstract

In this thesis a detailed tropospheric chemistry model is coupled to a size-resolved aerosol microphysics model, and extended to include a treatment of bromine and iodine chemistry. This is the first global coupled-chemistry-aerosol model to include a description of bromine and iodine chemistry suitable for studying halogen-sulfur-aerosol interactions in the troposphere.

The newly developed coupled model accurately simulates global distribtions of DMS, SO_2 and CCN. A stronger oxidant limitation is simulated in the northern hemisphere winter in the coupled model than a model using prescribed oxidant fields. The increased oxidant limitation acts to re-distribute sulfate mass from existing accumulation mode particles to growth of Aitken mode particles, resulting in an increased number of smaller CCN.

The first simulations of N_2O_5 hydrolysis on aerosol and cloud droplets in TOMCAT show the reaction provides an important sink for NO_x in winter. Zonally averaged NO_x mixing ratios decrease by $>$40% in the mid and high latitude northern hemisphere winter due to large aerosol surface areas and favourable conditions for N_2O_5 formation. The reduction in NO_x impacts on the production of ozone, decreasing ozone mixing ratios by up to 12%.

The inclusion of bromine chemistry shows modelled BrO is in good agreement with ground-based and satellite observations. Model simulations suggest BrO contributes 36% of the global annual DMS oxidation sink and results in a 42% reduction in the global DMS burden and lifetime. Bromine chemistry also results in a decrease in zonally averaged CCN number concentrations of 10-25% over the southern hemisphere oceans during the summer due to changes in DMS oxidation pathways and transport. Furthermore, when an alternative DMS source parameterisation is used, resulting in an increase in the DMS flux of 45%, the sea salt bromine source in the southern hemisphere summer is enhanced by 11-17% because of additional aerosol acidity. This DMS-SO_2-sea salt-BrO marine aerosol feedback mechanism acts to suppress the response in CCN to increases in DMS.

The first global simulations of iodine chemistry in the troposphere show modelled methyl iodide concentrations that are in agreement with measurements at eight remote stations. Modelled IO at the Cape Verde Atmospheric Observatory in the tropical East Atlantic Ocean shows the model is unable to reproduce the observations when only organic iodine emission fluxes are included (IO $\sim$0.1 pptv), suggesting an additional source of reactive iodine species is required to explain the observations of daytime IO.

A detailed comparison with observed daytime ozone loss at the Cape Verde Atmospheric Observatory shows the basic TOMCAT model underpredicts the observed ozone loss by 1.85 ppbv day^{-1}. Reactions involving bromine and iodine species contribute an additional 0.91 ppbv day^{-1}, suggesting reactive halogen species are an important sink for ozone in this region.

Contents

Declaration of Authorship **i**

Acknowledgements **ii**

Abstract **iii**

List of Figures **viii**

List of Tables **xii**

1 Introduction **1**
- 1.1 Introduction 1
- 1.2 Motivation 2
- 1.3 Thesis Aims 5
- 1.4 Layout of Thesis 5

2 Literature Review **7**
- 2.1 Introduction 7
- 2.2 The Earth's Atmosphere - Key Principles 7
- 2.3 Tropospheric Chemistry 9
- 2.4 Tropospheric Aerosols 14
  - 2.4.1 Sources of Aerosols 14
  - 2.4.2 Microphysical Processes and the Aerosol Life Cycle 15
- 2.5 The Sulfur Cycle 16
- 2.6 Tropospheric Halogen Chemistry 18
  - 2.6.1 Sources of Halogens 18
  - 2.6.2 Reaction Cycles 23
  - 2.6.3 Observational and Modelling Evidence for Reactive Halogen Chemistry in the Marine Boundary Layer 27
- 2.7 Global Chemistry and Aerosol Models 29
- 2.8 Limitations of Past Modelling Studies 31

3 Development and Evaluation of a Coupled Chemistry and Aerosol Model **33**
- 3.1 Introduction 33
- 3.2 TOMCAT Chemical Transport Model 34

3.2.1 Advection and Convection 34
3.2.2 Dry and Wet Deposition 35
3.2.3 Chemistry Scheme 35
3.2.4 Emissions 36
3.3 GLOMAP Aerosol Microphysics Scheme 37
3.3.1 GLOMAP-Bin 37
3.3.2 GLOMAP-Mode 37
3.3.3 Emissions 38
3.3.4 Aerosol Microphysics 40
3.4 Numerical Treatment 44
3.5 Model Development 45
3.5.1 Phase 1 - Coupling of the Aerosol and Chemistry 46
3.5.2 Phase 2 - Introduction of Bromine Chemistry 48
3.5.2.1 Organic Bromine Emissions 49
3.5.2.2 Sea Salt Bromine Emissions 50
3.5.2.3 Aqueous Phase Reaction of HOBr + SO_2 53
3.6 Model Evaluation and Interpretation of Coupled and Uncoupled Model Simulations 55
3.6.1 Model Experiments 55
3.6.2 Model Evaluation Data 56
3.6.3 Coupled vs Uncoupled Model - Changes in DMS 57
3.6.4 Coupled vs Uncoupled Model - Changes in SO_2 62
3.6.5 Coupled vs Uncoupled Model - Changes in Sulfate Aerosol 68
3.6.6 Coupled vs Uncoupled Model - Changes in CN and CCN concentrations 75
3.6.7 Coupled vs Uncoupled Model - Changes in Oxidants 80
3.7 Heterogeneous Reaction of N_2O_5 on Aerosols - Impact on Ozone and NO_x 82
3.8 Summary and Conclusions 85

4 Impact of Bromine on DMS and Aerosol in the Remote Marine Boundary Layer 88
4.1 Introduction 88
4.2 Model Experiments 89
4.3 Evaluation of the Bromine Model - Comparison with Observations 90
4.4 Changes to Background Tropospheric Chemistry due to Inclusion of Bromine . . 108
4.5 Detailed Comparison with Cape Verde Atmospheric Observatory Dataset 113
4.6 Coupled Bromine and Sulfur Interactions 116
4.6.1 DMS Oxidation Budget 116
4.6.2 Changes to DMS, SO_2 and DMSO 118
4.7 Changes to Marine Aerosol Formation 126
4.8 Possible Marine Aerosol Feedback Mechanism Between DMS-Sea Salt and BrO 133
4.9 Discussion and Conclusions 137

5 Iodine 141
5.1 Introduction 141
5.2 Model Description and Experiments 142
5.2.1 Organic Iodine Emissions 143
5.2.2 Inorganic Iodine Emissions 147
5.3 Model Experiments 147

5.4 Evaluation of the Iodine Model - Global Distributions 148
5.5 Evaluation of the Iodine Model - Comparisons with Observations 159
5.6 Impact of Iodine on Daytime Ozone Loss 162
5.7 Impact of Iodine on Global Ozone Budgets 165
5.8 Conclusions 168

6 Conclusions 171
6.1 Summary of Results 171
6.2 Synthesis 173
6.3 Implications for Future Work 175

A List of Reactions in the Coupled TOMCAT-GLOMAP Bromine and Iodine Model 177

References 193

List of Figures

1.1 Radiative forcing of climate between 1750 and 2005. 2
1.2 Diagram of aerosol indirect interactions with radiation 3
1.3 Diagram of the CLAW hypothesis. 4

2.1 Diagram showing the temperature structure of the atmosphere 9
2.2 Observed size-resolved sea salt bromide enrichment factors. 19
2.3 Diagram of the important gas and aerosol phase reactions in the recycling of reactive bromine 26

3.1 Process splitting in the TOMCAT/GLOMAP model 45
3.2 Surface average DMS mixing ratio in the coupled model simulation during DJF and JJA. 57
3.3 Absolute change in the surface DMS mixing ratio in the coupled model simulation during DJF and JJA. 58
3.4 Absolute contribution of OH and NO_3 to DMS oxidation in the coupled and uncoupled model simulations. 59
3.5 Percentage change in NO_3 and OH in the coupled model compared to the chemistry only model. 60
3.6 Comparisons of observed and modelled monthly mean DMS mixing ratios at Amsterdam Island, Cape Grim and Dumont Durville. 62
3.7 Comparisons of observed and modelled monthly mean DMSO mixing ratios at Amsterdam Island and Dumont Durville. 63
3.8 Column SO_2 mass concentration in the coupled simulation for DJF and JJA. . . . 63
3.9 Percentage change in column SO_2 mass concentration in the coupled simulation for DJF and JJA. 64
3.10 Comparison of modelled and observed SO_2 from the EMEP network. 65
3.11 Coupled Model vs EMEP and EANET observations of SO_2 in DJF and JJA. . . . 66
3.12 Comparisons of observed and modelled monthly mean SO_2 mixing ratios at Amsterdam Island and Cape Grim 67
3.13 Simulated ${SO_4}^{2-}$ column mass concentration in the coupled model in DJF and JJA 68
3.14 Percentage change in total column ${SO_4}^{2-}$ in DJF and JJA in the coupled model compared to the uncoupled model. 69
3.15 Percentage change in ${SO_4}^{2-}$ formation during DJF and JJA in the coupled model compared to the uncoupled model. 70
3.16 Percentage change in H_2O_2 in in DJF and JJA in the coupled model compared to the uncoupled model. 71
3.17 EMEP ${SO_4}^{2-}$ comparisons with the coupled and uncoupled simulation 73
3.18 Comparison of the coupled model with EMEP and EANET observations of ${SO_4}^{2-}$ 74

3.19 Comparison of the coupled and uncoupled model simulations with observations of non-sea-salt ${SO_4}^{2-}$ at five remote marine stations. 75
3.20 Simulated CN and CCN number concentration in the coupled model in DJF and JJA 77
3.21 Zonally averaged percentage change in column CN and CCN number concentrations in the coupled simulation compared to the uncoupled simulation. 78
3.22 Zonally averaged absolute change in accumulation mode mean radius in the coupled simulation compared to the uncoupled simulation. 79
3.23 Comparison of observed CCN at Cape Grim with the coupled and uncoupled simulations. 79
3.24 Percentage change in zonally averaged NO_x in the coupled simulation compared to the chemistry only simulation. 80
3.25 Percentage change in zonally averaged HO_x in the coupled simulation compared to the chemistry only simulation. 81
3.26 Simulated average surface NO mixing ratio during DJF and JJA in the coupled simulation 81
3.27 Percentage change in zonally averaged O_3 in the coupled simulation compared to the chemistry only simulation. 82
3.28 Zonally averaged percentage change in N_2O_5 in the $HETN_2O_5$ simulation compared to the coupled simulation. 83
3.29 Zonally averaged percentage change in NO_x in the $HETN_2O_5$ simulation compared to the coupled simulation. 84
3.30 Zonally averaged percentage change in O_3 in the in the $HETN_2O_5$ simulation compared to the coupled simulation. 84
3.31 Comparison of the $HETN_2O_5$ simulation with EMEP observations of NO_2. . . . 85

4.1 Surface and zonally averaged total inorganic bromine during December and June. 91
4.2 Zonally averaged total inorganic bromine partitioning in December and June. . . 94
4.3 Monthly surface bromine species plots in December and June. 96
4.4 Monthly mean zonally averaged bromine species plots in December and June. . . 98
4.5 Monthly mean surface bromine species plots in December and June. 100
4.6 Comparison of observed and modelled diurnal BrO cycle at Cape Verde Atmospheric Observatory from November 2006 to June 2007. 102
4.7 Comparisons of observed and modelled monthly mean and maximum surface BrO mixing ratios at Cape Verde Atmospheric Observatory. 103
4.8 Modelled monthly mean diurnal cycle in total inorganic bromine speciation at Cape Verde Atmospheric Observatory. 105
4.9 Comparison of modelled and observed troposphere column BrO in March. 107
4.10 Modelled surface BrO mixing ratio at 10:30am local time in March 107
4.11 Percentage change in zonally averaged ozone concentrations during December and June. 108
4.12 Percentage change in zonally averaged NO_x concentrations during December and June. 112
4.13 Percentage change in zonally averaged HO_x and OH:HO_2 ratio during December and June. 113
4.14 Comparison of observed and modelled monthly mean daytime ozone loss at Cape Verde Atmospheric observatory 114

4.15 Comparison of observed and modelled 30-day running average daytime NO mixing ratio at Cape Verde Atmospheric Observatory 115
4.16 Annual mean DMS oxidation % for OH, NO_3 and BrO. 117
4.17 Comparisons of observed and modelled monthly mean DMS mixing ratios at Amsterdam Island, Cape Grim and Dumont Durville. 119
4.18 Comparisons of observed and modelled monthly mean SO_2 mixing ratio at Amsterdam Island and Cape Grim. 120
4.19 Comparisons of observed and modelled monthly mean DMSO mixing ratios at Amsterdam Island and Dumont Durville 121
4.20 Annual total in-cloud sulfate formation and percentage change between the bromine and no bromine simulations. 122
4.21 Annual mean percentage contribution of H_2O_2, O_3 and HOBr to in-cloud sulfate formation in the coupled bromine simulation. 124
4.22 Comparison of the bromine and no bromine simulations with observations of non-sea-salt ${SO_4}^{2-}$ at five remote marine stations. 127
4.23 Zonally averaged percentage change in CN and CCN in the bromine simulation compared to the no bromine simulation. 129
4.24 Comparison of seasonal cycle in CCN number concentrations at 1km altitude at 0.23% supersaturation in SH latitude bands. 130
4.25 Comparison of key processes controlling CCN formation from DMS emissions in the remote SH ocean during December 2004. 132
4.26 Annual cycle in bromine emissions from sea salt in the bromine and no bromine simulations. 134
4.27 Absolute change in zonally averaged CCN number concentrations due to a higher DMS flux. 136

5.1 Ocean mixed layer Chl-a concentration field in January and July. 145
5.2 Calculated CH_3I flux in the model in January and July. 145
5.3 Surface and zonally averaged monthly mean CH_3I mixing ratio. 148
5.4 Zonally averaged monthly mean organic iodine mixing ratio during January and July. 149
5.5 Surface monthly mean total inorganic iodine mixing ratio. 150
5.6 Zonally averaged monthly mean total inorganic iodine mixing ratio. 151
5.7 Zonally averaged monthly mean inorganic iodine partitioning during January. . . . 152
5.8 Zonally averaged monthly mean inorganic iodine partitioning during July. 152
5.9 Surface monthly mean inorganic iodine partitioning during January. 154
5.10 Surface monthly mean inorganic iodine partitioning during July. 154
5.11 Surface monthly mean inorganic iodine mixing ratios during January. 156
5.12 Surface monthly mean inorganic iodine mixing ratios during July. 156
5.13 Zonally averaged monthly mean inorganic iodine mixing ratios during January. . 158
5.14 Zonally averaged monthly mean inorganic iodine mixing ratios during July. . . . 158
5.15 Modelled monthly mean CH_3I at 8 remote monitoring stations compared to observations. 160
5.16 Comparisons of observed and modelled monthly mean and maximum IO mixing ratios in the tropical North Atlantic Ocean 161
5.17 Comparisons of observed and modelled monthly mean daytime ozone loss at Cape Verde Atmospheric Observatory. 162

5.18 Comparisons of observed and modelled daytime 30-day average NO mixing ratios in tropical North Atlantic Ocean. 163
5.19 Comparisons of observed and modelled monthly mean daytime ozone loss in the tropical North Atlantic Ocean 164
5.20 Comparisons of observed and modelled monthly mean daytime IO and BrO mixing ratios and ozone loss due to halogen oxides in the tropical North Atlantic Ocean 165
5.21 Surface change in monthly mean Ozone between the organic iodine and no iodine simulations. 166
5.22 Zonally averaged change in monthly mean Ozone between the iodine and no iodine simulations. 167

List of Tables

2.1 Main Sources of atmospheric aerosols and their estimated annual source flux . . 15
2.2 Organic halogen species, chemical formula, estimated annual source flux and lifetime. Taken from Clerbaux & Cunnold (2006) and Law & Sturges (2006) 23

3.1 TOMCAT surface emission fluxes 36
3.2 GLOMAP modes and size ranges used in this study 38
3.3 Sulfur reaction scheme in the coupled TOMCAT-GLOMAP model. 46
3.4 Bromine species included in the model 49
3.5 Emissions of organic bromine in the coupled model 50
3.6 Sea salt bromide depletion factors used in this study, calculated from Sander *et al.* (2003) 53
3.7 DMS budgets for 2004 in the **COUPL** and **GLO** simulations and previously published coupled aerosol-chemistry studies. 58
3.8 SO_2 budgets for 2004 in the **GLO** and **COUPL** models and previous published coupled aerosol-chemistry studies. 67
3.9 ${SO_4}^{2-}$ budgets in the **COUPL**, **GLO** and previous published coupled chemistry-aerosol studies. 72

4.1 Ozone burdens and Budgets in the **BR**, **NOBR** simulations and previous published studies. 110
4.2 Global bromine, OH, methane, DMS and SO_2 budgets for 2004 in the **BR**, **NOBR** simulations. 125
4.3 Changes in zonal mean latitude band CCN number concentrations (cm^{-3}) for December 2004 in the **BR** and **NOBR** simulations 131
4.4 Global ${SO_4}^{2-}$ budgets for 2004 in the **BR** and **NOBR** simulations. 133
4.5 Changes in bromine budgets, DMS emissions and CCN number concentrations for December 2004 in the **BR** and **NOBR** simulations 137

5.1 Iodine species included in the model. 142
5.2 Organic halogen species fluxes (nmol m^{-2} day^{-1}) in simulations **I** and **IORG**. . . 146
5.3 Global emissions of organic iodine (Tg I yr^{-1}) in the coupled model derived for this work and estimated fluxes from Law & Sturges (2006) and Jones *et al.* (2010) 146
5.4 Ozone burdens and budgets in the **NOI**, **IORG** simulations and previous published studies. 168

A.1 Chemical Species in the TOMCAT CTM 178
A.2 CTM Gas-Phase Bimolecular Reactions 179
A.3 CTM Gas-Phase Termolecular and Thermal Decomposition Reactions 187
A.4 CTM Heterogeneous Reactions 188

A.5 CTM Photolysis Reactions 189

Chapter 1

Introduction

1.1 Introduction

The study of the Earth's atmosphere has received increased attention over the last few decades. Increased emissions of greenhouse gases such as carbon dioxide and methane from human activity, since the industrial revolution in the 19th century, are driving an "enhanced greenhouse effect". Global average surface temperatures are predicted to rise by 2-6°C by 2100 (Forster *et al.*, 2007). Policy- makers require accurate predictions of regional changes in key climate parameters (including precipitation patterns, storm intensity and drought) for humanity to adapt to and mitigate the effects of global climate change on society. However, there remain large uncertainties in our understanding of atmospheric processes and cycles which puts limitations on current ability to forecast future changes in the climate system. The climate response is further complicated by the strong coupling of the atmospheric system to the oceanic and terrestrial environments, which results in biological, chemical and physical responses in the climate system. These, in turn, drive feedbacks that amplify or dampen the sensitivity of the climate to changes in radiative forcing.

1.2 Motivation

Atmospheric composition is an important forcing component for the Earth's climate (Forster *et al.*, 2007). Composition encompasses both forcing from changes in trace gases such as carbon dioxide, methane and ozone, and forcing from changes in atmospheric aerosols, most notably sulfate, sea salt, dust and carbonaceous aerosol. Figure 1.1 shows the estimated contribution of various components of atmospheric composition to radiative forcing compared to the pre-industrial atmosphere. Ozone is an important radiative trace gas and is also important indirectly by acting as the primary initiator for the formation of radical species that control the lifetime and removal of methane another important greenhouse gas. The largest source of uncertainty in Figure 1.1 is the effects of atmospheric aerosol.

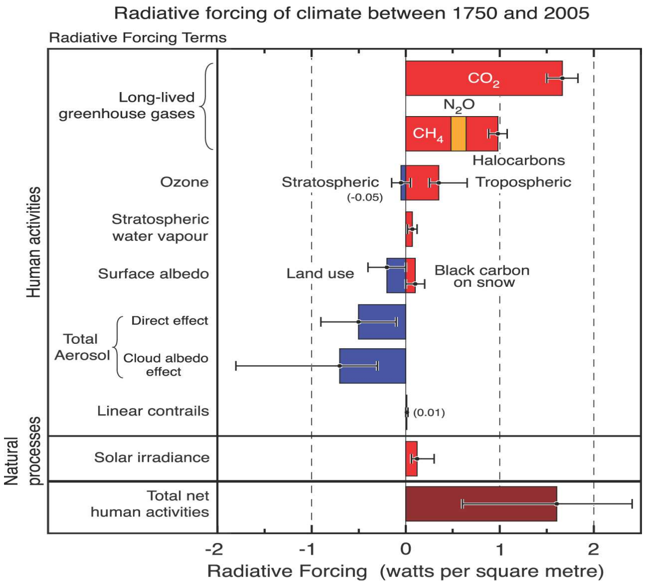

Figure 1.1: Radiative forcing of climate between 1750 and 2005. Taken from Forster *et al.* (2007).

Atmospheric aerosol can impact the Earth's climate via a number of different processes. Aerosols scatter sunlight (direct effect) (CHARLSON *et al.*, 1992), alter the radiative properties of clouds by (i) providing condensation nuclei onto which cloud droplets form, (ii) increasing cloud droplet number concentrations (indirect effect) (Twomey, 1974) and (iii) reducing droplet diameter which suppresses precipitation and increases cloud lifetime (2nd indirect effect). The main indirect aerosol interactions with radiation are summarised in Figure 1.2.

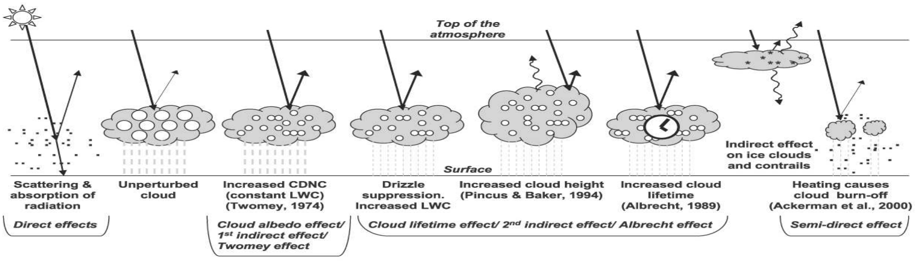
Top of the atmosphere
Surface
Scattering & absorption of radiation
Unperturbed cloud
Increased CDNC (constant LWC) (Twomey, 1974)
Drizzle suppression. Increased LWC
Increased cloud height (Pincus & Baker, 1994)
Increased cloud lifetime (Albrecht, 1989)
Indirect effect on ice clouds and contrails
Heating causes cloud burn-off (Ackerman et al., 2000)
Direct effects
Cloud albedo effect/ 1st indirect effect/ Twomey effect
Cloud lifetime effect/ 2nd indirect effect/ Albrecht effect
Semi-direct effect

Figure 1.2: Schematic diagram of the main indirect interactions of aerosol with radiation. Taken from Haywood & Boucher (2000).

A key aspect that is not detailed in Figure 1.2 is the complex interaction between chemistry and aerosols that control their spatial and temporal distributions. Aerosols provide surfaces that catalyse the recycling and removal of trace gases (Dentener & Crutzen, 1993; Jacob, 2000; Tie *et al.*, 2001). The availability of trace gases in turn influences oxidising capacity which feeds back onto the lifetime and transport of aerosol precursor species and ultimately controls secondary aerosol formation and ageing (Liao *et al.*, 2003). Aerosol also impacts photolysis of species by interacting with radiation (Martin *et al.*, 2003).

In oceanic regions a key precursor species to the formation of sulfate aerosol is dimethylsulfide (DMS) emitted by phytoplankton over the oceans (Charlson *et al.*, 1987). Model studies and observations have found a clear correlation between DMS emission and the seasonality in cloud condensation nuclei (CCN) number concentrations over the remote southern hemisphere ocean (Ayers & Gillett, 2000; Korhonen *et al.*, 2008). Recently, Thomas *et al.* (2010) showed the annual mean top of atmosphere radiative forcing from DMS emissions is -2.0 Wm^{-2}. Over the southern hemisphere oceans during the summer this rises to -9.32 Wm^{-2}, emphasising the importance of DMS emissions for perturbing cloud properties and climate.

The link between phytoplankton, DMS, and CCN led Charlson *et al.* (1987) to propose a climate feedback mechanism. Charlson *et al.* (1987) suggested increases in oceanic productivity in response to global warming would lead to higher DMS emission, increased CCN number concentrations and hence enhanced reflectivity of clouds. This became known as the “CLAW” hypothesis, after the four authors of the Charlson *et al.* (1987) study, and is shown in Figure 1.3.

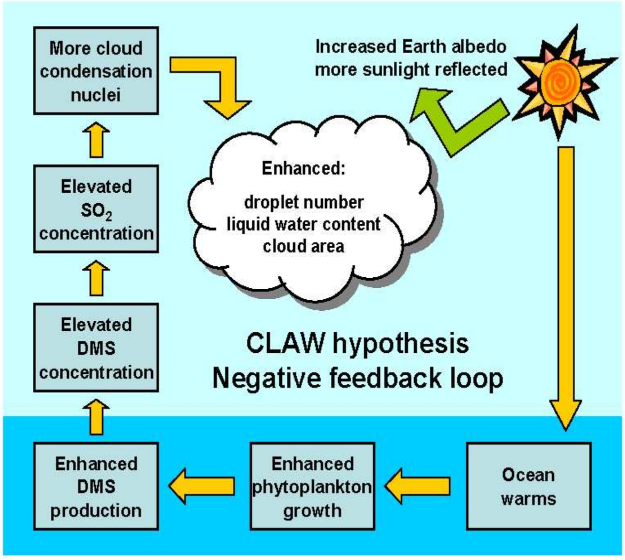
More cloud condensation nuclei
Elevated SO_2 concentration
Elevated DMS concentration
Enhanced DMS production
Enhanced phytoplankton growth
Ocean warms
Increased Earth albedo more sunlight reflected
Enhanced:
droplet number
liquid water content
cloud area
CLAW hypothesis
Negative feedback loop

Figure 1.3: Diagram of the key processes in the CLAW hypothesis. Taken from Charlson *et al.* (1987).

Over the past decade, observations of reactive halogen (chlorine, bromine and iodine) species in the marine atmosphere and from satellites have become available. Mixing ratios of iodine monoxide and bromine monoxide greater than 1pptv have been measured at several locations in the remote marine boundary layer from the tropics to high latitudes (Alicke *et al.*, 1999; Allan *et al.*, 2000; Saiz-Lopez *et al.*, 2004; Read *et al.*, 2008). Satellites have also detected BrO and IO in the troposphere (Fitzenberger *et al.*, 2000; Saiz-Lopez *et al.*, 2007). The primary sources of these radical species have been identified as macroalgae, phytoplankton and sea salt aerosol over the oceans (Carpenter, 2003; Sander *et al.*, 2003). Reactive halogen chemistry is of interest to tropospheric composition because it can strongly impact on oxidising capacity (Chameides & Davis, 1980), and subsequently burdens of ozone and methane. Also, BrO may provide an important oxidant for DMS (Toumi, 1994), potentially reducing formation of CCN (Von Glasow & Crutzen, 2004a). Understanding the importance of reactive halogen species for tropospheric chemistry and aerosol is a key challenge to the atmospheric composition community.

Global models of atmospheric processes are a vital tool for understanding the complex processes controlling the impact of chemistry and aerosols on the Earth's climate. Understanding the complex interactions between aerosols and chemistry will require the use of detailed coupled chemistry and aerosol models that can account for feedbacks between oxidants and aerosols. This thesis presents work using a newly developed three-dimensional chemical transport model coupled to a detailed size-resolved aerosol microphysics module with a treatment of bromine and iodine chemistry to investigate sulfur-halogen-oxidant-aerosol interactions.

1.3 Thesis Aims

The overarching aim of this thesis is to examine the impact of tropospheric halogen chemistry on oxidising capacity and aerosol formation in the troposphere. Specifically, this thesis will address the following:

1. Couple the TOMCAT CTM to the GLOMAP aerosol scheme to allow for interactions between oxidants, sulfur chemistry and aerosol. Assess the impact of using coupled oxidants compared to prescribed oxidants on distributions of DMS, SO_2 and CCN. Evaluate the coupled model using observations from remote marine and land-based stations. Investigate how the inclusion of sulfur chemistry and hydrolysis of N_2O_5 on aerosol impacts global distributions of NO_x, O_3 and HO_x.

2. Investigate the importance of bromine chemistry for oxidising capacity, DMS oxidation and aerosol formation in the troposphere. Evaluate modelled distributions and speciation of bromine in the troposphere and at the Cape Verde Atmospheric Observatory in the tropical East Atlantic Ocean. Understand the global contribution of BrO to DMS oxidation, and how bromine chemistry impacts on CCN number concentrations in the troposphere. Assess any potential implications of bromine chemistry for the “CLAW hypothesis”.

3. Investigate the role of iodine chemistry in the troposphere. Investigate potential distributions of organic and inorganic iodine species in the troposphere. Evaluate the modelled IO and daytime ozone loss at the Cape Verde Atmospheric Observatory.

1.4 Layout of Thesis

In Chapter 2 the key concepts and literature for tropospheric chemistry and aerosol are discussed. A detailed description of halogen chemistry in the troposphere is also provided. The key model developments undertaken as part of this thesis are outlined in Chapter 3. The new coupled chemistry and aerosol model is then evaluated through comparison with observations, and the differences between the uncoupled chemistry and aerosol model are discussed. Chapter 4 presents the results from the inclusion of bromine chemistry in the coupled model. The impact of bromine species on background chemistry, DMS oxidation and marine aerosol formation in the troposphere are investigated. Possible chemical and aerosol feedbacks linked to halogen-sulfur-aerosol interactions in the remote marine atmosphere are discussed. In Chapter 5 an iodine scheme is incorporated into the coupled model, including an organic and inorganic source paramaterisation. Modelled concentrations of methyl iodide are compared with observations from remote marine measurement stations. Global distributions and speciations of I_y in the troposphere are also presented. A detailed comparison with measurements from the Cape Verde Atmospheric Observatory in the tropical East Atlantic Ocean is provided. Finally, Chapter 6 summarises the results in this thesis and outlines the key implications for future work.

Chapter 2

Literature Review

2.1 Introduction

This chapter introduces the main background chemistry of the troposphere, tropospheric halogen chemistry and aerosols and the key processes that control their formation, loss and abundance. Global aerosol and chemistry models are described and their limitations discussed.

An introduction to the atmosphere is given in Section 2.2. Section 2.3 outlines the main background chemistry of the troposphere and gives a summary of the key sources, sinks and reaction mechanisms. Section 2.4 provides an overview of aerosols in the troposphere and their main sources, sinks and microphysical processes. In Section 2.6 an overview of tropospheric halogen chemistry is given and the importance of halogen chemistry for background tropospheric chemistry and aerosols is provided. Section 2.7 provides a description of global models of chemistry and aerosols, their development and importance for understanding the Earth's climate. Finally, Section 2.8 gives an overview of previous chemical and aerosol studies and discusses their limitations.

2.2 The Earth's Atmosphere - Key Principles

The atmosphere of planet Earth is approximately 100 km thick, extending from the surface to the edge of space. This thin envelope of air, equivalent to piece of paper on a beach ball, supports all life on Earth. The main constituents of atmosphere are N_2 (78%), O_2 (21%) and other trace gases (1%). In the upper atmosphere gas molecules of O_2 and O_3 absorb harmful shortwave cosmic rays and UV radiation and prevent them from reaching the surface. Surface temperatures would be on average 33°C colder if the Earth had no atmosphere. This natural greenhouse effect is controlled by the presence of a small number of key trace gases that absorb longwave radiation emitted from the Earth's surface. The atmosphere also has a self-cleaning capacity, driven by photochemical formation of highly reactive radical species that break down harmful pollutants.

The driving force behind the dynamics of the atmosphere is energy from the Sun. This energy drives heat and moisture fluxes that cause pressure gradients which in turn drive winds. The wind fields are in turn influenced by the rotating motion of the Earth on its axis, which skews the horizontal component of the wind field to the east or west. This effect is known as the Coriolis effect. The horizontal and vertical transport of heat and moisture generates temperature and precipitation patterns.

The atmosphere below 100 km is conventionally divided into four levels according to the temperature structure. The lowest level, the troposphere is characterised by a negative temperature gradient (Figure 2.1). The troposphere contains 75% of the mass of the atmosphere and is where all the world's weather takes place, though tropospheric climate is influenced by the stratosphere. The lowest 1-2 km of the troposphere is termed the planetary boundary layer (PBL). The PBL is of particular interest because it is the region populated by humans and vegetation and where land-atmosphere and ocean-atmosphere exchanges take place. The PBL is also where many atmospheric measurements are conducted. Over the oceans the PBL is referred to as the marine boundary layer (MBL) Above the PBL, the free troposphere (FT) extends to the top of troposphere known as the "tropopause". Above the troposphere, in the stratosphere, temperatures increase with altitude due to the absorption of ultraviolet (UV) radiation by ozone. The temperature inversion that caps the top of the troposphere inhibits mixing between the troposphere and stratosphere. The mesosphere extends from 50-85 km above the Earth's surface and exhibits a negative temperature gradient. Above the mesosphere, the thermosphere extends from 85 km to the thermopause at 250-500 km. The thermosphere is characterised by a positive temperature gradient due to absorption of shortwave radiation by molecular oxygen. The vertical temperature structure of the atmosphere is shown in Figure 2.1. A general introduction to key concepts of the earth's atmosphere is provided in Ahrens (1999).

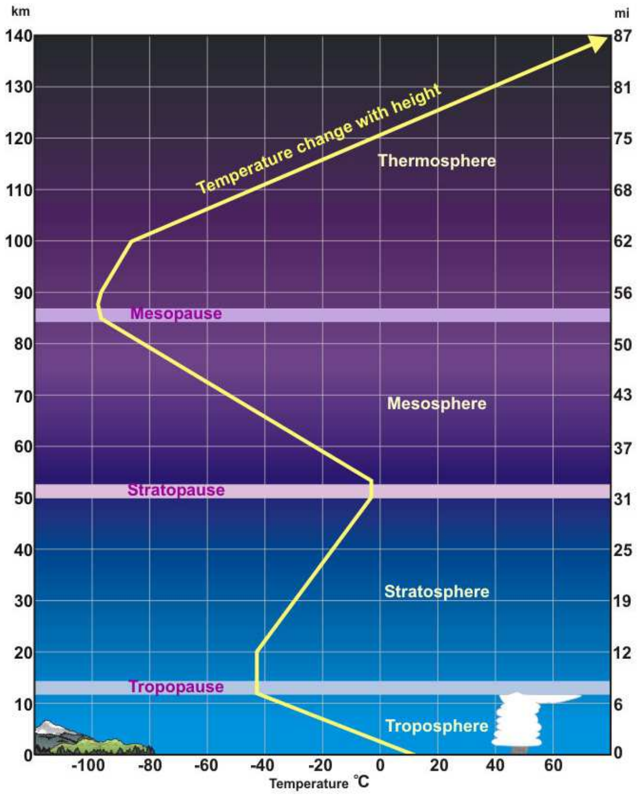

Figure 2.1: Temperature structure of the atmosphere. Taken from National Oceanic and Atmospheric Administration (NOAA)[www.srh.noaa.gov].

2.3 Tropospheric Chemistry

The driving force behind the chemistry of the troposphere is sunlight. Photolysis reactions drive the formation of highly reactive radical species which control the removal and abundance of all major trace gases. A key species in the troposphere is ozone (O_3). The main sources of ozone in the troposphere are in-situ chemical formation (Crutzen, 1973; Chameides & Walker, 1973) and transport from the stratosphere. Chemical formation of ozone is driven by reactions involving nitrogen oxide (NO + NO_2), collectively known as NO_x and volatile organic compounds (VOCs). NO_x is emitted by fossil fuel and biomass burning, fertiliser use, industrial processes and formed from lightning (Forster *et al.*, 2007). The most important VOC, methane (CH_4), is mainly emitted from rice paddies, wetlands and agriculture (Chen & Prinn, 2006). Ozone has a number of key roles in the atmosphere. In the stratosphere ozone is the principle absorber of shortwave radiation and prevents UV-A and UV-B radiation from reaching the surface where it can be damage plants and animals. At the surface high ozone concentrations are also harmful to plants and animals.

Ozone's primary importance for tropospheric chemistry is as the dominant precursor to the formation of the hydroxyl radical species (OH) (Levy, 1971). The hydroxyl radical is the principal oxidising free radical species in the troposphere and controls 70% of methane oxidation and 90% of carbon monoxide loss (Wayne, 2000). Chemical formation of ozone in the troposphere is driven by the photolysis of NO_2.

$$NO_2 + hv \longrightarrow NO + O \tag{2.1}$$

$$O + O_2 + M \longrightarrow O_3 + M \tag{2.2}$$

Photolysis of ozone is the initiation reaction for the production of the hydroxyl radical, (OH). The excited oxygen atom, $O(^1D)$, formed in Reaction 2.3 may then collisionally deactivate to its ground state (Reaction 2.4) or react with water vapour to form two OH molecules (Reaction 2.5).

$$O_3 + hv \longrightarrow O(^1D) + O_2 \tag{2.3}$$

$$O(^1D) + M \longrightarrow O(^3P) + M \tag{2.4}$$

$$O(^1D) + H_2O \longrightarrow OH + OH \tag{2.5}$$

This makes the tropics a key region for the production of OH given the ample availability of sunlight and water vapour.

In unpolluted remote marine regions OH reacts primarily with CO and CH_4 (Monks, 2005). Oxidation of CO can represent a source or sink for O_3 depending on the availability of NO. Low NO_x regions such as the remote ocean represent a sink for ozone (LIU *et al.*, 1987; Penkett *et al.*, 1997).

$$OH + CO \longrightarrow H + CO_2 \tag{2.6}$$

$$H + O_2 + M \longrightarrow HO_2 + M \tag{2.7}$$

$$HO_2 + O_3 \longrightarrow OH + 2O_2 \tag{2.8}$$

$$NET = CO + O_3 \longrightarrow CO_2 + O_2 \tag{2.9}$$

In polluted regions, where there are higher NO concentrations, the HO_2 formed in reaction 2.7 reacts with NO instead of O_3 to form NO_2. This photolyses to reform ozone as in reactions 2.3 and 2.2.

$$HO_2 + NO \longrightarrow OH + NO_2 \tag{2.10}$$

The net reaction in a NO_x-rich environment is;

$$NET = CO + O_2 + hv \longrightarrow CO_2 + O_3 \tag{2.11}$$

The reaction cycles above show that the availability of NO_x controls whether a region is a source or sink for ozone. The threshold mixing ratio for NO_x at which the chemistry produces O_3 varies between 10 and 50 pptv, depending on the latitude and season and is termed the "ozone compensation point" (Jacob *et al.*, 1996; Lee *et al.*, 2009a).

In very polluted regions high levels of NO_x can provide a sink for OH and O_3. Reaction 2.13 provides an important removal mechanism for NO_x in polluted regions.

$$O_3 + NO \longrightarrow NO_2 + O_2 \tag{2.12}$$

$$OH + NO_2 + M \longrightarrow HNO_3 + M \tag{2.13}$$

The oxidation of hydrocarbons is also central to the chemistry of the troposphere. Methane oxidation is initiated by reaction with OH, and leads to the formation of the peroxy radical species, CH_3O_2.

$$CH_4 + OH + (O_2) \longrightarrow CH_3O_2 + H_2O \tag{2.14}$$

The fate of CH_3O_2 depends on the availability of NO. If NO is present at sufficiently high concentrations, Reaction 2.15 conserves the peroxy radical and forms NO_2 which can photolyse to reform ozone.

$$CH_3O_2 + NO + (O_2) \longrightarrow HCHO + HO_2 + NO_2 \tag{2.15}$$

Photolysis of HCHO produces two radical species that can yield two more peroxy radicals.

$$HCHO + hv \longrightarrow HCO + H \tag{2.16}$$

$$HCO + O_2 \longrightarrow CO + HO_2 \tag{2.17}$$

The H formed in reaction 2.16 reacts with O_2 in reaction 2.7. The net result of Reactions 2.14 to 2.7 is therefore;

$$NET = CH_4 + OH + 4O_2 + NO \longrightarrow H_2O + NO_2 + 2HO_2 + CO \tag{2.18}$$

The reaction cycle above requires sufficient NO_x for the reaction of methyl peroxy (CH_3O_2) to react with NO. In low NO_x regions reaction of CH_3O_2 with HO_2 over NO is favoured.

$$CH_3O_2 + HO_2 \longrightarrow CH_3OOH + O_2 \tag{2.19}$$

The product methyl hydrogen peroxide (CH_3OOH) is highly soluble and dissolves in cloud droplets where it may be deposited to the surface in precipitation (Logan *et al.*, 1981). Hence, Reaction 2.19 is an important removal process for peroxy radicals in remote marine regions. This reduces the cycling of NO to NO_2 in reactions 2.10 and 2.15 and limits ozone production.

Another important sink for HO_2 in remote low-NO_x regions is the self-reaction of HO_2. The product H_2O_2 is highly soluble and is dissolves in cloud droplets, where it can oxidise SO_2 (Hoffmann & Calvert, 1985) or deposit to the surface.

$$HO_2 + HO_2 \longrightarrow H_2O_2 + O_2 \tag{2.20}$$

At nighttime, in the absence of photochemistry, the formation of OH shuts off and the nitrate radical (NO_3) becomes the principal oxidising species in the troposphere. Formation of NO_3 takes place via the reaction of NO_2 with O_3 (Platt & Janssen, 1995).

$$NO_2 + O_3 \longrightarrow NO_3 + O_2 \tag{2.21}$$

During the daytime concentrations of NO_3 are unable to build up as it is rapidly photolysed.

$$NO_3 + hv \longrightarrow NO + O_2 \tag{2.22}$$

$$NO_3 + hv \longrightarrow NO_2 + O \tag{2.23}$$

Reaction of NO_3 with NO_2 forms N_2O_5. The formation of N_2O_5 is favoured at low temperatures.

$$NO_2 + NO_3 + M \rightleftharpoons N_2O_5 + M \tag{2.24}$$

N_2O_5 is rapidly photolysed; however, at nighttime it can be the dominant NO_x reservoir species.

$$N_2O_5 + hv \longrightarrow NO_2 + NO_3 \tag{2.25}$$

A key species for the transport of NO_x to remote regions is peroxyacetylnitrate, PAN ($CH_3C(O)OONO_2$). PAN is formed in NO_x source regions when hydrocarbons are oxidised in the presence of NO_2 (Wayne, 2000). In the cold free troposphere PAN has a long lifetime and can be transported over large distances. If it sinks to the surface PAN can fall apart under higher temperatures to form NO_2. PAN provides an important pathway for transporting NO_x to remote regions (Moxim *et al.*, 1996). Global 3-D model simulations have shown that PAN decomposition is the principal source of NO_x to the remote troposphere (Bey *et al.*, 2001; Staudt *et al.*, 2003).

$$CH_3CO.O_2 + NO_2 + M \longrightarrow CH_3CO.O_2NO_2 + M \tag{2.26}$$

$$CH_3CO.O_2NO_2 + M \longrightarrow CH_3CO.O_2 + NO_2 + M \tag{2.27}$$

Aerosol particles and cloud droplets provide surfaces that catalyse chemical reactions that are less favourable in the gas-phase (Jacob, 2000; Ravishankara, 1997; Andreae & Crutzen, 1997). This can either result in loss of a species from the gas-phase or a recycling of that species to a different compound. Heterogeneous reactions can impact tropospheric ozone by perturbing HO_x and NO_x cycles (Jacob, 2000) or by the production and recycling of reactive halogen species (Vogt *et al.*, 1996). An important heterogeneous reaction of interest in the troposphere is the reaction of N_2O_5 with H_2O (Dentener & Crutzen, 1993).

$$N_2O_5 + H_2O \longrightarrow 2HNO_3 \tag{2.28}$$

The product HNO_3 can be photolysed or react with OH but these reactions are slow in the troposphere (Wayne, 2000). The high solubility of HNO_3 makes wet deposition the dominant sink. As a result Reaction 2.28 can provide an important removal mechanism for NO_x in the troposphere (Dentener & Crutzen, 1993; Tie *et al.*, 2001).

2.4 Tropospheric Aerosols

Aerosols in the atmosphere are tiny particles of solid or liquid matter suspended in the air. These particles range in diameter from a few nanometres (nm) to tens of microns (μm). Aerosols can be composed of sea salt, sulfate, black carbon, organic carbon, dust or a mixture of the different components. The formation, growth and composition of aerosol particles is controlled by several complex microphysical processes.

Atmospheric aerosol can be classified into four distinctive size sections referred to as modes. The smallest particles, known as nucleation mode particles, have diameters of 3-10 nm. Particles between 10 and 100 nm diameter are termed Aitken mode particles. The accumulation mode covers size fractions 100 nm 1.0 μm diameter. Coarse mode particles are aerosol larger than 1.0 μm in diameter.

The relatively short lifetimes of aerosol particles (minutes to days) means concentrations are highly variable in space and time. In polluted continental regions aerosol number concentrations as high as 100,000 particles per cm^{-3} have been observed. In clean marine regions number concentrations are much lower, usually 200 to 500 cm^{-3} (Hobbs, 1993).

The main emissions, microphysical processes and deposition mechanisms are outlined in Sections 2.4.1 and 2.4.2.

2.4.1 Sources of Aerosols

Aerosols in the atmosphere are emitted from a variety of natural sources including dust, sea spray and volcanoes and anthropogenic sources such as industrial activities (Seinfeld, 1999). Aerosol particles can either be mechanically injected into the atmosphere from the surface (primary formation) or formed through gas-to-particle conversion of low-volatility gases (secondary formation).

Sources of primary aerosols include wind-blown dust, sea salt and black carbon from biomass burning. Emission of these particles occurs as a result of wind stress at the Earth's surface. Primary aerosols are typically emitted at sizes larger than 0.1 μm dry diameter and are the dominant source of aerosol larger than 1.0 μm.

Sources of secondary aerosols include emissions of SO$_2$ from volcanoes and anthropogenic sources such as power stations. Emissions of dimethysulfide (DMS) from phytoplankton in the oceans

Table 2.1: Main Sources of atmospheric aerosols and their estimated annual source flux

Aerosol Type	Est. Flux (Tg a^{-1})	Reference
Sea Salt	7925 ± 50%	Forster *et al.* (2007)
Dust	2150 ± 80%	Forster *et al.* (2007)
Black Carbon	7.7	Dentener *et al.* (2006)
Organic Carbon	12-70	Forster *et al.* (2007)
Sulfate (emitted as SO_2)	91-125	Forster *et al.* (2007)

also provides an important source of secondary aerosol in the remote marine atmosphere (Charlson *et al.*, 1987; Ayers *et al.*, 1991). Secondary aerosol formation occurs when a volatile gaseous species is present at a concentration larger than its equilibrium vapour pressure. The nucleation rate depends on the amount of condensible vapour available, the pre-existing aerosol surface area and the temperature. Nucleation is favoured at low temperatures, and low aerosol surface area, hence the upper free troposphere is an environment conducive to nucleation (Curtius, 2006). Formation of sulfate aerosols has been studied for many years, but the precise nucleation mechanisms and rates remain uncertain (Curtius, 2006). Oxygenated volatile organic compounds (OVOCs) formed from the oxidation of biogenic emissions from vegetation have also been identified as a possible source of secondary aerosol (O'Dowd *et al.*, 2002a). The main sources of aerosols and their estimated source flux is shown in Table 2.1.

2.4.2 Microphysical Processes and the Aerosol Life Cycle

The life cycle of an aerosol in the atmosphere begins with emission as either a primary or secondary particle. Aerosol emitted into the nucleation mode grow to Aitken mode sizes either by condensation of H_2SO_4 vapour onto the aerosol nucleus or by colliding with and sticking to another aerosol particle, a process known as coagulation. Coagulation is important in regions of high aerosol number concentrations because the rate of coagulation is proportional to the square of the aerosol number concentration. Growth of an aerosol particle into the accumulation mode by condensation and coagulation is a slow process. Alternatively, if an Aitken mode particle grows to a sufficient size, it will start to take in water vapour and form a cloud droplet. This critical "activation diameter" is typically 80 nm for a sulfate aerosol, but varies as according to the ambient supersaturation and aerosol composition. Once the aerosol particle forms a droplet, gaseous species such as SO_2 are taken up into the droplet and are oxidised by aqueous-phase reactions. When the droplet evaporates, the residual aerosol nucleus is larger than that prior to activation. This process is known as cloud processing and is the most important source of sulfate aerosol mass in the troposphere (Hobbs, 1993).

Removal of aerosol in the atmosphere occurs through dry and wet deposition. Larger particles ($>$ 1μm) gravitationally settle to the surface with the deposition rate increasing with larger particle mass. Smaller particles ($<$ 1μm) diffuse to the Earth's surface, with the deposition rate fastest for the smaller size particles. Aerosol particles in the accumulation mode (0.1-0.7μm) are least efficiently dry deposited. Wet deposition is the main removal mechanism for particles of these sizes.

2.5 The Sulfur Cycle

The atmospheric sulfur cycle is extremely complex encompassing natural and anthropogenic sources, gas and aqueous phase chemistry, aerosol formation and aerosol composition. The study of the sulfur cycle has been motivated by the clear link between the emission of sulfur species in to the atmosphere and the formation of sulfate aerosols (Charlson *et al.*, 1987; CHARLSON *et al.*, 1992).

The dominant source of sulfur to the atmosphere is anthropogenic emissions of sulfur dioxide (SO_2) from power stations and industrial processes. Natural sources of SO_2 include volcanoes and biomass burning. Gas-phase oxidation of SO_2 forms sulfuric acid, which can nucleate to form new condensation nuclei (CN) or grow existing CN through condensation.

$$SO_2 + OH \xrightarrow{O_2, H_2O} H_2SO_4 + HO_2 \tag{2.29}$$

SO_2 can also be oxidised in cloud droplets to form sulfate, via reactions involving H_2O_2

$$SO_2 + H_2O \rightleftharpoons HSO_3{}^- + H^+ \tag{2.30}$$

$$HSO_3{}^- + H_2O_2 \leftrightharpoons SO_2OOH^- + H_2O \tag{2.31}$$

$$SO_2OOH^- + H^+ \longrightarrow H_2SO_4 \tag{2.32}$$

and O_3;

$$SO_3{}^{2-} + O_3 \leftrightharpoons SO_4{}^{2-} + O_2 \tag{2.33}$$

The reaction with O_3 (Reaction 2.33) is only important at pH>6 (CHAMEIDES, 1984). Reactions 2.31 and 2.32 are independent of pH (MCARDLE & HOFFMANN, 1983). SO_2 that is not oxidised to sulfate in the reactions above is wet deposited to the surface.

In remote marine regions emissions of dimethylsulfide (DMS) constitute the largest natural source of sulfur to the atmosphere (Chin *et al.*, 1996). DMS is formed in the ocean from dimethylsulfoniopropionate, produced by certain species of marine algae, phytoplankton and benthic diatoms (Trevena *et al.*, 2000). Supersaturation of DMS in surface waters forms an air-sea concentration gradient which drives a flux of DMS into the atmosphere proportional to the surface wind speed (Liss & Merlivat, 1986; Nightingale *et al.*, 2000). The estimated flux of DMS to the atmosphere is between 10 and 25 Tg S a^{-1} (Adams & Seinfeld, 2002; Berglen *et al.*, 2004; Spracklen *et al.*, 2005a).

DMS oxidation in the atmosphere can proceed along two separate reaction channels. The abstraction channel is initiated through oxidation by NO_3 and OH (at higher temperatures) and leads to the eventual formation of SO_2 (Barnes *et al.*, 2006).

$$DMS + OH \longrightarrow SO_2 + HCHO + CH_3O_2 \tag{2.34}$$

$$DMS + NO_3 \longrightarrow SO_2 + HNO_3 \tag{2.35}$$

The addition pathway is initiated by OH (favoured at lower temperatures) and leads to the formation of dimethylsulfoxide (DMSO).

$$DMS + OH \longrightarrow DMSO + HO_2 \tag{2.36}$$

DMSO can be deposited to the surface, taken up to existing aerosol particles or oxidised to form methanesulfonic acid (MSA).

$$DMSO + OH \longrightarrow MSA \tag{2.37}$$

The critical difference between the two reaction pathways is the end products of the addition pathway cannot provide a source of sulfate aerosol. DMSO and MSA can only grow existing aerosol particles (Von Glasow & Crutzen, 2004a). Therefore, the degree to which DMS is oxidised along each channel controls the formation and number of aerosol nuclei. A key uncertainty in DMS oxidation is if a cross channel pathway exists for DMSO to be oxidised to form SO_2. A detailed discussion of DMS oxidation and the main uncertainties is given in Barnes *et al.* (2006).

2.6 Tropospheric Halogen Chemistry

In the last 10 years the importance of halogen species, bromine, iodine and chlorine in the troposphere has received large attention. Halogens, particularly bromine and iodine, can provide an important sink for ozone and may perturb HO_x and NO_x partitioning (Chameides & Davis, 1980). In addition, halogens species react with DMS (Toumi, 1994) influencing the marine sulfur cycle and potentially altering the formation of marine aerosols (Von Glasow *et al.*, 2004b).

The discovery that bromine monoxide (BrO) and iodine monoxide (IO) are present at concentrations greater than 1 pptv in the MBL (Allan *et al.*, 2000; Saiz-Lopez *et al.*, 2004; Read *et al.*, 2008) provides evidence that halogen species could play a significant role in determining the chemistry there. Modelling studies by Von Glasow *et al.* (2004b) and Yang *et al.* (2005) suggest bromine compounds are globally important for the oxidative capacity of the troposphere and should be included in global climate models.

This section provides an overview of tropospheric halogen chemistry. The main sources, reaction cycles and evidence for reactive halogen chemistry in the MBL are discussed.

2.6.1 Sources of Halogens

The primary source of bromine to the atmosphere is from sea salt aerosol. Observational evidence for sea salt providing a source of bromine to the atmosphere is provided by measurements of aged sea salt often show a significant bromide depletion compared to fresh sea salt (Ayers *et al.*, 1999; Sander *et al.*, 2003; Newberg *et al.*, 2005; Keene *et al.*, 2009), implying a net source of bromine from the aerosol. Sander *et al.* (2003) published a compilation of the observed bromide depletions in sea salt aerosols shown in Figure 2.2.

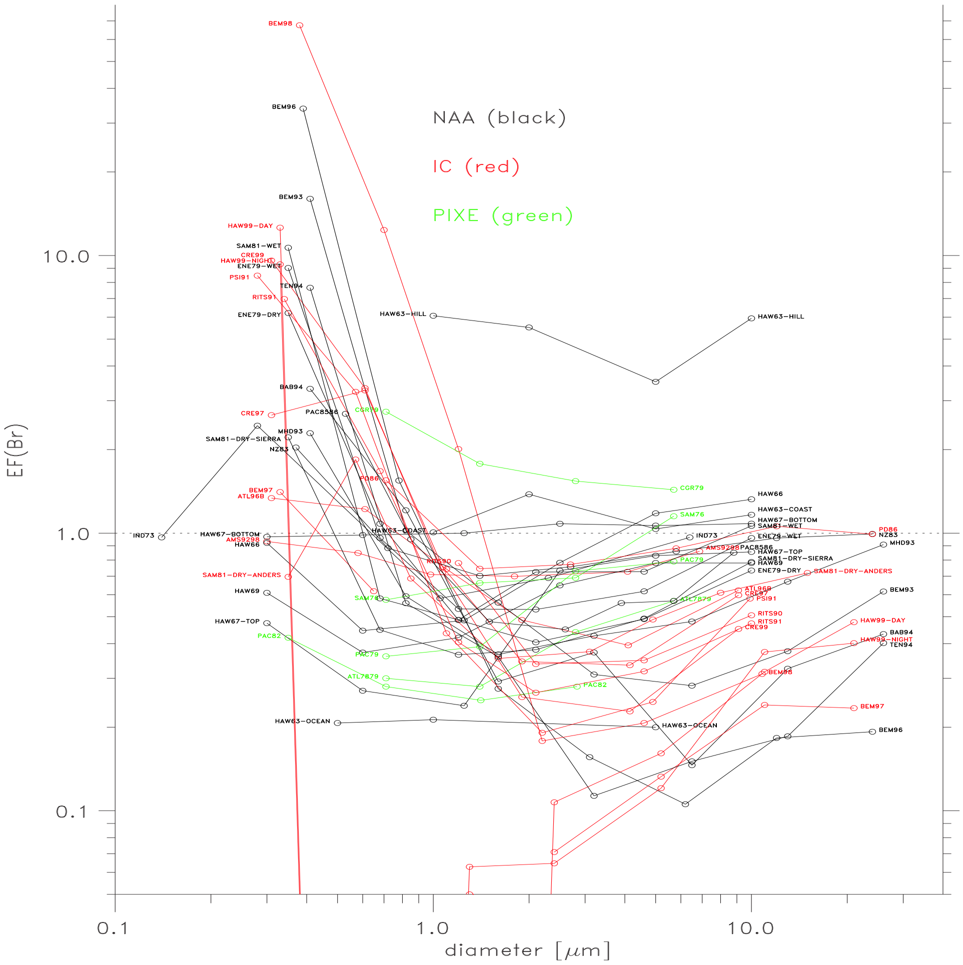

Figure 2.2: Observed size-resolved sea salt bromide enrichment factors (EF), as a function of particle diameter (taken from Sander et al., (2003)). Enrichment factors calculated as the ratio of Br:Na in the measured sea salt compared to the Br:Na ratio in seawater. Na is generally a conservative tracer of sea salt in the MBL (Keene & Galloway, 1986) with the exception of high mineral dust loading regions. Different coloured lines represent different analytical methods. Each line is labelled according to location and year of measurement.

Figure 2.2 shows a clear size dependence in the measured enrichment factor (EF). Sub-micron sea salt particles are often enriched in Br^- (EF>1) and represent a sink of bromine from the gas-phase. The mechanism for the observed enrichment at these sizes is not understood. Sea salt particles from 1 to 10 μm in diameter typically show a significant depletion in bromide ($EF \ll 1$). The largest sea salt aerosols exhibit small depletions in Br^- ($EF \sim 1$). These particles have a lower surface to volume ratio, hence rates of alkalinity titration are slow. Due to their large mass, fast gravitational settling results in short lifetimes. However, because sea salt aerosols larger than 10 μm have a large source, small negative values of EF could potentially constitute a significant source of reactive bromine.

From here on in this thesis sea salt bromide deficits will be referred in terms of depletion factors

(DF) instead of enrichment factors (EF) as shown in Figure 2.2. The DF value is defined as 1.0 - EF.

The mechanism for the release of bromine from sea salt is a complex process. Degassing of HBr from the aerosol is not possible due to its high solubility. As HBr is 600 times more soluble than HCl, one would observe significant Cl^- loss before HBr begins to evaporate. In contrast, all observations show only a small Cl^- depletion and much higher Br^- loss (Sander *et al.*, 1999; Keene *et al.*, 2009).

In polluted regions the reaction of N_2O_5 on the surface of sea salt particles with Br^- can produce $BrNO_2$ and $BrONO_2$ (Behnke *et al.*, 1994), however, this pathway cannot explain the bromide deficits observed in remote regions where NO_x mixing ratios are low.

$$N_2O_{5(aq)} + Br^-{}_{(aq)} \longrightarrow BrNO_{2(g)} + NO_3{}^-{}_{(aq)} \tag{2.38}$$

$$BrNO_{2(g)} + hv \longrightarrow Br_{(g)} + NO_{2(g)} \tag{2.39}$$

Mozurkewich (1995) suggested that an acid-catalysed process could explain the release of bromine from sea salt. This process starts with the uptake of HOBr to a sea salt particle followed by the degassing of the less soluble species Br_2 to the gas-phase where it is photolysed and undergoes a series of reactions with O_3 and HO_2 to reform HOBr (Cycle I).

$$HOBr_{(aq)} + Br^-{}_{(aq)} + H^+{}_{(aq)} \longrightarrow Br_{2(aq)} + H_2O_{(aq)} \tag{2.40}$$

$$Br_{2(aq)} \longrightarrow Br_{2(g)} \tag{2.41}$$

$$Br_{2(g)} + hv \longrightarrow 2Br_{(g)} \tag{2.42}$$

$$2(Br_{(g)} + O_{3(g)} \longrightarrow BrO + O_{2(g)}) \tag{2.43}$$

$$2(BrO_{(g)} + HO_{2(g)} \longrightarrow HOBr_{(g)} + O_{2(g)}) \tag{2.44}$$

The net reaction is hence

$$2HO_{2(g)} + 2O_{3(g)} + Br^{-}{}_{(aq)} + H^{+}{}_{(aq)} \longrightarrow HOBr_{(g)} + 4O_{2(g)} + H_2O_{(aq)} \tag{2.45}$$

Alternatively, the reaction cycle above can proceed via reaction of HOBr with Cl$^-$ in the aerosol phase (Cycle II) (Vogt *et al.*, 1996).

$$HOBr_{(aq)} + Cl^{-}{}_{(aq)} + H^{+}{}_{(aq)} \longrightarrow BrCl_{(aq)} + H_2O_{(aq)} \tag{2.46}$$

$$BrCl_{(aq)} + Br^{-}{}_{(aq)} \longrightarrow Br_{2(aq)} + Cl^{-}{}_{(aq)} \tag{2.47}$$

Cycle II continues as reactions 2.41 to 2.44 in Cycle I. Alternatively, if there is insufficient Br$^-$ for Reaction 2.47, BrCl can volatilise (Cycle III).

$$BrCl_{(aq)} \longrightarrow BrCl_{(g)} \tag{2.48}$$

$$BrCl_{(g)} + hv \longrightarrow Br_{(g)} + Cl_{(g)} \tag{2.49}$$

$$Br_{(g)} + O_{3(g)} \longrightarrow BrO_{(g)} + O_{2(g)} \tag{2.50}$$

$$BrO_{(g)} + HO_{2(g)} \longrightarrow HOBr_{(g)} + O_{2(g)} \tag{2.51}$$

Laboratory studies show Cycles I, II and III are restricted to acidified sea salt aerosols only (pH less than 7) (Fickert *et al.*, 1999; Keene & Savoie, 1998). At low pH the rate of Reaction 2.46 is slow, allowing HOBr to diffuse back out of the droplet before aqueous phase reaction takes place (Fickert *et al.*, 1999). Fresh sea salt particles are emitted at pH 8, similar to that of seawater (Butler, 1982). These particles can then be acidified in remote regions by uptake of trace gases such as SO_2, HNO_3 and organic acids (RCOOH) (Sievering *et al.*, 1992). In polluted regions condensation of HNO_3 and H_2SO_4 vapours provide important sources of aerosol acidity (Davies & Cox, 1998; Song & Carmichael, 1999; Guimbaud *et al.*, 2002).

The degree to which the recycling will go via Cycle I, II or III depends on the level of bromide (Br$^-$) depletion in the aerosol. This is important as Cycles I and II yield 2 Br atoms per HOBr recycled whereas Cycle III only yields 1 Br atom. Fickert *et al.* (1999) showed that Cycle I is favoured when the aerosol is not significantly depleted in Br^- and Cycle II dominates when there is large Br^- depletion.

The requirement for sea salt aerosol to be acidified before it can release Br_2 or BrCl is thought to explain the seasonality in the depletion factors observed at remote marine locations in the southern hemisphere (Ayers *et al.*, 1999; Sander *et al.*, 2003). Higher aerosol depletion factors are observed in the southern hemisphere summer, suggesting a possible link between the source of acidifying sulfur species and halogen liberation from sea salt (Ayers *et al.*, 1999). An additional explanation is the higher total aerosol alkalinity due to higher wind speeds increasing the source of sea salt in the winter (Sander *et al.*, 2003).

Sander *et al.* (1999) also showed uptake of $BrONO_2$ onto sea salt and sulfate aerosol can accelerate loss of Br^- from the aerosol without requiring aerosol acidity if the aerosol is not depleted in Br^-. The reactions of $BrONO_2$ on aerosol also increase loss of NO_x from the gas-phase.

$$BrONO_{2(aq)} + Br^-{}_{(aq)} \longrightarrow Br_{2(aq)} + NO_3{}^-{}_{(aq)} \tag{2.52}$$

Organic halogen compounds provide an additional source of reactive halogens to the atmosphere. Table 2.2 below shows the main organo-halogen compounds, their estimated source fluxes and lifetimes. These compounds are emitted primarily at the ocean surface by phytoplankton and in coastal regions by macroalgae species such as seaweed. The oceanic source represents 90-95% of the total source of all the organic halogen compounds in Table 2.2 with the exception of methyl bromide which has a large industrial source fraction (Law & Sturges, 2006). Shallow coastal areas, tropical oceans and upwelling regions have been identified as of high importance for the emission of oceanic halocarbons (Quack & Wallace, 2003; Butler *et al.*, 2007). Yokouchi *et al.* (2001) found a strong correlation between emissions of CH_3I and sea surface temperature. The organo-halogen compounds are photochemically oxidised to provide a source of reactive halogens. The short lifetime of the organo-halocarbons and highly spatially variable emission rates makes constraining the source magnitudes difficult.

Additional sources of reactive bromine include volcanoes (Bobrowski *et al.*, 2003) and salt flats (Stutz *et al.*, 2002). Methyl bromide is also emitted from biomass burning (Andreae & Merlet, 2001), leaded petrol combustion (Gabriel *et al.*, 2002). In sea ice zones of polar regions frost flowers (Kaleschke *et al.*, 2004) and blowing snow events (Yang *et al.*, 2008) have been suggested to provide a source of reactive bromine.

Table 2.2: Organic halogen species, chemical formula, estimated annual source flux and lifetime. Taken from Clerbaux & Cunnold (2006) and Law & Sturges (2006)

Species	Formula	Est. Source (Tg Br or I a^{-1})	Lifetime
Bromoform	$CHBr_3$	0.2 - 0.8	25 days
Methyl Bromide	CH_3Br		8 months
Dibromomethane	CH_2Br_2	0.122	4 months
Bromochloromethane	CH_2BrCl		5 months
Dibromochloromethane	$CHBr_2Cl$	0.023	2 months
Bromodichloromethane	$CHBrCl_2$	0.019	2 months
Methyl Iodide	CH_3I	0.14-1.30	7 days
Diiodomethane	CH_2I_2		Minutes
Chloroiodomethane	CH_2ICl	0.095	Hours
Bromoiodomethane	CH_2IBr		Hours
Ethyl Iodide	CH_2H_5I		4 days
Isopropyl iodide	C_3H_7I		1.2 days

In addition to emissions of organic iodine compounds a second potentially significant source of reactive iodine to the MBL has been suggested to occur following the deposition of ozone to the ocean surface and subsequent reaction with iodide (I^-) (Garland & Curtis, 1981) in seawater. Garland *et al.* (1980) showed up to 20% of ozone deposited on the ocean surface reacts with I^-. Garland & Curtis (1981) suggested this mechanism could provide a source of I_2 from the ocean surface equivalent to 6 to 12 Tg I a^{-1}. I_2 at the sea surface produced in the reaction of ozone with I^- can also react with dissolved organic matter (DOM) to form dissolved organic iodine (DOI) (Truesdale *et al.*, 1995). Martino *et al.* (2009) showed a small fraction of DOI is present as highly reactive volatile organo-iodine compounds such as CH_2I_2, $CHClI_2$ and CHI_3 which escape into the atmosphere. These compounds are difficult to measure in the atmosphere because of their extrememly short lifetimes, but could provide an important source of iodine to the marine atmosphere.

During periods of extreme low tides I_2 may be injected directly into the atmosphere when ozone deposits on intertidal macroalgae (McFiggans *et al.*, 2004). Field studies have shown extremely high levels of I_2 are observed during low tide events (Saiz-Lopez & Plane, 2004).

2.6.2 Reaction Cycles

The key reaction cycle involving halogen species in the atmosphere is the destruction of ozone (X = Br or I).

$$X + O_3 \longrightarrow XO + O_2 \tag{2.53}$$

$$XO + HO_2 \longrightarrow HOX + O_2 \tag{2.54}$$

$$HOX + hv \longrightarrow X + OH \tag{2.55}$$

$$Net = O_3 + HO_2 \longrightarrow 2O_2 + OH \tag{2.56}$$

The high efficiency of bromine and iodine species for ozone destruction is explained by their inability to form a stable reservoir compound (Fickert *et al.*, 1999). The reaction of Br / I atoms with CH_4 and unsaturated hydrocarbons is extremely slow.

In clean remote regions where XO is an important loss process for HO_2, Reaction 2.54 acts to reduce the $[HO_2]/[OH]$ ratio by delaying the reformation of OH in the HO_x radical cycles (Chameides & Davis, 1980; Davis *et al.*, 1996). Uptake of HOX to aerosol further decreases the $[HO_2]/[OH]$ ratio as HO_2 is lost from the gas-phase. In clean remote regions the self reaction of BrO is far less important than in the Arctic troposphere because BrO mixing ratios are much lower in the MBL.

Halogen atoms also perturb NO_x cycles by shifting the NO to NO_2 ratio and reducing the efficiency of ozone formation (Chameides & Davis, 1980).

$$XO + NO \longrightarrow X + NO_2 \tag{2.57}$$

If the NO_2 is photolysed to produce O_3, Reaction 2.57 would not necessarily represent a source of O_3, because the formation XO consumes an O_3 molecule in Reaction 2.53. NO_2 photolysis can only constitute a source of O_3, if the NO_2 is formed by NO reacting with a compound that is not a member of the odd oxygen (O_x) family such as HO_2 or CH_3O_2.

The reaction of XO with NO_x species can also form short-lived reservoir species (XNO_2 and $XONO_2$). However, both these species are efficiently photolysed.

$$XO + NO \longrightarrow XNO_2 \tag{2.58}$$

$$XO + NO_2 \longrightarrow XONO_2 \tag{2.59}$$

$$XNO_2 + hv \longrightarrow X + NO_2 \tag{2.60}$$

$$XONO_2 + hv \longrightarrow X + NO_3 \tag{2.61}$$

$XONO_2$ is efficiently recycled on aerosol particles. Reactions 2.59 and 2.62 could provide an important NO_x loss mechanism at elevated levels of XO (Sander *et al.*, 1999).

$$XONO_{2(aq)} \xrightarrow{H_2O} HOX_{(g)} + HNO_{3(g)} \tag{2.62}$$

Reaction with oxidised organic species such as HCHO and CH_3CHO provides the main loss reactions for reactive bromine. HBr is highly soluble and will dissolve into cloud droplets and be removed by precipitation.

$$Br + HCHO + O_2 \longrightarrow HBr + CO + HO_2 \tag{2.63}$$

The gas and aerosol phase reactions described above for bromine are shown in Figure 2.3.

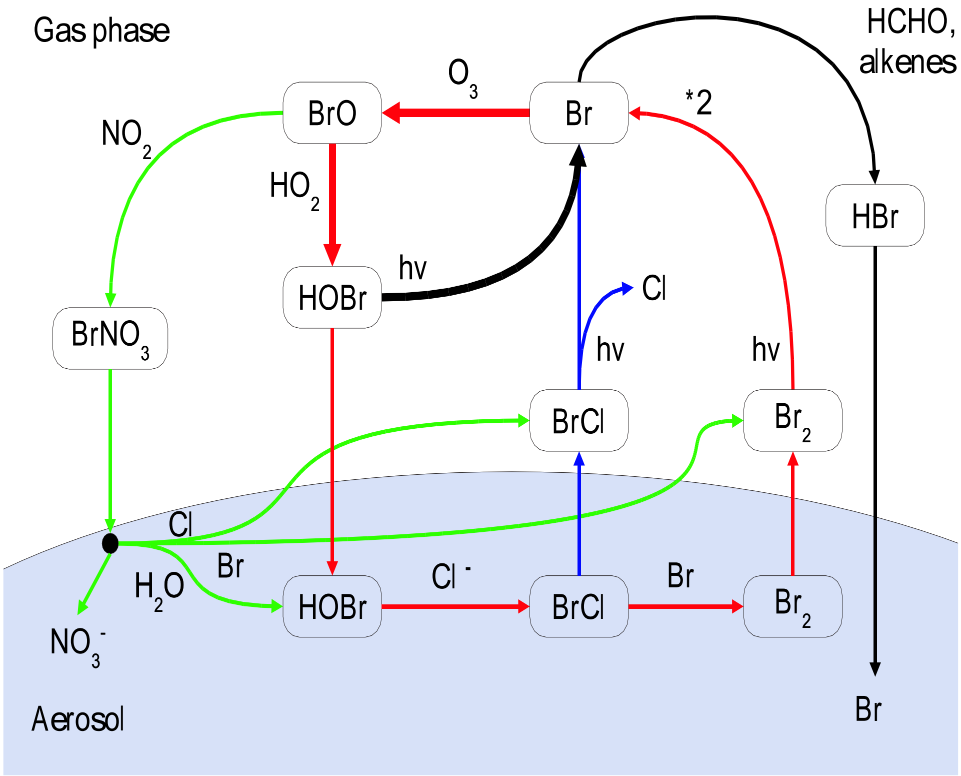

Figure 2.3: Diagram of the important gas and aerosol phase reactions in the recycling of reactive bromine (Sander *et al.*, 1999). Thick lines show bromine-catalysed ozone destruction cycle. Red lines show heterogeneous recycling of HOBr and production of Br_2 if aerosol is not depleted in Br^-. Blue lines show BrCl degassing if aerosol is depleted in Br^-. Formation and recycling of $BrONO_2$ shown by green lines.

BrO may react with dimethylsulfide (DMS) in marine regions. Toumi (1994) first suggested the reaction of BrO with DMS could contribute a significant sink for DMS in the remote MBL.

$$BrO + DMS \longrightarrow DMSO + Br \tag{2.64}$$

Reaction 2.64 may be especially important for the yield of SO_2 from DMS oxidation as it proceeds via the addition pathway yielding DMSO with unit efficiency. As discussed in Section 2.5 the addition pathway is thought to favour growth of existing aerosol over formation of new particles, because its products DMSO and MSA can only condense onto existing aerosol and nucleate to form new particles. Von Glasow & Crutzen (2004a) used a 1D model to confirm that oxidation of DMS by BrO reduces the yield of SO_2. The reaction of IO with DMS is too slow and is not important (Barnes *et al.*, 2006).

Halogen species can also perturb the sulfur cycle by providing additional oxidants for the aqueous phase oxidation of SO_2 (Vogt *et al.*, 1996). Von Glasow & Crutzen (2004a) showed HOBr and HOCl could provide an important oxidation pathway for oxidation of SO_2 and in-cloud sulfate formation.

Heterogeneous chemistry is of particular importance in for halogen species. If gas-phase reactions alone are used in model studies the cycling of HOBr, HBr and $BrONO_2$ is too slow and the model cannot reproduce the observed halogen concentrations (Von Glasow *et al.*, 2002).

A key difference between iodine and bromine is the potential for iodine to form higher oxides and provide a source of new particle formation (O'Dowd *et al.*, 2002b). Iodine-driven particle formation events have been observed during the daytime at low tide at Mace Head, Ireland (O'Dowd *et al.*, 1998).

2.6.3 Observational and Modelling Evidence for Reactive Halogen Chemistry in the Marine Boundary Layer

The most compelling evidence for reactive halogen chemistry in the remote MBL comes from the Cape Verde Observatory, off the West Coast of Africa (16.8°N, 24.9°W). Daytime mixing ratios of IO and BrO were measured at several pptv (Read *et al.*, 2008). At these mixing ratios halogen species would considerably perturb the background chemistry of the MBL. The observations from Cape Verde are especially important because the island is thought to experience only a small localised organo-halogen source due to minimal seaweed cover on the coastlines. This suggests the observations are representative of the larger scale rather than a localised hot-spot for halogen chemistry.

The measurements at Cape Verde are in agreement with measurements of IO at Tenerife where an average mixing ratio of 1 pptv has been observed (Allan *et al.*, 2000). Leser *et al.* (2003) observed BrO in the 1pptv range in the boundary layer north of Tenerife (30-37°, 13°W). Saiz-Lopez *et al.* (2006) measured BrO at Mace Head on the west coast of Ireland, with a maximum daytime mixing ratio of 6.5pptv.

Satellite, balloon and ground-based observations suggest BrO is present at 0.2 - 2.0 pptv in the free troposphere (Wagner & Platt, 1998; Fitzenberger *et al.*, 2000; Wagner *et al.*, 2001; Van Roozendael *et al.*, 2002; Schofield *et al.*, 2004; Hendrick *et al.*, 2007). Satellite measurements of BrO from the global ozone monitoring experiment (GOME) (Burrows *et al.*, 1999) provide global coverage of the spatial extent of BrO in the troposphere. Observations show total troposphere column BrO is in the range 0.5 - 3.0 molecules cm^{-2}, with maxima during the polar springtime and minima in the tropics.

Measurements of ozone in remote marine regions also provide evidence for a role for reactive halogen chemistry. Nagao *et al.* (1999b) identified a sunrise ozone depletion (SOD) at Ogasawara Hahajima Island (26°N,142°E) in the sub-tropical north-west Pacific that cannot be explained by the daytime ozone depletion (DOD) driven by photolysis. The SOD correlated with sea-salt aerosols and the authors concluded this was a likely signal of reactive halogen chemistry.

Analysis of 13 years of observations of ozone concentrations at the Cape Grim, Australia (40°S,144°E) monitoring station also show a SOD mechanism that is distinctive to the DOD (Galbally *et al.*, 2000). The authors also attribute this SOD to reactions involving halogen species. Watanabe *et al.* (2005) also observed strong ozone depletion of 2.5-3.0 ppbv hr^{-1} immediately after sunrise during measurements on board a commercial vessel in the North Pacific during spring 2001.

In an offline 3D chemical transport model Yang *et al.* (2005) showed emissions of reactive bromine from sea salt aerosols and bromocarbons could provide a large sink for ozone in the free troposphere. Ozone concentrations were reduced by 4-6% in the Northern Hemisphere and up to 30% in the Southern Hemisphere high latitudes when an organic and sea salt bromine source was included in the model simulations. Yang *et al.* (2005) estimated the source of bromine to be 1.15 to 2.0 Tg Br a^{-1}. There is significant modelling and observational evidence that BrO could provide an important sink for DMS in the remote MBL. Sciare *et al.* (2000a), using data from the Albatross cruise in the Atlantic Ocean during October 1996, showed that measured OH concentrations were not sufficient to explain the observed daytime variation in DMS in a photochemical box model. They suggested that the presence of 2-3 pptv of daytime BrO would allow the model to match the observations of DMS.

De Bruyn *et al.* (2006) measured DMS mixing ratios in the boundary layer on Oahu, Hawaii (21°N,158°W) during April and May 2000. They observed a decrease in DMS in the early morning that could not be explained by photochemical loss by OH in a box model. This suggested the presence of an additional unidentified oxidation process such as reaction with BrO or dynamical mixing of DMS free-air into the boundary layer from the free troposphere. The authors concluded that dynamical mixing was the likely cause because oxidation of DMS by BrO could not reproduce the observed SO_2 mixing ratios; however, a contribution from BrO could not be ruled out.

The first global model study of BrO and DMS used a global sulfur cycle model in a General Circulation Model (GCM) with fixed oxidants and a constant BrO mixing ratio of 1 pptv in the lowest 1.3 km of the atmosphere (Boucher *et al.*, 2003). This study estimated that BrO could contribute up to 29% of the annual DMS sink.

In a second study, Von Glasow *et al.* (2004b) used a 3D chemical transport model (CTM) with a comprehensive treatment of tropospheric gas-phase chemistry including a bromine scheme to study the impact of a series of bromine source scenarios on DMS oxidation. The source used was that required to sustain a tropospheric inorganic bromine concentration of 7.5×10^7molecules cm^{-3}, as observed in BrO columns, assuming a lifetime of 1-2 weeks in the free troposphere. In the high latitude source scenario the tropospheric DMS burden was reduced by 26%. In the tropical source scenario a 23% reduction in the DMS burden was modelled.

In addition, a number of global modelling studies have suggested oxidation of DMS by OH and NO_3 alone leads to an overestimation in modelled DMS concentrations when compared with observations (Chin *et al.*, 1996; Barth *et al.*, 2000; Spracklen *et al.*, 2005a). This indicates the presence of additional oxidants in the remote MBL, such as BrO.

Modelling studies of iodine chemistry have thus far been restricted to 1-dimensional models. In a column model study Mahajan *et al.* (2010) showed observed emission fluxes of organic iodine compounds could only reproduce about 30% of the observed daytime mixing ratios of IO at Cape Verde. An additional source of iodine from the ocean assumed to be 2% of the ozone deposition flux was required to reproduce the observed daytime IO.

2.7 Global Chemistry and Aerosol Models

In the study of global atmospheric composition two different types of model may be used. General Circulation Models (GCMs) calculate meteorological fields online in the model. Chemical Transport Models (CTMs) use analysed meteorological fields to drive the chemistry and aerosol. GCMs and CTMs generally use an Eulerian grid method approach. The atmosphere is divided up in the horizontal and vertical in to a series of grid boxes, in which each grid box is treated independently and wind fields are used to derive fluxes for the advection of mass from one box to another. GCMs have the advantage that they can account for feedbacks in chemical, meteorological and aerosol variables, but are also computationally expensive. CTM studies cannot account for feedbacks between meteorology and composition, but use real wind and temperature fields, so are useful for investigating processes and sensitivities.

The first generation models of atmospheric composition were very different to today. Early chemistry model studies were only used for short seasonal simulations. Current models can be run over multi-annual timescales, and include more detailed mixed-phase chemical schemes. Early aerosol models carried only a single moment, mass. As these models did not carry the aerosol number, no information on the aerosol size distribution was available. More recent two moment aerosol schemes carry number and mass, allowing complex size distributions to be simulated (Adams & Seinfeld, 2002; Vignati *et al.*, 2004; Spracklen *et al.*, 2005a).

In order to minimise computational expense a number of aerosol models have used prescribed oxidant fields to simulate oxidation of sulfur species and the formation of sulfate aerosols (Spracklen *et al.*, 2005a; Koch *et al.*, 1999). Monthly mean concentrations of OH and NO_3 are typically read in at 6-hourly intervals, to account for the diurnal cycle in the oxidants. Chemistry studies also use prescribed aerosol fields to simulate surface areas for heterogeneous reactions (e.g. Shindell *et al.*, 2001).

The use of prescribed fields is computationally cheaper as it does not require both the aerosol and chemistry schemes to be run simultaneously. However, this method does not account for the two-way interactions between chemistry and aerosols. Gas-phase species control the formation and growth of secondary aerosol particles which in turn impact on gas-phase species through heterogeneous reactions (Liao *et al.*, 2003). Model simulations using prescribed oxidant fields cannot capture depletions in oxidants such as H_2O_2 (Roelofs *et al.*, 1998) or NO_3 (Platt & LeBras, 1997) and, therefore, may not provide an accurate representation of the aerosol size distribution for calculation of cloud condensation nuclei (CCN) number concentration. The use of monthly mean fields will also fail to represent short term variations in oxidants and aerosols caused by transport and deposition.

A number of previous studies comparing coupled chemistry and aerosol schemes with sulfur schemes decoupled from the main photochemistry have reported large decreases in in-cloud sulfate formation in polluted regions. Roelofs *et al.* (1998) reported a 29% reduction in SO_2 oxidation by H_2O_2 in a coupled simulation compared to a simulation using prescribed monthly mean oxidant fields. The author also stated the largest differences in SO_2 oxidation by H_2O_2 are seen in winter when oxidant limitations are more important.

In coupled aerosol-chemistry models (Tie *et al.*, 2001; Liao *et al.*, 2003; Bell *et al.*, 2005) the oxidant and aerosol fields can interact with each other. Coupled models provide a more realistic tool for capturing the complex aerosol and chemical interactions and feedbacks. Oxidant depletions and the subsequent impact on aerosol formation and growth are represented. Allowing for interactions between chemistry and aerosol is critical in studies, for example, that investigate the response in aerosol formation to changing emissions of aerosol precursor trace gases.

2.8 Limitations of Past Modelling Studies

All previous published studies to date of the aerosol model used in this work, GLOMAP have used prescribed oxidant fields (e.g. Spracklen *et al.* (2005a); Manktelow *et al.* (2007); Korhonen *et al.* (2008); Woodhouse *et al.* (2010)). Given that all secondary aerosol formation is controlled by the availability of oxidants, which in turn are responsive to emissions of aerosol precursor trace gases, this represents an important limitation of the GLOMAP model. Previous studies using the chemistry model used in this work, TOMCAT (e.g. Arnold *et al.*, 2005) did not include any aerosol fields for heterogeneous reactions. In Section 2.6.3, the results from three previous global modelling studies of bromine chemistry in the troposphere were presented. Those studies represented an important step forward in understanding reactive bromine chemistry and its impact on oxidative capacity and DMS. However, all three studies contained important limitations. The assumption of 1.0 pptv of BrO in the lowest 1.3 km in Boucher *et al.* (2003) fails to account for any seasonality or any spatial and temporally variability in BrO. Von Glasow *et al.* (2004b) did not explicitly account for a sea salt or short-lived organohalogen source of bromine in the MBL. The Yang *et al.* (2005) study did account for both an organic and a sea salt source of bromine. However, the assumption of a constant sea salt DF of 0.5, is too high at larger sea salt size fractions, which dominate the mass flux, and almost certainly resulted in an overestimate in the sea salt bromine source flux. Also Yang *et al.* (2005) did not account for acidity limitations in the release of bromine from sea salt. In regions of limited availability of acidifying trace gases and high wind speed, hence strong sea salt alkalinity emission, larger sea salt size are unlikely to be acidified and to provide a source of bromine. Again the assumption of a constant DF value would lead to an overestimate in the bromine source from sea salt.

Clearly the studies of Boucher *et al.* (2003), Von Glasow *et al.* (2004b) and Yang *et al.* (2005) have demonstrated bromine could impact the oxidative capacity of the troposphere and DMS oxidation on a global scale. As detailed is Sections 2.5 and 2.6.2, a large contribution of BrO to DMS oxidation could potentially reduce the SO_2 yield from DMS and shift the products towards favouring growth of existing aerosol over formation of new aerosol particles. However, to date no global modelling study has investigated how bromine chemistry impacts marine aerosol formation. All global aerosol modelling studies that have simulated sulfate aerosol formation have assumed DMS is oxidised by OH and NO_3 (Chin *et al.*, 1996; Adams & Seinfeld, 2002; Pozzoli *et al.*, 2008a), thus ignored any contribution from BrO.

In a recent study by Woodhouse *et al.* (2010), the GLOMAP model using prescribed oxidants was used to study how CCN number concentrations may respond to future increases in DMS. Woodhouse *et al.* (2010) suggested the sensitivity of CCN number concentrations to an increased DMS flux is likely to be low. However, that study because of its simple treatment of oxidants ignored any potential chemical feedbacks between DMS, HO_x and NO_x. As reported by Platt & LeBras (1997) and Monks *et al.* (1998) in the remote marine atmosphere DMS can provide an additional sink for OH and NO_3, the only two DMS oxidants in the Woodhouse *et al.* (2010) study. Clearly, oxidant feedbacks could be important for the DMS lifetime, oxidation pathways and CCN formation. Furthermore, if reactive bromine chemistry is present in DMS source regions, chemical feedbacks may be further complicated by interactions between bromine, HO_x and NO_x.

To date there have been no global modelling studies of iodine chemistry in the troposphere that have attempted to address the importance of iodine for oxidative capacity. Mahajan *et al.* (2010) used a column model to show organic iodine fluxes as measured in the vicinity of Cape Verde could not reproduce the observed IO at the Cape Verde atmospheric observatory. The IO could only be reproduced in the model when an additional open ocean source of iodine assumed to be 2% of the ozone dry depositon flux was included.

Chapter 3

Development and Evaluation of a Coupled Chemistry and Aerosol Model

3.1 Introduction

The use of prescribed oxidants for sulfate aerosol formation, or prescribed aerosol fields for heterogeneous chemical reactions, does not allow for two-way interactions between aerosols and chemistry and is an important limitation of such studies (Roelofs *et al.*, 1998; Tie *et al.*, 2001; Bell *et al.*, 2005). Coupled chemistry-aerosol models can account for such interactions and allow complex chemical and aerosol feedbacks to be investigated. In this Chapter the TOMCAT CTM is coupled to the GLOMAP aerosol microphysics scheme. This chapter presents the first results from the newly developed coupled model. The differences in the sulfur chemistry, sulfate aerosol and oxidants in the coupled and uncoupled simulations are explored.

Sections 3.2 and 3.3 describe the TOMCAT and GLOMAP models and key parameterisations. Section 3.4 describes the numerical treatment in the models. In section 3.5 the model development undertaken as part of this thesis is described, results from the model are then discussed. Changes to the sulfur species, aerosol distributions and oxidants in the coupled model are discussed in Section 3.6. The results are interpreted through comparisons with observations from the European Monitoring and Evaluation Programme (EMEP), the Acid Deposition Monitoring Network in East Asia (EANET) and with remote marine measurement stations. In Section 3.7 the first simulations of heterogeneous chemistry in TOMCAT using on-line aerosol surface areas are presented. The impact of heterogeneous uptake of N_2O_5 on aerosol and cloud drops on the background chemistry is discussed.

3.2 TOMCAT Chemical Transport Model

TOMCAT is an Eulerian three-dimensional chemical transport model (CTM) used to study tropospheric and stratospheric chemistry (Chipperfield, 2006). The model has a variable resolution, the longitudinal resolution is regular, but the latitudinal and vertical resolution can be irregular. In the vertical TOMCAT uses a hybrid σ-p coordinate scheme. Near the surface model levels are terrain-following (σ) while at higher altitudes they follow pressure levels. Large-scale transport and meteorology is specified from 6-hourly European Centre for Medium-Range Weather Forecasts (ECMWF) analyses. Vertical mass fluxes are calculated from the divergence of the horizontal flow field. This method assumes the boundary condition that the vertical mass flux is equal to zero when the pressure is zero and ensures the horizontal and vertical mass fluxes are consistent. The use of vertical wind fields from the analyses is not used as the interpolation from the analysis grid to the model grid can lead to inconsistencies between the horizontal and vertical winds. The non-local closure scheme of Holtslag & Boville (1993) is used to calculate vertical turbulent mixing. This scheme explicitly calculates boundary layer (BL) height and includes entrainment of air at the top of the BL.

3.2.1 Advection and Convection

TOMCAT uses a conservation of 2nd order moments advection scheme (Prather, 1986) for horizontal and vertical tracer advection. This scheme maintains sharp tracer gradients and minimises numerical diffusion. The mass flux scheme of Tiedtke (1989) is used to calculate sub-grid scale moist convection in cumulus clouds. This scheme allows cloud fields and the entrainment and detrainment of air associated with updrafts and downdrafts to be represented explicitly.

3.2.2 Dry and Wet Deposition

Dry and wet deposition provides an important sink for trace gases in the troposphere. Dry deposition depends on the meteorological conditions and the surface roughness and the scheme in TOMCAT is based on Giannakopoulos *et al.* (1999). This scheme calculates the rate constant for dry deposition by extrapolating the specified deposition velocity for the species to the middle of the surface model level according to Sorteberg & Hov (1996) which assumes neutral boundary layer conditions. The rate constant for dry deposition (r_d) is determined through division of V_d by the height (H) of the lowest model grid box.

$$r_d = \frac{V_d}{H} \tag{3.1}$$

For the wet deposition scheme frontal precipitation is parameterised using the scheme of Giannakopoulos *et al.* (1999). Excess water (determined from humidity analyses) above supersaturation is allowed to precipitate. Convective precipitation is calculated according to Tiedtke (1989) and is assumed to take place in 20% of the gridbox. Effective Henry's law coefficients H_{eff} are calculated using Henry's constant and the aqueous phase equilibrium constant.

3.2.3 Chemistry Scheme

TOMCAT includes a detailed tropospheric chemistry scheme containing O_x-NO_y-HO_x-C1-C2-C3- NMHCs and isoprene (Law *et al.*, 1998; Arnold *et al.*, 2005). The ASAD numerical solver (Carver *et al.*, 1997) is used to solve time-dependent chemical rate equations. A key feature of ASAD is it allows the use of chemical families. This is computationally advantageous as it reduces the required number of tracers that need to be transported in the model, allows the use of less costly integration packages and reduces the stiffness of the chemical equations. Photolysis reactions are computed using the code of Hough (1988). This scheme considers the direct and scattered beam for 203 wavelength bins from 121nm to 850nm. Photolysis rates are calculated every chemical timestep using cross sections, quantum yields and the solar flux every chemical timestep and account for model profiles of temperature, ozone and a specified simple cloud field (Arnold *et al.*, 2005). A full list of the chemical reactions used in this study is provided in Appendix A.

For uncoupled GLOMAP simulations prescribed monthly mean 6-hourly oxidant fields for OH, NO_3, HO_2, H_2O_2 and O_3 generated from a standard TOMCAT simulation without sulfur chemistry are used. A semi-prognostic treatment for H_2O_2 is used, to allow for depletion by aqueous phase reaction with SO_2. Replenishment of H_2O_2 by HO_2 is limited to the concentration in the prescribed H_2O_2 field (Jones *et al.*, 2001). In coupled simulations the sulfur chemistry, aerosol and background chemistry are fully interactive.

TOMCAT uses process splitting to separate the calculation of advection, convection, boundary layer mixing, emissions and chemistry.

3.2.4 Emissions

Emissions of methane, carbon monoxide, formaldehyde, NO_x and hydrocarbons are taken from the IPCC third assessment report (TAR) (Houghton *et al.*, 2001). Biogenic acetone emissions are inferred from POET monoterpene emissions (Granier *et al.*, 2005). Biogenic isoprene emissions are included from Guenther *et al.* (1995). Emissions of NO_x and CO from biomass burning are taken from the Global Fire Emission Dataset (GFED) and prescribed as climatological monthly means (N. Richards, pers. comm. 2010). A 1°x1° emissions grid is used for monthly mean emissions of key species. Table 3.1 shows the annual mean fluxes of the emitted species in the model.

Table 3.1: TOMCAT surface emission fluxes

Species	Emissions [Tg year^{-1}]
CO	1078
CH_4	324
NO_x	148
CH_3CHO	4.9
CH_3COCH_3	27
HCHO	1.2
CH_3OH	7.9
C_2H_2	13.5
C_2H_4	13.5
C_2H_6	9.6
C_3H_8	8.6
C_5H_8	503

3.3 GLOMAP Aerosol Microphysics Scheme

GLOMAP (GLObal Model of Aerosol Processes) is a detailed size-resolved aerosol microphysics scheme used to study aerosol in the troposphere. GLOMAP has been developed to work in either bin (sectional) (Spracklen *et al.*, 2005a) or mode (modal) form (Mann *et al.*, 2010).

GLOMAP in its full version is capable of modelling up to 5 aerosol components; sulfate (SU), sea salt (SS), black carbon (BC), organic carbon (OC) and dust (DU) in a series of size-dependent soluble or insoluble modes. All particles are assumed to be spherical. GLOMAP carries dry particle radius or mass at 0% relative humidity.

3.3.1 GLOMAP-Bin

GLOMAP Bin uses a two-moment sectional fixed edge, moving centre method to represent the aerosol size distribution (Jacobson, 1997). The model carries total number and average particle mass for each aerosol component in a series of size sections. GLOMAP Bin uses 20 separate size bins, geometrically spaced between 0.001 μm and 25 μm. The requirement to carry total number and average particle mass for each aerosol component in each bin is computationally expensive. However, two moment schemes greatly reduce numerical diffusion (in radius space) and allow for complex aerosol size distributions to be accurately represented (Spracklen *et al.*, 2005a).

3.3.2 GLOMAP-Mode

GLOMAP Mode (Mann *et al.*, 2010) transports particle number and component mass in a series of log-normal modes. The two-moment modal approach is considerably computationally cheaper than the bin model. For example, simulating two aerosol components in two separate soluble modes, requires only only 10 advected tracers instead of 60. The disadvantage is the requirement to make an assumption about the shape of the aerosol size distribution in each mode by fixing the the standard deviation of each mode. Modal aerosol schemes have been implemented in a number of global models (e.g. Liu *et al.*, 2005; Stier *et al.*, 2005).

In GLOMAP-mode the particle number concentration for each mode and the mass concentration of each component are traced following Vignati *et al.* (2004) and Stier *et al.* (2005). Where the mean radius exceeds the mode upper limit the fraction of mass and number that exceeds the upper boundary is transferred using a mode merging scheme to the next largest mode. The modes, size intervals and geometric standard deviations are shown in Table 3.2. In total GLOMAP can simulate up to seven modes, four soluble and three insoluble (Nucleation insoluble is not required because insoluble particles are not significant at these small sizes).

Table 3.2: GLOMAP modes and size ranges used in this study

Mode	Dry Radius Size Interval	Mode Geometric σ	Composition
Nucleation-sol	<5 nm	1.59	SU, OC
Aitken-sol	5 - 50 nm	1.59	SU, BC, OC
Accumulation-sol	50 - 500 nm	1.59	SU, BC, OC, SS, DU
Coarse-sol	>500 nm	2.0	SU, BC, OC, SS, DU
Aitken-insol	5 - 50 nm	1.59	BC, OC
Accumulation-insol	50 - 500 nm	1.59	DU
Coarse-insol	>500 nm	2.0	DU

Mann *et al.* (2010) provides a detailed description of GLOMAP-mode and shows the model accurately simulates present-day aerosol mass and number concentrations, size distributions and CCN number concentrations in the marine and continental atmosphere.

3.3.3 Emissions

Primary Aerosol Emission

Sea salt aerosols are produced by bursting bubbles and breaking waves on the ocean surface (Woodcock, 1953; Blanchard & Woodcock, 1980; Fitzgerald, 1991). Bubble bursting produces film ($r_{dry} < 0.5\mu$m) and jet (0.5μm $\geq r_{dry} \leq 4.0\mu$m) droplets. Larger spume droplets ($r_{dry} >$ 4.0μm) are produced by the tearing of wave crests by the wind. Emission of sea salt particles is a complex process as it is dependent on many different factors including sea surface temperature, fetch, sea state and the instantaneous and past wind velocity field. Sea salt source parameterisations generally calculate the sea salt flux as a function of the 10m wind speed (Gong, 2003; Smith & Harrison, 1998). In TOMCAT the 10m wind speed is calculated by interpolating ECMWF analysed wind speeds between the middle and bottom of the lowest grid cell to 10m. A log wind profile is assumed for the 10m wind calculation in equation 3.2 (Seinfeld & Pandis, 1998).

$$u_{10} = \frac{u^*}{k_v} ln \frac{10}{z_0} \tag{3.2}$$

where u^* is the friction velocity, k_v is the von Karman constant (approx 0.4) and z_0 is the roughness length, assumed to be 0.001m at the sea surface.

The friction velocity, u^* is calculated according to

$$u^* = \frac{k_v}{ln\left(\frac{z}{z_0}\right)} u_z \tag{3.3}$$

where z is the height (m) and U_z is the wind speed at height, z.

GLOMAP allows the use of the sea salt emission parameterisations of Gong (2003) and Smith & Harrison (1998) which are both discussed in Guelle *et al.* (2001). Gong (2003) is based on the sea salt flux parameterisation of Monahan *et al.* (1986) and is valid down to 0.2 μm dry radius. At sizes larger than 4.0 μm dry radius Monahan *et al.* (1986) is thought to overestimate the sea salt flux (Andreas *et al.*, 1995). The Smith & Harrison (1998) scheme is only applicable down to 0.5 μm dry radius. Guelle *et al.* (2001) showed Smith & Harrison (1998) gives a more accurate sea salt mass flux at sizes greater than 1.5 μm than Gong (2003).

Emissions of ultrafine sea salt particles (Martensson *et al.*, 2003) can provide an important source of CCN in remote marine regions (Pierce & Adams, 2006) but are not accounted for in this work.

Secondary Aerosol Precursor Emissions

Emissions of SO_2 from explosive volcanoes (Halmer *et al.*, 2002) and continuously erupting volcanoes (Andres & Kasgnoc, 1998) use recommended injection heights from Dentener *et al.* (2006). Biomass burning SO_2 follows monthly mean emission fluxes taken from GFED v1 (van der Werf *et al.*, 2003) for the year 2000, with injection heights recommended for AEROCOM (Dentener *et al.*, 2006). Anthropogenic emissions of SO_2 from power plants, road transport, industry, off-road transport and shipping are taken from the IIASA inventory (Cofala *et al.*, 2005) for the year 2000.

Emissions of SO_2 from large point sources such as power stations can lead to formation of particulate sulfate in the plume. These small-scale, high density sub-grid processes are not resolved by the model. The fraction of SO_2 that forms particulate sulfate in plumes is a key source of uncertainty in global aerosol simulations (Spracklen *et al.*, 2005b). In this study 2.5% of SO_2 is assumed to be emitted as particulate sulfate according to AEROCOM recommendations and size assumptions as suggested in Stier *et al.* (2005).

Emissions of DMS from the sea surface are calculated using

$$F = K_w \times \left(\frac{C_{air}}{H} - C_{ocean} \right) \tag{3.4}$$

where F is the DMS flux, C_{air} and C_{ocean} are the atmosphere and ocean concentration of DMS, K_w is the sea-air gas transfer velocity and H is Henry's law constant. In normal atmospheric conditions C_{air} is much lower than C_{ocean}, hence the C_{air}/H term is small compared to C_{ocean}.

The DMS seawater concentration is calculated from the Kettle database (Kettle & Andreae, 2000) which uses approximately 30,000 in-situ measurements of DMS to produce a monthly $1^\circ \times 1^\circ$ latitude-longitude climatology. DMS seawater concentrations show a strong seasonal fluctuation as concentrations are controlled by the formation of phytoplankton blooms that require sunlight. Peak seawater DMS concentrations are observed in the summer with the highest values observed in the southern hemisphere high latitudes.

The sea-to-air gas transfer velocity of DMS depends on the horizontal wind speed 10m above the surface. GLOMAP contains two possible sea-to-air transfer velocity parameterisations to be used, Nightingale *et al.* (2000) and Liss & Merlivat (1986). The Liss & Merlivat (1986) parameterisation is based on data from a lake study using the tracer sulfur hexafluride (SF_6) and provides three separate methods for calculating the sea-air transfer velocity, K_w depending on the 10m wind speed. For u_{10} <3.6 ms^{-1} (smooth surface regime), 3.6 $ms^{-1} \leq U_{10} \leq$ 13 ms^{-1} (rough surface regime), and U_{10} >13 ms^{-1} (breaking wave regime). The Nightingale *et al.* (2000) parameterisation is based on two tracer experiments in the North Sea and uses a quadratic dependence of K_w on U_{10n}.

3.3.4 Aerosol Microphysics

GLOMAP treats the main aerosol microphysical processes including coagulation, condensation, dry and wet deposition and cloud processing. These processes are now described.

Nucleation

Gas-to-particle conversion (nucleation) of low volatility gases including sulfuric acid and oxygenated volatile organic compounds (OVOCs) is an important source of nucleation mode particles (Mirabel & Katz, 1974; Marti *et al.*, 1997). The precise mechanism is poorly understood and parameterisations often fail to capture observed nucleation events. Proposed mechanisms include binary (H_2SO_4-H_2O) (Mirabel & Katz, 1974) and ternary (H_2SO_4-NH_3-H_2O) (Kulmala *et al.*,

2000) nucleation. Nucleation is favoured at lower temperatures, low existing particle surface areas and high relative humidity; hence the upper troposphere provides an environment conducive to nucleation.

GLOMAP uses the binary H_2SO_4-H_2O scheme from the equation in Kulmala *et al.* (1998). This scheme prescribes the nucleation rate as a non-linear function of temperature, relative humidity and the H_2SO_4 vapour pressure. The Kulmala *et al.* (1998) scheme is valid for temperatures from 298K to 233K and relative humidity from 10% to 100%. Below 233K the rate at 233K is used.

Boundary layer nucleation events have also been observed (Covert *et al.*, 1992). However, they are not accounted for in this work.

Condensation

Condensation of H_2SO_4 is an important contributor to growth of nucleation mode and Aitken mode particles. This process increases mass and conserves number. The rate of condensation depends on the existing particle surface areas, the concentration of H_2SO_4 and a condensation coefficient. GLOMAP uses the modified Fuchs-Sutugin equation (Fuchs & Sutugin, 1971) to calculate the condensation rate of H_2SO_4 onto an aerosol particle. Free molecular effects for small particles and limitations in the interfacial mass transport are accounted for by using correction factors in the calculation of the condensation coefficient.

Coagulation

Coagulation is the collision and sticking together of aerosol particles to form a single larger particle. In this process aerosol mass is conserved but particle number is not. Hence coagulation represents an important sink for aerosol number concentrations. In polluted regions high number densities of particles in the nucleation and Aitken mode can lead to fast coagulation of these particles and this mechanism represents an important growth process. In clean remote regions, where particle number densities are low, coagulation is slow. GLOMAP-mode includes both coagulation of particles in the same mode (intra-modal) and coagulation of particles in different modes (inter-modal). The coagulation kernel is calculated according to Seinfeld & Pandis (1998).

Dry and Wet Deposition

Dry deposition is important for removing particles larger than 5.0μm diameter which gravitationally settle to the surface and particles smaller than 0.05μm which diffuse to the surface. GLOMAP uses the dry deposition scheme from Zhang *et al.* (2001) which is based on Slinn (1982). The scheme includes the processes of gravitational settling, Brownian diffusion, impaction, interception, particle rebound and sedimentation. The deposition rates depend on the land use category, surface wind speed and particle size. There are 9 possible land use categories in GLOMAP including soil, ice, water and 6 vegetated surface types.

The deposition rate, V_d is given by equation 3.5.

$$V_d = V_g + \frac{1}{R_a R_g} \tag{3.5}$$

where, V_g is the gravitational settling velocity, R_a is the aerodynamic resistance, and R_g is the surface resistance. These terms are described in detail in Zhang *et al.* (2001).

Wet deposition represents an important sink for aerosol in the troposphere, removing as much as 70-80% of all secondary aerosol in temperate latitudes (Hobbs, 1993). GLOMAP simulates removal of aerosol by both nucleation (formation of a droplet around an aerosol nuclei) and impaction scavenging (collection by falling raindrops). Nucelation scavenging uses the rain rate for large-scale (dynamic) and convective rainfall diagnosed in TOMCAT from ECMWF analysis fields. As in Spracklen *et al.* (2005a), large-scale rainout is assumed to remove 99.9% of aerosol at a constant removal rate over a period of 6 hours. Convective rain is assumed to remove aerosol in 30% of the gridbox at a cloud-to-rainwater conversion rate calculated using the Tiedtke (1989) convective parameterization. Only particles in the accumulation and coarse modes are nucleation scavenged. Nucleation scavenging only occurs in gridboxes where precipitation is formed, determined by comparing the rainfall rate in the gridbox with the level above (Pringle, 2006).

GLOMAP uses an assumed raindrop size distribution and size-dependent raindrop-aerosol collection efficiency look-up tables to calculate removal by impaction scavenging. The collection efficiencies are derived according to the Marshall-Palmer distribution with modifications to account for rainfall intensity from Sekhon & Srivasta (1971). The raindrop terminal velocity is calculated using an empirical relationship from Easter & Hales (1983).

Cloud Processing

Cloud processing of aerosol encompasses both the chemical transformation of SO_2 to sulfate ($SO_4{}^{2-}$) in cloud droplets and collision-coalescence of cloud droplets to form a single larger aerosol nucleus. GLOMAP only treats the chemical component of these processes, i.e. the in-cloud sulfate formation pathway.

The process of in-cloud sulfate formation begins when an aerosol particle grows large enough to be activated and starts to take up water vapour to form a cloud droplet. The aerosol dry radius at which the particle "activates" depends upon factors such as the aerosol composition, ambient supersaturation and updraft velocity. Larger particles activate at lower supersaturation's. Also, particles that have a higher solute concentration activate at lower supersaturation (solute effect) (Seinfeld & Pandis, 1998). SO_2 diffuses into the droplet and is oxidised in the aqueous phase by H_2O_2, O_3 (Seinfeld & Pandis, 1998) or a hypohalous acid (HOX) (Vogt *et al.*, 1996). When the water evaporates from the aerosol the sulfate formed from the reaction is left behind and the aerosol grows in size. This represents the dominant mechanism of sulfate mass formation in the troposphere (Hobbs, 1993).

In GLOMAP in-cloud oxidation of SO_2 takes place in low clouds only. The cloud fraction in each grid box is calculated using the vertical cloud fraction and the low cloud field. Low cloud fields are taken from the International Satellite Cloud Climatology Project (ISSAC) D1 database (Rossow & Schiffer, 1999). A globally uniform cloud base of 900hPa is assumed as no information on cloud base is given in the ISCCP dataset. Cloud cover is assumed to be vertically uniform between 900hPa and the cloud top height, which is provided in the ISCCP dataset. The droplet size spectrum is calculated from the aerosol size distribution; soluble particles with a radius larger than 35nm are assumed to be activated to form cloud droplets.

GLOMAP treats aqueous oxidation of SO_2 by H_2O_2 and O_3. The reaction between SO_2 and H_2O_2 is calculated according to Seinfeld & Pandis (1998). Where total loss of either species in a given time step exceeds the number density of the species the reaction is limited to the species number density. The aqueous reaction of SO_2 + O_3 in cloud droplets is also calculated according to Seinfeld & Pandis (1998). This reaction is strongly pH-dependent and effectively shuts off at pH < 4. As cloud droplet pH is not currently calculated in GLOMAP the reaction rate is calculated according to an assumed droplet pH based on the SO_2 mixing ratio. If the SO_2 mixing ratio is greater than 0.5ppbv the droplet pH is set to 4.0. For SO_2 mixing ratios below 0.5ppbv the droplet pH is set to 5.0 (Manktelow, 2008). The treatment of the O_3 + SO_2 reaction in GLOMAP is currently an over simplification. When cloud droplet pH can be calculated in the model this reaction should be updated.

The newly formed dissolved sulfate mass is then partitioned between the soluble accumulation and coarse modes according to their relative number concentrations as in Stier *et al.* (2005). The approach used in Stier *et al.* (2005) restricts cloud processing only to particles already in the accumulation mode. In reality, larger particles in the Aitken mode can activate to form cloud droplets and be cloud-processed. To account for this, in cloudy grid boxes GLOMAP-mode transfers particles of a radius larger than the activation radius to the accumulation mode.

3.4 Numerical Treatment

As noted above, TOMCAT uses operator splitting for chemistry, advection and convection. GLOMAP also uses operator splitting to consider the competition between nucleation and condensation of H_2SO_4. A microphysical sub-timestep equivalent to 0.2 of the chemical timestep is used. In the simulations in this thesis, the advection timestep is 30 minutes. This is split into two chemical timesteps and the microphysical timestep is further split into 5 microphysical timesteps, giving a microphysical timestep of 3 minutes. The completion timestep between nucleation and condensation is half that of the microphysical timestep. The process splitting in TOMCAT/GLOMAP is summarised in Figure 3.1.

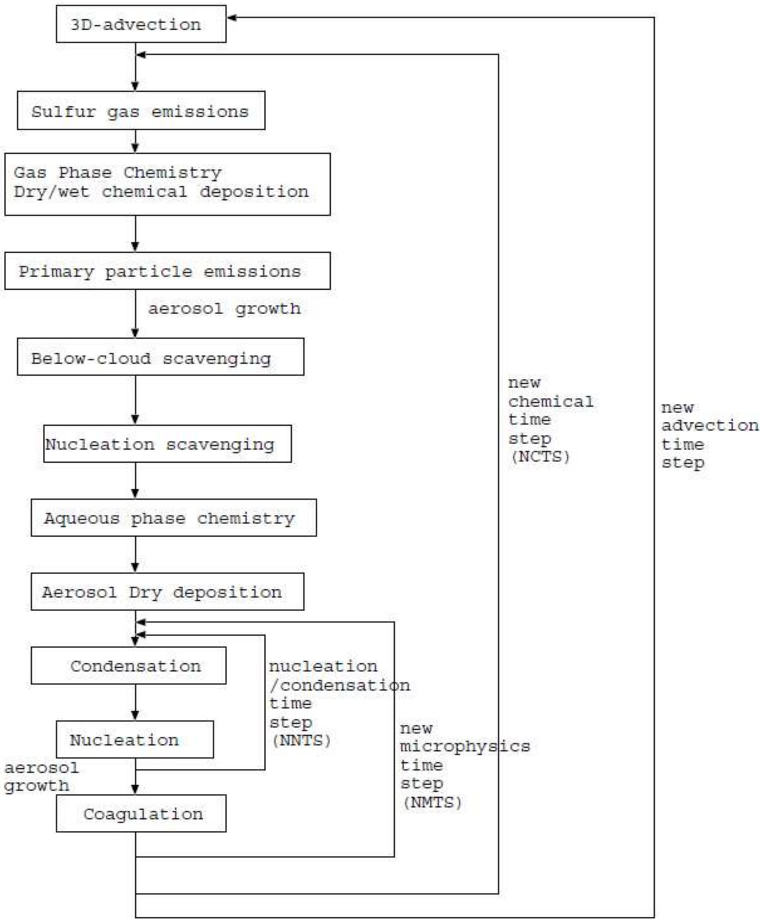
3D-advection
Sulfur gas emissions
Gas Phase Chemistry
Dry/wet chemical deposition
Primary particle emissions
aerosol growth
Below-cloud scavenging
Nucleation scavenging
Aqueous phase chemistry
Aerosol Dry deposition
Condensation
Nucleation
aerosol growth
Coagulation
nucleation /condensation time step (NNTS)
new microphysics time step (NMTS)
new chemical time step (NCTS)
new advection time step

Figure 3.1: Process splitting in the TOMCAT/GLOMAP model. Taken from Spracklen *et al.* (2005b)

3.5 Model Development

This section provides an overview and description of the key model development work undertaken as part of this thesis. This development can be divided into three phases. Phase 1 was the coupling of the GLOMAP aerosol microphysics scheme to the full chemistry in the TOMCAT CTM. In Phase 2 a bromine chemistry scheme was incorporated into the coupled model including parameterisations of organic and inorganic bromine emissions. Finally, in Phase 3 an iodine chemistry scheme was included in the coupled model. The development undertaken as part of phase 3 is presented in Chapter 5 and is not included in this Chapter.

3.5.1 Phase 1 - Coupling of the Aerosol and Chemistry

The first part of this work involved the coupling of the standard tropospheric chemistry to the sulfur chemistry. The second part involved the inclusion of heterogeneous reactions in the model.

The sulfur chemistry scheme used in the original uncoupled GLOMAP model was based on Pham *et al.* (1995). This simple scheme includes 8 sulfur species: DMS, SO_2, H_2SO_4, COS, CS_2, H_2S, DMSO and MSA. The sulfur reaction scheme, shown in Table 3.3, has been updated to include additional reaction products such as HCHO and CH_3O_2 necessary for coupled chemistry studies (Barnes *et al.*, 2006). No photolysis reactions are included in the sulfur scheme. Dry deposition velocities for SO_2, DMSO, H_2SO_4 and MSA are specified from Pham *et al.* (1995). Wet deposition of SO_2 is calculated from the effective Henry's law coefficient which accounts for the effects of solubility and dissociation. The full reaction scheme in the coupled model is shown in Appendix A. Clearly representing all the complexity of DMS oxidation (See Barnes *et al.*, 2006) using just 8 species and reactions requires many assumptions as to exact reaction products and fate of intermediate species. As reported by Lucas & Prinn (2005) the paramaterised scheme of Pham *et al.* (1995) yielded similar DMS levels compared to more detailed DMS oxidation schemes including 50 reactions.

Table 3.3: Sulfur reaction scheme in the coupled TOMCAT-GLOMAP model.

Reactants		Products	Reference
DMS + OH	$\longrightarrow$	SO_2 + CH_3O_2 + HCHO	Atkinson (2000)
DMS + OH	$\longrightarrow$	0.6 SO_2 + 0.4 DMSO + 0.6 CH_3O_2 + 0.4 HO_2	Pham *et al.* (1995)
DMSO + OH	$\longrightarrow$	0.6 SO_2 + 0.4 MSA + 0.6 CH_3O_2	Pham *et al.* (1995)
DMS + NO_3	$\longrightarrow$	SO_2 + HNO_3 + CH_3O_2 + HCHO	Atkinson (2000)
H_2S + OH	$\longrightarrow$	SO_2 +OH	Pham *et al.* (1995)
CS_2 + OH	$\longrightarrow$	SO_2 + COS +OH	Pham *et al.* (1995)
COS + OH	$\longrightarrow$	SO_2 +OH	Pham *et al.* (1995)
SO_2 + OH + M	$\longrightarrow$	H_2SO_4 + HO_2 + M	Pham *et al.* (1995)

The second development stage involved the introduction of heterogeneous chemistry into the model. As described in Section 2.3, reactions on the surface of aerosol particles and cloud droplets can strongly influence the partitioning of NO_x and halogen species (e.g. Jacob (2000); Tie *et al.*

(2001); Pozzoli *et al.* (2008a)). The heterogeneous reaction of N_2O_5 on the surface of aerosols and cloud droplets has been included in the coupled model simulations.

$$N_2O_{5(g)} + H_2O_{(aq)} \longrightarrow 2HNO_{3(g)} \tag{3.6}$$

The heterogeneous reaction rate coefficient is calculated using the equation in Schwarz (1986).

$$k^{'} = \frac{A}{\left(\frac{r}{D_g}\right) + \left(\frac{4}{\gamma\omega}\right)} \tag{3.7}$$

Where A is the aerosol surface area (cm^2 cm^{-3}), ω is the mean molecular speed (cm s^{-1}), D_g is the gas diffusion coefficient (cm^{2}s^{-1}) and γ is the uptake coefficient.

The first term in the denominator in Equation 3.7 accounts for uptake to the particle surface by gas-phase diffusion. This term dominates for cloud droplets (r>10μm); i.e. uptake of gases to cloud droplets is generally diffusion limited. The diffusion coefficient D_g typically has a value in the troposphere of 0.2 cm^{2}s^{-1}.

The second term in the denominator in equation 3.7 accounts for free molecular collisions of gas molecules with the aerosol surface. This is controlled by the value of γ; the probability that a molecule impacting the surface of an aerosol will undergo reaction (Schwarz, 1986; Ravishankara, 1997). γ accounts for the processes of absorption into the aerosol phase, known as the accommodation coefficient (α) and the reaction probability. γ is determined through laboratory experiments and varies as a function of temperature, relative humidity and aerosol composition (Jacob, 2000). In this work the γ for N_2O_5 is calculated according to Evans & Jacob (2005) which is based on Kane *et al.* (2001) and Hallquist *et al.* (2003). Uptake of gases to aerosol in the Aitken and accumulation mode is generally limited by the free-molecular collision rate.

Reaction 3.6 occurs on aerosol particles and cloud droplets. Some previous global modelling studies that have included heterogeneous reactions have used a prescribed aerosol and cloud droplet surface area and number density. For example Yang *et al.* (2005) assumed a simple aerosol surface area density of 2μm cm^{-3} in all grid boxes without any precipitation. For clouds a mean droplet radius of 10 μm and droplet number density of 70 cm^{-3} was assumed in cloudy fireboxes. Other studies have used prescribed aerosol surface area fields output from aerosol simulations (e.g Wang *et al.*, 1998). Studies that included an on-line aerosol mass only (single moment) scheme (e.g. Tie *et al.*, 2001; Liao *et al.*, 2003) are advantageous over using prescribed field as they can account for interactions between gas-phase species and the aerosol mass, but, are limited by the requirement to assume a shape of the entire aerosol size distribution. For example Liao *et al.* (2003) assumed a log normal size distribution with a median radius of 0.05 μm and a geometric standard deviation of 2.0 for sulfate aerosol. Clearly having to make such an assumption is not ideal considering the aerosol size spectra can shift according to the source type (primary or secondary), source proximity and efficiency of removal processes.

Coupled chemistry and aerosol schemes that simulate aerosol number and mass (two-moment schemes) (e.g. Adams & Seinfeld, 2002; Spracklen *et al.*, 2005a; Pozzoli *et al.*, 2008a) provide the most advanced and accurate tool for calculating heterogeneous reactions. Aerosol bin schemes (e.g. Adams & Seinfeld, 2002; Spracklen *et al.*, 2005a) provide detailed information of the aerosol size distribution but are computationally expensive. Modal aerosol schemes have been shown to accurately reproduce aerosol size and number distributions (Pozzoli *et al.*, 2008a; Mann *et al.*, 2010) while being significantly computationally cheaper. In this study a two-moment modal aerosol scheme is used. The aerosol surface area in each mode (cm^2 cm^{-3}) in GLOMAP is calculated as

$$A = 4\pi {r_w}^2 N exp^{\left(2ln^2\sigma\right)} \tag{3.8}$$

where r_w is the average wet radius an aerosol particle in the mode (cm), N is the number concentration in the mode (cm^{-3}) and σ is the mode geometric standard deviation.

More recently, next generation aerosol models have been developed that also simulate internally mixed particles and thus the aerosol mixing state, important for the uptake (γ) of gas-phase species to aerosol (Pozzoli *et al.*, 2008a). Internally mixed particles are not accounted for in this study.

3.5.2 Phase 2 - Introduction of Bromine Chemistry

The bromine chemistry scheme incorporated into TOMCAT is based on that published in Yang *et al.* (2005). The scheme includes 7 inorganic and 6 organic bromine species shown in Table 3.4.

Table 3.4: Bromine species included in the model

Inorganic	Organic
Br	CH_3Br
BrO	CH_2Br_2
HOBr	$CHBr_3$
HBr	CH_2BrCl
$BrNO_2$	$CHBr_2Cl$
$BrONO_2$	$CHBrCl_2$
Br	

The reactions in the bromine scheme in the model are shown in Appendix A. Dry deposition velocities for HBr and HOBr and values for determining an effective Henry's law coefficient required for wet removal for HBr, HOBr, and Br_2 are taken from Yang *et al.* (2005).

Two heterogeneous reaction are included in the bromine scheme.

$$BrONO_{2(g)} + H_2O_{(aq)} \longrightarrow HOBr_{(g)} + HNO_{3(g)} \tag{3.9}$$

$$HOBr_{(g)} + HBr_{(g)} \longrightarrow Br_{2(g)} + H_2O_{(aq)} \tag{3.10}$$

For HOBr, HBr and $BrONO_2$ γ values are taken from Yang *et al.* (2008). Reaction 3.9 occurs on aerosol particles and cloud droplets; reaction 3.10 only occurs on aerosols. No pH dependence of the reations is assumed.

3.5.2.1 Organic Bromine Emissions

Emissions of the 6 organic bromine species are taken from Warwick *et al.* (2006) Scenario 2B. Warwick *et al.* (2006) tested 6 different source scenarios in a 3-D CTM against measurements of the latitudinal and vertical distributions of bromocarbons (Schauffler *et al.*, 1999). Scenario 2B assumes 75% of the total flux is emitted over the tropical oceans (20°N to 20°S) and 25% is emitted over the mid-latitude oceans (20° to 50° latitude). Warwick *et al.* (2006) also tested a globally uniform oceanic source and a tropical oceans only souce distribution. Scenario 2B was found to give the best agreement with the observations. This source distribution Table 3.5 shows the species and their annual assumed source fluxes in the model. No seasonal cycle or interannual variability is included in the emissions.

Table 3.5: Emissions of organic bromine in the coupled model

Species	Emission Flux Tg Br yr^{-1}
$CHBr_3$ Coastal	0.295
$CHBr_3$ Ocean	0.300
CH_2Br_2	0.113
CH_3Br	0.131
CH_2BrCl	0.0068
$CHBr_2Cl$	0.023
$CHBrCl_2$	0.016
Total	**0.885**

Emissions of bromoform ($CHBr_3$) are separated into a tropical coastline source and an open ocean source as recommended by Warwick *et al.* (2006). The open ocean component is distributed as 75% in the tropical oceans and 25% in the mid latitude oceans. Coastlines are determined from the MODIS percentage water cover maps (Saloman *et al.*, 2004). All inland lakes are removed from the data and coastal gridboxes are determined as where the percentage water cover in the box is greater than 10% and less then 90%.

The longer lived halon species are not included in this study as they are not expected to contribute a significant source of bromine to the troposphere (Clerbaux & Cunnold, 2006).

3.5.2.2 Sea Salt Bromine Emissions

Emission of bromine from sea salt also provides a large source of bromine to the troposphere. As discussed in Section 2.6 the release of bromine from sea salt involves complex mixed phase reactions, requiring the calculation of the aerosol pH. To include all the required reactions in a global model would be computationally very expensive.

An alternative method, requiring significantly less computational cost, involves using observed size-resolved sea salt bromide depletion factors. Sander *et al.* (2003) compiled a database of sea salt bromide depletion factors collected by field campaigns dating back to 1960. The use of observed depletion factors allows the bromine flux from sea salt to be constrained, without the need for mixed-phase chemistry in the model. If the bromide deficit (DF) is known, the bromine emissions can be calculated from the mass flux of sea salt (SSMF) and the mass ratio (MR) of Br/Na in the aerosol ($0.00223\mathrm{g\ g^{-1}}$) using equation 3.11.

$$Br\ flux = SSMF \times MR \times DF \tag{3.11}$$

This method was first used in a global modelling study to estimate a source of bromine from sea salt aerosol by Yang *et al.* (2005). They used the dataset of Sander *et al.* (2003) to calculate a series of size-dependent sea salt bromide depletion factors. This method segregated the observations into a series of geometrically spaced size bins. The final DF values were obtained by interpolating the mean DF values in each size bin onto a sea salt emission grid.

In the southern hemisphere observations show the sea salt bromide DF exhibits a distinct seasonal cycle (Ayers *et al.*, 1999; Sander *et al.*, 2003). Maximum DF values are seen in the summer and minimum in winter. This seasonality may be driven by changes in biological productivity and emissions of acidifying trace gases, sea salt aerosol loading or a combination of the two. In order to account for the seasonality in DF in the southern hemisphere, Yang *et al.* (2005) used a correcting sine function south of 30°S shown in equation 3.12.

$$DF = \frac{DF_{max} + \frac{(DF_{min} - DF_{max})}{2}\left(sin\left(\left(\frac{month}{6} - 0.5\right)\pi\right) + 1\right)}{0.6} \tag{3.12}$$

Using this method Yang *et al.* (2005) calculated a Br flux of 1.15 Tg Br $\mathrm{yr^{-1}}$ for the Smith & Harrison (1998) sea salt source function and 2.09 Tg Br $\mathrm{yr^{-1}}$ for the Gong (2003) sea salt source function.

A problem with the method used by Yang *et al.* (2005) is that it does not fully account for potential limitations in the acidification of the sea salt required for the release of Br_2 and BrCl (Keene & Savoie, 1998; Fickert *et al.*, 1999). The Yang *et al.* (2005) scheme also does account for seasonal variations in sea salt bromide depletions as observed in the southern hemisphere. However, sea salt fluxes can vary by an order of magnitude over a time period of hours as the sea salt flux varies as a power function of the windspeed (Gong, 2003). Higher wind velocities result in an increase in the total alkalinity flux and a shift in the emitted sea salt size spectrum towards larger particles with smaller surface-to-volume ratios and shorter lifetimes due to faster rates of deposition (Sander *et al.*, 2003). During periods of high windspeed the ambient acidity may be unable to acidify the sea salt size spectrum and Br emissions will be restricted to smaller size fractions significantly reducing bromine emissions.

In addition, in regions of high precipitation, sea salt may be rained out on a much shorter timescale than loss due to dry deposition. The shorter lifetime of the particle may restrict acidification and prevent the release of bromine from the aerosol. Not accounting for the lifetime limitation will lead to an overestimate in the bromine source from sea salt.

In this work, in order to account for the acidification requirement, the parameterisation of Yang *et al.* (2005) has been extended to include the work of Alexander *et al.* (2005). As in Alexander *et al.* (2005), alkalinity and acidity fluxes are calculated and compared in each aerosol size bin. The alkalinity flux is calculated according to the mass flux of fresh sea salt (in kg) multiplied by 0.07 following Gurciullo *et al.* (1999). The 0.07 represents the equivalent amount of acidity required to titrate the alkalinity in 1.0 kg of dry sea salt assuming the alkalinity of sea salt aerosol is equal to that of seawater. The acidity flux is determined by the uptake of SO_2 to fresh sea salt aerosol and the dry deposition flux of HNO_3. A dry deposition velocity of 1.0 cm s^{-1} to the ocean surface is assumed. The lifetime of HNO_3 against deposition is $\approx$1 day compared to $\approx$1 hour for uptake by sea salt. Therefore, it is assumed that uptake by sea salt dominates (assuming alkaline sea salt) (Alexander *et al.*, 2005). Uptake of SO_2 is calculated using equation 3.7. The uptake coefficient for SO_2 on sea salt is assumed to be 0.05 for relative humidities greater than 50% and 0.005 for relative humidities less than 50% following Song & Carmichael (2001). Uptake of H_2SO_4 to sea salt is not accounted for as Alexander *et al.* (2005) found this to be a negligible source of aerosol acidity compared to SO_2 and HNO_3.

Size bins are only assumed to be acidified if the alkalinity flux is exceeded by the acidity flux during the model dynamical timestep of 30 minutes or during the lifetime of the sea salt aerosol in the bin, whichever is shorter. The particle lifetime is calculated according to the rate of wet and dry deposition. If the aerosol size bin has been acidified the emission of Br_2 into the lowest model grid box only is calculated using equation 3.11.

The DF value in this study is calculated by segregating the data in Sander *et al.* (2003) into a series of size bins and then interpolating the median DF in each bin onto the GLOMAP aerosol size grid. This study uses the median DF values in order to remove the influence of outliers in the dataset that strongly influence the mean. Sub-micron sea salt size bins have a negative DF down to -1.98. For super-micron size bins up to 8 μm dry radius the DF varies from 0.21 to 0.51. The DF values in each size bin are shown in Table 3.6. The sea salt emission parameterisations of Gong (2003) is used for sizes below 1.5μm dry radius and Smith & Harrison (1998) for sizes larger than 1.5μm dry radius. For latitudes south of 30°S the DF values are corrrected to account for seasonality as shown in equation 3.12. At the smallest sizes, where DF values are negative the sea salt particles are assumed to provide a sink for gas phase Br_2. However, these size fractions represent such a small fraction of the total sea salt mass flux, loss of BR_2 is almost negligible.

Table 3.6: Sea salt bromide depletion factors used in this study, calculated from Sander *et al.* (2003)

Size Bin Mid Dry Radius (μm)	Depletion Factor (DF)
0.12	-1.98
0.19	-0.58
0.30	0.31
0.48	0.45
0.77	0.51
1.23	0.48
2.00	0.29
3.14	0.39
5.02	0.36
8.03	0.21
12.8	0.00

The extension of sea salt bromine emission scheme in this study is clearly an improvement on the Yang *et al.* (2005) study as limitations in the acidification of sea salt aerosols are accounted for. Note that the model studies presented in this thesis do not include a source of bromine from blowing snow on sea ice. Yang *et al.* (2008) showed this might represent a large source of bromine in polar regions.

3.5.2.3 Aqueous Phase Reaction of HOBr + SO_2

Aqueous phase reaction of dissolved SO_2 to sulfate S(VI) is the most important process contributing to sulfate mass formation in the troposphere (Seinfeld, 1999). As discussed in Section 3.3.4 the principal oxidants for SO_2 in the aqueous phase are thought to be H_2O_2 and O_3 (Hoffmann & Calvert, 1985). However, a number have studies have proposed the potential importance of HOBr and HOCl as aqueous phase oxidants for SO_2 (Vogt *et al.*, 1996; Von Glasow & Crutzen, 2004a).

In GLOMAP the aqueous phase concentration of a gas-phase species, A is calculated using Henry's law;

$$[A_{aq}] = H_A p_A \tag{3.13}$$

where p_A is the partial pressure of species A and H_A is Henry's law coefficient at temperature, T determined from;

$$H_A = H_A(298) exp\left(\frac{\Delta H_A}{R}\left(\frac{1}{T} - \frac{1}{T_{298}}\right)\right) \tag{3.14}$$

ΔH_A is the heat of dissolution of A (kcal mol^{-1}), $H_A(298)$ is Henry's law coefficient of A at 298K (M atm^{-1}) and R is the universal gas constant (J mol^{-1} K^{-1}) (Seinfeld & Pandis, 1998). For HOBr ΔH_A = -11.64 kcal mol^{-1} and H_{298}=93.0 M atm^{-1} (Sander *et al.*, 2005). For SO_2 ΔH_A = -6.23 kcal mol^{-1} and H_{298}=1.23 M atm^{-1} (Seinfeld & Pandis, 1998; Pandis & Seinfeld, 1989).

Dissolution of SO_2 in water results in the formation of three chemical species: The sulfite ion ($SO_3{}^{2-}$), the bisulfite ion ($HO_3{}^-$) and hydrated SO_2 ($SO_2 \cdot H_2O$), collectively termed S(IV). The relative partitioning of dissolved SO_2 to each species depends on the droplet pH. In the pH range 2-7, most S(IV) partitions to $HSO_3{}^-$. A more detailed explanation of aqueous SO_2 chemistry is provide in Seinfeld & Pandis (1998).

The rate of the reaction of HOBr and SO_2 in the aqueous phase is then given by equation 3.15 according to the EMAC (formerly MESSY) model (Jockel *et al.*, 2006).

$$-\frac{d[S(IV)]}{dt} = \left(k_1[HSO_3{}^-] + k_2[SO_3{}^{2-}]\right)[HOBr_{(aq)}] \tag{3.15}$$

where k_1 = 5.0x10^9 M^{-1}s$^-$1 and k_2 = 5.0x10^9 M^{-1}s$^-$1. The product of reaction 3.15 is Br_2 which degasses from the droplet. In the model it is assumed each HOBr + SO_2 reaction releases 0.5 Br_2.

3.6 Model Evaluation and Interpretation of Coupled and Uncoupled Model Simulations

Chapter 2 highlighted the limitations of using prescribed oxidant and aerosol fields in atmospheric composition studies. All previous GLOMAP studies used prescribed oxidant fields, while previous TOMCAT simulations ignored aerosol and had a very crude representation of heterogeneous chemistry.

In this work the TOMCAT CTM and GLOMAP aerosol microphysics scheme have been coupled together to allow for interactions between the aerosol and chemistry. This chapter presents the first results from the newly developed coupled model. The sulfur chemistry, sulfate aerosol and background chemistry in the coupled model are discussed and compared with uncoupled simulations of chemistry and aerosols. The discussion focuses on the principal constituents of the sulfur cycle, DMS, SO_2 and ${SO_4}^{2-}$ and changes in oxidant chemistry. The model simulations are compared with observations from the European Monitoring and Evaluation Programme (EMEP) and the Acid Deposition Monitoring Network in East Asia (EANET) measurement network and remote marine ground stations.

An early application of the coupled model was in the study of Schmidt *et al.* (2010) to study the impact of the 1783–1784 AD Laki eruption on global aerosol formation and cloud condensation nuclei (CCN). The coupled model allowed for interactions between SO_2, oxidants and aerosol formation to be captured that could not have been represented as accurately had prescribed oxidant fields been used given the strong coupling between SO_2 and H_2O_2 chemistry in high SO_2 source regions (Roelofs *et al.*, 1998). This paper is provided in Appendix B, but no further results are shown in this thesis.

3.6.1 Model Experiments

For the discussion of DMS, SO_2, ${SO_4}^{2-}$ and CCN the coupled model is compared with a GLOMAP simulation that uses prescribed oxidant fields to drive the sulfur chemistry. For the discussion of the changes in the oxidant fields the coupled model is compared with a TOMCAT simulation that does not include sulfur chemistry. From here on the uncoupled GLOMAP aerosol simulation will be referred to as **GLO**, the TOMCAT chemistry-only simulation will be referred to as **CHEM** and the coupled simulation will be referred to as **COUPL**.

All simulations are for 2004 allowing for a spin-up period of 4 months. The model was run at a resolution of 2.8° ×2.8° and forced by ECMWF analyses. The vertical resolution uses 31 hybrid σ-p levels from the surface to 10 hPa. Emissions of DMS are calculated using Liss & Merlivat (1986). In-cloud oxidation of SO_2 takes place via reaction with H_2O_2 and O_3. The sea salt emission parameterisations of Gong (2003) is used for sizes below $1.5\mu m$ dry radius and Smith & Harrison (1998) for sizes larger than $1.5\mu m$ dry radius.

Prescribed oxidant fields used in the **GLO** simulation are taken from a TOMCAT simulation that did not include sulfur chemistry. In the simulations only sulfate and sea salt aerosol components are simulated in a series of four externally mixed modes; water-soluble nucleation, Aitken, accumulation and coarse.

3.6.2 Model Evaluation Data

Evaluation of the **COUPL** model in this chapter uses observational data from the EMEP and EANET acid deposition networks. The EMEP network is a European programme tasked with monitoring atmospheric concentrations of ozone, heavy metals, particulate matter and acidifying trace gases such as SO_2, sulfate and NO_x. More information about EMEP and the data used in this study is available on the EMEP website (http://www.emep.int).

The EANET observation network is the East Asian programme that monitors and reports on measurements of acidifying trace gases. EANET is a transnational organisation that has monitoring stations in countries throughout the region, including Russia, China, Japan and Malaysia. In this study only sites classified by EANET as “Remote” are used for comparison. Sites classified as “Urban” or “Rural” are not used. More information about EANET is available on the EANET website (http://www.eanet.cc).

3.6.3 Coupled vs Uncoupled Model - Changes in DMS

DMS, as discussed in Section 2.5, is an important precursor species to sulfate aerosol formation in remote marine regions. Understanding the chemical sinks of DMS is important for model studies to accurately predict the DMS lifetime and its transport to the free troposphere. In this section differences in DMS oxidation in the **COUPL** and **GLO** simulations are presented and explained. The model simulations are evaluated through comparison with observations from Amsterdam Island, Cape Grim and Dumont Durville.

The surface mixing ratio of DMS in the **COUPL** model is shown in Figure 3.2. The largest DMS mixing ratios occur over the southern hemisphere (SH) oceans during the December, January and February (DJF). During this period the **COUPL** model simulates maximum DMS mixing ratios of 500 - 1000 pptv. This is consistent with previous model studies that show peak DMS mixing ratios in the SH high latitude oceans (Berglen *et al.*, 2004). In June, July and August (JJA) the peak DMS mixing ratios shift to the northern hemisphere (NH) oceans.

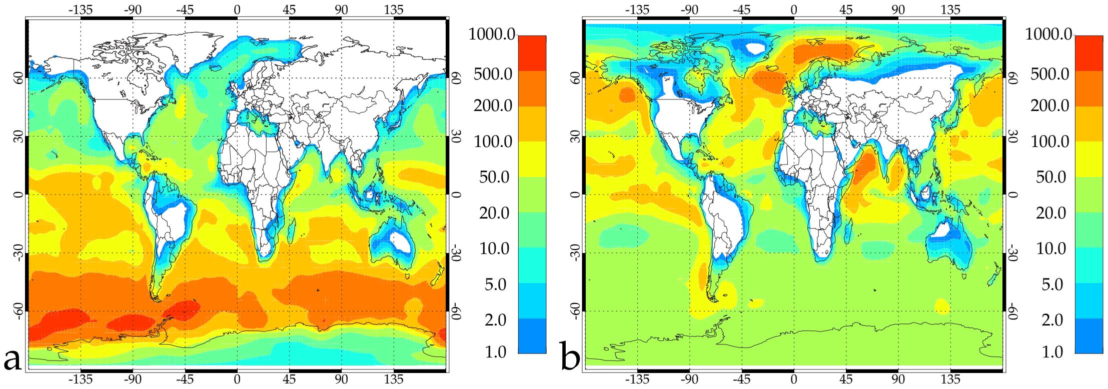

Figure 3.2: Surface DMS mixing ratio (pptv) in the **COUPL** simulation in (a) DJF and (b) JJA.

The change in DMS between the **COUPL** and **GLO** simulations (Figure 3.3) shows a large increase in the surface mixing ratio of DMS in the **COUPL** simulation. The largest increase is simulated in SH oceans during DJF when DMS increases by greater than 40 pptv throughout the 40-70°S latitude band. During JJA increases in DMS in the **COUPL** model are less significant with 40 pptv increases simulated in parts of the North Atlantic, North East Pacific and Arabian Sea. At high northern latitudes surface DMS decreases in the **COUPL** model due to increased availability of oxidants. This is because the **COUPL** simulation does not include heterogeneous uptake of N_2O_5 to aerosol resulting in a higher DMS sink from reaction with NO_3.

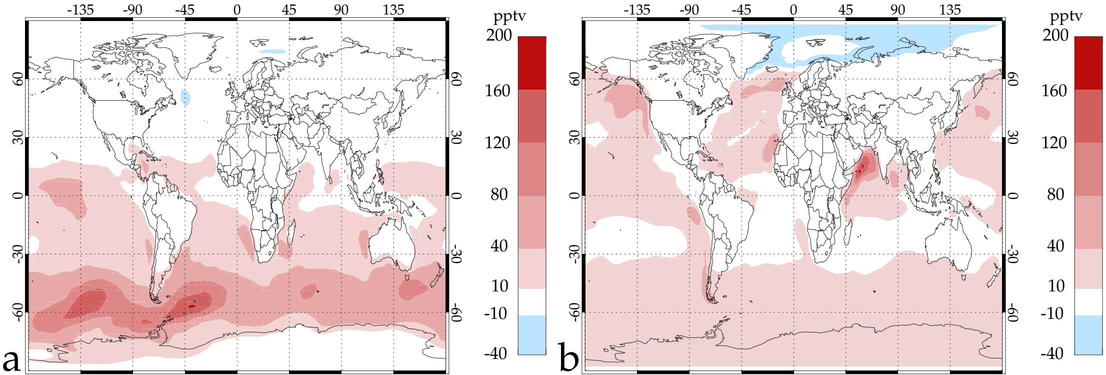

Figure 3.3: Absolute change in surface DMS mixing ratio (pptv) in the **COUPL** model simulation compared to the **GLO** simulation in (a) DJF and (b) JJA.

Table 3.7 compares the DMS budgets in the **GLO** and **COUPL** simulations with the results from previous global coupled aerosol-chemistry modelling studies. The DMS burden shows a significant increase in the **COUPL** simulation compared to the **GLO** simulation and improves the comparison with previous studies.

Table 3.7: DMS budgets for 2004 in the **COUPL** and **GLO** simulations and previously published coupled aerosol-chemistry studies.

	GLO	**COUPL**	**AS02**	**B04**	**E04**	**P08**
DMS emissions (Tg S)	12.55	12.55	10.8	11.95	19.2	
DMS + OH	11.4%	70.7%		72.6%		
DMS + NO_3	88.6%	29.3%		27.4%		
DMS Burden (Tg S)	0.021	0.05	0.05	0.06	0.15	0.05
DMS lifetime (days)	0.60	1.35	1.7	1.93	1.7	2.8

AS02=Adams & Seinfeld (2002), **B04**=Berglen *et al.* (2004), **E04**=Easter *et al.* (2004), **P08**=Pozzoli *et al.* (2008a).

Table 3.7 also shows a large increase in the DMS lifetime in the **COUPL** simulation from 0.60 to 1.35 days. The longer DMS lifetime in the **COUPL** model is in better agreement with previous studies. A longer DMS lifetime suggests a decrease in oxidant concentrations in the **COUPL** model. In the simulations in this chapter DMS is only oxidised by OH and NO_3. The annual mean oxidation of DMS by OH and NO_3 in the **COUPL** and **GLO** simulations is shown in Figure 3.4. There are large changes in the DMS oxidation patterns between these simulations. In the North Atlantic and Mediterranean both the **COUPL** and **GLO** simulations suggest NO_3 is the dominant DMS oxidant, in agreement with the observations in these regions (Yvon & Saltzman, 1996;

Aldener *et al.*, 2006; Stark *et al.*, 2007; Vrekoussis *et al.*, 2007; Osthoff *et al.*, 2009). In the remote oceans of other regions the contribution of NO_3 is lower in the **COUPL** simulation. In total, NO_3 contributes 88% of the total DMS oxidation in the **GLO** model and 29% in the **COUPL** simulation. Comparison with the Berglen *et al.* (2004) study in Table 3.7 shows better agreement with the **COUPL** model suggesting the oxidation of DMS by NO_3 is overestimated in the **GLO** model. The **COUPL** model predicts OH is the primary DMS oxidant in the remote South Atlantic, Pacific, Indian and Southern Oceans. This agrees with observations of DMS oxidation in these regions (e.g. Yvon *et al.* (1996b); Nagao *et al.* (1999a); Sciare *et al.* (2001)).

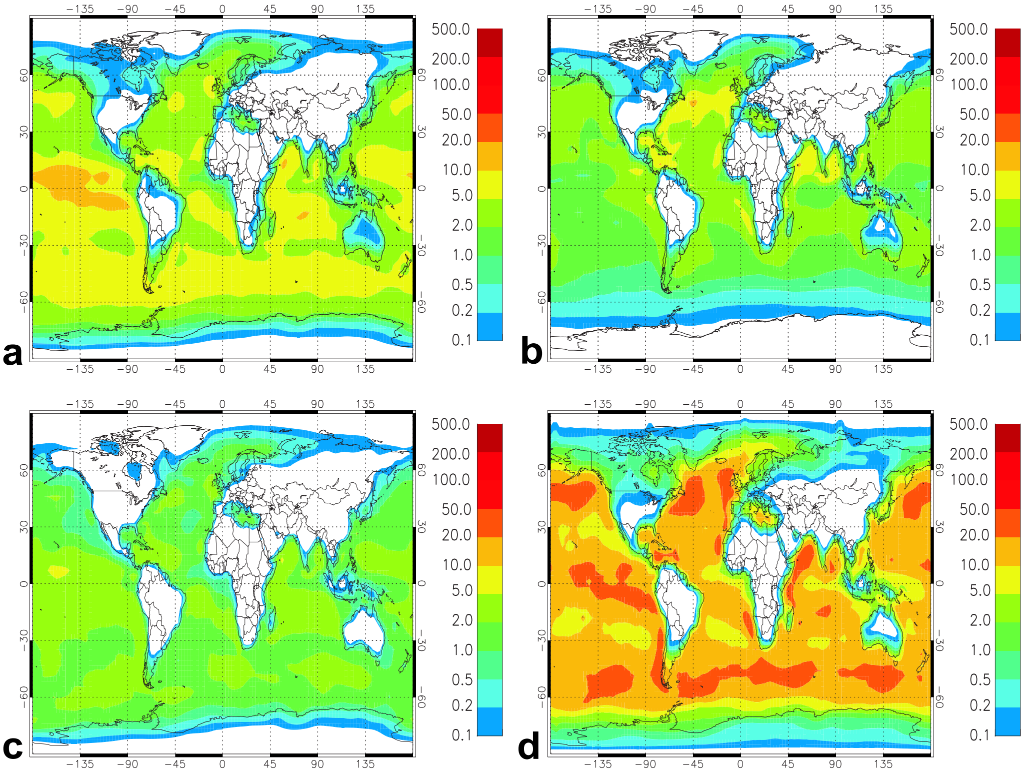

Figure 3.4: 2004 Annual mean oxidation of DMS [μgS m^{-3}] by OH (a & c)and NO_3 (b & d) in the **COUPL** (a & b) and **GLO** (c & d) model simulations.

The difference in modelled DMS between the **COUPL** and **GLO** model simulations can be explained by the immediate replenishment of oxidants in the **GLO** model. In the **GLO** model NO_3 fields are set to the prescribed values at the end of each model chemical timestep. This ignores the removal of NO_3 through the formation of HNO_3, the product of DMS + NO_3 reaction in equation 2.35. Hence, in remote marine regions the **GLO** model substantially overestimates the oxidation of DMS by NO_3 as it does not account for the removal of NO_3 through reaction by DMS. This inability to account for oxidant depletion feedbacks is a clear limitation in the use of prescribed oxidant fields. This representation could have been improved if the prescribed oxidant fields were calculated from a TOMCAT simulation that included sulfur chemistry and emissions of DMS. However, at the time the prescribed oxidant fields were generated this was not possible because the TOMCAT CTM did not include sulfur chemistry. The importance of DMS as a sink for NO_3 in remote marine regions can be seen in Figure 3.5a. Surface NO_3 mixing ratios decrease by more than 40% throughout marine regions. Almost complete loss of NO_3 occurs in the southern hemisphere mid and high latitude oceans. The potential for DMS to act as a sink for NO_x has been reported by Yvon *et al.* (1996a); Platt & LeBras (1997); Matsumoto *et al.* (2006); Aldener *et al.* (2006).

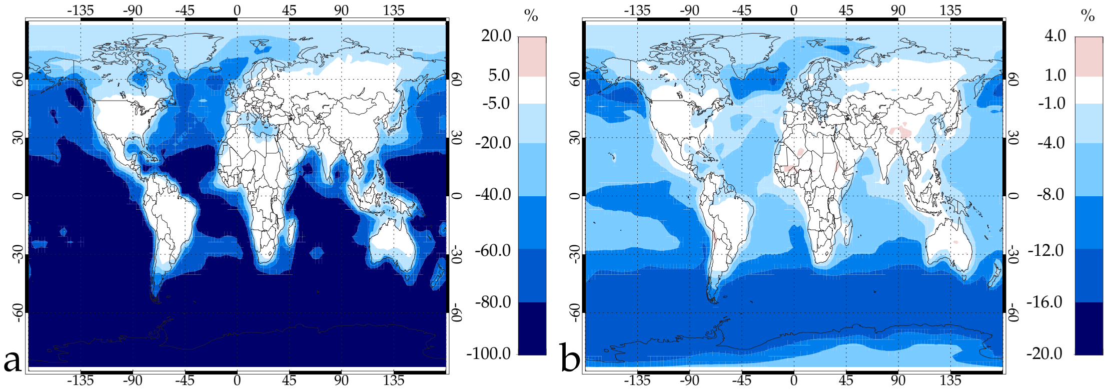

Figure 3.5: Annual mean % change in surface (a) NO_3 and (b) OH in the **COUPL** model compared to the **CHEM** model.

Figure 3.5b shows a decrease in surface OH mixing ratios of between 8 and 16% over large parts of the remote oceans with the largest reductions over the Southern Ocean. The potential for DMS to provide a sink for OH has previously been reported by Monks *et al.* (1998), who calculated that DMS mixing ratios of 100 pptv observed at Cape Grim during the SOAPEX campaign in 1995 would result in a 2% loss in OH. This study predicts a higher decrease in OH at Cape Grim of approximately 8%. The higher sensitivity of OH to DMS in simulation **COUPL** can be explained by DMS leading to the enhanced removal of NO_x through reaction with NO_3. As discussed by Penkett *et al.* (1997) and Carpenter *et al.* (1997), ozone production in the clean remote marine boundary layer is highly dependent on the available NO_x. The decrease in NO concentrations in the **COUPL** model results in a decrease in ozone production and therefore reduces the formation of OH. This result is in agreement with Platt & LeBras (1997) who first suggested DMS could impact ozone formation by perturbing NO_y partitioning. The larger OH depletion south of Cape Grim in the Southern Ocean is explained by the higher DMS mixing ratios there and a decreased contribution from CH_4 to OH loss according to the strong inverse temperature relation of the CH_4 + OH rate constant.

Figure 3.6 shows a comparison of the **COUPL** and **GLO** simulations with observations of monthly mean DMS mixing ratios at Amsterdam Island, Cape Grim and Dumont Durville. For analysis the normalised root mean squared deviation value (*nrmsd*) is provided. This represents a statistical measure of the comparison between the estimator, $\hat{\theta}$, with respect to the estimated parameter, θ.

$$nrmsd = \frac{\sqrt{\Sigma\left(\frac{(\hat{\theta}-\theta)^2}{n}\right)}}{\theta_{max}-\theta_{min}} \tag{3.16}$$

The **COUPL** model compares better with the observations at Amsterdam Island (Figure 3.6a) than the **GLO** model (**COUPL** *nrmsd* = 0.27, **GLO** *nrmsd* =0.33). However, the **COUPL** model overestimates DMS mixing ratios at Cape Grim throughout most of the year. Previous coupled oxidant studies have also reported an overestimation of DMS mixing ratios at Cape Grim (Berglen *et al.*, 2004), suggesting the DMS seawater concentrations in the Kettle & Andreae (2000) database may be to too high in the region. The **GLO** model shows good agreement with the observations at Cape Grim possibly indicating that the too high DMS source flux is compensated for by an overestimation in the oxidant fields and hence provides a misleading result.

A key oxidation product of DMS is DMSO, formed in the addition channel in equation 2.36. Figure 3.7 shows a comparison of monthly mean DMSO mixing ratios at Amsterdam Island and Dumont Durville. The **COUPL** model clearly compares better with the DMSO observations at Amsterdam Island (**COUPL** *nrmsd* = 0.36, **GLO** *nrmsd* =0.51) however it fails to capture the high DMSO mixing ratios observed at this station during January-March. At Dumont Durville the *nrmsd* values are similar for both runs, however the **COUPL** model *nrmsd* value is strongly weighted by the large overestimation during January-March. Throughout the rest of the year the **COUPL** comparison is significantly better than the **GLO** model. The underestimation of DMSO at both sites in the **GLO** model is explained by the dominance of the NO_3 + DMS reaction which does not form DMSO (Barnes *et al.*, 2006). These comparisons emphasise the **COUPL** model better represents DMS oxidation in remote marine regions than the **GLO** model. At Amsterdam Island the underestimation in DMSO in the **COUPL** model during January to March may also suggest additional oxidants that favour formation of DMSO, such as BrO may be important in that region.

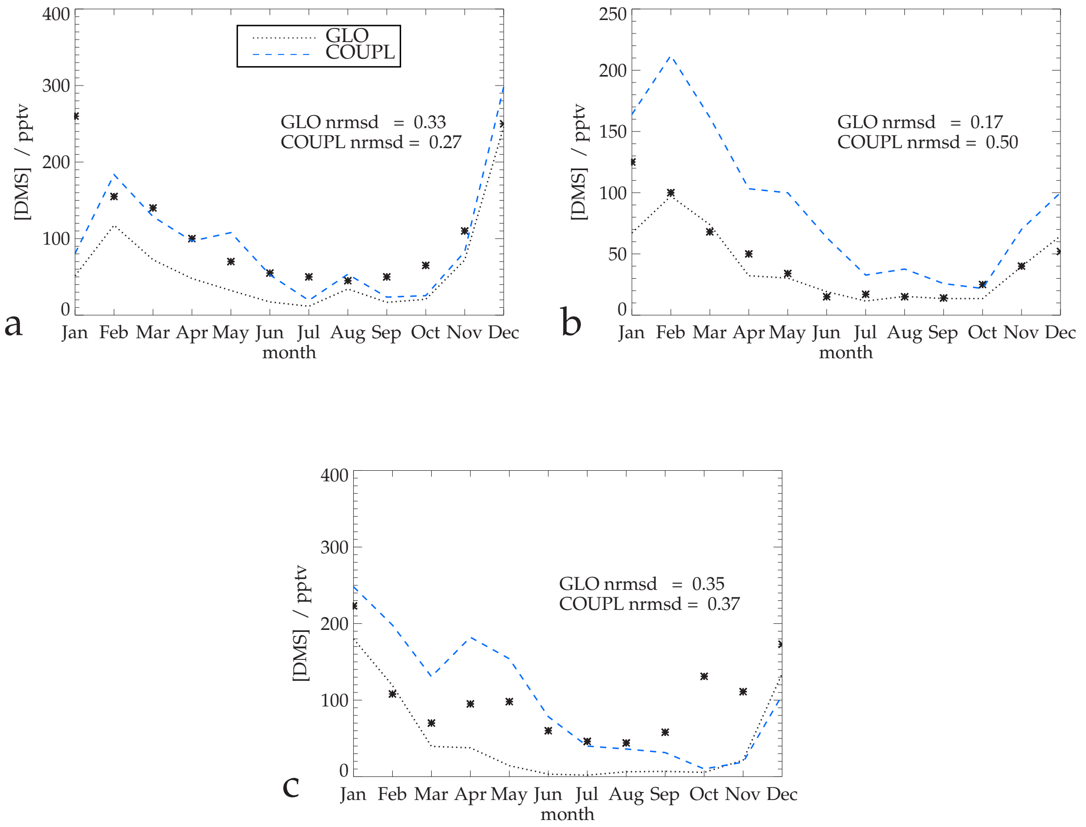

Figure 3.6: Monthly mean observed and modelled DMS mixing ratio (pptv) from runs **GLO** and **COUPL** at (a) Amsterdam Island [37.83°S, 77.50°E] (Nguyen *et al.*, 1992), (b) Cape Grim [40.68°S, 144.68°E] (Ayers *et al.*, 1991) and (c) Dumont Durville [66.70°S, 140.00°E] (Jourdain & Legrand, 2001).

3.6.4 Coupled vs Uncoupled Model - Changes in SO_2

SO_2 is a key constituent of the atmospheric sulfur cycle. Natural sources of SO_2 are dominated by DMS oxidation in remote marine regions (Davis *et al.*, 1999) and volcanic emissions also provide a large but localised source (See Table3.8 for estimated global SO_2 emissions). The most important source of SO_2, however, is from anthropogenic activities including fossil fuel combustion and industrial processes (Adams & Seinfeld, 2002; Stier *et al.*, 2005). The fate of SO_2 is strongly coupled to the availability of oxidants especially in industrialised regions (Roelofs *et al.*, 1998). The use of models that can accurately capture oxidant processes is important for quantifying how SO_2 contributes to the aerosol size distribution. In this section changes to SO_2 in the **COUPL** and **GLO** models are discussed and evaluated against observations.

The column SO_2 mass in the **COUPL** simulation (Figure 3.8) shows the largest concentrations of SO_2 close to the main source regions, reflecting the relatively short lifetime of SO_2 (approx 2 days

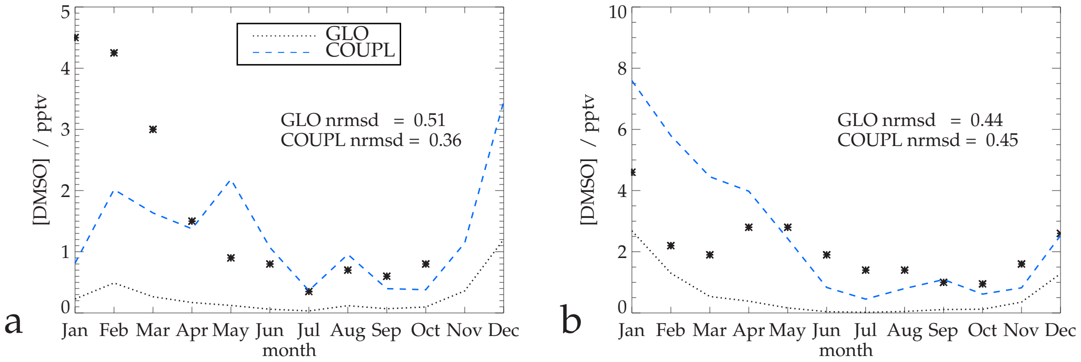

Figure 3.7: Comparisons of DMSO (pptv) in the **COUPL** and **GLO** simulations with observations at (a) Amsterdam Island [37.83°S, 77.50°E] (Sciare *et al.*, 2000b) and (b) Dumont Durville [66.70°S, 140.00°E](Jourdain & Legrand, 2001).

(Easter *et al.*, 2004)). The key anthropogenic source regions of East Asia, Europe and the East Coast of the US clearly show elevated SO_2 levels. The localised elevated SO_2 concentrations over Indonesia, South and Central America indicate emissions of SO_2 from volcanoes. Higher SO_2 mass concentrations are simulated in the NH winter months. This is a result of less photochemical production of oxidant species during the winter providing a smaller sink for SO_2. Column SO_2 concentrations are larger in the SH mid-latitudes in the SH winter. This is explained by lower oxidant availability during the wintertime, leading to an increased SO_2 lifetime and SO_2 from volcanoes, biomass burning and industrialised regions spreading over a larger region.

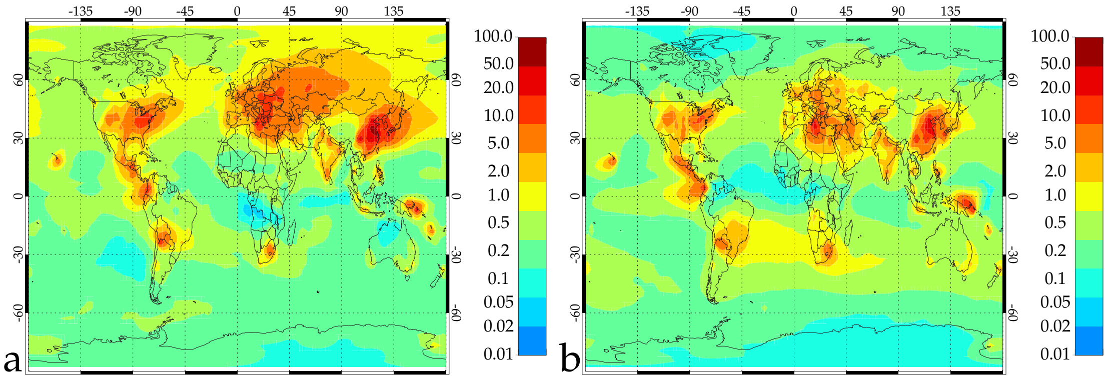

Figure 3.8: Column SO_2 total mass concentration [μg m^{-2}] in the **COUPL** simulation for (a) DJF and (b) JJA.

Figure 3.9a shows that the total column burden of SO_2 is larger during DJF in the **COUPL** simulation compared to the **GLO** simulation. The largest increase is observed in regions of high SO_2 emissions such as Europe and East Asia. This large increase in the SO_2 column over the main anthropogenic source regions can be explained by a reduction of in-cloud oxidation of SO_2 by

H_2O_2. As discussed in Section 2.7, aqueous phase oxidation of SO_2 is strongly coupled to H_2O_2 concentrations and photochemistry. In regions of high SO_2 concentrations, modelling studies have shown H_2O_2, the principal in-cloud oxidant for SO_2, may become depleted and limit the loss of SO_2 (Roelofs *et al.*, 1998). A reduction in H_2O_2 is also found in the **COUPL** simulation (See Section 3.6.5 for discussion). In the southern hemisphere the increased column SO_2 in the **COUPL** simulation during DJF (Figure 3.9a) can be explained by the longer lifetime of DMS which results in increased transport to the free troposphere. During the JJA months (Figure 3.9b) column SO_2 decreases throughout most of the NH. This can be explained by an increase in oxidants in the **COUPL** model explained by an increased source of CH_3O_2 and HCHO from DMS oxidation which are oxidised to HO_x and O_3.

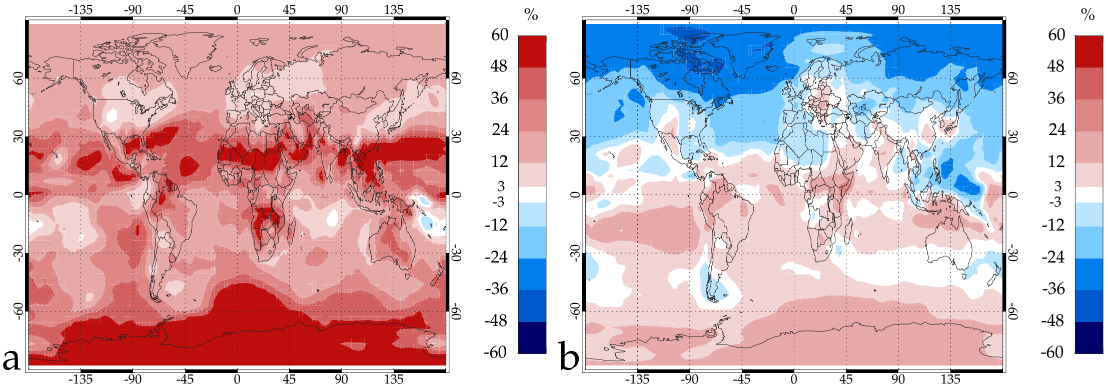

Figure 3.9: Annual mean % change in troposphere column SO_2 mass concentration for (a) DJF and (b) JJA in the **COUPL** simulation compared to the **GLO** simulation.

To further investigate SO_2 differences in the **COUPL** and **GLO** model simulations, the results are compared with observations of SO_2 from the EMEP and EANET. Comparisons with SO_2 at three remote marine stations are also provided. Figure 3.10 shows a comparison of the simulated SO_2 mass concentrations in the **COUPL** and **GLO** simulations with observations from nine EMEP and three EANET sites during 2004. The two models show a very small difference and the relative agreement with the stations is the same for both simulations. There is good agreement at Jungfraujoch, Peyrusse Vielle and Cubuk II. However, SO_2 is overestimated throughout the year at Topolnicky, Bredlaken and Westerland. SO_2 mass concentrations are underestimated at Spitsbergen and Terelj in the **COUPL** model. The **COUPL** model compares reasonably well with SO_2 observations at Cheju and Happo, but fails to capture the seasonal cycle at Terejl.

A comparison of the mean observed SO_2 concentrations at all EMEP and EANET stations with SO_2 measurement data compared to the **COUPL** simulation for DJF and JJA is shown in Figure

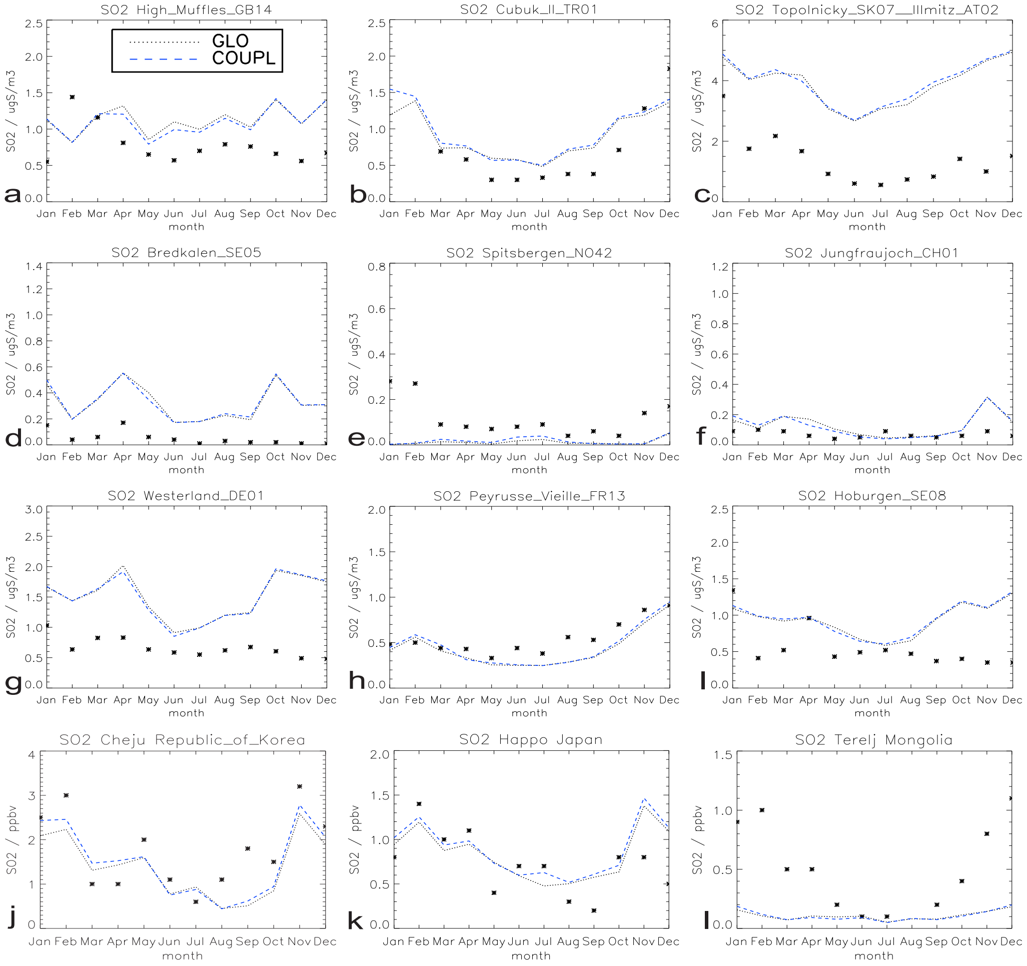

Figure 3.10: Monthly mean observed and modelled SO_2 mass concentrations (μg/m^3) at EMEP (a-i) and SO_2 volume mixing ratio ppbv at EANET (j-l) observation stations.

3.11. The **COUPL** model overestimates the observed SO_2 mass concentrations at EMEP stations in JJA (mean bias = 1.17ppb) and DJF (mean bias = 1.40ppb). A number of previous model studies have reported an overestimation in predicted SO_2 concentrations compared to EMEP and east Asian remote measurement stations (Barth *et al.*, 2000; Chin *et al.*, 2000; Easter *et al.*, 2004; Liu *et al.*, 2005). Suggested explanations for the overestimation of SO_2 in the models include issues with sampling locations (Chin *et al.*, 2000), insufficient boundary layer mixing (Lohmann *et al.*, 1999) and underpredicted SO_2 dry deposition rates (Easter *et al.*, 2004). At EANET stations the **COUPL** model agrees well with observations in DJF (mean bias = 0.15ppb) and in JJA (mean bias = 0.13ppb).

The *nrmsd* values show little difference between the **COUPL** and **GLO** simulations with the exception of EANET JJA when the **GLO** model compares slightly better. There a clear over prediction in both models at EMEP stations during summer and winter.

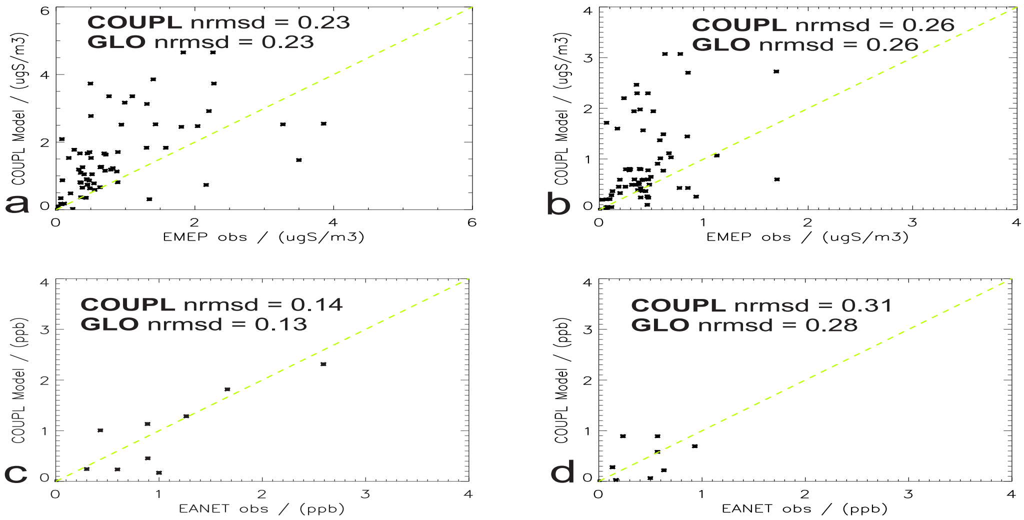

Figure 3.11: **COUPL** model compared to EMEP (a and b) and EANET (c and d) observations of SO_2 in (a) and (c) DJF and (b) and (d) JJA. **GLO** not plotted, *nrmsd* value given on plots for comparison with **COUPL**. Yellow dashed line indicates 1to1 line.

Observations of SO_2 in the remote southern hemisphere are limited to only a small number of sites, making model evaluation difficult. Figure 3.12 shows a comparison of monthly mean SO_2 mixing ratios at Cape Grim and Amsterdam Island with the **COUPL** and **GLO** simulations. At Amsterdam Island both model simulations fail to capture the high SO_2 mixing ratios observed during December and January. The simulations compare well during the SH autumn but underestimate the observed SO_2 during the SH spring. At Cape Grim both models overestimate SO_2 throughout the year. The **COUPL** model shows slightly better agreement at Cape Grim from December to March. The overprediction in SO_2 at Cape Grim could be due to an overestimate in the DMS source, missing oxidants in the model that favour the formation of DMSO instead of SO_2 such as BrO (Toumi, 1994) or oxidation of SO_2 on aqueous sea salt particles (Chameides & Stelson, 1992; Sievering *et al.*, 1992). Korhonen *et al.* (2008) showed the latter process could explain the overestimation of SO_2 at Cape Grim. This process is not accounted for in the simulations presented in this chapter but is investigated in Chapter 4. Easter *et al.* (2004) show better agreement with the SO_2 observations at Amsterdam Island; this is probably explained by the significantly higher DMS source in that study (see Table 3.7).

Table 3.8 shows the main SO_2 budget terms for this and previous coupled aerosol-chemistry model studies. The SO_2 burden and lifetime are lower in the **COUPL** simulation compared to Adams & Seinfeld (2002) and Easter *et al.* (2004) (See table 3.8). This is likely a result of the higher SO_2 emissions in those studies and hence an increased oxidant limitation, which leads to a higher burden and longer lifetime.

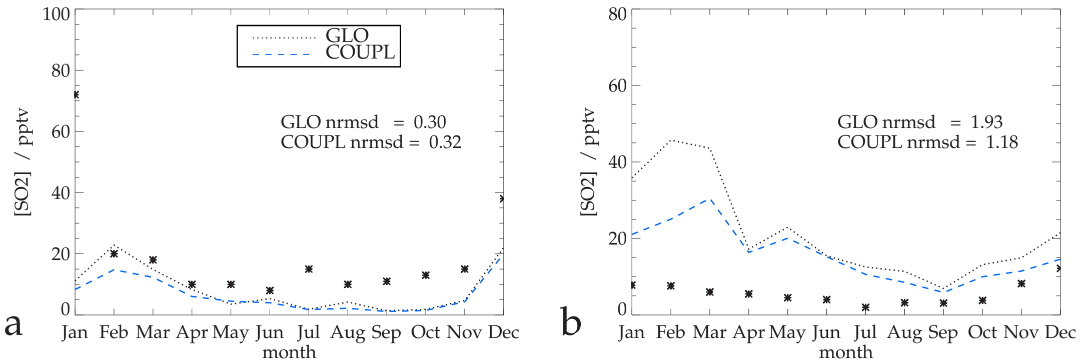

Figure 3.12: Monthly Mean observed and modelled SO_2 mixing ratio (pptv) at (a) Amsterdam Island [37.83°S, 77.50°E] (Nguyen *et al.*, 1992) and (b) Cape Grim [40.68°S, 144.68°E] (Ayers *et al.*, 1991).

Table 3.8: SO_2 budgets for 2004 in the **GLO** and **COUPL** models and previous published coupled aerosol-chemistry studies.

	GLO	**COUPL**	**AS02**	**B04**	**E04**	**P08**
Sources (Tg S yr^{-1})						
Industrial	54.2	54.2	70.8	67.79	59.0	
Biomass Burning				2.25	2.2	
Volcanoes	13.3	13.3		8.0	8.0	
DMS oxidation	12.3	12.1	9.7	10.88	17.0	
Total	79.8	79.6	80.5	89.80	86.2	72.5
Sinks						
SO_2 + OH	11.3	11.7	14.8	7.94	6.9	
$SO_2 + H_2O_2$	29.6	27.4	27.5	28.90	37.8	
$SO_2 + O_3$	4.6	5.0		5.80	10.8	
Other loss				4.01		
Dry Deposition	26.8	27.4	36.7	41.49	23.0	
Wet Deposition	7.9	8.4	1.4	1.57	7.1	
SO_2 Burden (Tg S)	0.31	0.33	0.66		0.44	0.77
SO_2 lifetime (days)	1.41	1.50	3.0		1.80	3.8

AS02=Adams & Seinfeld (2002), **B04**=Berglen *et al.* (2004), **E04**=Easter *et al.* (2004), **P08**=Pozzoli *et al.* (2008a)

3.6.5 Coupled vs Uncoupled Model - Changes in Sulfate Aerosol

DMS and SO_2 are the primary natural and anthropogenic sources of sulfate aerosol. Hence, the changes to DMS and SO_2 discussed in the previous sections could impact on the formation of sulfate aerosol in the troposphere. In this section changes to the sulfate aerosol ($SO_4{}^{2-}$) in the **COUPL** model compared to the **GLO** model are discussed and compared with observations.

Figure 3.13 shows column $SO_4{}^{2-}$ mass concentrations during DJF and JJA. The highest $SO_4{}^{2-}$ levels are observed in the northern hemisphere summer due to large anthropogenic emissions of SO_2 and high availability of oxidants. During the wintertime $SO_4{}^{2-}$ formation is limited by the availability of oxidants, especially in SO_2 source regions. The seasonal cycle of $SO_4{}^{2-}$ is less pronounced in the southern hemisphere. Very low $SO_4{}^{2-}$ mass concentrations are observed in the southern hemisphere high latitudes during the winter, due to the small source of SO_2 from DMS.

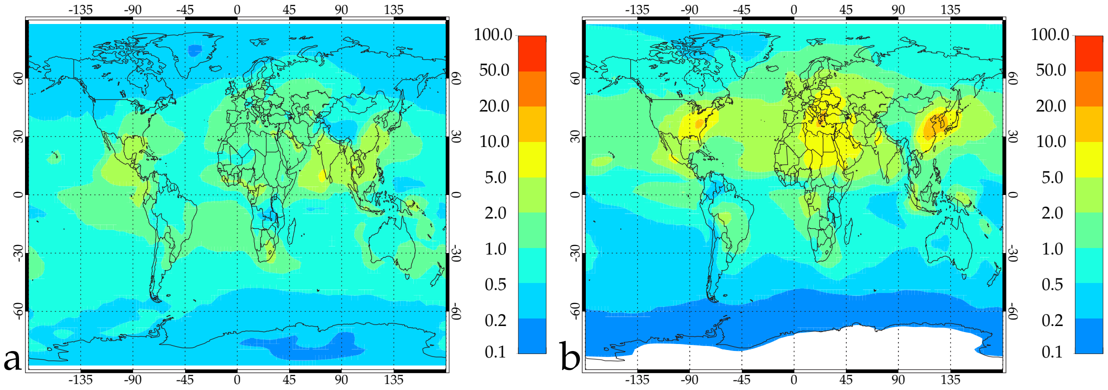

Figure 3.13: Simulated $SO_4{}^{2-}$ mass concentration [mg m^{-2}] in the **COUPL** model in (a) DJF and (b) JJA.

Figure 3.14 shows the percentage change in total column $SO_4{}^{2-}$ between the **COUPL** and **GLO** simulations. The largest decrease in column $SO_4{}^{2-}$ is simulated over East Asia (-50%) during DJF. Large localised decreases are also evident over Papua New Guinea, Central America and the Andes mountains indicating a reduction in in-situ oxidation of SO_2 from volcanoes in these regions. Over the oceans outside tropical regions during DJF column $SO_4{}^{2-}$ increases due to the increased lifetime of SO_2 and $SO_4{}^{2-}$. During JJA column $SO_4{}^{2-}$ decreases are less significant indicating oxidant availability in the **COUPL** and **GLO** models is similar.

The changes in $SO_4{}^{2-}$ in Figure 3.14 can be explained by changes in its formation pathways. Figure 3.15 shows the percentage change in $SO_4{}^{2-}$ formation from in-cloud oxidation of SO_2

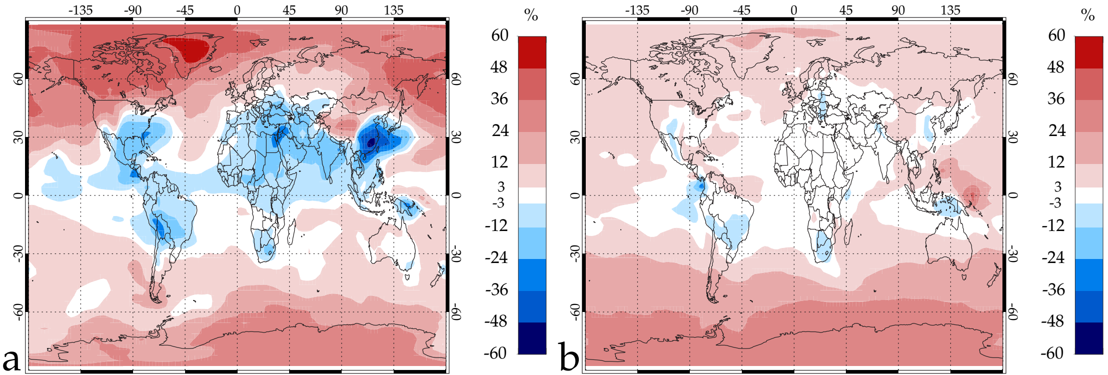

Figure 3.14: Percentage change in total column $SO_4{}^{2-}$ mass concentration in the **COUPL** model compared to the **GLO** model during (a) DJF and (b) JJA.

and gas-phase oxidation of H_2SO_4 in the **COUPL** simulation compared to the **GLO** simulation. The source of $SO_4{}^{2-}$ from in-cloud oxidation decreases by more than 40% during DJF (Figure 3.15a) in the main SO_2 source regions of East Asia, North America and Europe. Figure 3.15b also shows a decrease in gas-phase oxidation of H_2SO_4 in the main SO_2 source regions. In both Figures 3.15a and 3.15b the formation of $SO_4{}^{2-}$ in the northern hemisphere increases away from the main SO_2 source regions. This is explained by the increased lifetime of SO_2 and transport further from the source where it is subsequently oxidised. In the southern hemisphere during DJF column $SO_4{}^{2-}$ formation increases by 10-40% south of 30°S. This is due to the increased DMS lifetime simulated in the **COUPL** model leading to transport of DMS out of the boundary layer and subsequent oxidation to sulfate.

This decrease in $SO_4{}^{2-}$ formation by in-cloud and gas-phase oxidation is explained by the stronger oxidant limitation in the **COUPL** model. As emissions of SO_2 are very large in the main NH industrial regions the key oxidant, H_2O_2, may become depleted and limit the formation of $SO_4{}^{2-}$. The oxidant limitation is stronger in the **COUPL** model because the depletions in oxidant species are allowed to feedback onto the background chemistry. In the **GLO** model oxidant concentrations are replenished at the start of each model timestep, hence depletions in the oxidant fields are ignored. The decrease in H_2O_2 in the **COUPL** simulation due to in-cloud sulfate formation is clearly shown in Figure 3.16. The largest reductions in H_2O_2 are simulated during the NH winter (10-50%). During DJF depletions in H_2O_2 concentrations of more than 24% are evident throughout large areas of the northern hemisphere. In JJA the largest decreases in H_2O_2 are seen over the main industrial regions of East Asia, Europe and the east coast of the US. In Figure 3.16a there is also a large reduction of H_2O_2 concentrations over the SH oceans. This is explained by a large

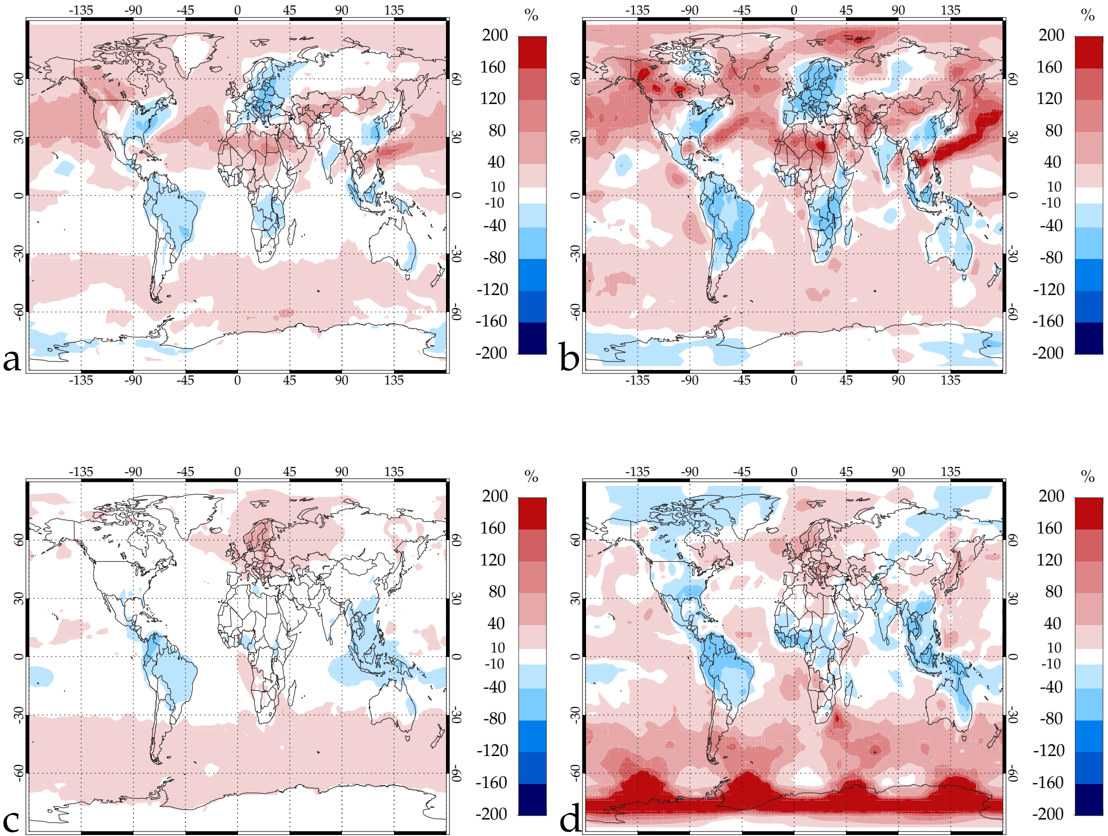

Figure 3.15: Simulated % change in the **COUPL** simulation in SO_4^{2-} formation during DJF and JJA compared to **GLO** by (a and c) in-cloud oxidation and (b and d) H_2SO_4 condensation. Panels (a) and (b) are for DJF and (c) and (d) JJA.

source of SO_2 from DMS oxidation, which consumes the H_2O_2. Replenishment of H_2O_2 in the remote southern oceans is slow due to less available oxidants and slower oxidant formation cycles.

Roelofs *et al.* (1998) found a similar decrease of in-cloud oxidation of SO_2 by H_2O_2 when comparing the use of coupled vs uncoupled oxidants to drive the sulfur chemistry in the ECHAM4 GCM. Roelofs *et al.* (1998) found the largest depletions in H_2O_2 in the NH in the winter in agreement with this study. Bell *et al.* (2005) also addressed the impact of chemistry-aerosol coupling on sulfate aerosol formation in the GISS GCM, 'Model E' (Schmidt *et al.*, 2006). The Bell *et al.* (2005) study found a much smaller difference between the coupled and uncoupled simulations. However, a key difference in Bell *et al.* (2005) was the prescribed oxidant fields were generated from a simulation which included the sulfur oxidation cycle, hence oxidant depletions were accounted for. At the time the prescribed oxidant fields for GLOMAP were generated, there was no sulfur chemistry in TOMCAT, hence it was not possible to create oxidants that accounted for the sulfur chemistry. It is also important to point out that in the Bell *et al.* (2005) study, oxidants are low before the emitted sulfur species have been consumed, thus the model will underestimate the oxidant sink. Clearly coupled oxidant studies provide a more accurate method for simulating secondary aerosol formation in the troposphere.

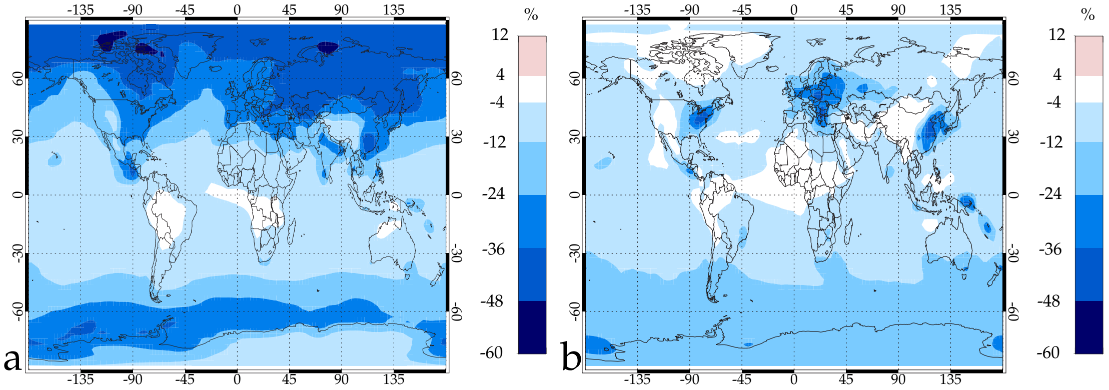

Figure 3.16: Simulated % change in troposphere column H_2O_2 concentrations in the **COUPL** simulation compared to **CHEM** for (a) DJF and (b) JJA.

Table 3.9 shows the global annual mean SO_4^{2-} budgets for the **COUPL**, **GLO** and previous coupled aerosol-chemistry models. The decrease in aqueous phase oxidation of SO_2 by H_2O_2 between the **COUPL** and **GLO** simulations is evident. Gas-phase oxidation by OH and aqueous phase oxidation by O_3 increase in response, but are unable to fully compensate for the decrease in the H_2O_2 pathway. As a result net SO_4^{2-} formation decreases by 3%. The shift towards sulfate formation in the gas-phase results in an increase in the SO_4^{2-} lifetime as removal processes are less efficient for gas-phase formation.

Table 3.9: $SO_4{}^{2-}$ budgets in the **COUPL**, **GLO** and previous published coupled chemistry-aerosol studies.

	GLO	**COUPL**	**AS02**	**B04**	**E04**	**P08**
Sources (Tg S yr^{-1})						
Primary Emission	1.72	1.72	2.0	3.39	1.2	1.86
Nucleation	0.01	0.01	0.04			0.07
H_2SO_4 Condensation	11.26	11.72	14.8	7.94	6.9	26.93
SO_2 + H_2O_2	29.55	27.39	27.5	28.90	37.8	44.90
SO_2 + O_3	4.60	5.01		5.80	10.8	
SO_2 ox sea salt/dust				4.01		4.24
TOTAL	47.14	45.85	44.3	50.04	57.3	78.0
Sinks (Tg S yr^{-1})						
Dry Deposition	5.4	5.32	1.0	7.4	9.5	2.2
Wet Deposition	41.68	40.46	43.3	42.6	47.7	73.1
Sedimentation						2.7
$SO_4{}^{2-}$ Burden (Tg S)	0.60	0.61	0.8	0.5	1.07	0.87
$SO_4{}^{2-}$ Lifetime (days)	4.77	4.83	6.6	5.5	6.8	4.0

AS02=Adams & Seinfeld (2002), **B04**=Berglen *et al.* (2004), **E04**=Easter *et al.* (2004), **P08**=Pozzoli *et al.* (2008a)

The **COUPL** and **GLO** model simulations are now compared with aerosol observations of $SO_4{}^{2-}$ from the EMEP and EANET acid deposition monitoring networks. Figure 3.17 shows a comparison between annual mean $SO_4{}^{2-}$ observations and the **COUPL** and **GLO** simulations for 2004. The two model simulations give very similar results at all sites. At most EMEP stations the **COUPL** model overestimates the summertime $SO_4{}^{2-}$ mass concentrations. At the EANET stations the **COUPL** model significantly underestimates $SO_4{}^{2-}$ at all three sites throughout most of the year.

Figure 3.18 shows a comparison $SO_4{}^{2-}$ mass concentrations during DJF and JJA in the **COUPL** model with observations from all EMEP and EANET remote stations. At EMEP stations the **COUPL** model overestimates $SO_4{}^{2-}$ in the summer (mean bias = $1.20\mu gm^{-3}$) and underestimates $SO_4{}^{2-}$ in the winter (mean bias = $-0.31\mu gm^{-3}$). The underestimation of $SO_4{}^{2-}$ in DJF could be due to a number of factors. Firstly, Figure 3.11 showed the **COUPL** model overestimates SO_2 over Europe during the winter suggesting an improved treatment of the O_3 + SO_2 reaction may be required to better capture the dependence of this reaction on cloud droplet pH. A second explanation could be not accounting for a diurnal cycle in the emissions of SO_2. Langmann *et al.* (2008) showed that including diurnally varying anthropogenic SO_2 emissions fluxes improves the comparison with observation of sulfate. Thirdly, the model assumption of a cloud droplet pH of 4 or 5 depending on the ambient SO_2 mixing ratio may also be a factor. The O_3 + SO_2 reaction pathway is highly pH-dependent, assuming a droplet pH that is too low will underestimate the formation of $SO_4{}^{2-}$.

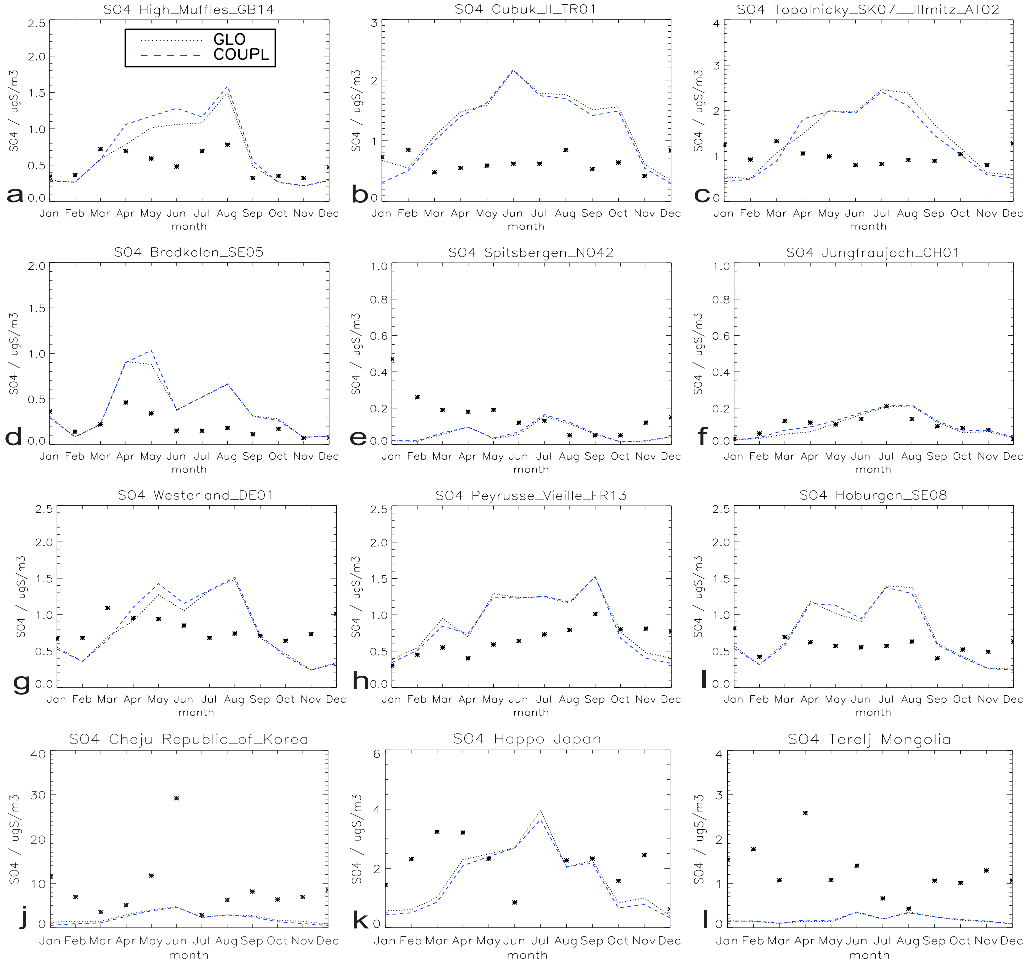

Figure 3.17: Simulated 2004 monthly mean SO_4^{2-} mass concentrations (μg/m^3) in the **COUPL** and **GLO** models compared with EMEP and EANET observations.

The overprediction of SO_4^{2-} and SO_2 during JJA over Europe suggests deposition rates for SO_2 are underestimated in the model.

At the EANET measurement stations the **COUPL** model underestimates the SO_4^{2-} during both JJA (mean bias = -0.49μgm^{-3}) and DJF (mean bias = -0.77μgm^{-3}). This is likely to be due to uncertainties in the emissions of SO_2 or particulate sulfate in the region. Referring back to Figure 3.11 the model compares well with SO_2 over East Asia suggesting the source of primary sulfate in the model in the region may be too low or that removal of SO_4^{2-} is too fast. However, Lu *et al.* (2010) showed SO_2 emissions in China increased by 53% between 2000 and 2005. The emissions in this study are for the year 2000 (Cofala *et al.*, 2005), hence the SO_2 emissions are too low for the comparison year, 2004. The better agreement with SO_2 EANET observations in Figure 3.11 indicates either oxidants or removal processes are too low in the region or there are missing oxidant pathways in **COUPL** model.

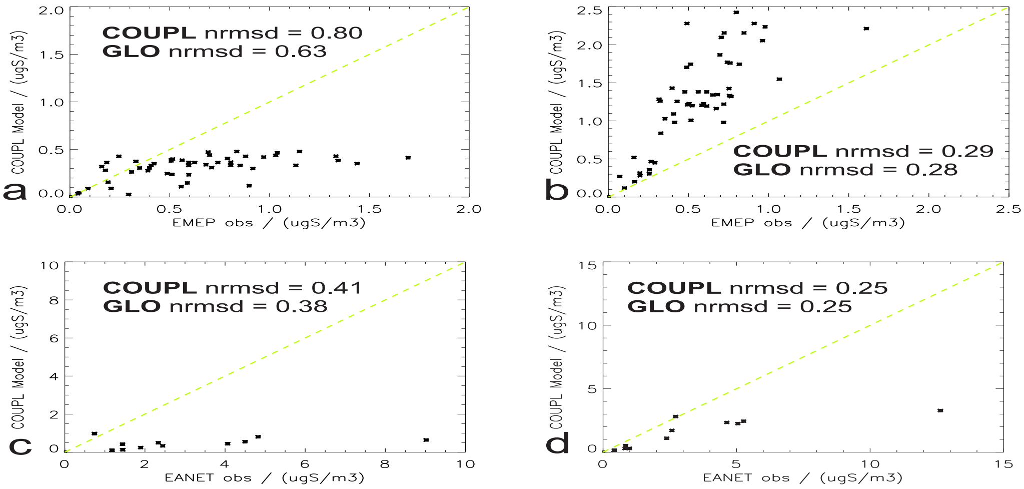

Figure 3.18: Simulated monthly mean $SO_4{}^{2-}$ mass concentrations in the **COUPL** model compared to EMEP (a and b) and EANET observational stations (c and d) during DJF (a and c) and JJA (b and d). **GLO** not plotted, *nrmsd* value given on plots for comparison with **COUPL**.

Figure 3.19 shows comparisons of non-sea-salt $SO_4{}^{2-}$ with observations from five remote marine stations in Antarctica. At Dumont Durville, Mawson and Neumayer both models fail to capture the amplitude in the seasonal cycle and fail to capture the high $SO_4{}^{2-}$ mass concentrations during the summer. At Halley Bay and Palmer the **COUPL** model compares better with the observations than the **GLO** model (See *nrmsd* values on Figure 3.19).

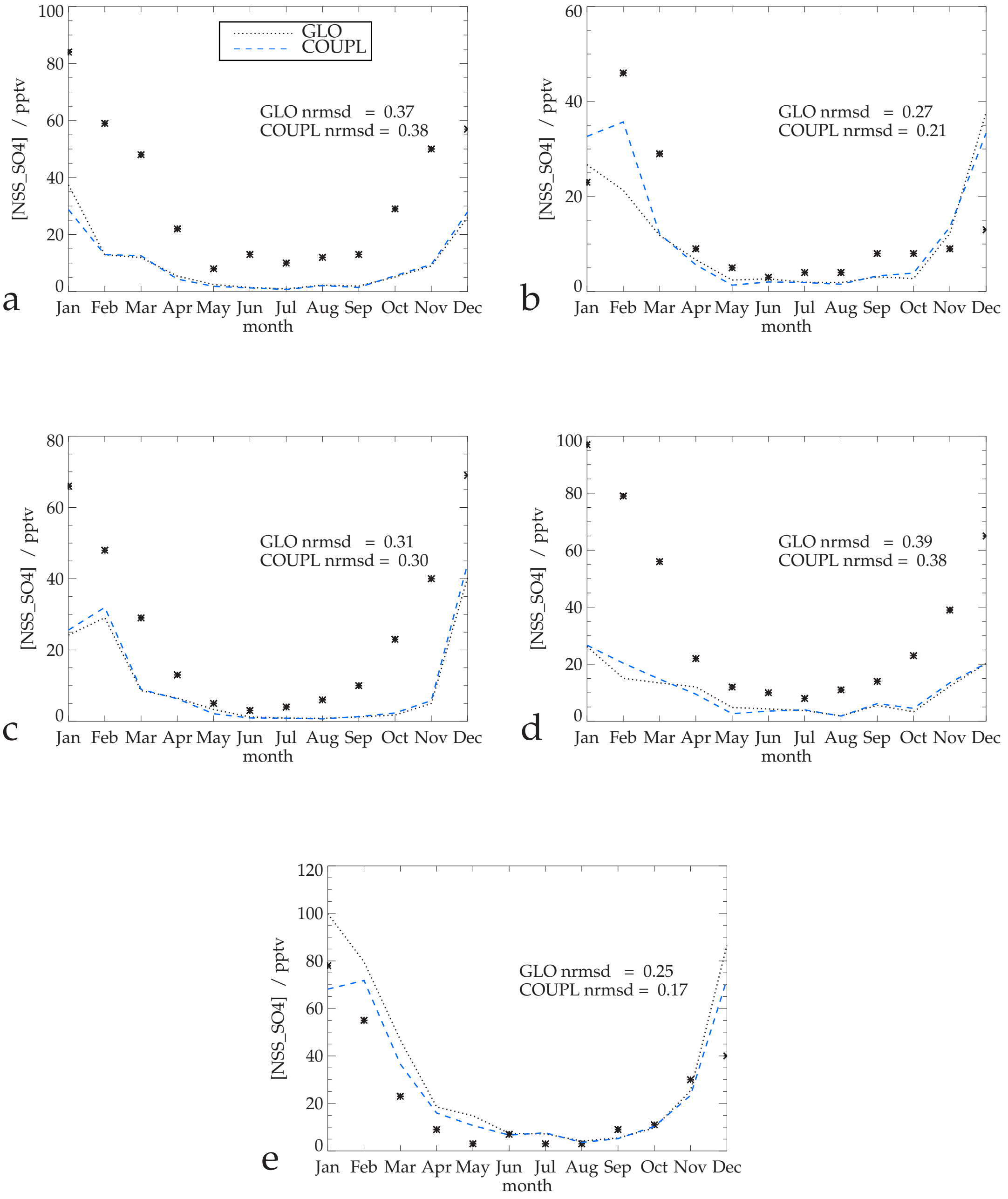

Figure 3.19: Simulated monthly mean non-sea-salt SO_4^{2-} mixing ratio (pptv) in the **COUPL** and **GLO** models at (a) Durmont Durville [66.70°S, 140.00°E], (b) Halley Bay [73.35°S, 26.19°E],(c) Mawson [67.36°S, 62.30°E], (d) Neumayer [70.39°S, 8.15°E], and (e) Palmer [64.46°S, 64.03°E]. Observations are from Minikin *et al.* (1998) and SAVOIE *et al.* (1993).

3.6.6 Coupled vs Uncoupled Model - Changes in CN and CCN concentrations

The changes to sulfate aerosol discussed in Section 3.6.5 will have implications for the formation of CCN. In this section changes in the CN and CCN number concentrations are discussed.

Figure 3.20 shows modelled zonally averaged CN and CCN number concentrations in the **COUPL** simulation during DJF and JJA. The number of CCN is calculated as all soluble aerosol particles with a dry radius greater than 35nm. This is a typical activation radius for an aerosol particle at 0.23% supersaturation.

Figure 3.20a and 3.20b shows the highest CN number concentrations in the tropical upper free troposphere. This is explained by the formation of nucleation mode particles in this region where nucleation of H_2SO_4 is favoured at the low temperatures, high relative humidity and low existing aerosol surface area. Elevated CN number concentrations are shown at a lower altitude during the hemisphere winter. This is due to nucleation occurring over a greater depth of the free troposphere during winter (Spracklen *et al.*, 2005a). The higher simulated CN at high latitudes during the winter in the SH can be explained by the lower aerosol surface area and cooler temperatures in the SH than in the NH.

The highest CCN number concentrations (200-500 cm^{-3}) are found at 30° - 40°N where primary sulfate and SO_2 emissions are largest. CCN number concentrations are largest in the NH during JJA, which is explained by higher OH concentrations in the summertime leading to greater production of gas-phase sulfuric acid. The sulfuric acid preferentially condenses onto existing aerosol since nucleation is inhibited by the warmer summertime temperatures (Spracklen *et al.*, 2005a). During the hemisphere summer elevated CCN concentrations penetrate further into the free troposphere indicating more vigorous mixing of boundary layer air driven by convective processes (Spracklen *et al.*, 2005a). The seasonal cycle in CCN is more pronounced in the SH explained by a large variation in the summer and winter DMS source and the advance of sea ice in the winter that restricts the emissions of sea salt aerosol (Yoon & Brimblecombe, 2002; Pierce & Adams, 2006).

Depletions in CN and CCN are evident in both seasons throughout the Inter-Tropical Convergence Zone (ITCZ) indicating efficient removal of aerosol by cloud scavenging (Spracklen *et al.*, 2005a).

Figure 3.21 shows the percentage changes in CN and CCN in the **COUPL** model compared to the **GLO** model during DJF and JJA. CN number concentrations increase significantly in the upper troposphere (UT) (12-36%) during both seasons due to increased nucleation of gas-phase sulfuric acid. At higher latitudes CN concentrations decrease in the NH during both seasons. This is explained by the reduced H_2SO_4 concentrations in the region due to lower OH and hence less nucleation. The increase in CN in the SH in JJA months is explained by the longer SO_2 lifetime from sources such as biomass burning and volcanic emissions.

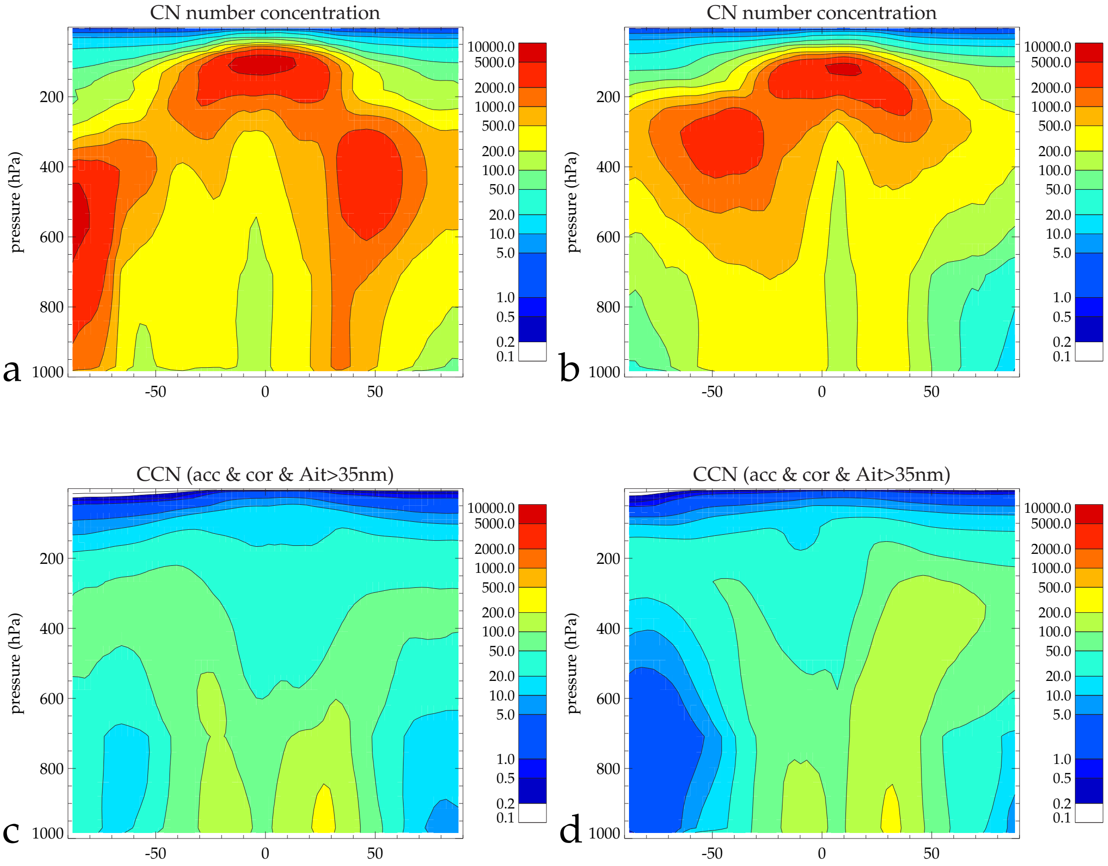

Figure 3.20: Simulated CN (a and b) and CCN (c and d) number concentration (cm^{-3}) in the **COUPL** model in (a and c) DJF and (b and d) JJA.

In the NH winter CCN increases by 12-36%. This is explained by the stronger oxidant limitation in the **COUPL** model which restricts the growth of existing accumulation mode aerosol particles through in-cloud sulfate formation. A higher fraction of SO_2 is oxidised in the gas-phase by OH to H_2SO_4 which either nucleates to form nucleation mode particles or condenses onto existing Aitken mode aerosol. The increased oxidant limitation in the **COUPL** simulation hence acts to re-distribute the sulfate mass from pre-existing accumulation mode aerosol to the growth of Aitken mode aerosol. The net result is an increased number of smaller CCN (See Figures 3.21 and 3.22). In the NH summertime the oxidant limitation is less important and the change in CCN is smaller.

In the SH summer the increase in CCN (3-24%) can be explained by the increased lifetime of DMS in the **COUPL** model, which results in more DMS transported to the free troposphere and subsequent oxidation to SO_2. In the SH winter higher CCN concentrations are explained by the longer lifetime of SO_2 emitted from biomass burning and volcanoes.

The absolute difference in the accumulation mode mean radius in the **COUPL** and **GLO** models

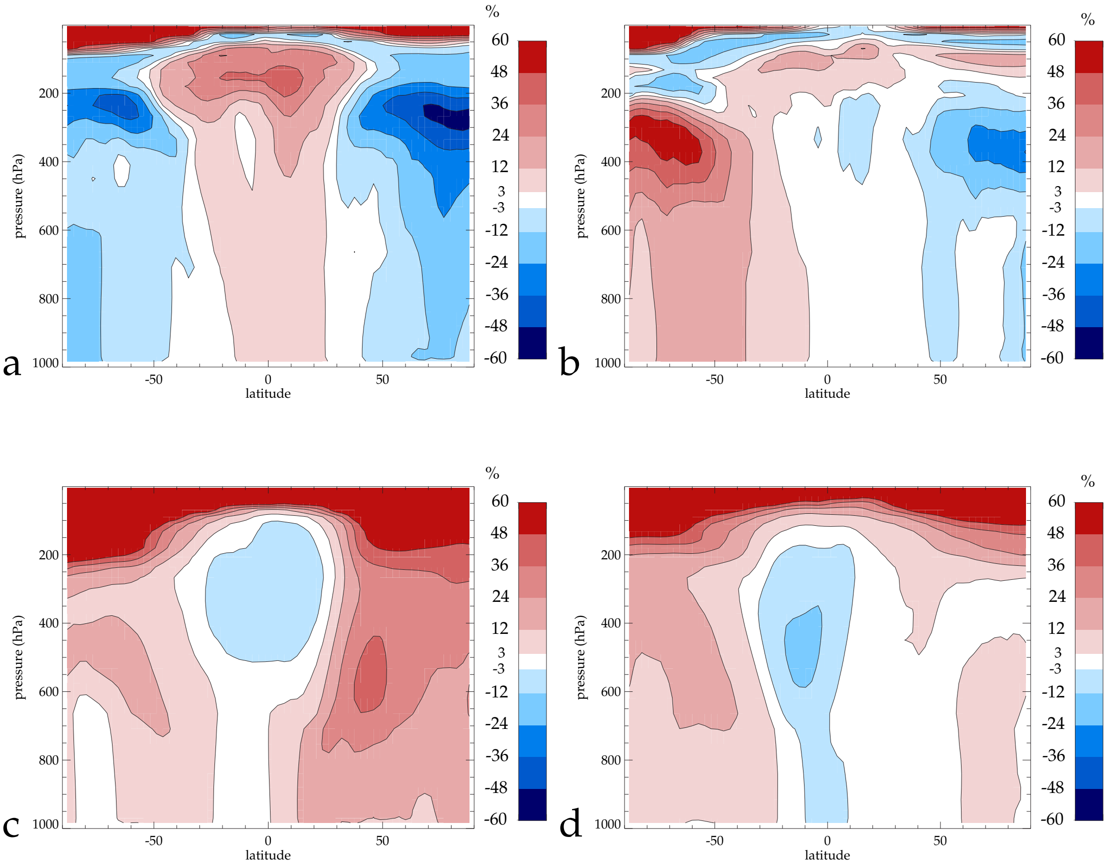

Figure 3.21: Zonally averaged % change in CN (a and b) and CCN (c and d) number concentrations in the **COUPL** simulation compared to the **GLO** simulation for DJF (a and c) and JJA (b and d).

is shown in Figure 3.22. The clear decrease in the accumulation mode mean radius in the NH winter (4-8 nm) can be seen in agreement with the aqueous phase oxidant limitation previously discussed. There is also a decrease in the accumulation mode mean radius during the SH summer and winter of 1-4 nm in the mid-latitudes suggesting emissions of DMS may provide an enhanced HO_x sink in this region. A discussion of the impact of DMS on HO_x is provided in Section 3.6.7.

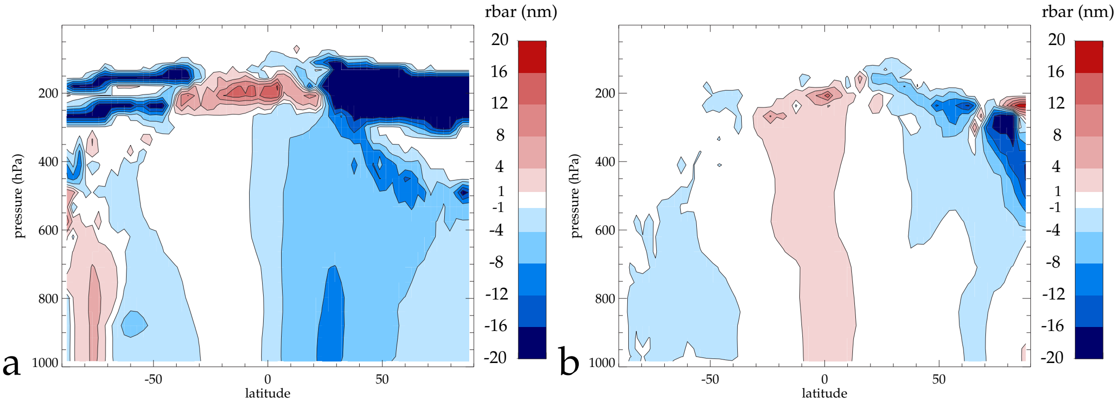

Figure 3.22: Zonally averaged absolute change in the accumulation mode mean radius (nm) in the **COUPL** simulation compared to **GLO** for (a) DJF and (b) JJA.

A secondary factor which can explain higher CCN in the NH in the **COUPL** simulation is that a higher fraction of CCN are present at sizes below the cut-off size for wet deposition. GLOMAP uses a fixed particle diameter for determining rainout of aerosol. In the tropical UT CCN number concentrations decrease in the **COUPL** model. In JJA this can be explained by an increase in the accumulation mode mean diameter which results in an increased fraction of CCN wet deposited for reasons described above.

Figure 3.23 shows modelled monthly mean CCN number concentrations at 0.23% and 0.75% supersaturation compared to observations at Cape Grim. CCN is calculated according to the Kohler equation. This calculates an activation radius based on the supersaturation and aerosol solubility. All soluble aerosol particles with a radius larger than the activation radius are assumed to act as a CCN.

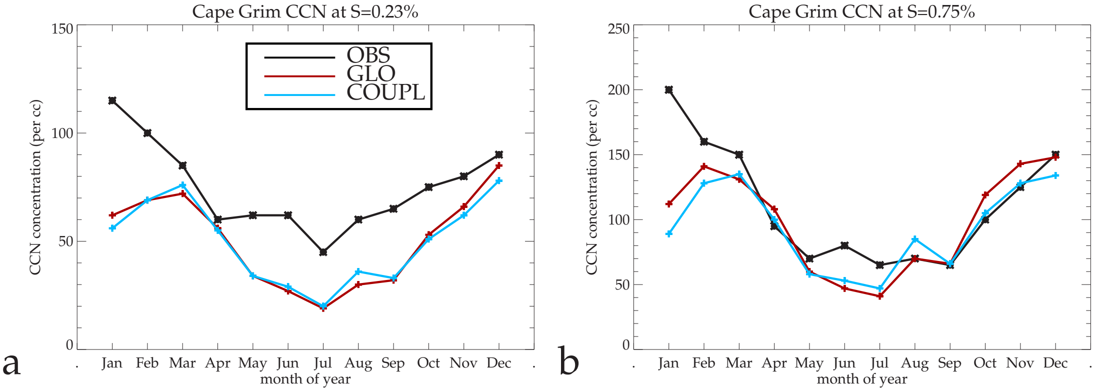

Figure 3.23: Comparison of CCN at (a) 0.23% and (b) 0.75% supersaturation in the **COUPL** and **GLO** models with observations from Cape Grim [40.68°S, 144.68°E](Ayers & Gras, 1991).

3.6.7 Coupled vs Uncoupled Model - Changes in Oxidants

The introduction of sulfur chemistry into the TOMCAT CTM model can significantly perturb background species shown in Section 3.6.3 for NO_3 and OH and 3.6.5 for H_2O_2. In this section changes in ozone, HO_x and NO_x species due to the introduction of the sulfur chemistry are described and discussed.

A number of observations have previously reported that DMS provides an important NO_x sink in the remote marine atmosphere (Yvon *et al.*, 1996a; Platt & LeBras, 1997; Matsumoto *et al.*, 2006; Aldener *et al.*, 2006). Figure 3.24 shows the zonally averaged percentage change in NO_x concentrations during DJF and JJA. The largest change is simulated in the SH during JJA where NO_x concentrations decrease by 32-40%. During DJF SH NO_x decreases by 8-24%. The larger NO_x decreases is simulated in the SH winter because NO_3 is an important nighttime reservoir species for NO_x. The long nights in the SH JJA months south of 50°S result in high NO_x loss. During the SH summer when DMS emissions are highest, the nights are short, NO_x partitions to NO_3 for a shorter period and therefore loss of NO_x by the DMS + NO_3 pathway is reduced. In the NH NO_x decreases are smaller than than the SH. In NH DJF DMS emissions are not sufficient to perturb the simulated NO_x north of the tropics. In NH JJA months, when DMS emissions are large, zonally averaged NO_x decreass by 2-8%. In the tropics below 700 hPa NO_x mixing ratios are reduced by 8-24% in DJF and JJA due to a sustained DMS source in both seasons.

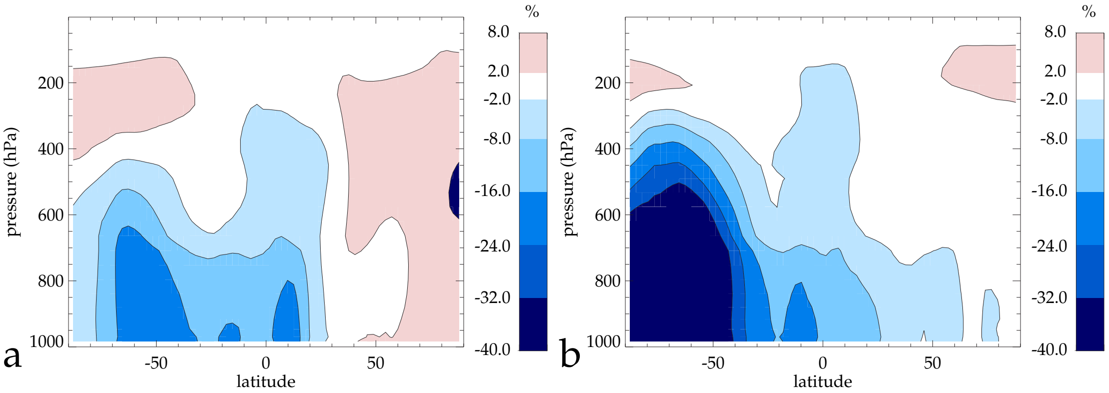

Figure 3.24: Simulated % change in zonally averaged NO_x during (a) DJF and (b) JJA between the **COUPL** and **CHEM** model runs.

Figure 3.25 shows the zonally averaged percentage change in HO_x concentrations during DJF and JJA. Inclusion of sulfur chemistry leads to a decrease in HO_x species in the southern hemisphere of 3-12% between 40° and 80°S. The simulated reductions in HO_x in the SH mid-high latitudes is a result of a number of processes. Firstly, loss of H_2O_2 via in-cloud oxidation of SO_2 and secondly the NO_x chemistry in the region. The inital reaction of DMS with OH or NO_3 leads to the formation of CH_3O_2. In NO_x-rich environments the cycle continues via reaction with NO to yield NO_2, HCHO and HO_2. However, in a NO_x-limited environment, such as the southern hemisphere high latitudes, where NO levels are less than a threshold level of 30 pptv (Carpenter *et al.*, 1997), the chain reaction sequence (see reactions 2.15-2.17) may be cut short as the CH_3O_2 reacts with HO_2 to form CH_3OOH (reaction 2.19). The high solubility of CH_3OOH leads to its removal by wet deposition. Figure 3.26 shows the average surface NO mixing ratio is lower than 5 pptv throughout large parts of the SH during DJF and JJA due to limited NO_x sources in the region. In the NH the small increase in HO_x in DJF can be explained by a source of DMS oxidised to provide a small additional source of HO_x.

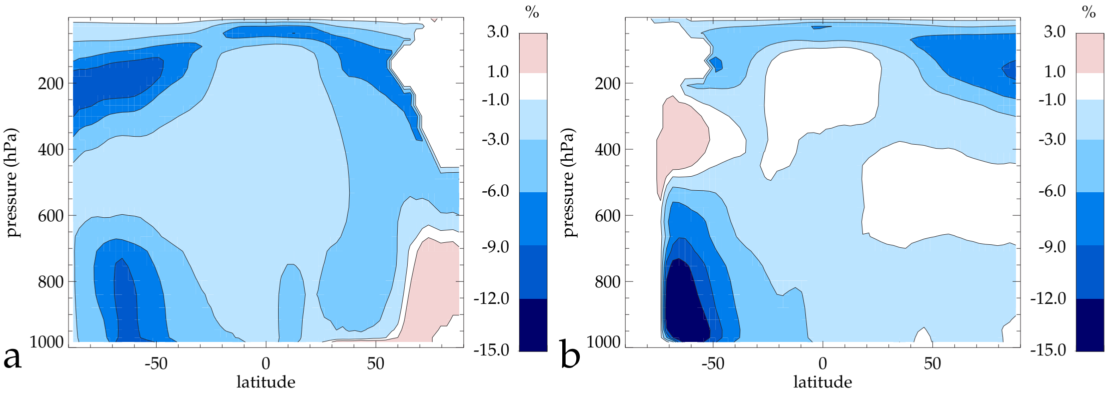

Figure 3.25: Simulated % change in zonally averaged HO_x during (a) DJF and (b) JJA between the **COUPL** and **CHEM** model runs.

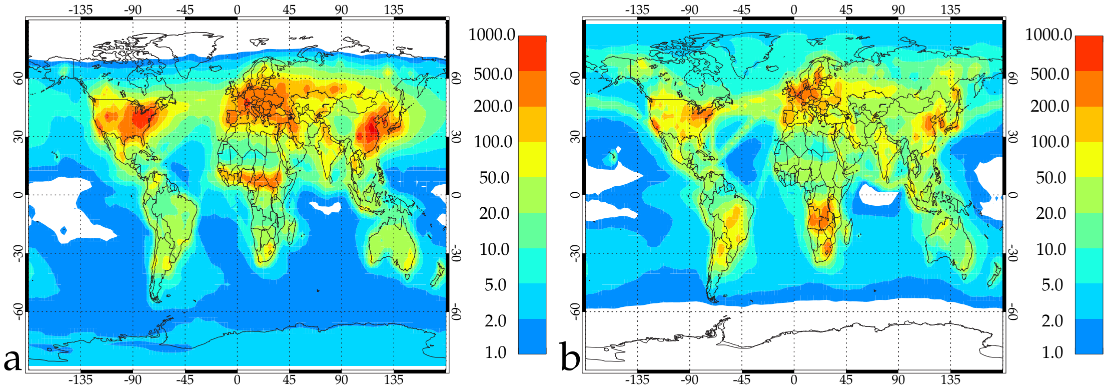

Figure 3.26: Simulated average surface NO mixing ratio during (a) DJF and (b) JJA in the **COUPL** model

Figure 3.27 shows the zonally averaged percentage change in O_3 mixing ratios during DJF and JJA. During DJF O_3 decreases by 4-6% throughout large parts of the tropics and the NH. Over the mid-high latitude SH troposphere column O_3 decreases by 6-8%. In JJA 2-6% decreases in O_3 are found in the tropics. In the NH during JJA there is a smaller decrease in O_3 (0.5-2%) compared to the SH (6-8%). The differences in O_3 can be explained by a combination of the aqueous phase O_3 + SO_2 reaction and changes to NO_x chemistry in the **COUPL** model. In the SH and tropics the decrease in NO_x in Figure 3.24 due to DMS emissions will reduce the ozone production efficiency in agreement with Platt & LeBras (1997). In the NH the decrease in O_3 during DJF can be explained by the large contribution of O_3 to aqueous phase SO_2 during this period when H_2O_2 mixing ratios are low.

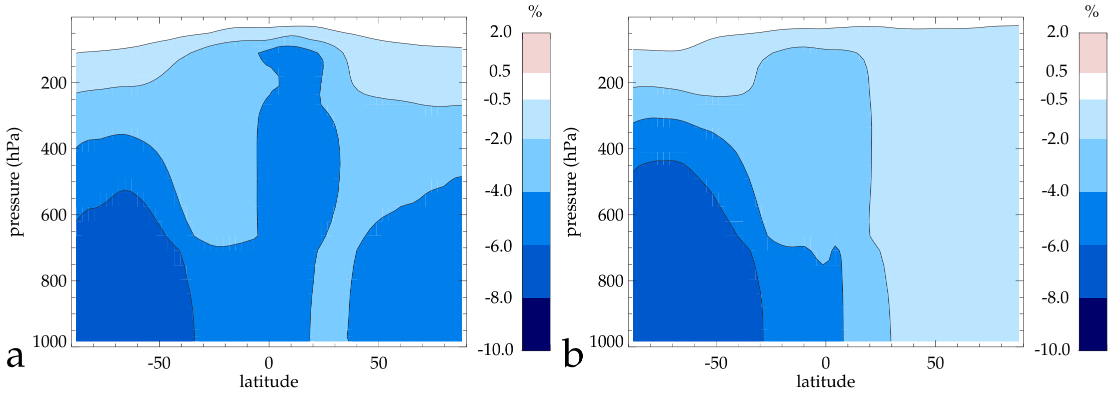

Figure 3.27: Simulated % change in zonally averaged O_3 during (a) DJF and (b) JJA between the **COUPL** and **CHEM** model

To understand the global change in tropospheric ozone, the total troposphere ozone burden is compared in simulations **COUPL** and **CHEM**. The troposphere is defined as where monthly average ozone mixing ratio's are less than 150 ppbv following Stevenson *et al.* (2004). In simulation **COUPL** the annual ozone burden is 342 Tg O_3, 3.1% lower than the ozone burden of 353 Tg O_3 in the **CHEM** simulation.

3.7 Heterogeneous Reaction of N_2O_5 on Aerosols - Impact on Ozone and NO_x

This section presents the results from implementing the heterogeneous reaction of N_2O_5 on sulfate and sea salt aerosols in the coupled model. The aerosol microphysics scheme enables the aerosol surface area to be calculated on-line from the aerosol size distribution. GLOMAP carries both aerosol number and mass in a series of 4 separate size modes, hence there is no requirement to assume a mean aerosol radius for the surface area calculation as done in mass-only aerosol models (e.g. Tie *et al.* (2001)).

The uptake of N_2O_5 is calculated according to equation 3.7 in Section 3.5. The uptake coefficient (γ) for sulfate and sea salt is calculated from Evans & Jacob (2005). Gamma values for sulfate aerosol used in this study are in the range of 0.05-0.001, which is lower than γ values of around 0.1 used in previous studies (e.g. Dentener & Crutzen (1993); Tie *et al.* (2001)). For the discussion in this section simulation **COUPL** is the coupled model, used in the previous section (i.e. without the heterogeneous reaction of N_2O_5 + H_2O) and simulation **COUPL-HETN2O5** includes heterogeneous reaction of $N_2O_5 + N_2O_5$.

Figure 3.28 shows the zonally averaged percentage change in N_2O_5 in the **COUPL-HETN2O5** model compared to the **COUPL** model. During DJF (Figure 3.28a) N_2O_5 decreases by 80-100% throughout the NH mid and high latitudes. In JJA (Figure 3.28b) there is a large reduction in N_2O_5 in the SH mid latitudes (40-80%). Larger percentage decreases are simulated during the wintertime because background N_2O_5 concentrations are much higher due to a reduction in the photolysis of NO_3 which provides the source of N_2O_5. The decrease is larger in the NH winter than the SH winter because of the higher sulfate aerosol loading in the NH (see Figure 3.13).

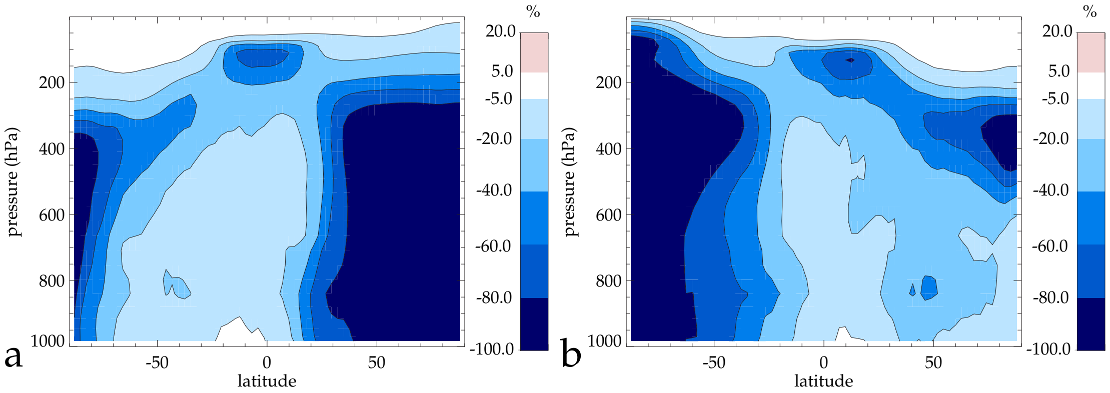

Figure 3.28: Zonally averaged % change in N_2O_5 in **COUPL-HETN2O5** model compared to the **COUPL** model in (a) DJF and (b) JJA.

The decreases in N_2O_5 lead to large reductions in NO_x as shown in Figure 3.29. NO_x decreases of 60-100% is predicted in the NH during DJF (Figure 3.29a). NO_x loss in the SH during JJA in the lower-mid free troposphere is much smaller (5-40%). The simulated changes in NO_x in the NH during JJA in this study (5-20%) are similar than those in Tie *et al.* (2001) who predicted a decrease in NO_x of 10-15% in the same region.i

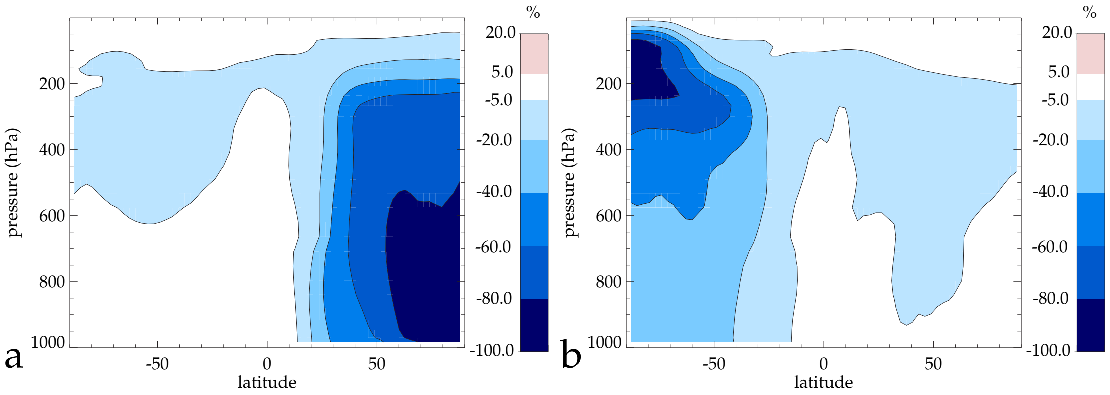

Figure 3.29: Zonally averaged % change in NO_x in the **COUPL-HETN2O5** compared to the **COUPL** model in (a) DJF and (b) JJA.

The production of ozone in the troposphere involves the oxidation of hydrocarbons and CO and is catalysed by the presence of HO_x and NO_x species. Therefore, the changes in NO_x in Figure 3.29 may impact on the production of ozone in the troposphere. Figure 3.30 shows the zonally averaged percentage change in O_3 due the the reaction of N_2O_5 on aerosols. O_3 concentrations decrease by up to 6-12% in the NH mid and high latitudes during DJF. In JJA the decrease in O_3 is smaller (3-6%). The largest change is simulated during the NH winter months because the reduction in NO_x is much larger during this period (80-100%). However, the change in ozone as a fraction of the change in NO_x is lower in the wintertime because oxidation of hydrocarbons and CO is small. The decrease in O_3 of 9-12% in the NH winter in this study is in agreement with Tie *et al.* (2001) and lower than the 25% decrease in zone due to N_2O_5 hydroloysis suggested by Dentener & Crutzen (1993). Ozone decreases are smaller in the SH than the NH because NO_x concentrations are very low in the high latitude SH; hence this region does not represent a significant source region for O_3.

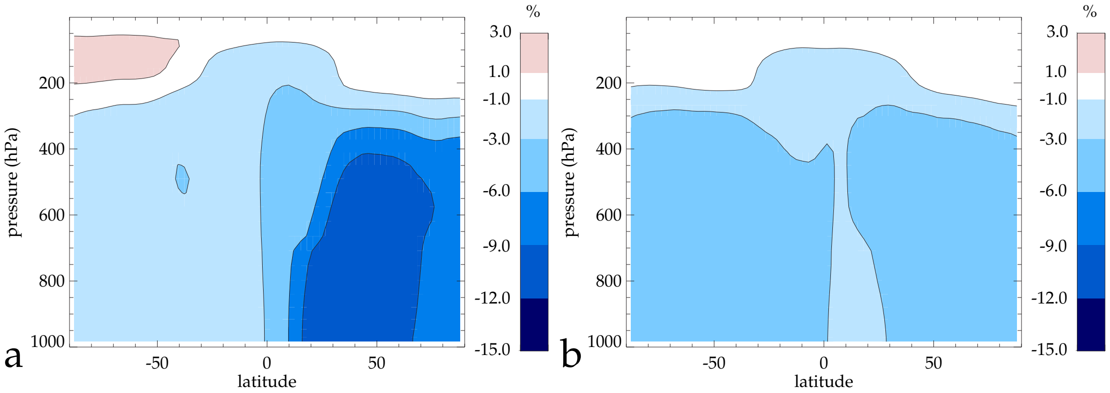

Figure 3.30: Zonally averaged % change in O_3 in **COUPL-HETN2O5** model compared to **COUPL** model in (a) DJF and (b) JJA.

The introduction of the hydrolysis of N_2O_5 on sulfate and sea salt aerosol in the troposphere results in a 3.8% lower troposphere ozone burden. The simulated ozone burden falls from 342 Tg O_3 in simulation **COUPL** to 329 Tg O_3 in simulation **COUPL-HETN2O5**.

Figure 3.31 shows a comparison **COUPL-HETN2O5** model with EMEP NO_2 observations. The model simulation without N_2O_5 hydrolysis compares better with the observations during DJF. This suggests over Europe in winter either NO_x sinks are overestimated or NO_x sources are underestimated in TOMCAT.

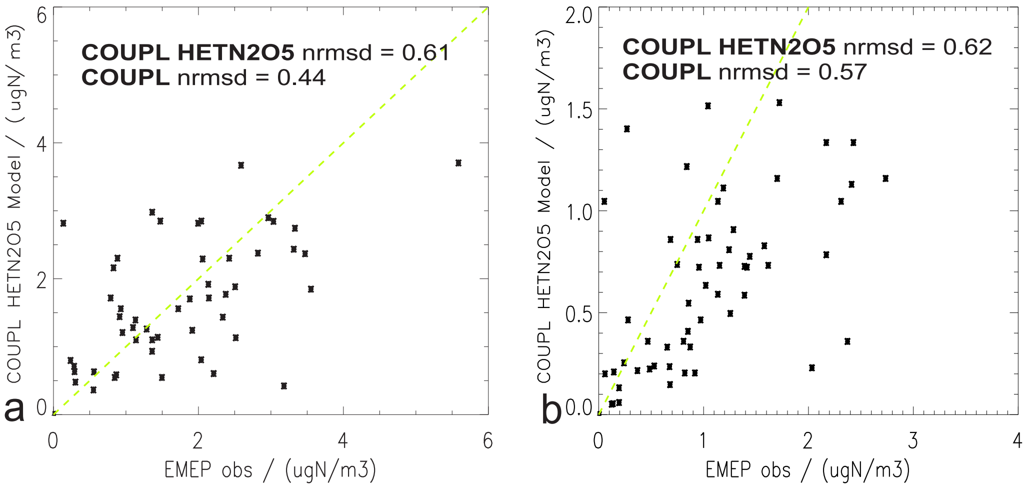

Figure 3.31: Simulated monthly mean NO_2 mass concentrations in the **COUPL-HETN2O5** model compared to EMEP during (a) DJF and (b) JJA. **COUPL** not plotted, *nrmsd* value given on plots for comprison with **COUPL-HETN2O5**.

This section shows the reaction of N_2O_5 on the surface of aerosols plays an important role in controlling the abundance of NO_x and O_3 in the troposphere. Previous TOMCAT simulations did not include this reaction and therefore were missing an important NO_x sink. The coupling of the aerosol and chemistry scheme in this work has allowed this to be addressed.

3.8 Summary and Conclusions

A size-resolved global aerosol microphysics scheme, including a description of sulfur chemistry, has been incorporated into a detailed chemical transport model. The coupling of the sulfur chemistry with the full chemistry provides a more realistic representation of the sulfur cycle and the chemical processes involved. All previous GLOMAP studies have used prescribed oxidant fields (e.g. Spracklen *et al.* (2005a); Manktelow (2008); Korhonen *et al.* (2008)), thus these studies ignored any sulfur-oxidant interactions. The inclusion of the aerosol microphysics scheme also allows for heterogeneous reactions on the surface of aerosols to be calculated from an interactive aerosol size distribution, negating the requirement to use prescribed aerosol surface area fields. This chapter presented the first results from the newly developed coupled model.

The coupled model shows large changes in the oxidation of DMS and SO_2. Oxidant depletions driven by DMS-NO_x-HO_x-O_x interactions in the coupled model results in an increased DMS burden and lifetime compared to the uncoupled model where these DMS driven chemical feedbacks are not accounted for. Large increases in SO_2 during the NH winter are simulated over the main SO_2 source regions of East Asia, North America and Europe in the coupled model due to depletions in H_2O_2, the primary SO_2 oxidant. The changes in DMS and SO_2 oxidation impact on the formation of sulfate aerosol and cloud condensation nuclei (CCN) number concentrations. Sulfate mass concentrations decrease by 25-60% over East Asia in winter due to lower oxidant availability. Smaller reductions in sulfate are also simulated over North America and eastern Europe. Interestingly, during NH winter sulfate mass concentrations decrease over large areas, but CCN number concentrations increase by 12-36% as the increased oxidant limitation in the coupled model acts to re-distribute sulfate mass from existing accumulation mode particles to growth of Aitken mode particles, resulting in an increased number of smaller CCN. The introduction of sulfur chemistry into the TOMCAT CTM results in a 3.1% decrease in the troposphere ozone burden.

Comparisons with observations shows the coupled model compares well with monthly mean DMS and SO_2 observations at Amsterdam Island but overestimates at Cape Grim and Dumont Durville. The overestimation may be explained by uncertainties in DMS seawater concentrations or by missing oxidants in the model. The coupled model also compares well with observations of SO_2 mass concentrations from the EMEP and EANET measurement networks. Differences between predicted and observed SO_2 and sulfate mass concentrations are similar for the coupled and uncoupled models. Comparisons with sulfate mass concentrations from EMEP measurement stations shows the coupled model under predicts sulfate during the winter and over predicts during the summer. This may be explained by uncertainties in modelled boundary layer mixing, SO_2 dry deposition rates or missing oxidant pathways. At EANET observations stations sulfate mass concentrations are underestimated in the coupled model during the summer and winter, probably due to an underestimate in anthropogenic SO_2 emissions for the comparison year 2004.

The first simulations in TOMCAT of the reaction of N_2O_5 on the surface of aerosols and cloud droplets show this reaction provides an important sink for NO_x in wintertime in agreement with Tie *et al.* (2001)and Dentener & Crutzen (1993). NO_x mixing ratios are reduced by greater than 60% during winter in the northern hemisphere. Smaller decreases in NO_x (20-40%) in the SH winter are simulated because of lower available aerosol surface areas. The reduction in NO_x impacts on the production of ozone, decreasing ozone mixing ratios by up to 9-12% in the NH winter. The simulated ozone loss in the NH winter is lower than that predicted by Dentener & Crutzen (1993) but in agreement with Tie *et al.* (2001). The introduction of N_2O_5 hydroloysis reaction results in a 3.8% lower troposphere ozone burden than the simulation without this reaction.

The work in this chapter emphasises the importance of oxidants in controlling lifetime and burden of DMS and SO_2 and their impact on the aerosol size distribution and CCN formation. Sulfur-oxidant-aerosol interactions have been identified in the coupled simulation that cannot be accounted for in the uncoupled simulation. In addition the inclusion of heterogeneous chemistry of N_2O_5 has been shown to be of significance for controlling ozone and NO_x. The coupled model provides a significantly improved platform for the study of chemical and aerosol processes and interactions in the troposphere.

Chapter 4

Impact of Bromine on DMS and Aerosol in the Remote Marine Boundary Layer

4.1 Introduction

The previous chapter provided a description and evaluation of a newly developed coupled aerosol and chemistry model. The results showed DMS concentrations in the coupled model are overestimated compared to observations. Possible explanations for this could be an overestimate of the DMS source, underestimated oxidant fields or missing additional oxidants for DMS in the model. As discussed in Section 2.6.2, BrO may provide an important oxidant for DMS in the remote marine boundary layer. The evidence for BrO as a possible sink for DMS is substantial. Detailed modelling studies and observations of DMS and BrO indicate a potentially large contribution of BrO to DMS oxidation on a global scale (Boucher *et al.*, 2003; Von Glasow *et al.*, 2004b). This evidence was discussed in more depth in Section 2.6.

Previous studies that have attempted to assess the importance of BrO for DMS oxidation have used prescribed amounts of BrO in the boundary layer and lower troposphere. The first global model study of BrO and DMS used a global sulfur cycle model in a GCM with fixed oxidants and a constant BrO mixing ratio of 1 pptv in the lowest 1.3 km of the atmosphere (Boucher *et al.*, 2003). That study estimated that BrO could contribute up to 29% of the DMS sink. Von Glasow *et al.* (2004b) used a 3-D chemical transport model (CTM) with a comprehensive treatment of tropospheric gas-phase chemistry, including a bromine scheme, to study the impact of 0.5-2 pptv of BrO on DMS and ozone in the free troposphere. They found up to a 26% reduction in the tropospheric DMS burden due to bromine chemistry. However, they did not explicitly account for a sea salt or short-lived organohalogen source of bromine in the MBL. These studies were limited by their inability to account for spatial and temporal variations in BrO and possible chemical and aerosol interactions that control bromine emissions and recycling.

DMS is an important precursor gas to the formation of cloud condensation nuclei (CCN) in remote marine regions (Charlson *et al.*, 1987; Ayers *et al.*, 1991; Korhonen *et al.*, 2008). Clearly changes in oxidation capacity driven by emissions of bromine species could alter aerosol formation by perturbing oxidation pathways and the DMS lifetime and transport to the free troposphere. No previous studies have investigated the role of BrO for impacting marine aerosol formation. This thesis is the first study to examine the importance of bromine chemistry for marine aerosol formation using a detailed size-resolved global aerosol microphysics scheme.

In this chapter the coupled model described in Chapter 3 is extended to include a bromine chemistry scheme and a newly developed detailed parameterisation of bromine emissions from sea salt aerosol. In Section 4.3 model fields for total inorganic bromine and partitioning are discussed. The model is also compared with ground-based observations and satellite retrievals of tropospheric BrO. Section 4.4 addresses changes in HO_x, NO_x and ozone in the bromine simulation. Section 4.5 provides a detailed comparison of the coupled bromine model with observations of ozone, NO_x and HO_x at the Cape Verde Atmospheric Observatory (CVAO). Interactions between sulfur species and bromine chemistry are presented in Section 4.6. In Section 4.7 changes in aerosol mass and number concentrations are discussed. Finally, possible interactions and feedbacks between the marine sulfur cycle, sea salt aerosol and bromine chemistry are presented in Section 4.8.

Some of work presented in this chapter has been published in Breider *et al.* (2010), *Impact of BrO on DMS in the remote marine boundary layer.* Note that runs analysed here have been updated compared to the paper and so the same results are quantitatively different. The model resolution has increased to 2.8° × 2.8° from 5.6° × 5.6° in the paper, the aerosol scheme is now a modal scheme instead of a bin scheme and the methane field has been updated.

4.2 Model Experiments

In this chapter six model simulations are discussed. Run **BR** is the base run with organic and sea-salt bromine emissions and the DMS flux parameterisation scheme of Liss & Merlivat (1986). Run **NOBR** is the same as **BR** but does not include any bromine emissions. Run **BRORG** is the same as **BR** but includes organic bromine emissions only. Runs **BRNI** and **NOBRNI** are the same as runs **BR** and **NOBR**, respectively, but use the DMS flux scheme of Nightingale *et al.* (2000). The sulfur chemistry scheme used is described in Section 3.5. The calculation for bromine emissions from sea salt is explained in Section 3.5.2.2. Finally, run **NODMS** does not include emissions of bromine or DMS.

All simulations are for 2004 allowing for a spin-up period of 6 months. For the CVAO observation comparisons in Sections 4.3 and 4.5, the model simulation is for the observational period (Nov 2006 to June 2007), with a spin-up period of 6 months. The model was run at a resolution of $2.8^\circ \times 2.8^\circ$ and forced by ECMWF analyses. The vertical resolution uses 31 hybrid σ-p levels from the surface to 10 hPa. In-cloud oxidation of SO_2 takes place via reaction with H_2O_2, O_3 and HOBr. The sea salt emission parameterisations of Gong (2003), for sizes below $1.5\mu m$ dry radius, and Smith & Harrison (1998), for sizes larger than $1.5\mu m$ dry radius. In the simulations only sulfate and sea salt aerosol components are simulated in a series of 4 externally mixed modes; water-soluble nucleation, Aitken, accumulation and coarse.

In addition to inclusion of bromine chemistry all simulations in this chapter include uptake of SO_2 and HNO_3 to freshly emitted sea salt aerosol. This is the only difference between simulation **NOBR** and **COUPL** in the previous chapter.

4.3 Evaluation of the Bromine Model - Comparison with Observations

Figure 4.1 shows the surface and zonally averaged mixing ratio of total inorganic bromine (Br_y) in simulation **BR** during December and June. Br_y is calculated as the sum of all modelled inorganic bromine species (HBr, HOBr, Br, $2\times Br_2$, BrO, BrONO and $BrONO_2$). The model predicts 0-20 pptv of surface Br_y over the oceans. In the tropics simulated Br_y ranges from 0-12 pptv. Elevated Br_y is simulated over parts of the tropical open oceans (8-12 pptv). The northern Indian Ocean and tropical Western Pacific Ocean show very low Br_y ($<$ 2 pptv) because of high precipitation and hence, fast removal of HBr. The highest Br_y mixing ratios are simulated in the North Atlantic Ocean during the winter ($>$ 20 pptv). This is explained by high emissions of sea salt, ample availability of acidifying trace gases from anthropogenic sources and reduced photochemical activity in the wintertime. Over the southern hemisphere (SH) oceans the model simulates a clear seasonal cycle in Br_y, with higher mixing ratios in the summer months (2 - 10 pptv) compared to less than

2 pptv during the winter months. Simulation **BR** predicts high Br_y mixing ratios (14-18 pptv) in June in the Arabian Sea and in the South China Sea in Dec (12-18 pptv), explained by high wind speeds driving a high sea salt flux associated with the monsoon season.

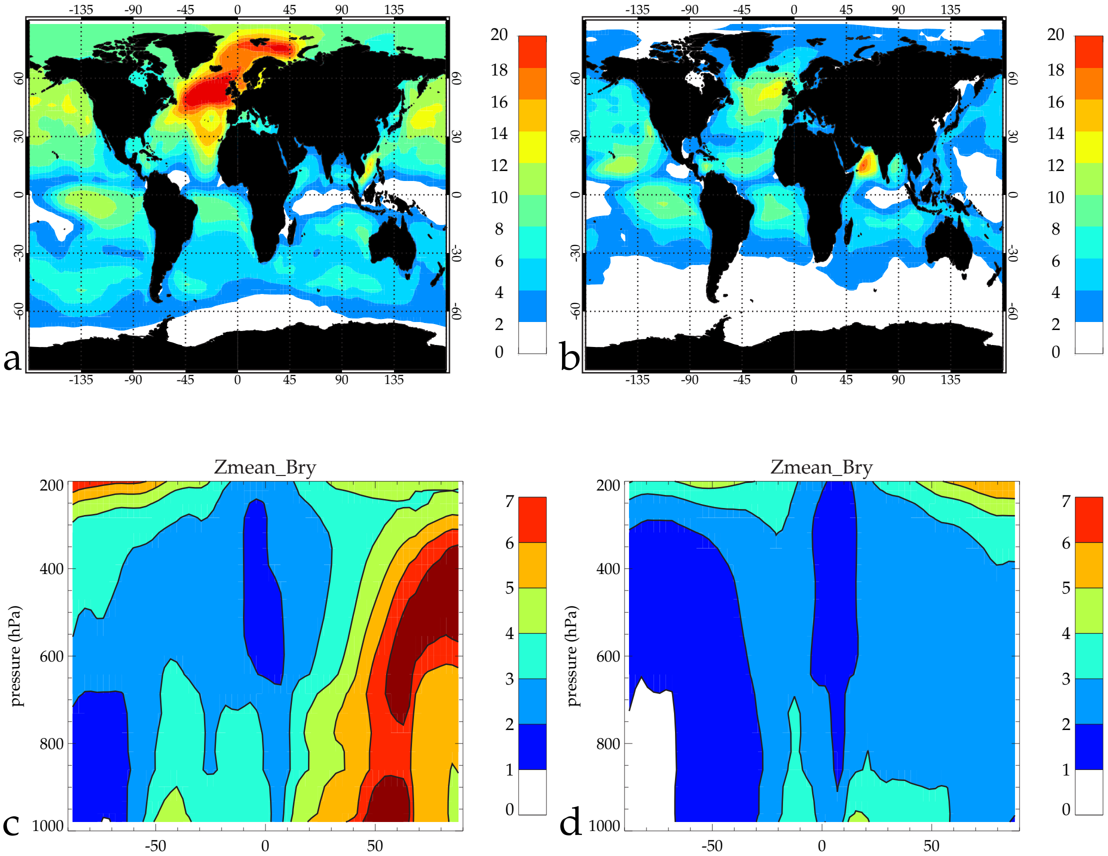

Figure 4.1: Surface and zonally averaged total inorganic bromine (Br_y) mixing ratio (pptv) in simulation **BR** during (a) and (c) December and (b) and (d) June.

The variability of Br_y in the SH is explained by the source of bromine from sea salt aerosol. In the SH summer there is increased availability of SO_2 from DMS oxidation to acidify the aerosol and release the bromine. Also, because wind speeds are relatively lower, surface exchange processes are less efficient, resulting in a longer aerosol lifetime for acidification (Kerkweg *et al.*, 2008). As a result the sea salt bromide depletion factor is higher in the model (max. 0.58 at 0.77 μm dry radius) and larger sea salt size bins will be acidified to release Br_2. In the wintertime there is low availability of acidifying trace gases, wind speeds are higher leading to shorter sea salt aerosol residence times due to faster exchange processes. As a result the sea salt bromide depletion factor is low (max. 0.08 at 0.77 μm dry radius) and larger size bins are not acidified to provide a source of Br_2. This is important because the larger size bins dominate the mass flux of sea salt and provide a proportionally larger source of bromine than the smaller size bins.

Observations of surface Br_y over the remote oceans are very limited. Pszenny *et al.* (2004) measured 3-8 pptv at Hawaii (20°N, 155°W), and 3-4 pptv Br_y was observed during June at the equator in the tropical Atlantic Ocean (0°N, 0°W) (Kritz & Rancher, 1980). The model slightly overestimates Br_y in the tropical Atlantic in June (4-6 pptv) but agrees well with the observations at Hawaii. Keene *et al.* (2009) measured Br_y during a cruise down the west coast of Africa in October and November 2003. Br_y was observed at 23-30 pptv in the mid-latitude north Atlantic (25-33°N), 18-21pptv in the tropics north of the Inter tropical Convergence Zone (ITCZ) (12-20°N), 4 pptv in the ITCZ and 5-8 pptv in the tropical South Atlantic. The model compares well in the ITCZ and South Atlantic, but under predicts the observed Br_y in the mid-latitude North Atlantic (14-16 pptv) and northern hemisphere (NH) tropics (8-12 pptv). This under prediction in the model may be explained by a higher sea salt flux in October and early November during the observation period.

In the zonal mean plots, (Figure 4.1c, d) high levels of Br_y (4-8 pptv) are simulated in December in the NH mid-high latitudes. During June in the NH simulated Br_y is only 2-4 pptv. The lower levels of Br_y can be explained by the reduced sea salt flux in the summer and increased photochemical activity. In the SH peak concentrations of Br_y of 4-5 pptv are simulated in the 30-50° latitude band during December from the surface to 900 hPa. In SH June less than 2 pptv Br_y is simulated due to the limited source of bromine from sea salt. In the tropics Br_y mixing ratios of 1-5 pptv are simulated during both December and June. Highest Br_y mixing ratios are simulated in the tropical wintertime hemisphere, explained by higher wind speeds, leading to a larger source of Br_2, and lower photochemical activity.

Simulation **BR** compares well with Yang *et al.* (2005) in the NH and tropics during both December and June. The highest Br_y mixing ratios are predicted in the North Atlantic oceans during December. However, simulation **BR** predicts lower Br_y mixing ratios in the SH mid-high latitudes during December than Yang *et al.* (2005), who simulated $>$ 8 pptv Br_y throughout large areas of the southern mid-latitude oceans. This study predicts 6-8 pptv in limited regions southwest and southeast of South America and southwest of Australia. There are a number of possible explanations for these differences. Firstly, in this study the source of bromine from sea salt is limited by the availability of acidifying trace gases. This clearly restricts the bromine source in the SH oceans compared to Yang *et al.* (2005) who did not account for this limitation. Secondly, Yang *et al.* (2005) used a fixed DF value for all sea salt sizes of 0.5, at higher size intervals this value is too high resulting in an overestimate in the flux. Yang *et al.* (2005) estimated the source of bromine from sea salt to be 1.15 to 2.09 Tg Br yr^{-1} compared to just 0.46 Tg Br yr^{-1} in simulation **BR**. Simulation **BR** may also underestimate the release of bromine from sea salt because acidification by organic acids

(RCOOH) (Keene & Galloway, 1986) is not accounted for and aerosol acidification timescales are restricted to 30 minutes. In reality sea salt particles may be acidified on timescales longer than 30 minutes and hence provide an additional source of bromine. A final factor is that oxidation of DMS provides a source of HCHO during the SH summer months when DMS emissions are high. This additional source increases HCHO mixing ratios by up to 30% over DMS source regions. Higher HCHO mixing ratios increases cycling of Br to HBr and favours removal of Br_y.

Figure 4.2 shows the zonally averaged Br_y partitioning during December and June. Figures 4.2a and 4.2b shows BrO is generally less than 10% of the total Br_y during these periods with the exception of the SH mid-latitudes and the mid-high latitude upper troposphere where BrO represents 10-20% of Br_y. The BrO/Br_y fraction is much lower in the troposphere than the stratosphere where it exceeds $>$50% (Theys *et al.*, 2007). The lower BrO/Br_y fraction in the troposphere is explained by lower NO_x levels and slower photochemistry. $BrONO_2$ represents 10-30% of Br_y during the NH mid-high latitude wintertime (Figures 4.2c). Larger partitioning of Br_y to $BrONO_2$ in the SH winter (10-50%) than the NH winter (10-30%) is explained by faster heterogeneous recycling of $BrONO_2$ in the NH due to higher aerosol surface areas. In the NH summer a higher fraction of Br_y partitions to $BrONO_2$ (10-20%) than in the SH summer (0-10%) due to higher NO_x emissions in the NH. Interestingly, in the stratosphere the model overestimates the partitioning of Br_y to $BrONO_2$ compared to Theys *et al.* (2007) suggesting missing heterogeneous chemistry important in the stratosphere. This is as expected because the troposphere model used here is not designed for the stratosphere and does not include stratospheric sulfate aerosols or chlorine chemistry. Away from the high latitudes of the winter hemisphere, HBr is generally the dominant fraction of Br_y (30-80%) because of photochemical cycling of Br to HBr (Figures 4.2e and f) via the reaction of Br with HCHO and HO_2. In the high latitude winter, the absence of sunlight reduces HBr formation and Br_y partitions to other species. The lower HBr fraction in the NH summer in the free troposphere at 20-50°N can be explained by the formation of $BrONO_2$ which is recycled on the surface of aerosol to HOBr. HOBr constitutes 10-50% of Br_y in most of the troposphere (Figures 4.2g and h). The decrease in HOBr fraction at 700-900 hPa is explained by in-cloud oxidation of SO_2, which provides a sink for HOBr. Also the enhanced HOBr fraction at the surface in the NH during June (40-60%) is explained by $BrONO_2$ recycling on aerosol to form HOBr. This effect is less evident in the SH where NO_x and aerosol surface areas are lower. At high latitudes during the winter the absence of sunlight partitions almost all Br_y to Br_2 (not shown).

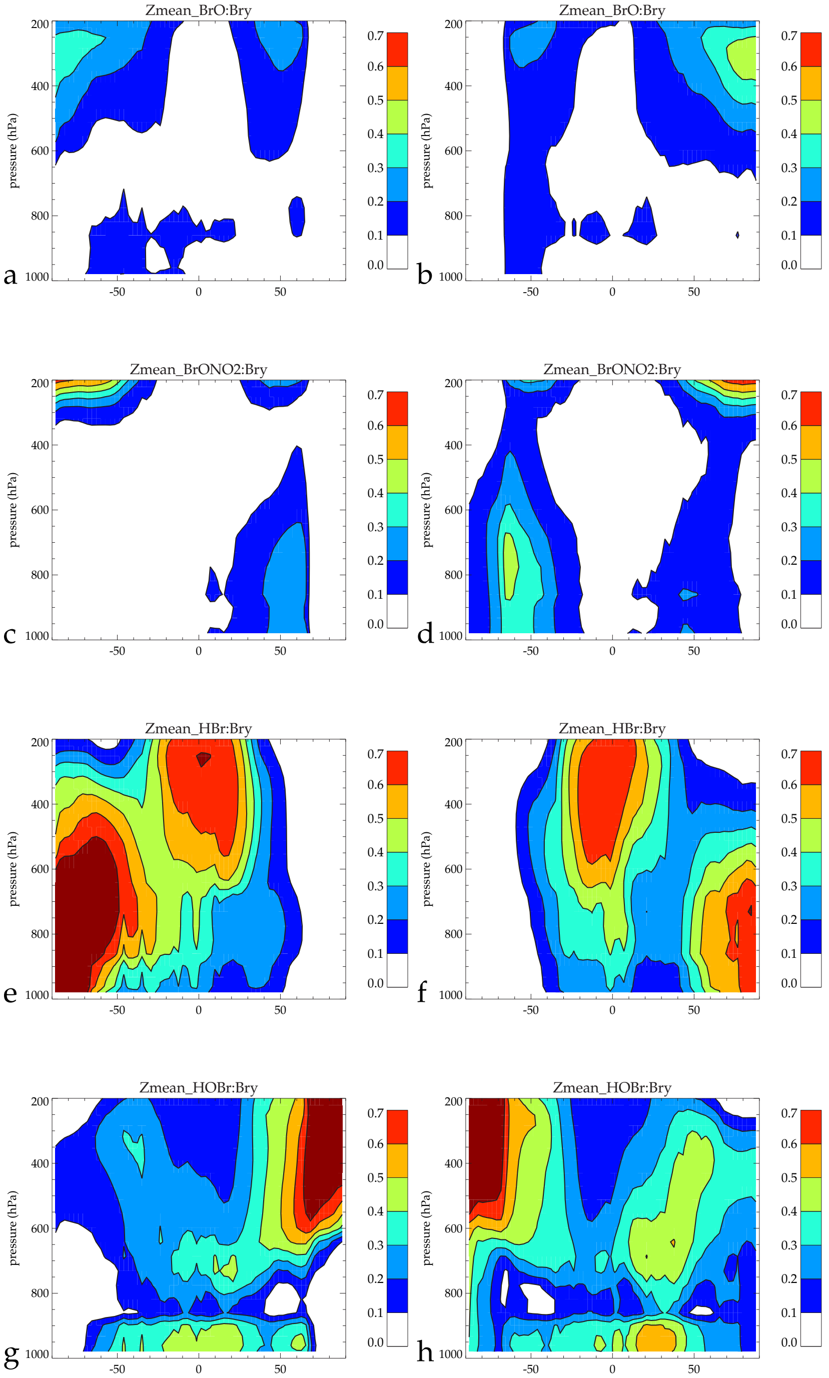

Figure 4.2: Zonally averaged Bromine partitioning plots from model simulation **BR** for (a) and (b) BrO:Br$_y$ ratio, (c) and (d) BrONO$_2$:Br$_y$ ratio, (e) and (f) HBr:Br$_y$ ratio, (g) and (h) HOBr:Br$_y$ ratio. Plots (a), (c), (e) and (g) are for December. Plots (b), (d), (f) and (h) are for June.

Figure 4.3 shows the monthly averaged surface Br_y partitioning during December and June. Figures 4.3a and b shows BrO represent a maximum of 30% of total Br_y. The BrO:Br_y fraction is higher in the summertime when daytimes are longer. Around coastlines the BrO:Br_y fraction is lower due to higher NO_x levels. The $BrONO_2$:Br_y ratio is higher during the wintertime when nights are longer and around coastlines where NO_x levels are higher (4.3 c and d). In the North Atlantic and North Pacific oceans during the summer the $BrONO_2$:Br_y ratio is increased relative to the SH oceans during the winter because of NO_x emissions from shipping traffic. Simulation **BR** shows HBr represents the dominant fraction of surface Br_y at high latitudes during the summer ($>$50%). An increased fraction of Br_y partitions to HBr in the SH summer than the NH summer due to higher NO_x levels in the NH which favours partitioning to $BrONO_2$. Figures 4.3g and h shows HOBr represents the dominant fraction of Br_y in simulation **BR** in the tropical oceans. The partitioning of Br_y to HOBr is likely to be overestimated in simulation **BR** due to the use of a low γ HOBr value for the recycling of HOBr on aerosol. At high latitudes during the winter Br_y partitions almost completely to Br_2 (not shown) due to the absence of sunlight.

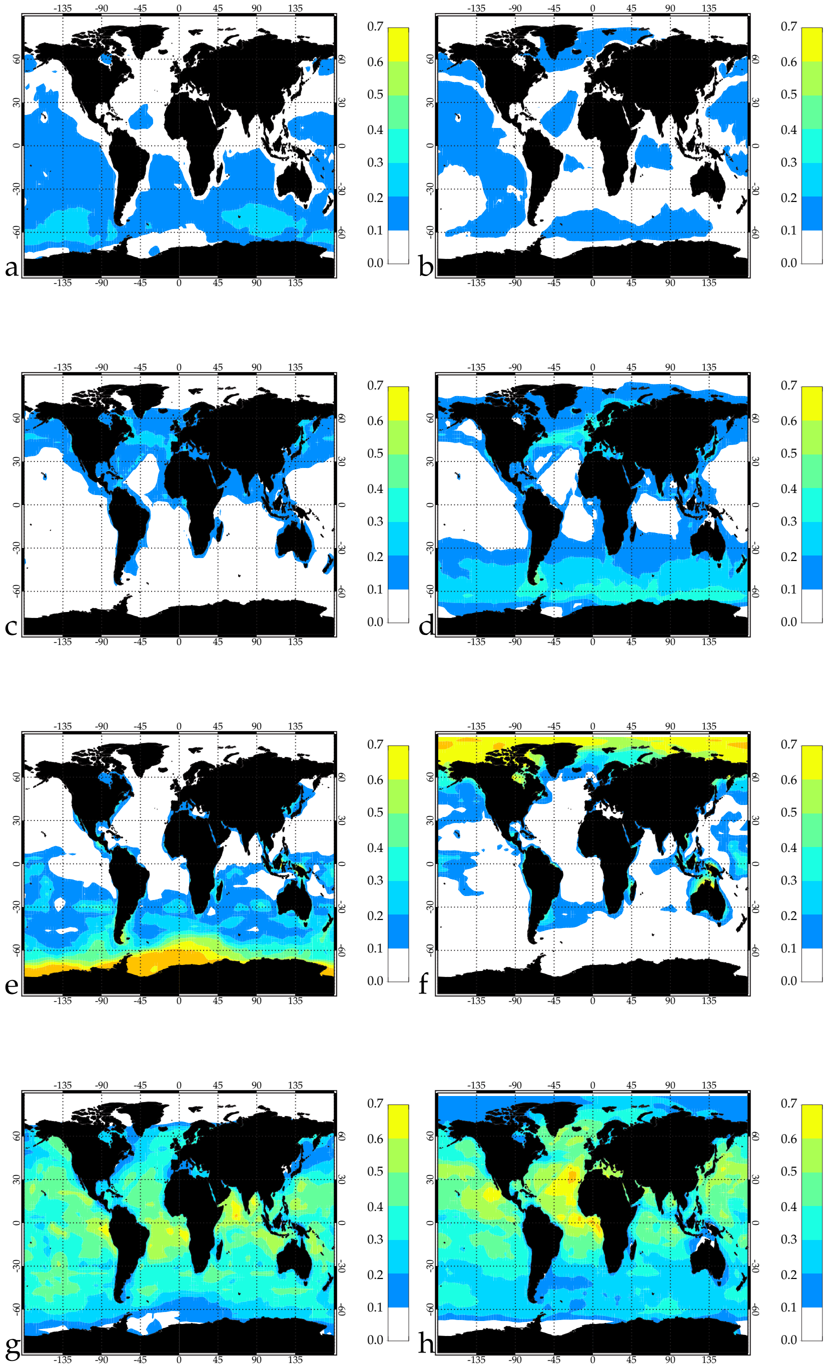
a
b
c
d
e
f
g
h
-135
-90
-45
0
45
90
135
60
30
0
-30
-60
0.7
0.6
0.5
0.4
0.3
0.2
0.1
0.0

Figure 4.3: Monthly mean surface bromine species plots (pptv) from model simulation **BR** for (a) and (b) BrO, (c) and (d) $BrONO_2$, (e) and (f) HBr, (g) and (h) HOBr. Plots (a), (c), (e) and (g) are for December. Plots (b), (d), (f) and (h) are for June.

Figure 4.4 shows the monthly averaged zonal mean mixing ratios of four main bromine species during December and June. BrO mixing ratios are higher in the lower troposphere during January. The highest BrO mixing ratios are simulated at the surface in the SH between 30 and 60°S. Elevated BrO is also simulated in the NH in January around 60°N between 850 and 600hPa (Figures 4.4a and b). Lower BrO is simulated in SH winter because of a reduced source of Br_2 form sea salt aerosol (See Figure 4.26). In the NH summer simulated BrO is also low due to faster removal of Br_y (more efficient photochemistry driving formation of soluble species HOBr and HBr) and cycling of BrO to HOBr via $BrONO_2$ hydrolysis. $BrONO_2$ mixing ratios are higher during the winter (Figures 4.4c and d), as it is efficiently photolysed, longer nights favour a longer lifetime and higher mixing ratios. Higher $BrONO_2$ mixing ratios are simulated in the NH due to increased sources of NO_x. Simulation **BR** shows HBr mixing ratios are highest in the summer (Figures 4.4e and f). Maximum HBr levels are simulated in the SH in december around 40°S between 800 and 700hPa. This maximum is explained by a strong source of Br_2 from sea salt, active photochemistry and low NO_x levels that inhibit formation of $BrONO_2$. For HOBr a clear gradient in the mixing ratios is simulated at the top of the boundary layer. This can be explained by the reaction of HOBr with SO_2 in cloud droplets. In both December and June monthly mean HOBr mixing ratios in the tropical boundary layer are greater than 1.8 pptv due to high availability of HO_2 in this region. Maximum HOBr is simulated in the boundary layer at 50-60°N in December, due to the reaction of $BrONO_2$ on sea salt and sulfate aerosol.

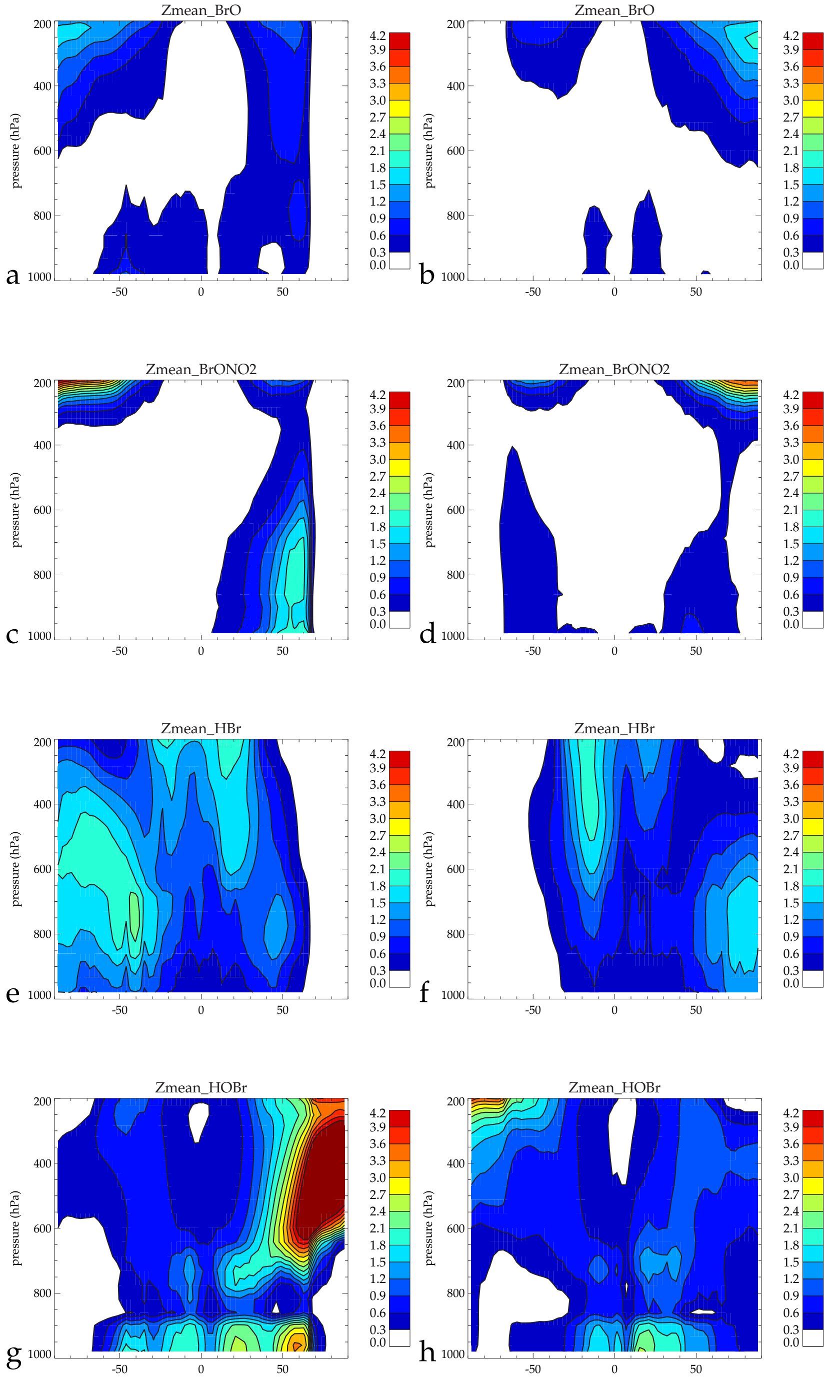

Figure 4.4: Zonal average monthly mean bromine species plots (pptv) from mod el simulation **BR** for (a) and (b) BrO, (c) and (d) $BrONO_2$, (e) and (f) HBr, (g) and (h) HOBr. Plots (a), (c), (e) and (g) are for December. Plots (b), (d), (f) and (h) are for June.

Figure 4.5 shows the monthly averaged surface mixing ratios of four main bromine species during December and June. The highest BrO mixing ratios are simulated in the East Pacific Ocean in two regions, the tropics and 40-60°S. Over the SH oceans during the winter BrO mixing ratios are low due to the low source of bromine from sea salt aerosol at this time (Figures 4.5a and b). In the NH seasonality in the BrO is less evident due to a sustained source of Br_2 from sea salt aerosol throughout the year. The difference between the NH and SH is driven by the availbility of acidifying trace gases to titrate sea salt alkalinity and produce a source of Br_2. Simulation **BR** shows mixing ratios of $BrONO_2$ are highest in theNH oceans (Figures 4.5c and d), with highest levels simulated in the North Atlantic Ocean, due to high shipping emissions of NO_x. HBr mixing ratios show a maximum in the summer and elevated levels around coastlines (Figures 4.5e and f). HOBr shows high surface mixingratios over the tropical oceans and in the NH oceans (>5pptv) (Figures 4.5g and f. HOBr mixing ratios are low in key rainout regions such as the Western Tropical Pacific Ocean and in the high latitude SH summer when there is a small source of Br_2 from sea salt. Here, again it is important to note HOBr mixing ratios may be overestimated in simulation **BR** due to a low γHOBr value used for recycling.

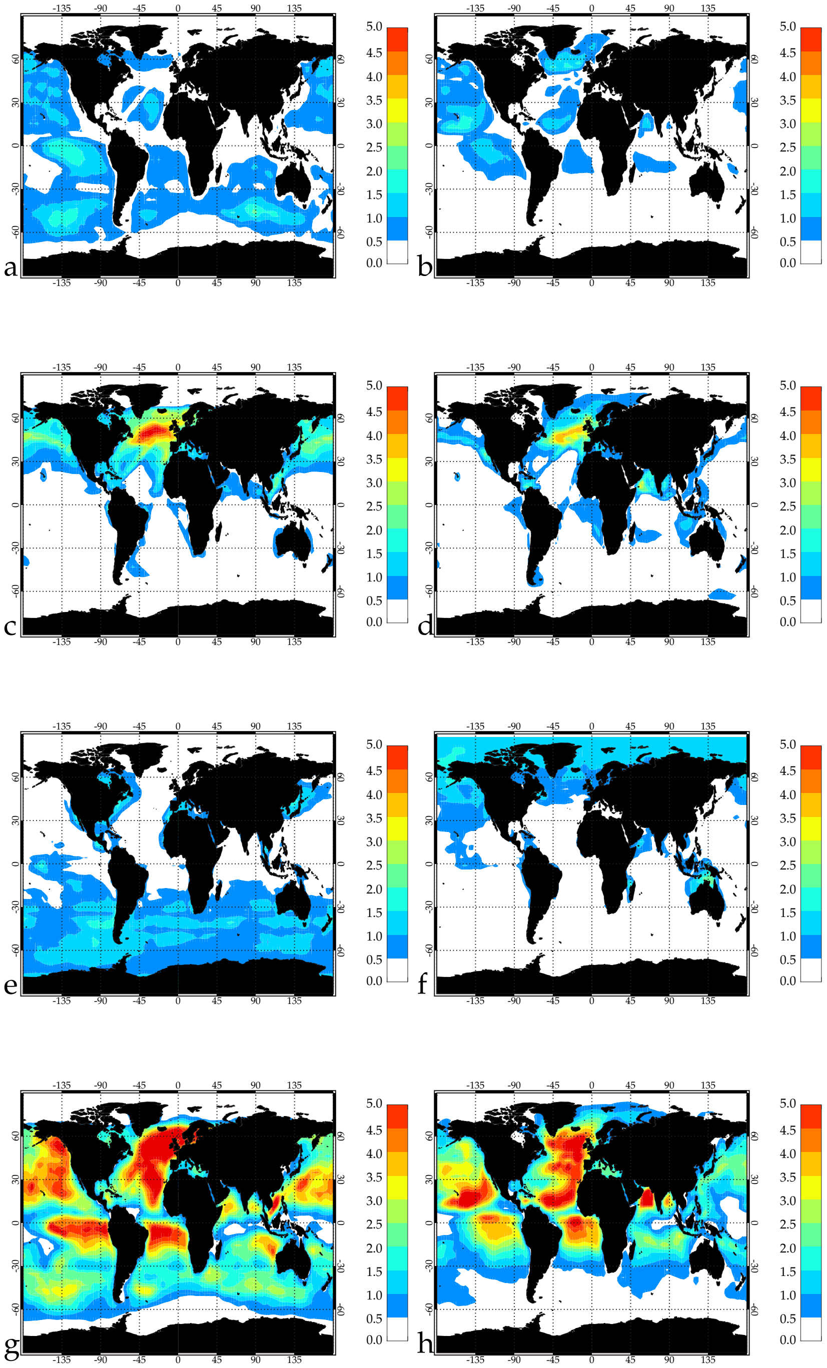

Figure 4.5: Surface monthly mean bromine species plots (pptv) from model simulation runa for (a) and (b) BrO, (c) and (d) $BrONO_2$, (e) and (f) HBr, (g) and (h) HOBr. Plots (a), (c), (e) and (g) are for December. Plots (b), (d), (f) and (h) are for June.

Observations of BrO over the remote oceans are very limited. The most comprehensive dataset is from the CVAO in the tropical East Atlantic Ocean (Read *et al.*, 2008; Mahajan *et al.*, 2010). CVAO provides an exceptional observation station representative of the background open ocean marine boundary layer as there are no seaweed beds or other local sources of halogen compounds

(Read *et al.*, 2008). Figure 4.6 shows the observed mean diurnal cycle in BrO mixing ratios from November 2006 to June 2007 at CVAO (16.85°N, 24.87°W) compared to the simulated BrO in model run **BR**. BrO is measured using a long-path Differential Absorption Spectroscopy Instrument (LP-DOAS) (Plane & Saiz-Lopez, 2006).

The measured diurnal cycle in BrO shows a distinct ‘top-hat’ profile. BrO builds up in the morning in response to photolysis of Br_2 and BrCl, the main nighttime Br_y reservoirs. Photolysis of organic bromine compounds cannot explain this early morning BrO burst given their long photolytic lifetimes in the lower atmosphere (Carpenter *et al.*, 1999). The midday minimum in BrO in the observations is explained by photochemical production of HO_2 that peaks around midday and provides a sink for BrO. Simulation **BR** shows good agreement with the observations in May and June but underestimates the observed BrO from November to April. Possible explanations for the underestimate of BrO in the winter include seasonality in sea salt bromide depletion factor values, driven by changes the sea salt source flux and a possible overestimate of HO_2 in the region. Keene *et al.* (2009) measured size-resolved DF values in the region during a cruise down the west coast of Africa in October and November 2003 (DF = 0.7 at 1-4μm) which are larger than used in this study.

During March and April the model appears to predict an earlier build-up of BrO than the observations. During May and June the model predicts a build up of BrO later than the observations. This is likely to be explained by missing chemistry in simulation **BR**. In this study the dominant nighttime reservoir of Br_y is Br_2. In box model studies that include chlorine chemistry, BrCl represents the dominant Br_y fraction at night (Keene *et al.*, 2009). As Br_2 is photolysed faster after sunrise than BrCl (Saiz-Lopez *et al.*, 2006), this can explain why BrO builds up too early in March and April in the model compared to the observations. The delayed build-up of BrO in the model in May and June may be explained by the simple treatment of clouds for calculation of the photolysis rates in the model, which do not account for any seasonality in cloud cover. The nighttime BrO in the observations is below the detection limit of the instrument (0.5 to 0.8 pptv) (Mahajan *et al.*, 2010).

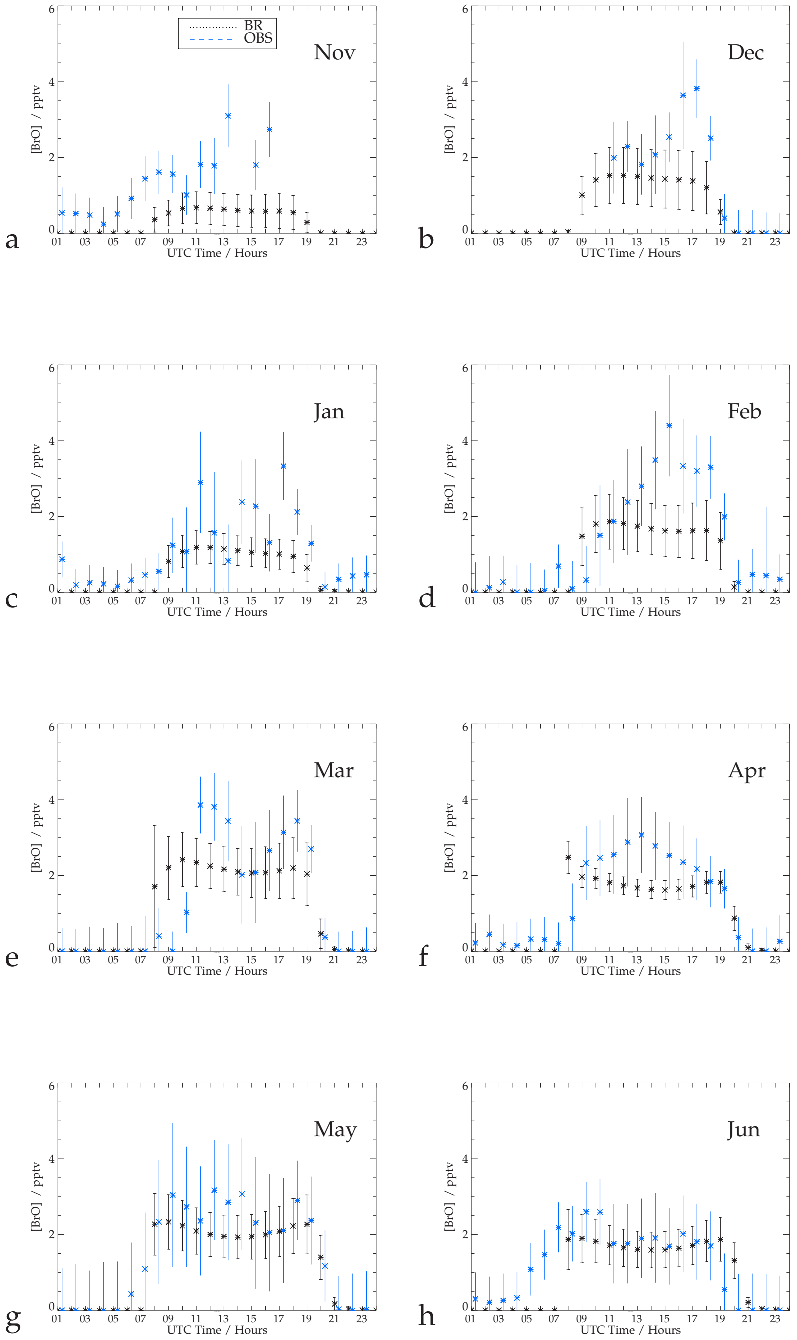

Figure 4.6: Comparison of observed and modelled surface diurnal BrO cycle (pptv) at CVAO [16.85°N, 24.87°W] from November 2006 to June 2007 for simulation **BR**. Model simulations are for the actual observation period. Observations taken from Mahajan *et al.* (2010). (a) Nov. 06, (b) Dec. 06, (c) Jan. 07, (d) Feb. 07, (e) Mar. 07, (f) Apr. 07, (g) May 07, (h) Jun 07.

Figure 4.7 shows the observed and modelled monthly daytime mean and maximum BrO mixing ratio at CVAO from November 2006 to June 2007 compared to simulations **BR** and **BRORG**. The **BR** simulation reproduces 80% of the observed mean BrO levels from March to June (**BR** Mar-Jun mean = 1.98 pptv, OBS Mar-Jun mean = 2.55 pptv) but significantly underestimates from November to February (**BR** Nov-Feb mean = 0.99 pptv, OBS Nov-Feb mean = 2.38 pptv) (see also Figure 4.6). The **BRORG** simulation severely underestimates the observed BrO throughout the whole observation period (**BRORG** mean = 0.2 pptv, OBS mean = 2.42 pptv), suggesting organic bromine emissions alone cannot explain the observed levels of BrO at CVAO in agreement with O'Brien *et al.* (2009).

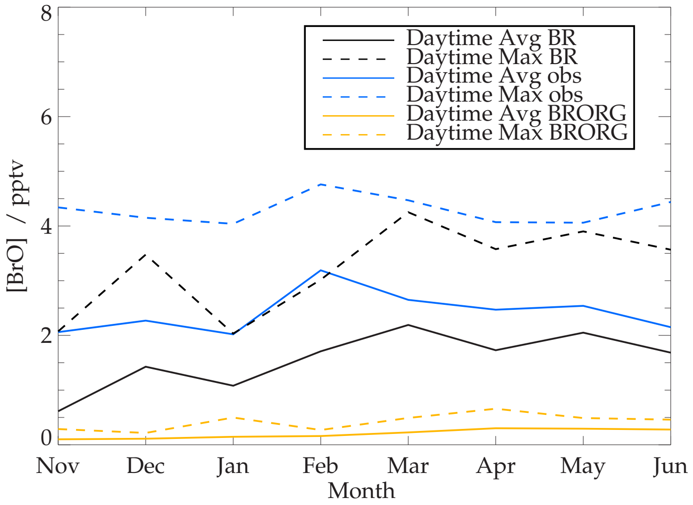

Figure 4.7: Monthly mean and maximum observed and modelled surface BrO mixing ratios (pptv) in runs **BR** and **BRORG** at CVAO [16.85°N, 24.87°W]. Observations taken from Read *et al.* (2008).

Figure 4.8 shows the monthly mean diurnal cycle in Br_y speciation at CVAO during the observation period. Simulation **BR** predicts HOBr as the dominant daytime Br_y species. At night Br_2 is dominant, but HOBr also contributes as a key reservoir at night. The late evening increase in HOBr from March to June is caused by recycling of $BrONO_2$ on aerosol. Br and $BrNO_2$ represent a very small fraction of total Br_y ($< 2\%$) throughout the observation period. In comparison, the box modelling studies of Saiz-Lopez *et al.* (2006), Keene *et al.* (2009) and Von Glasow *et al.* (2002) all predict a faster drop in HOBr after sunset. This can be explained by the treatment of the HOBr + HBr heterogeneous reaction in the model, which is the main nighttime sink for HOBr. This reaction in the model in most of the atmosphere is limited by uptake of HOBr because of its lower γ value, (γ HOBr = 0.05, γ HBr=0.2), but at CVAO in some months nighttime HBr approaches zero. The method of limiting HOBr uptake by availability of HBr prevents HOBr being recycled through the aerosol phase to Br_2 in this region. This method conserves total Br_y in the model but is likely to be the main reason for the overestimate of HOBr at CVAO in the evenings. Additional factors leading to overestimated HOBr in the evenings are an overestimate in HO_x in the region, in the model that favours a higher source of HOBr in the daytime, consistent with suppressed daytime BrO in Figure 4.6. An overestimate in NO_x at CVAO (see Figure 4.15) will also lead to an elevated late evening source of HOBr from recycling of $BrONO_2$.

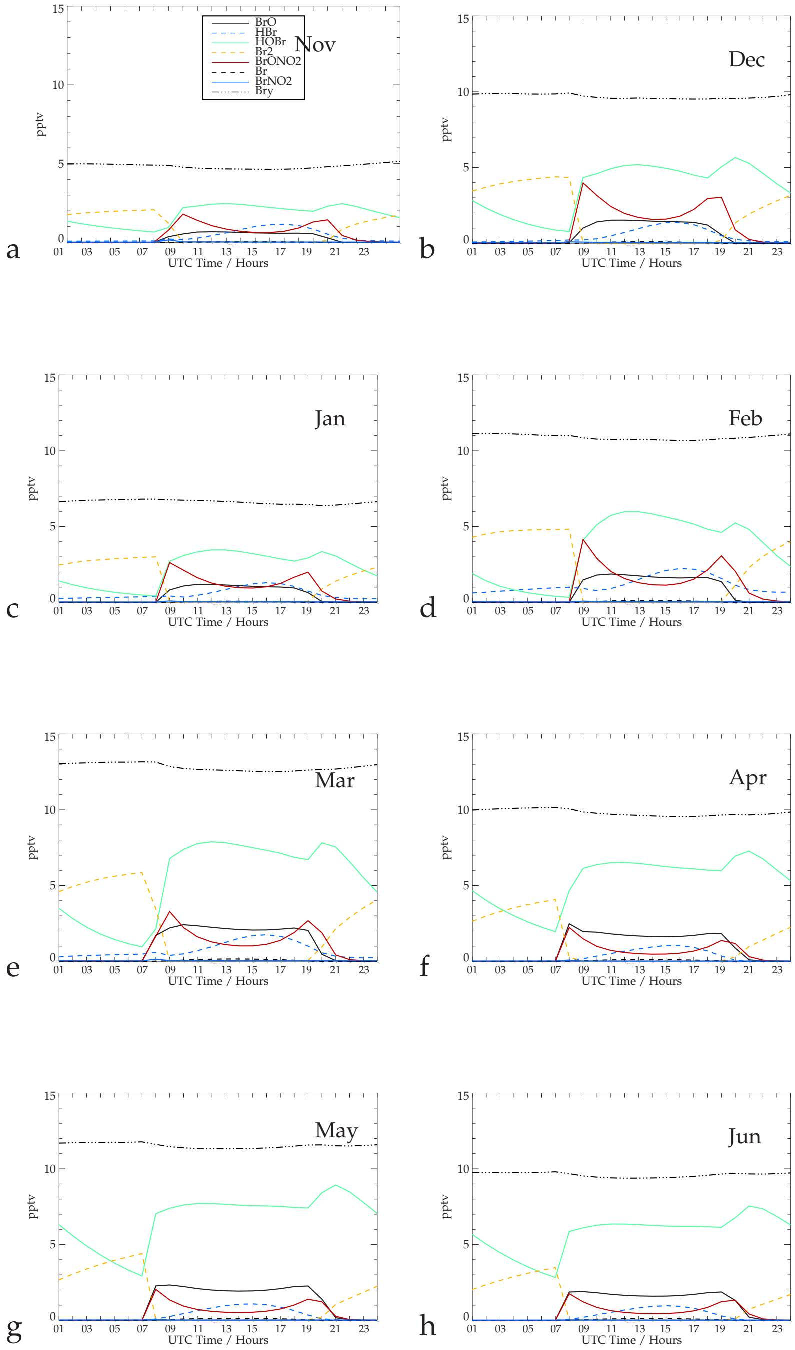

Figure 4.8: Monthly mean modelled Br$_y$ speciation (pptv) in run **BR** at CVAO [16.85°N, 24.87°W].

In addition to ground-based observations, satellites also provide an important observation platform for understanding the spatial extent of BrO in the troposphere (Fitzenberger *et al.*, 2000; Wagner *et al.*, 2001; Van Roozendael *et al.*, 2002). A limitation of satellite observations is they can only provide a direct measurement of the total column amount of BrO in the atmosphere; to determine the amount of BrO in the troposphere, the stratospheric component of BrO must be removed. This is usually done using a model simulation of the stratosphere (e.g. Chipperfield (2006) and Theys *et al.* (2009)).

Figure 4.9 shows a comparison of the simulated tropospheric column BrO compared and observations from the GOME instrument during March. The troposphere column amount of BrO is calculated by integrating the molecular density of BrO (cm^{-3}) in each model layer in the troposphere. Model layers with a potential vorticity (PV) $<$ 2 PVU[1]and potential temperature $\leq$ 380 K are assumed to be in the troposphere. Troposphere column BrO amounts are compared with measurements from the Global Ozone Monitoring Experiment (GOME) (Burrows *et al.*, 1999). GOME is an ultraviolet/visible, nadir viewing spectrometer on board the European Research Satellite (ERS-2). GOME measures in the spectral interval 240 - 793 nm with a resolution of 0.2 to 0.4 nm. GOME pixel sizes are 320 ×40 km. BrO absorption is measured in the wavelength interval 344.7 - 359 nm using the DOAS method from measured calibrated radiance's (Van Roozendael *et al.*, 2002). The stratospheric component is removed using a climatological ozone field from the BASCOE 3D chemical transport model (Theys *et al.*, 2009). The remaining tropospheric component is then corrected to account for the effects of surface albedo (Koelemeijer *et al.*, 2003), clouds (Koelemeijer *et al.*, 2001) and the vertical distribution of tropospheric BrO, the latter of which is very uncertain, using an air mass factor. The uncertainties in the GOME retrieval give a total error for the tropospheric BrO vertical column of 1 - 2 $\times 10^{13}$ molecules cm^{-2} (Yang *et al.*, 2010).

In the NH, simulation **BR** predicts large BrO tropospheric column amounts at higher latitudes in agreement with GOME observations. However, simulation **BR** over predicts troposphere column BrO compared to the observations by 0.5 to 1.0 $\times 10^{13}$ molecules cm^{-2} north of 30°N. In the tropics simulation **BR** over predicts the observed BrO approximately 1.0 $\times 10^{13}$ molecules cm^{-2}. Lower troposphere column BrO is predicted in simulation **BR** (0.6×10^{13} molecules cm^{-2}) in the high precipitation regions of the Western Tropical Pacific. In the SH troposphere column BrO is simulated to be around 0.8-2.0 $\times 10^{13}$ molecules cm^{-2}, in agreement with the GOME observations of 1.2-2.0 $\times 10^{13}$ molecules cm^{-2}. In summary the simulated BrO field is higher than the GOME observations, especially in the NH and the tropics. An explanantion for this is the low sensitivity of the GOME instrument in the boundary layer over low albedo surfaces (e.g. Ocean). Hence, the GOME instrument may underestimate the BrO over the oceans.

---

[1] $1PVU=1\times 10^{6}\ m^{2}\ s^{-1}\ K\ kg^{-1}$

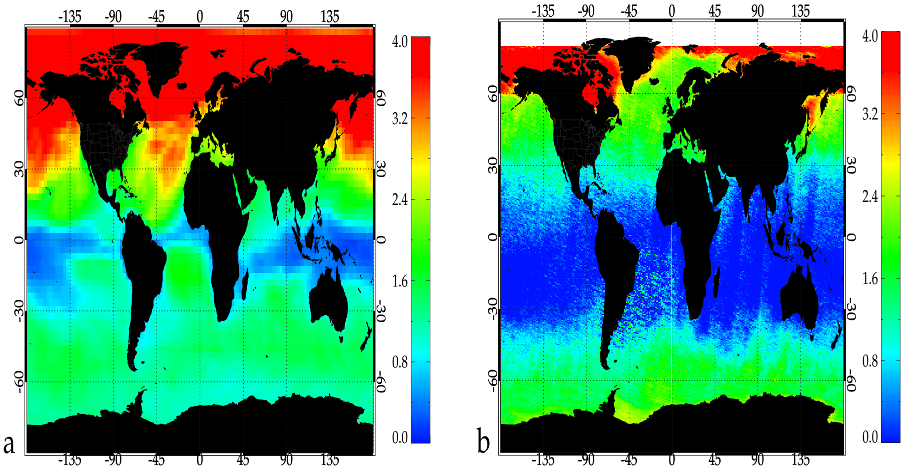
a
b
-135
-90
-45
0
45
90
135
60
30
0
-30
-60
4.0
3.2
2.4
1.6
0.8
0.0

Figure 4.9: Modelled and observed troposphere column BrO (x10^{13} molecules cm^{-2}) at 10:30am local time in (a) simulation **BR** March 2004 and (b) GOME satellite March 2000.

Figure 4.10 shows the modelled surface BrO in March at 10:30am local time in simulation **BR**. Highest BrO mixing ratios are simulated in the North Atlantic Ocean (>1 pptv). Elevated BrO is predicted throughout the open ocean of the NH compared to coastal regions, explained by the higher sea salt flux in the open ocean. In the SH oceans simulated BrO is less than 0.4 pptv in March. The lower BrO mixing ratios in the SH are explained by the lower availability of acidifying trace gases in the region.

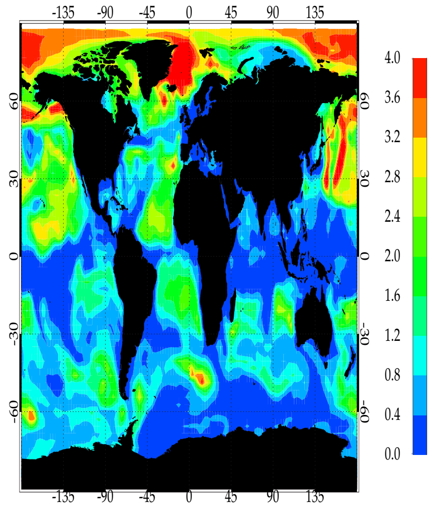
-135
-90
-45
0
45
90
135
60
30
0
-30
-60
4.0
3.6
3.2
2.8
2.4
2.0
1.6
1.2
0.8
0.4
0.0

Figure 4.10: Modelled surface BrO mixing ratio (pptv) in run **BR** at 10:30am local time in March 2004.

4.4 Changes to Background Tropospheric Chemistry due to Inclusion of Bromine

The introduction of the bromine chemistry scheme into the model can potentially perturb the concentrations of ozone, HO_x and NO_x species (Chameides & Davis, 1980; Von Glasow *et al.*, 2004b; Yang *et al.*, 2005). Figure 4.11 shows the zonally averaged change in ozone in run **BR** compared to run **NOBR**. The simulations show a 12-18% decrease in O_3 in run **BR** throughout the troposphere during June with the exception of the tropics and the low to mid-latitude NH where the decrease is smaller (<12%). During December a decrease in O_3 of 12-24% is simulated throughout the mid-latitudes of both hemispheres with a larger decrease of 24-30% south of 40°S. A larger decrease in O_3 is simulated during December because Br_y is higher at this time in both hemispheres (Figure 4.1). Yang *et al.* (2005) also showed large ozone loss in December (15%) in the SH mid-high latitudes, but simulated smaller ozone loss in the NH mid-high latitudes in December.

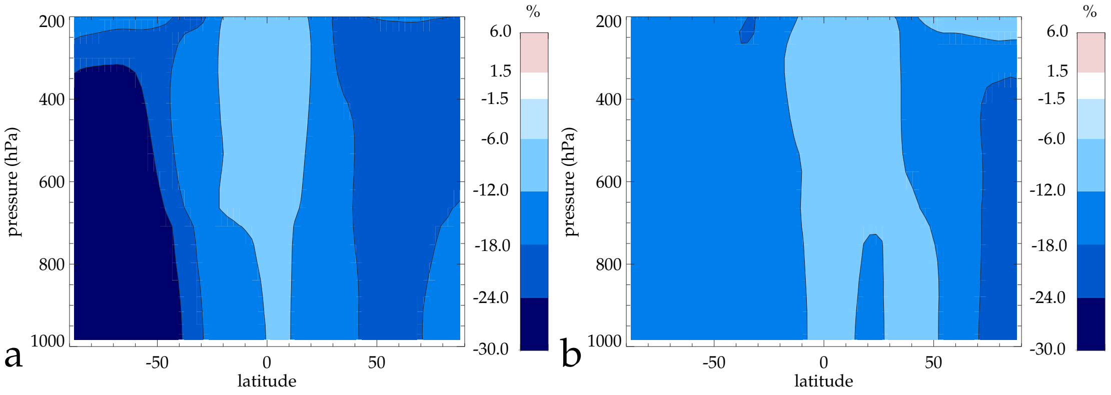

Figure 4.11: Simulated % change in zonally averaged O_3 during (a) December and (b) June between runs **BR** and **NOBR**.

Table 4.1 shows the change in the global tropospheric ozone budgets between simulations **NOBR** and **BR**. The inclusion of bromine chemistry decreases global tropospheric ozone by 26 Tg O_3 (7.8%) from 331 to 305 Tg O_3. Simulation **BR** shows the most important bromine sink for ozone is BrO + HO_2 (130 Tg O_3 yr^{-1}). $BrONO_2$ hydrolysis is the second most important sink (18.5 Tg O_3 yr^{-1}). Other loss pathways contribute 23.5 Tg O_3 yr^{-1}. The total ozone sink due to bromine reactions in simulation **BR** is 172.5 Tg O_3 yr^{-1}, considerably larger than O_3 loss from OH + NO_2 (104 Tg O_3 yr^{-1}) and OH + hyrdocarbons (84 Tg O_3 yr^{-1}). It is important to note the simulations show the inclusion of bromine chemistry also acts to reduce ozone chemical sources. The total chemical ozone source in simulation **BR** is reduced by 136 Tg O_3 yr^{-1} (3.1%) compared to simulation

NOBR. This is due to removal of NO_x from the hydrolysis of $BrONO_2$ on aerosol providing an increased NO_x sink.

Table 4.1: Ozone burdens and Budgets in the **BR**, **NOBR** simulations and previous published studies.

	NOBR	**BR**	Change (%)	**S04**	**S06**
Ozone Burden (Tg O_3)	331	305	-26 (-7.8%)	273	340 ±40
Ozone Chemical Sources (Tg O_3 yr^{-1})					
NO + HO_2	3129	3022	-107 (-3.4%)	3393	
NO + CH_3O_2	798	767	-31 (-3.8%)	876	
NO + Other	407	409	2 (+0.5%)	706	
Total Chemical Sources	4334	4198	-136 (-3.1%)	4975	5060±570
Ozone Stratosphere flux (Tg O_3 yr^{-1})	est. 644	NA		395	520±200
Ozone Sinks (Tg O_3 yr^{-1})					
$O^1D + H_2O$	1583	1488	-95 (-6.0%)	2355	
$O_3 + HO_2$	1079	989	-90 (-8.3%)	1224	
Other	758	697	-61 (-8.0%)	841	
BrO + HO_2		130			
$BrONO_2$ + Aerosol		18			
BrO + Other		24			
Total Bromine sinks		172			
Total Chemical Sinks	3420	3344	-76 (-2.2%)	4421	4560±720
Dry Deposition	1554	1471	-73 (-4.5%)	949	1010±220
Ozone Lifetime (days)	24.2	22.9	-1.3(-5.3%)	18.6	22.3±2.0

S04=Stevenson *et al.* (2004), **S06**=Stevenson *et al.* (2006)

Table 4.1 shows the chemical sources of ozone decrease by more than the total sinks in simulation **BR** compared to simulation **NOBR**, however, the ozone burden decreases. The simulated source/sink change in the budgets should result in an increase in the ozone burden. The reason for this discrepancy in the model results is the stratosphere-to-troposphere ozone flux, which represents an important source of ozone to the troposphere (≈520±200 Tg O_3 yr^{-1}, Stevenson *et al.*, 2006). Constraining the flux of ozone from the stratosphere to the troposphere in simulations **NOBR** and **BR** is difficult without considerable development of model code. In simulation **BR** the stratospheric ozone flux to the troposphere can be estimated as the imbalance between the total sources and sinks (644 Tg O_3 yr^{-1}). As the flux of ozone from the stratosphere to the troposphere depends on the concentration gradient of ozone across the tropopause, it can be assumed the transport of ozone into the troposphere increases in simulation **BR** due to lower levels of ozone in the troposphere. A stratosphere flux increase of 5% in simulation **BR** would more than offset the source/sink imbalance.

The chemical sources and sinks in simulations **BR** and **NOBR** are on the low side of estimates from Stevenson *et al.* (2006). An explanation for the low chemical sink in TOMCAT is the assumed fixed ozone deposition velocity to the ocean surface of 0.05 $cm^{-2}S^{-1}$. Studies that use an interactive ozone deposition scheme that take into consideration factors such as wind speed, destruction at the seawater interface and SST estimate significantly lower ozone deposition velocities (Ganzeveld *et al.*, 2008). The simulated ozone burden is within the range reported by Stevenson *et al.* (2006). The introduction of bromine chemistry results in a reduction in the lifetime of ozone in the troposphere from 24.2 days in simulation **NOBR** to 22.9 days in simulation **BR**. The troposphere ozone lifetimes are in agreement with the multi-model comparisons reported in Stevenson *et al.* (2006).

Bromine chemistry can also perturb NO_x chemistry. Formation of $BrONO_2$ through reaction of BrO with NO_2 followed by uptake to sea salt aerosol can provide a potentially significant sink for NO_x. Figure 4.12 shows the change in NO_x during December and June between simulations **BR** and **NOBR**. NO_x mixing ratios decrease by 40-60% in the SH storm track region (40-70°S) during December, due to the strong source of Br_2 and high sea salt loading. In the NH mid latitudes in December NO_x mixing ratios decrease in simulation **BR** by 20-80% explained by the large aerosol surface areas. North of 70°N in December, in the absence of sunlight, Br_y partitions to Br_2 and hence does not form $BrONO_2$. The NO_x increases in the high latitude NH in December are explained by lower ozone concentrations (Figure 4.11a) that reduces the cycling of NO_x to N_2O_5 and subsequently decreases NO_x loss via N_2O_5 hydrolysis on aerosol. In June the large changes in NO_x simulated in the NH are not predicted in the SH due to lower Br_y mixing ratios and smaller aerosol surface areas.

A final key impact of bromine chemistry is to influence HO_x (Chameides & Davis, 1980; Bloss *et al.*, 2005; Whalley *et al.*, 2010). Reactions 2.54 and 2.55 act to cycle HO_2 to OH, increasing the OH:HO_2 ratio, or to provide a sink for HO_x if uptake of HOBr onto aerosol is favoured over photolysis. Figure 4.13 shows the percentage change in HO_x and OH:HO_2 ratio in December and June. During December decreases in HO_x of 8-40% are simulated in the NH mid-latitudes, explained by high aerosol surface areas providing a large sink for HOBr. A decrease in HO_x is also simulated in the SH mid-latitudes in December (8-16%) corresponding to the regions of highest Br_y and sea salt loading. In June large decreases in HO_x greater than 8% are limited to the SH

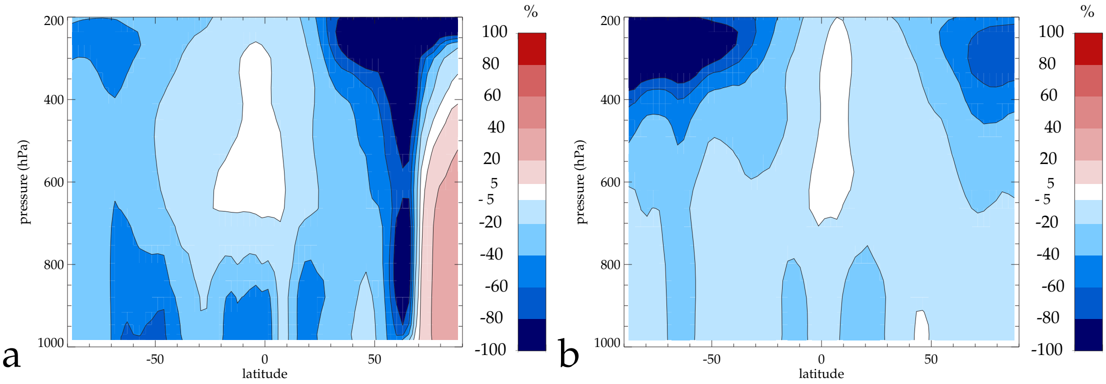

Figure 4.12: Simulated % change in zonally averaged NO_x during (a) December and (b) June between runs **BR** and **NOBR**.

high latitudes. The response in the OH:HO_2 ratio is complicated by whether HOBr is photolysed or recycled on aerosol. The largest increase in the OH to HO_2 ratio is simulated in the NH mid-latitudes in December due to photolysis of HOBr. In the high latitudes of each hemisphere during the winter the OH to HO_2 ratio decreases due to the absence of sunlight. The globally averaged OH concentration decreases by only 0.5% from 0.873 $\times 10^6$ molecules cm^{-3} in run **NOBR** to 0.869 $\times 10^6$ molecules cm^{-3} in run **BR**.

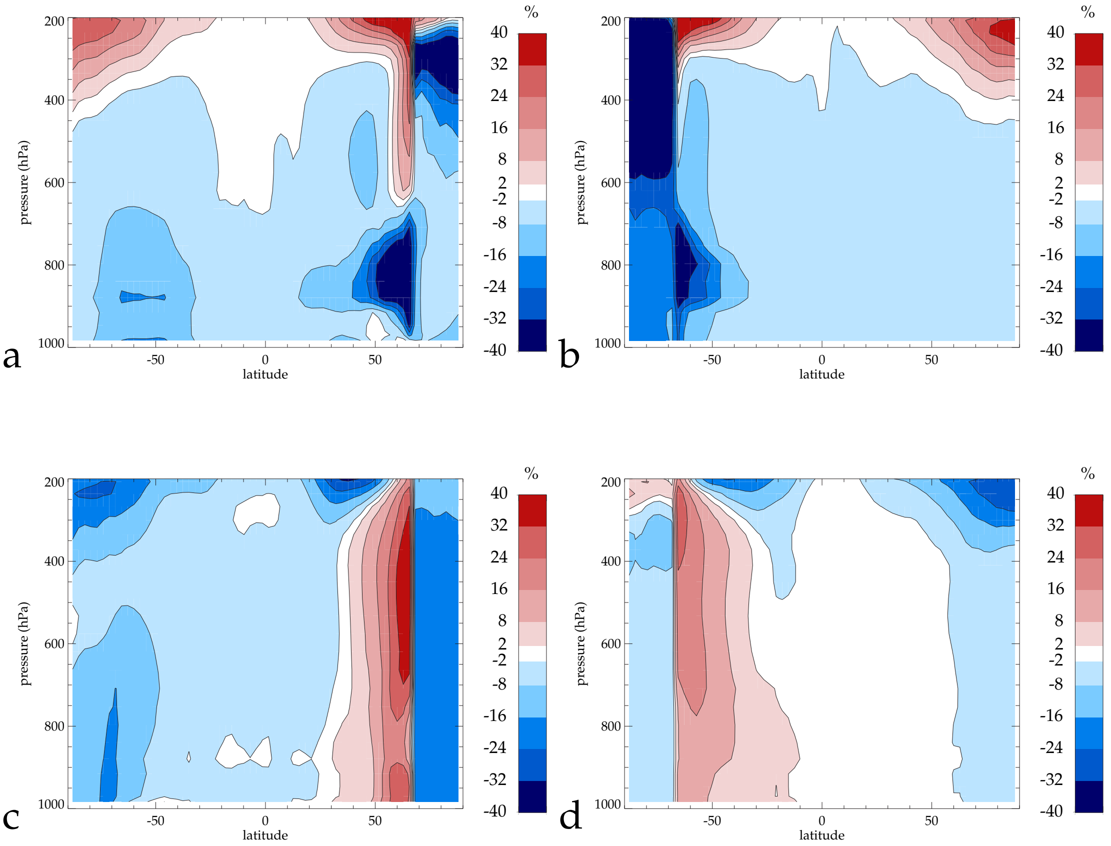

Figure 4.13: Simulated % change in zonally averaged (a) and (b) HO_x and (c) and (d) $OH:HO_2$ ratio in run **BR** compared to run **NOBR** during (a) and (c) December and (b) and (d) June.

4.5 Detailed Comparison with Cape Verde Atmospheric Observatory Dataset

Figure 4.14 shows the monthly averaged observed daytime ozone loss at CVAO from November 2006 to June 2007 (Read *et al.*, 2008) compared to simulations **BR** and **NOBR**. The ozone loss is calculated from the difference between 0900 and 1700 hours. The observations show daytime ozone loss varies between 2 ppbv day^{-1} in November to 5 ppbv day^{-1} in April, with higher values observed in the summer when photochemical loss is more active. Simulation **NOBR**, shows a similar seasonal trend to the observations but fails to capture the magnitude of the ozone loss at CVAO throughout the observation period, predicting an average daytime ozone loss of 0.82 ppbv day $^{-1}$. Near-zero ozone loss is simulated from November to February and underestimated by a factor 2-3 from March to June. The introduction of bromine chemistry in simulation **BR** slightly increases the modelled average daytime ozone loss to 0.96 ppbv day $^{-1}$, improving agreement with observations, but still significantly underestimates the observed average daytime ozone loss of 3.29 ppbv day $^{-1}$.

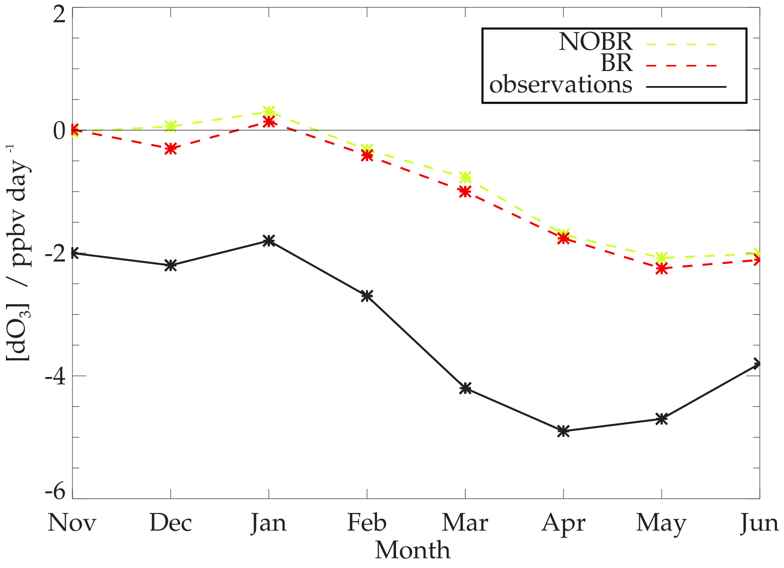

Figure 4.14: Comparison of observed and modelled monthly mean daytime ozone loss between 0900 and 1700 UTC at CVAO [16.85°N, 24.87°W] in simulations **BR** and **NOBR**. Observations from Read *et al.* (2008).

Read *et al.* (2008) presented comparisons of the daytime ozone loss in the region with box model and global model simulations from the Goddard Earth Observing System CTM (GEOS-CHEM) (Bey *et al.*, 2001). The model simulations in Read *et al.* (2008) predicted stronger daytime ozone loss at CVAO than simulation **BR** even without any halogen chemistry from November to May. GEOS-CHEM predicted 1.5 - 3.0 ppbv ozone loss day $^{-1}$. The large underestimate in daytime ozone loss at CVAO in simulations **BR** and **NOBR** suggests a more fundamental problem in TOMCAT with either NO_x or photochemistry in the region.

One possible explanation for the under prediction of daytime ozone loss at CVAO in simulations **BR** and **NOBR** may be the treatment of cloud fields used to determine photolysis rates. TOMCAT assumes cloud coverage fields of 31% low cloud, 15% mid-level cloud and 20% high cloud to calculate the attenuation of radiation in the atmosphere. There is no seasonality or spatial variability in the cloud fields. Clearly the uniform cloud distribution is an important limitation of this study. Seasonal and diurnal variations in clouds will impact the photochemistry and should be better represented in the model. An overestimate in cloud cover would suppress photochemical ozone loss.

A second explanation for an under prediction of ozone loss at CVAO in simulations **BR** and **NOBR** may be too high simulated NO_x in the region. Remote marine regions are typically characterised by daytime ozone destruction (LIU *et al.*, 1987) because of low mixing ratios of NO. When NO is below the "ozone compensation point" (Jacob *et al.*, 1996) the region constitutes a net sink for ozone. This threshold NO mixing ratio is not globally uniform but varies with latitude, season, transport pathways and HO_x sources and sinks. Estimates of this compensation point vary from 8-50pptv (Jacob *et al.*, 1996; Lee *et al.*, 2010).

Figure 4.15 shows the observed and modelled 30-day running average daytime NO mixing ratio at CVAO from November 2006 to October 2007 (Lee *et al.*, 2009b). Simulations **BR** and **NOBR** clearly overestimate the NO mixing ratio throughout the observation period. The lower modelled NO in simulation **BR** compared to **NOBR** can be explained by increased removal of NO_x through the recycling of $BRONO_2$ on aerosol. Critically for Figure 4.14, Lee *et al.* (2009b) estimates the ozone compensation point for the region to be somewhere between 17 and 34 pptv. Clearly the overestimate in NO in simulations **BR** and **NOBR** could explain a significant proportion of the under predicted daytime ozone loss in Figure 4.14. In contrast the GEOS-CHEM model compares well with observations of NO at CVAO (Read *et al.*, 2008).

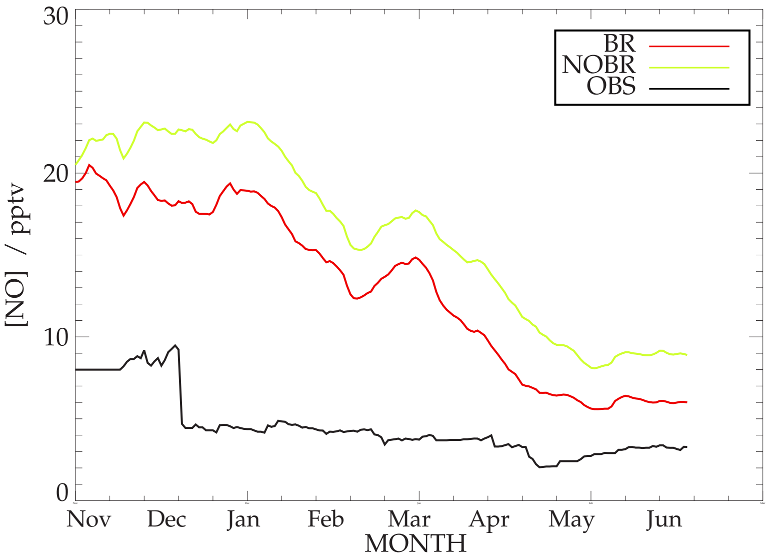

Figure 4.15: Comparison of observed and modelled 30-day running average daytime NO mixing ratio at CVAO [16.85°N, 24.87°W] in simulations **BR** and **NOBR** from November 2006 to June 2007. Observations taken from Lee *et al.* (2009b).

The overestimate in NO at CVAO in simulation **BR** is explained by the relatively coarse model resolution (2.8°×2.8°) and the strong NO_x gradiant between the West Coast of Africa and CVAO

(See Figure 3.26). The code that interpolates and outputs for CVAO, uses model fields from surrounding grid boxes to give an estimated value at a specific location. The use of such interpolation code where strong gradients exist results in the mixing of air containing higher NO from close to the continent and a subsequent over estimation in NO in the more remote regions.

4.6 Coupled Bromine and Sulfur Interactions

Section 4.3 showed that simulated BrO mixing ratios capture 65% of the observed surface BrO at CVAO (**BR** mean = 1.56 pptv, obs mean = 2.42 pptv). Simulated Br_y distributions show good agreement with observations and a previous global model study of tropospheric bromine chemistry. The coupled bromine model is now used to study interactions between bromine and sulfur chemistry in the troposphere. The importance of BrO for DMS oxidation in the remote marine boundary layer will also now be investigated.

4.6.1 DMS Oxidation Budget

In order to understand the importance of bromine chemistry for DMS oxidation a DMS budget has been diagnosed in the model. This provides a detailed insight into spatial and temporal changes in the DMS sinks, lifetime and burden.

As a global annual average (for 2004) the model simulations show BrO contributes approximately 36% of the total DMS sink in run **BR**. This is larger than NO_3 (19%), but less than OH (45%). The BrO contribution to DMS oxidation in this study is larger than the 19% reported in Breider *et al.* (2010) and is due to a large increase in the sea salt Br source (0.46 Tg Br yr^{-1} compared to 0.22 Tg Br yr^{-1} in Breider *et al.* (2010). The larger Br source in this study can be attributed to two factors. Firstly, we use a narrower aerosol size grid in our simulations. This results in a relatively smaller alkalinity flux in each aerosol size bin, therefore larger aerosol size bins are acidified to provided a source of Br_2. Secondly, the higher model resolution used here results in a larger DMS flux (12.6 Tg S yr^{-1} compared to 10.3 Tg S yr^{-1} reported previously) and increased aerosol acidification from DMS-sourced SO_2, which results in greater release of bromine from sea salt.

The global DMS burden decreases by 42% from 0.052 Tg S in run **NOBR** to 0.030 Tg S in run **BR**. Both burden values are lower than the 0.060 Tg S estimated by Berglen et al. [2004]. This difference can be explained mainly by the larger DMS source in the Berglen *et al.* (2004) study.

The BrO + DMS reaction is most active in the MBL due to surface sources of bromine and DMS. Oxidation of DMS at the surface increases by 44% in run **BR**. The global mean DMS lifetime decreases from 1.50 days in run **NOBR** to 0.87 days in run **BR**.

Figure 4.16 shows the annual mean contribution of OH abstraction, OH addition, NO_3 and BrO to the total DMS oxidation in run **BR**. Figure 4.16d shows some distinctive spatial features. In coastal areas, and in the high NO_x outflow areas of the North Atlantic, BrO contributes less than 10% of the annual DMS oxidant sink. This can be explained by NO_3 dominating the DMS oxidation in these regions (Figure 4.16c). This result agrees with observations in the Mediterranean and on the north east coast of the US which showed NO_3 is the most important DMS oxidant (Vrekoussis *et al.*, 2004; Stark *et al.*, 2007).

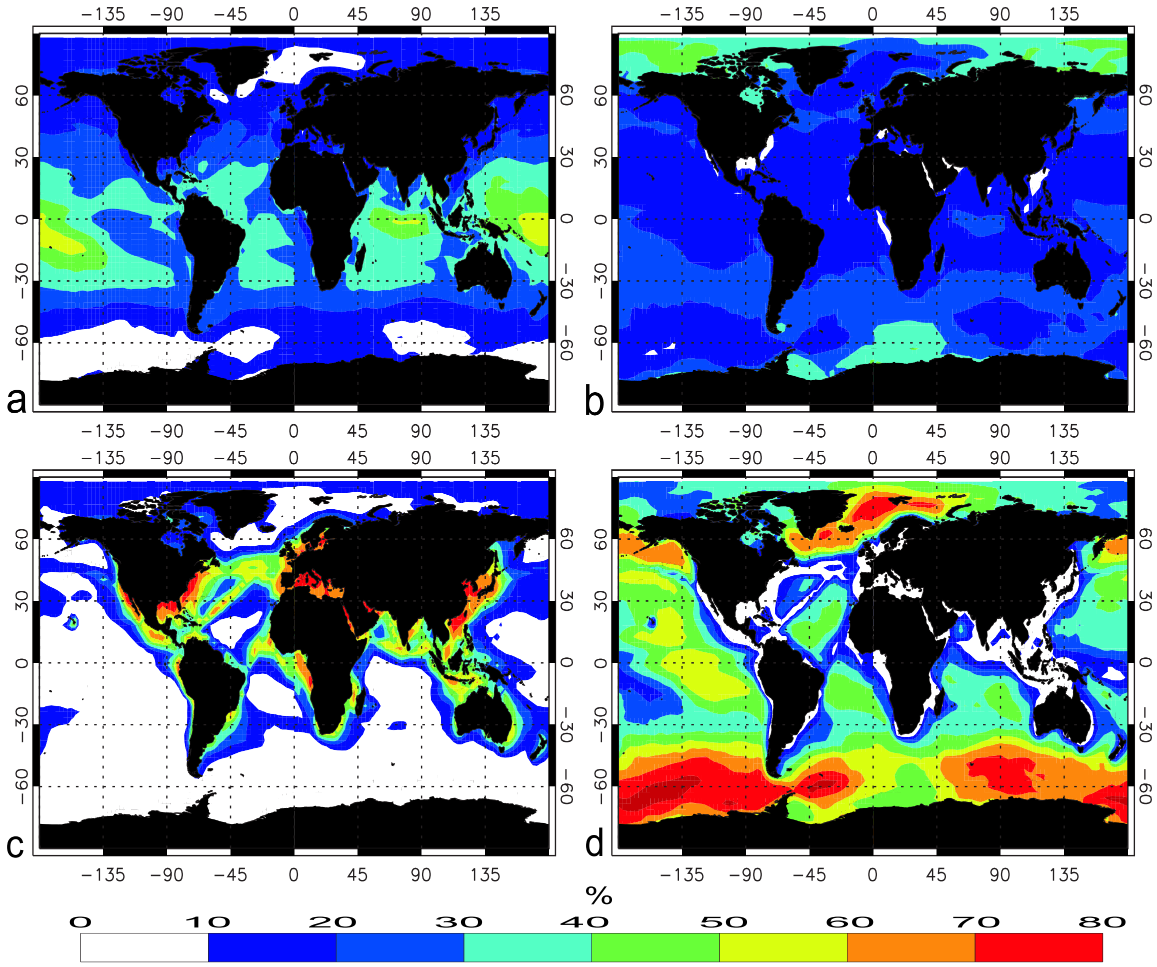

Figure 4.16: Annual mean contribution (%) of (a) OH abstraction, (b) OH addition, (c) NO_3 and (d) BrO to DMS oxidation for 2004.

In the tropics BrO contributes approximately 22% of the annual DMS oxidation sink. In this region the increased abundance of water vapour and ample year-round sunlight supports higher OH concentrations. The high OH and the presence of increased levels of NO_3 in coastal regions from primary NO_x sources out compete BrO for reaction with DMS. In total OH contributes 54% and NO_3, 24% of the annual DMS oxidation sink in this region.

Figure 4.16d shows the largest contribution from BrO is in the SH south of 40°. Throughout the 40° - 70°S latitude band over 50% of the annual DMS sink is due to BrO. In high DMS regions (70°S, 135°W) (Figure 3.2) this can be as large as 70%. The spatial pattern of BrO oxidation of DMS is in agreement with von Glasow et al. [2004b], who also found the largest BrO contribution in regions of high DMS emission. Reasons for this relationship are discussed in Section 4.8.

There are a number of explanations why BrO is more important for DMS oxidation in the SH remote ocean. First, the low NO_x levels do not make NO_3 a competitive sink for DMS south of 40°S (Figure 4.16c). Second, the nighttime bromine reservoir Br_2 is photolysed at longer wavelengths ($\lambda \leq$620nm) than $O_3 \rightarrow O(^1D)$ ($\lambda \leq$320nm). Under low NO_x conditions BrO concentrations are sustained for a longer period during the daytime than OH (Von Glasow *et al.*, 2002). A third factor is that DMS source regions may also be areas of elevated bromine emission from sea salt. As wind speeds are high in the SH remote ocean there is an abundant source of sea salt. The limiting factor is the available acidity. In clean remote marine regions away from anthropogenic and volcanic emissions, the dominant source of SO_2 is DMS (Davis *et al.*, 1999). Hence, the emission of DMS may control the release of bromine from the aerosol. This could represent a mechanism through which DMS regulates its own lifetime by controlling its oxidation sink. This mechanism is further discussed later in this chapter.

4.6.2 Changes to DMS, SO_2 and DMSO

The large contribution of BrO to DMS oxidation in simulation **BR**, and the subsequent change in the DMS lifetime, burden and oxidation pathway, could influence the concentrations of the different DMS oxidation products, SO_2 and DMSO. The modelled DMS, SO_2 and DMSO mixing ratios are now compared with observations from three remote marine observation stations.

Figure 4.17 shows DMS mixing ratios are lower from December to June in simulation **BR** compared to simulation **NOBR** at all three observation sites. At Amsterdam Island there is a decrease in monthly mean DMS mixing ratio of 40pptv from February to June in simulation **BR** compared to **NOBR**. Simulation **NOBR** compares better with the observations (*nrmsd* = 0.27) than **BR** (*nrmsd* = 0.29). The large underestimate in DMS in the models in January at Amsterdam Island can be explained by an underestimate in the DMS source in the region at that time. At Cape Grim (Figure 4.17b) run **BR** shows shows significantly better agreement with the observations (*nrmsd* = 0.24) than run **NOBR**(*nrmsd* = 0.50), however it still cannot explain the overestimate in DMS from February to May (30-50% overestimate). This could suggest DMS seawater concentrations are overestimated in the region during the period as suggested in Spracklen *et al.* (2005a). At Dumont Durville run **BR** improves the agreement with the obserations in February and March but from June to September run **NOBR** compares better. Both model simulations underestimate monthly mean DMS observations from October to December. Boucher *et al.* (2003) showed the aqueous-phase reaction of ozone with DMS can be an important DMS sink at high latitudes in the wintertime. This reaction is not included in simulations **BR** or **NOBR**.

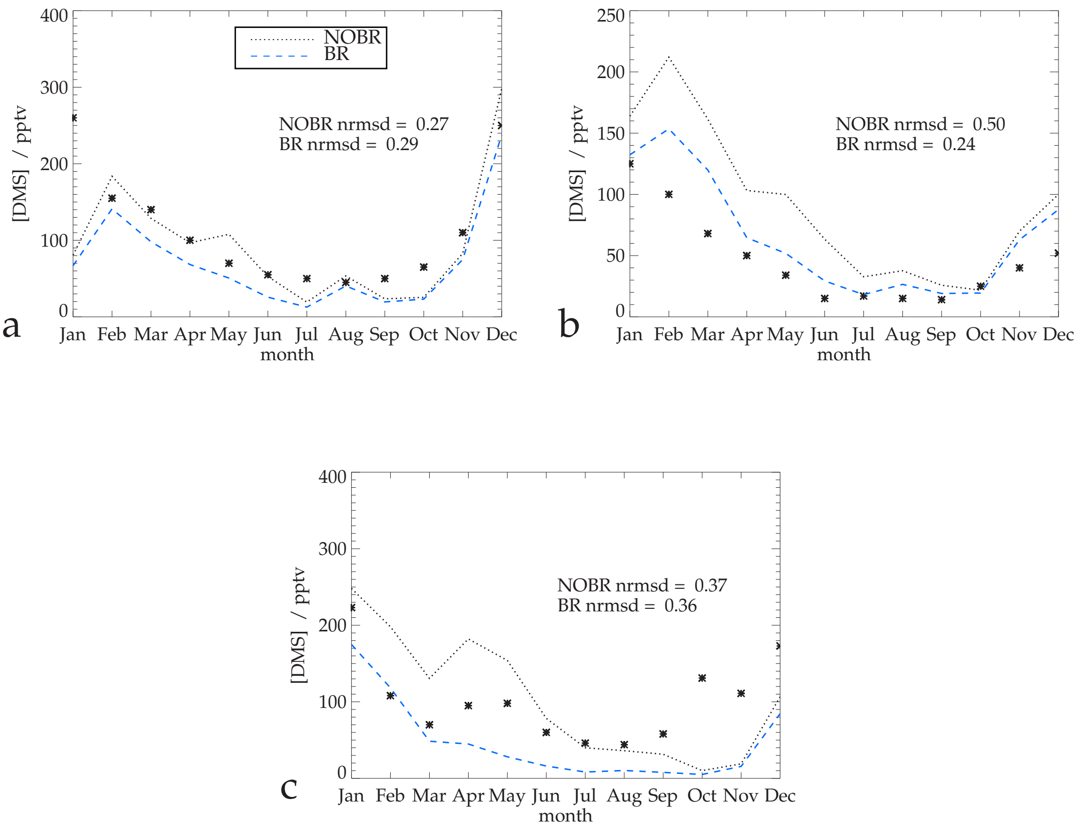

Figure 4.17: Monthly mean observed and modelled DMS mixing ratio (pptv) from runs **BR** and **NOBR** at (a) Amsterdam Island [37.83°S, 77.50°E] (Nguyen *et al.*, 1992), (b) Cape Grim [40.68°S, 144.68°E] (Ayers *et al.*, 1991) and (c) Dumont Durville [66.70°S, 140.00°E] (Jourdain & Legrand, 2001).

Figure 4.18 shows comparisons of observed and simulated monthly mean SO_2 mixing ratios at two remote marine stations. The two model simulations give similar results; SO_2 is lower in the **BR** simulation compared to **NOBR** as oxidation of DMS by BrO favours formation of DMSO. At Amsterdam Island (Figure 4.18a) run **BR** underestimates SO_2 and gives a slightly poorer comparison (*nrmsd*=0.34) than run **NOBR**(*nrmsd*=0.32). Both models overestimate SO_2 at Cape Grim, though the **BR** model shows a small improvement (**BR** *nrmsd*=0.94, **NOBR** *nrmsd*=1.18).

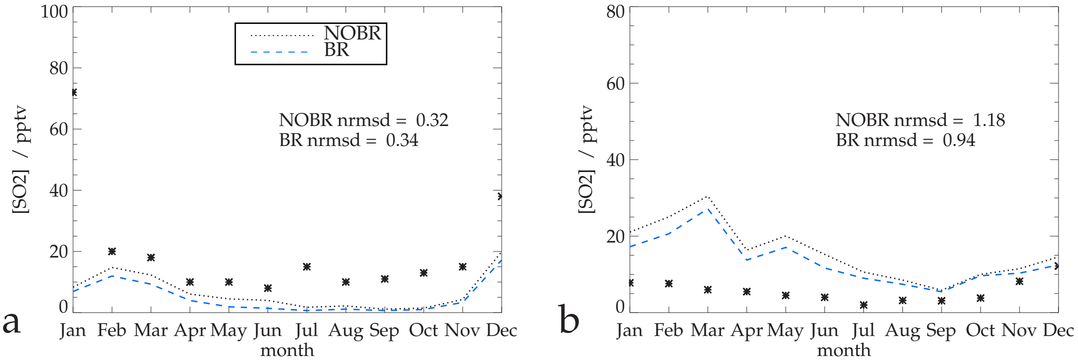

Figure 4.18: Monthly mean observed and modelled SO_2 mixing ratio (pptv) in runs **BR** and **NOBR** at (a) Amsterdam Island [37.83°S, 77.50°E] (Nguyen *et al.*, 1992), and (b) Cape Grim [40.68°S, 144.68°E] (Ayers *et al.*, 1991).

There are a number of possible explanations for the overestimation in SO_2 at Cape Grim. Firstly, observations at Cape Grim are filtered for clean marine origin air only, this is not possible in the model and hence the model may provide an anthropogenically sourced SO_2 signal. Secondly, previous modelling studies have shown aqueous phase oxidation of SO_2 by O_3 on alkaline sea salt aerosols can provide a large sink for SO_2 in the region (Alexander *et al.*, 2005; Korhonen *et al.*, 2008). Korhonen *et al.* (2008) found this process could explain the disagreement between the observed and modelled SO_2 mixing ratios at Cape Grim. However, this process is accounted for in simulations **BR** and **NOBR** but still cannot explain the observations. Globally this study estimates 0.3 Tg S yr^{-1} is oxidised in sea salt aerosol. Alexander *et al.* (2005) found this to be 2.7 Tg S yr^{-1} and Pozzoli *et al.* (2008b) estimated 3.7 Tg S yr^{-1}. Pozzoli *et al.* (2008b) did not account for uptake of HNO_3 which is likely to offset some of the SO_2 uptake. The main explanations for the smaller SO_2 sink in this study are, firstly, the use of a lower accommodation coefficient of SO_2 on sea salt of 0.05 (Song & Carmichael, 2001) at the sea surface compared to Alexander *et al.* (2005) who used a value of 0.11. Secondly, Alexander *et al.* (2005) and Korhonen *et al.* (2008) use the Gong (2003) sea salt source function from 0-10 μm, which is known to overestimate the sea salt source flux at sizes larger than 4 μm (Guelle *et al.*, 2001). Thirdly, neither Alexander *et al.* (2005), Korhonen *et al.* (2008) nor Pozzoli *et al.* (2008b) state if they accounted for the fast removal of the larger sea salt sizes which can be dry/wet deposited on a timescale of less than 1 hour, significantly reducing the capacity of the aerosol to provide a sink for SO_2. A final reason is the lifetime of aerosol in the coarse mode; GLOMAP-Mode estimates a sea salt coarse mode residence time of 0.2 days, compared to approximately 0.8 days in the ECHAM model used by Pozzoli *et al.* (2008b), (Textor *et al.*, 2006).

Figure 4.19 shows comparisons of observed and simulated DMSO mixing ratios at Amsterdam Island and Dumont Durville. DMSO is much higher in the **BR** simulation than **NOBR** at both sites, because the product of the BrO and DMS reaction is DMSO (Barnes *et al.*, 1991). Run **NOBR** compares significantly better with the observations than **BR** (See *nrmsd* values in Figure 4.19). The overestimate in DMSO in run **BR** from February to June at both sites can be explained by the simulations missing heterogeneous uptake of DMSO to sea salt aerosol. During January the underestimate in DMSO at Amsterdam Island in simulation **BR** is likely because of an underestimate in the DMS source see Figure 4.17.

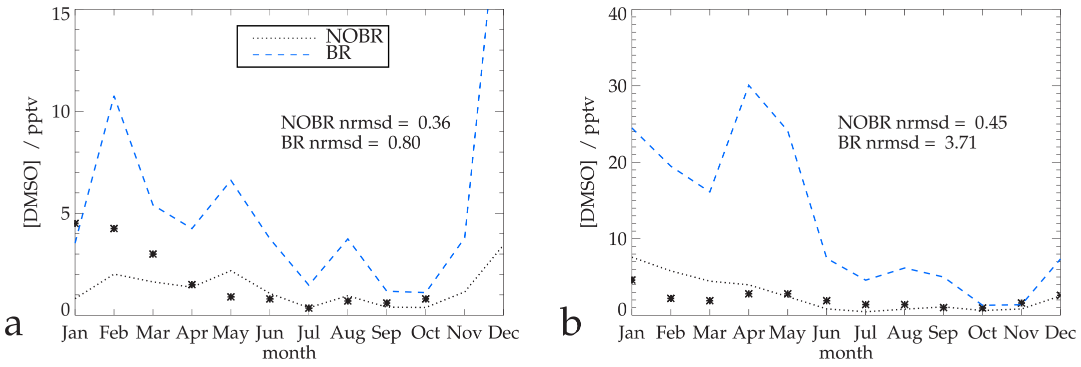

Figure 4.19: Monthly mean observed and modelled DMSO mixing ratio (pptv) in runs **BR** and **NOBR** at (a) Amsterdam Island [37.83°S, 77.50°E] (Sciare *et al.*, 2000b) and (b) Dumont Durville [66.70°S, 140.00°E] (Jourdain & Legrand, 2001).

Previous modelling studies have suggested HOBr and HOCl may provide additional aqueous phase oxidants for SO_2 in-cloud and provide a source of $SO_4{}^{2-}$ (Vogt *et al.*, 1996; Von Glasow & Crutzen, 2004a). Figure 4.20 shows the annual total aqueous phase oxidation in simulation **BR** and the change in simulation **BR** compared to **NOBR**. The regions of highest aqueous phase oxidation are the key industrialised areas in the NH where anthropogenic SO_2 emissions are high. Elevated in-cloud oxidation is also shown in the outflow regions of North America and Asia. Desert regions show very low aqueous oxidation, due to little or no cloud cover. The NH shows much higher levels of aqueous phase oxidation due to the much higher SO_2 industrial emissions.

Compared to the **NOBR** simulation the introduction of bromine chemistry does not significantly change in-cloud sulfate formation over the key industrial regions of the NH which are oxidant limited (Roelofs *et al.*, 1998). There is a small increase over Europe (2-8%) but China and the east coast of America show a small decrease (-2 to -8%). The decrease in these oxidant limited regions can be explained by bromine species cycling HO_2 to OH or removing HO_2 via reactions 2.54 and 2.55 and reducing the availability of H_2O_2. Over the tropical Indian Ocean, tropical western Pacific Ocean and western tropical North Atlantic Ocean, in-cloud sulfate formation increases by 2-16%. This can be explained by a decrease in in-situ in-cloud sulfate formation over industrial and volcanic SO_2 source areas and the availability of HOBr. Over the high latitude NH, in-cloud sulfate formation decreases by 8-24%. This is because bromine species provide a large sink for ozone, the dominant aqueous phase oxidant in this region. The decrease in in-cloud sulfate formation over the SH oceans (>-16%) is explained by the large reduction in the formation of SO_2 from DMS oxidation (see Table 4.2). Over some continental regions, in-cloud sulfate formation show large increases in simulation **BR** (e.g. Saharan Africa, North West U.S. and Alaska). The large percentage changes are most apparent over deserts or regions with low in-cloud sulfate formation (¡20 μgS m^{-2} day^{-1}), hence these large percentage increases are not significant. Globally, in-cloud sulfate formation decreases by 1.0 Tg S (3%) in simulation **BR** compared to **NOBR**.

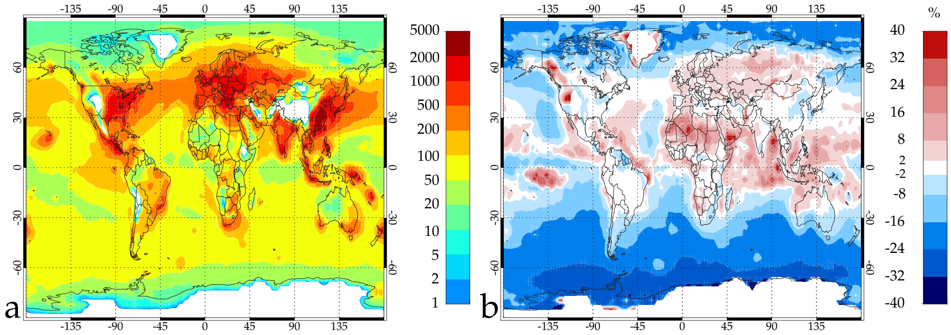

Figure 4.20: (a) Annual total in-cloud sulfate formation by H_2O_2, O_3 and HOBr in simulation **BR** (μgS m^{-2} day^{-1}). (b) Percentage changes in annual total in-cloud sulfate formation between simulations **BR** and **NOBR**.

Figure 4.21 shows the tropospheric column averaged percentage contribution of the different oxidant pathways to in-cloud oxidation of SO_2. In simulation **BR** the aqueous phase HOBr + SO_2 reaction contributes 6.5 Tg S yr^{-1}. This represents 20% of the total in-cloud oxidation with H_2O_2 contributing 67% and O_3 13%. The HOBr + SO_2 pathway is most important over the tropical and northern Pacific remote Oceans. In the North Atlantic Ocean and western North Pacific Ocean high NO_x outflow from the main industrialised regions of East Asia and the US results in a lower fractional contribution of HOBr. This is explained because the high NO_x concentrations results in larger partitioning of Br_y to $BRONO_2$ at the expense of HOBr. HOBr has a lower solubility than H_2O_2 and provides an important contribution to aqueous SO_2 oxidation in high precipitation regions of the tropics, where H_2O_2 is rained out. Simulation **BR** suggests HOBr is not an important aqueous phase oxidant over land, where H_2O_2 dominates. At high latitudes O_3 is the main aqueous phase oxidant for SO_2 in the NH and H_2O_2 is the primary oxidant in the SH. The large decrease in simulation **BR** shows HOBr does not make a significant contribution to SO_2 oxidation over the key SO_2 source regions ($<$10%) where sulfate formation is oxidant limited.

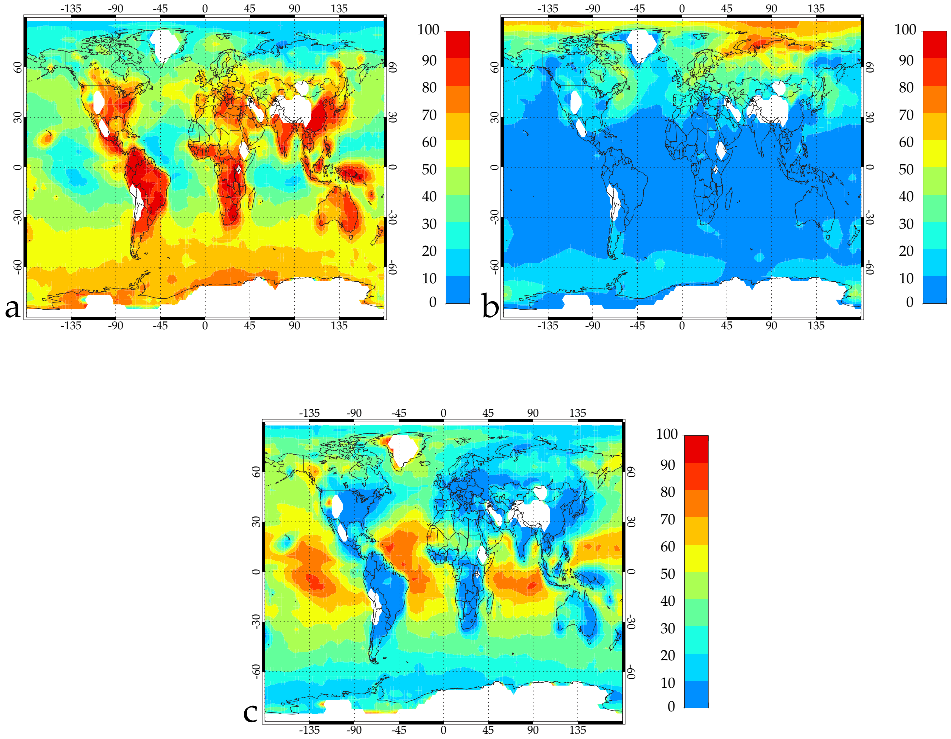
a
b
c
-135 -90 -45 0 45 90 135
60 30 0 -30 -60
100 90 80 70 60 50 40 30 20 10 0

Figure 4.21: Annual mean percentage contribution of (a) H_2O_2, (b) O_3 and (c) HOBr in simulation **BR**.

Table 4.2 summarises the key sources, sinks and budgets of DMS, SO_2 and OH. The net formation of SO_2 from DMS oxidation is reduced by 14% in simulation **BR** compared to **NOBR** due to the increased importance of the addition oxidation pathway.

Table 4.2: Global bromine, OH, methane, DMS and SO_2 budgets for 2004 in the **BR**, **NOBR** simulations.

	BR	**NOBR**	Change
Bromine			
Organic Br emissions (Tg Br yr^{-1})	0.885	-	-
Br sea salt emissions (Tg Br yr^{-1})	0.46	-	-
OH and Methane			
Global mean OH ($\times 10^6$ mol cm^{-3})	0.869	0.873	
CH_4 weighted global mean OH ($\times 10^6$ mol cm^{-3})	1.092	1.010	
CH_4 lifetime (Years)	9.093	9.073	
DMS (Tg S yr^{-1})			
DMS emissions	12.6	12.6	
DMS + OH	45%	73%	-
DMS + NO_3	19%	27%	-
DMS + BrO	36%	-	-
DMS $\rightarrow$ SO_2 (direct)	7.2	11.5	-37%
DMS $\rightarrow$ DMSO	5.3	1.0	410%
DMS $\rightarrow$ SO_2 (via DMSO)	2.8	0.58	386%
Net DMS $\rightarrow$ SO_2	10.0	12.1	-17%
DMS burden (Tg S)	0.030	0.052	-42%
DMS lifetime (days)	0.89	1.53	-42%
SO_2			
Sources (Tg S yr^{-1})			
DMS oxidation	10.0	12.1	-17%
Anthrop. emissions	54.2	54.2	
Natural emissions	13.0	13.0	
Sinks (Tg S yr^{-1})			
Dry deposition	26.4	26.8	-1.7%
Wet deposition	8.0	8.4	-4.1%
Gas phase oxidation by OH	10.8	11.0	-2.2%
SO_2 aq. ox. by H_2O_2	21.8	28.8	-24.2%
SO_2 aq. ox. by O_3	4.3	4.8	-8.7%
SO_2 aq. ox. by HOBr	6.5	-	
Total aqueous phase ox.	32.6	33.6	-3.0%
SO_2 burden (Tg S)	0.32	0.33	-3.4%
SO_2 lifetime (days)	1.45	1.50	-3.4%

4.7 Changes to Marine Aerosol Formation

Section 4.6.2 shows emissions of bromine species in remote marine regions can significantly perturb the oxidation of DMS and SO_2. Many previous studies have speculated about the potential for BrO in the marine boundary layer to impact on marine aerosol formation and reduce the number of CCN by shifting DMS oxidation along the addition pathway (Boucher *et al.*, 2003; Von Glasow *et al.*, 2004b; Von Glasow & Crutzen, 2004a). This study is the first to address this mechanism using a global size-resolved aerosol microphysics model.

Figure 4.22 shows a comparison of observed and simulated ${SO_4}^{2-}$ mass concentrations at five remote SH stations. The two simulations are similar at all sites. Simulation **BR** shows a decrease in ${SO_4}^{2-}$ at all sites. However, at all stations run **NOBR** gives a better comparison with the observations than **BR** (see *nrmsd* values in Figure 4.22). At Dumont Durville, Mawson and Neumayer both simulations fail to capture the amplitude of the seasonality in ${SO_4}^{2-}$. This may be explained by an underestimate in the summertime DMS flux in the model around coastal Antarctica.

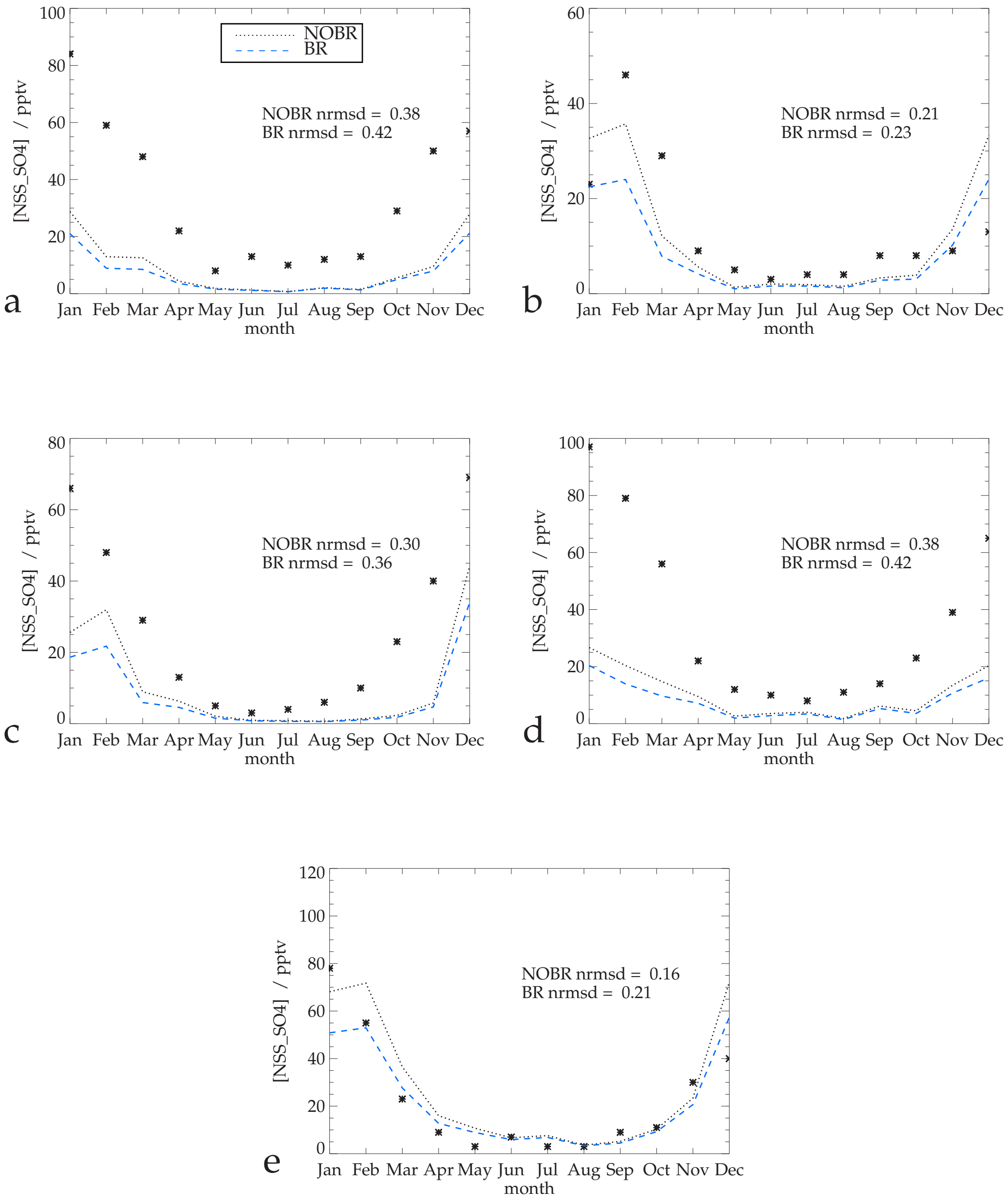

Figure 4.22: Simulated monthly mean non-sea-salt SO_4^{2-} mixing ratio (pptv) in the **BR** and **NOBR** models at (a) Durmont Durville [66.70°S, 140.00°E], (b) Halley Bay [73.35°S, 26.19°E],(c) Mawson [67.36°S, 62.30°E], (d) Neumayer [70.39°S, 8.15°E], and (e) Palmer [64.46°S, 64.03°E]. Observations are from Minikin *et al.* (1998) and SAVOIE *et al.* (1993).

Figure 4.23 shows the zonally averaged changes in CN and CCN during DJF and JJA in the **BR** simulation compared to the **NOBR** simulation. Here, CCN are defined as particles with a radius greater then 35nm, corresponding to a typical activation radius at 0.25% supersaturation. CN number concentrations decrease by 8-16% in the SH high latitude hemisphere in DJF in run

BR due to less nucleation of H_2SO_4 attributable to a lower source of SO_2 from DMS. CN concentrations are less sensitive to bromine chemistry in the NH than the SH because DMS does not represent an important source of the aerosol formation in the NH, which is dominated by anthropogenic sources of SO_2 and primary sulfate.

CCN number concentrations (Figure 4.23 c and d) decrease by 4-20% in the SH mid-high latitudes during DJF in run **BR** compared to run **NOBR**. This clearly shows emissions of bromine from sea salt and organic bromine compounds can have a large impact on CCN formation in the remote SH. A smaller decrease in CCN is simulated in the SH winter because DMS emissions are small and do not significantly impact on CCN formation during this period. In the NH during DJF CCN number concentrations increase by up to 20% at high latitudes ($>70°$N) in simulation **BR** compared to run **NOBR**. The increase in CCN is explained by a decrease in oxidant availability in the winter in run **BR**. Bromine chemistry decreases ozone (Figure 4.11) and HO_2 concentrations (Figure 4.13) at high latitudes which results in lower H_2O_2. The HOBr oxidation pathway is unable to compensate for less availability of H_2O_2 and O_3, hence, there is reduced growth of accumulation mode particles through in-cloud sulfate formation. As a result a higher fraction of the CCN have a size smaller than the cut-off diameter for removal by precipitation, hence the number of CCN increases.

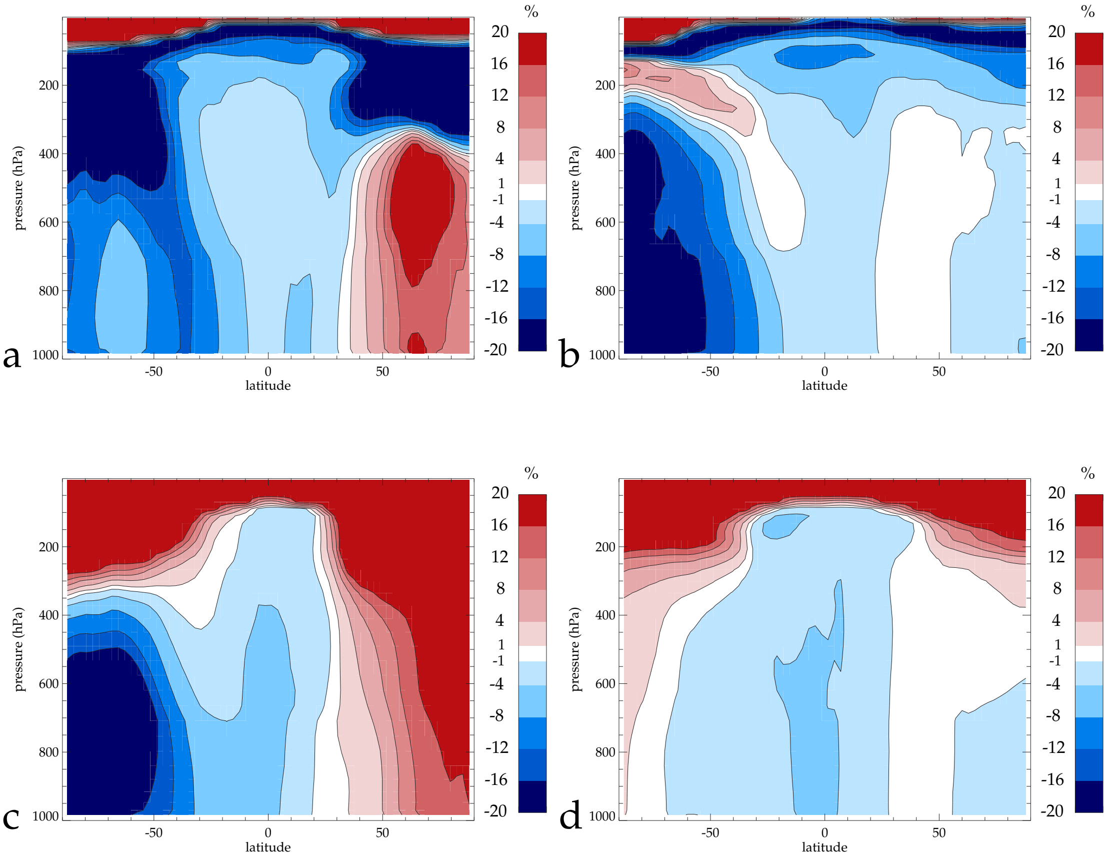

Figure 4.23: Zonally averaged % change in (a) and (b) CN and (c) and (d) CCN (r>35nm) in simulations **BR** and **NOBR** during (a) and (c) DJF and (b) and (d) JJA.

As shown in Figure 4.23 the largest change in CCN in simulation **BR** is over the SH mid-high latitudes. To better understand the spatial and temporal change CCN Figure 4.24 shows the seasonal cycle in CCN as an average across four latitude bands from 30°S to 70°S in simulations **BR**, **NOBR** and **NODMS**. CCN are calculated as particles that activate at 0.23% supersaturation, 1 km above surface, corresponding to a typical height of stratocumulus clouds. Firstly, Figure 4.24 shows in all latitude bands the seasonality in CCN is largely driven by emissions of DMS in agreement with Ayers & Gras (1991) and Korhonen *et al.* (2008). Secondly the CCN number concentrations are clearly lower in simulation **BR** than **NOBR** in all latitude bands from December to March. Typically bromine chemistry reduces the total number of CCN by 10-25% in December, with the largest effect in the 60-70°S latitude band. However, when the impact on only CCN formed from emissions of DMS is calculated the reduction in CCN is 23-43%. Again, the largest change is calculated in the 60-70°S latitude band. Table 4.3 summarises the changes in CCN in each latitude band during December.

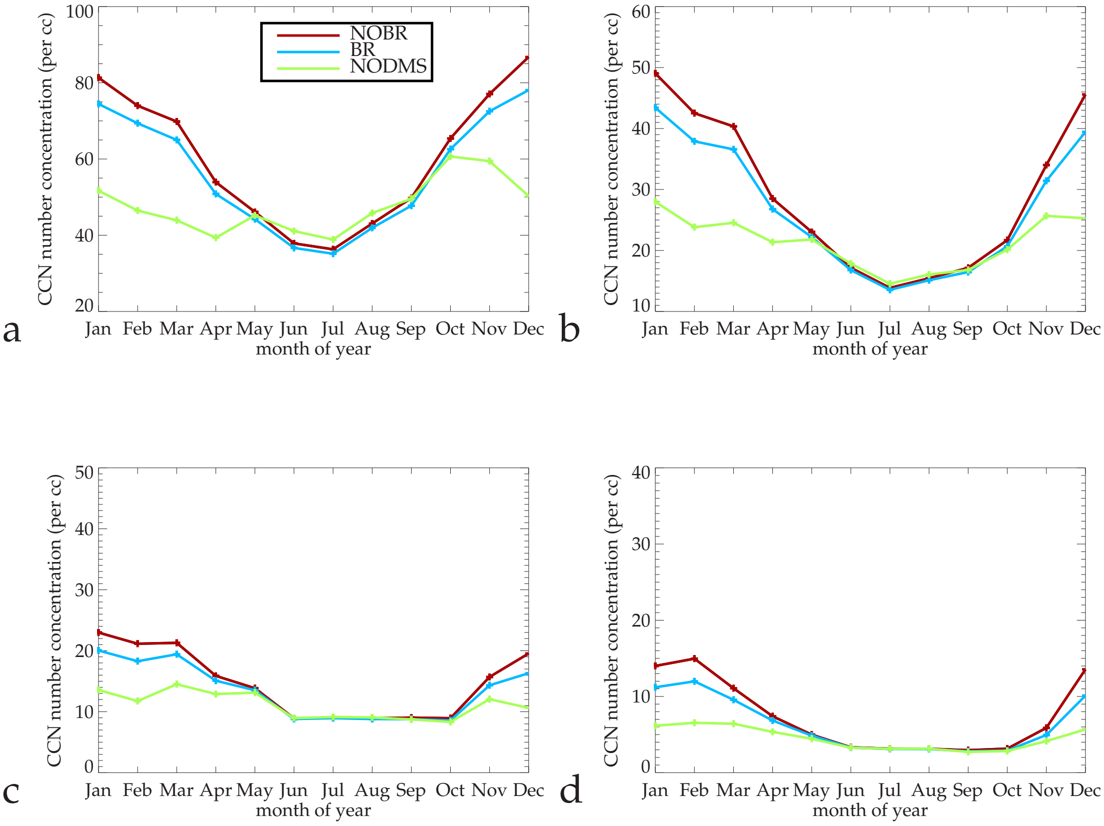

Figure 4.24: Seasonal cycle in CCN number concentrations (cm^{-3}) at 1km altitude at 0.23% supersaturation in runs **BR**, **NOBR** and **NODMS** for latitude bands (a) 30-40°S, (b) 40-50°S, (c) 50-60°S and (d) 60-70°S.

To understand the changes in CCN in simulation **BR** Figure 4.25 shows the budgets for the key processes that control the formation of CCN from emissions of DMS as a function of altitude in simulations **BR** and **NOBR**. A decrease in the DMS burden is shown in simulation **BR** (Figure 4.25a), because of the increased oxidation sink from BrO. Also the amount of DMS being oxidised to SO_2 both directly and via DMSO in simulation **BR** decreases (Figure 4.25d). This results in a lower SO_2 burden (Figure 4.25b) in the boundary layer and in the free troposphere (FT) above 800 hPa. In simulation **NOBR** the longer lifetime of DMS results in an elevated source of SO_2 in the free troposphere. The lower SO_2 burden in the FT in simulation **BR** results in less gas-phase oxidation of SO_2 to H_2SO_4 (Figure 4.25e) and a small decrease in new particle formation in the upper FT (Figure 4.25i). The decrease in nucleation is also evident in the number of nucleation mode particles in simulation **BR** (Figure 4.25k). The result of these processes is, as suggested by

Table 4.3: Changes in zonal mean latitude band CCN number concentrations (cm^{-3}) for December 2004 in the **BR** and **NOBR** simulations

	NOBR	**BR**	Change
CCN 30°-40°S	86.8	78.1	-10.0%
CCN 40°-50°S	45.6	39.5	-13.4%
CCN 50°-60°S	19.5	16.3	-16.4%
CCN 60°-70°S	13.6	10.1	-25.7%
DMS CCN 30°-40°S	36.4	27.8	-23.2%
DMS CCN 40°-50°S	20.3	14.1	-30.1%
DMS CCN 50°-60°S	8.9	5.7	-36.2%
DMS CCN 60°-70°S	7.9	4.4	-43.7%

previous studies, a reduction in Aitken and accumulation mode particles and hence fewer CCN (Figures 4.25k and l).

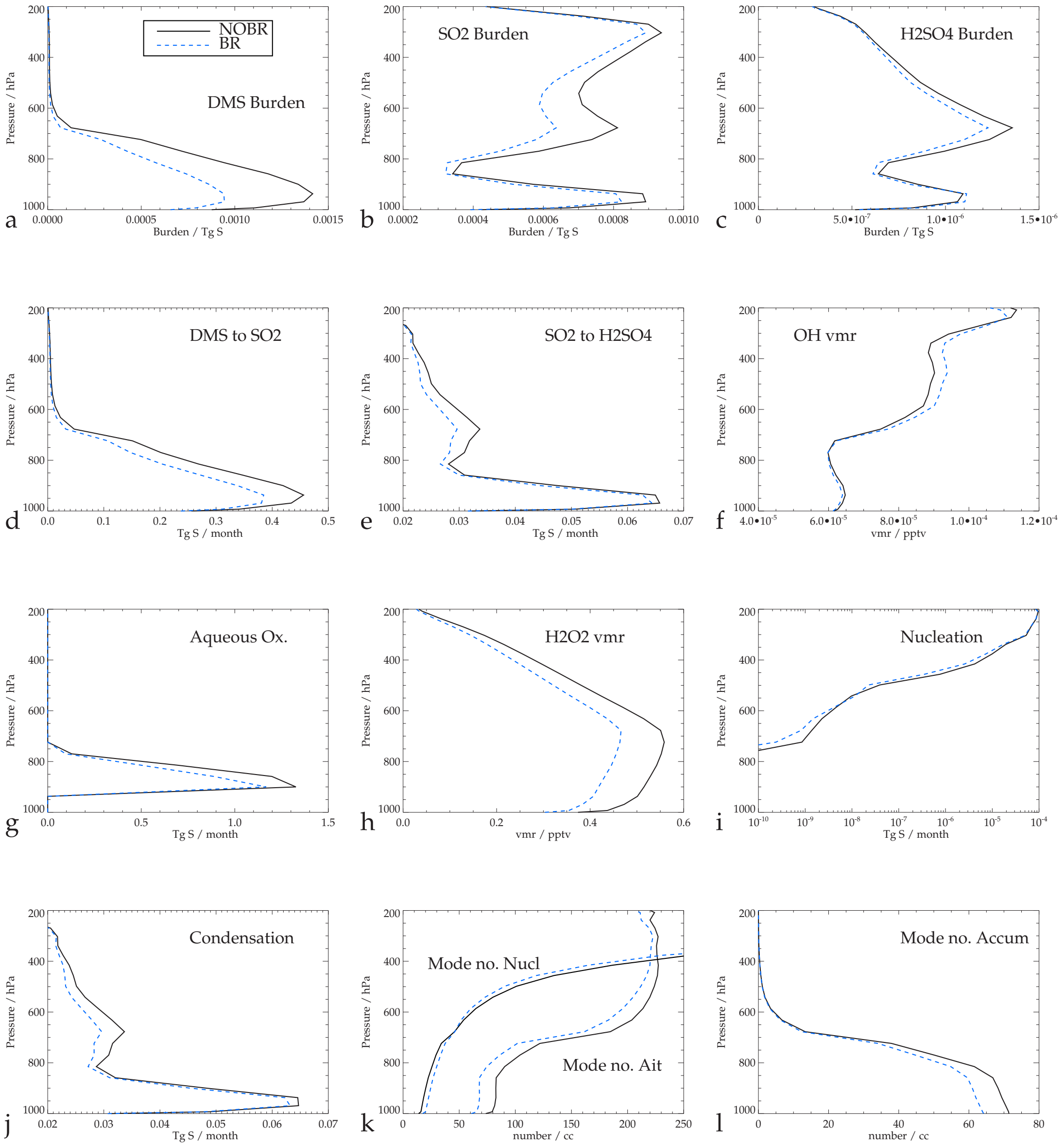

Figure 4.25: Change in the processes controlling CCN formation from DMS emissions during December 2004 in simulation **BR** compared to the **NOBR** simulation in the 30-50°S latitude band. Processes shown are (a) DMS burden, (b) SO_2 burden, (c) H_2SO_4 burden, (d) Mass of DMS oxidised to SO_2 (e) Mass of SO_2 oxidised to H_2SO_4 (f) OH mixing ratio (pptv), (g) Mass in-cloud $SO_4{}^{2-}$ formation, (h) H_2O_2 mixing ration (pptv), (i) Mass of nucleation of H_2SO_4 (j) Mass of condensation of H_2SO_4, (k) Nucleation and Aitken mode number concentrations (cm^{-3} and (l) Accumulation mode number concentration (cm^{-3}).

Table 4.4 shows the sulfate budgets for 2004 in simulations **BR** and **NOBR**. The inclusion of bromine chemistry results in a small decrease in the $SO_4{}^{2-}$ source, mainly attributable to changes in DMS oxidation pathways.

Table 4.4: Global $SO_4{}^{2-}$ budgets for 2004 in the **BR** and **NOBR** simulations.

	BR	**NOBR**	Change
Sources (Tg S yr^{-1})			
Primary emissions	1.12	1.12	
Condensation	10.8	11.0	-2.2%
Aqueous phase oxidation	32.6	33.6	-3.0%
Nucleation	0.01	0.01	-3.0%
Sinks (Tg S yr^{-1})			
Dry deposition	5.22	5.37	-2.8%
Wet deposition	39.86	40.85	-2.4%
$SO_4{}^{2-}$ burden (Tg S)	0.59	0.59	-0.2%
$SO_4{}^{2-}$ lifetime (days)	4.75	4.77	-2.3%

4.8 Possible Marine Aerosol Feedback Mechanism Between DMS-Sea Salt and BrO

Measurements of the sea salt bromide depletion factor (DF) in the SH show a distinctive seasonal cycle (Ayers *et al.*, 1999; Sander *et al.*, 2003) with a maxima in the summer. Given the limited anthropogenic sources of acidifying trace gases in the remote SH oceans, it is likely that biologically produced trace gases may be responsible for the seasonal cycle in sea salt bromide DFs in the region. Observations have shown DMS is the dominant source of SO_2 in the remote marine atmosphere (Davis *et al.*, 1999). It is therefore reasonable that the SO_2 produced by oxidation of DMS could provide an important source of aerosol acidity in remote marine regions and could enhance the release of bromine from sea salt aerosol.

To assess the importance of this mechanism the sea salt bromine source between run **BR** and run **BRNI**, (which has a 45% higher DMS source) is compared in Figure 4.26. The model predicts no sensitivity in the Br_2 source from sea salt aerosols in the NH. This is explained by the DMS source of SO_2 representing only a small fraction of the available gas-phase acidity in the NH, where anthropogenic sources dominate. In the SH summer the sea salt bromine source is enhanced by 11-17% in the **BRNI** simulation. Only a small increase is observed during the rest of the year.

Globally the sea salt Br source increases from 0.46 Tg Br yr^{-1} in run **BR** to 0.48 Tg Br yr^{-1} in run **BRNI**.

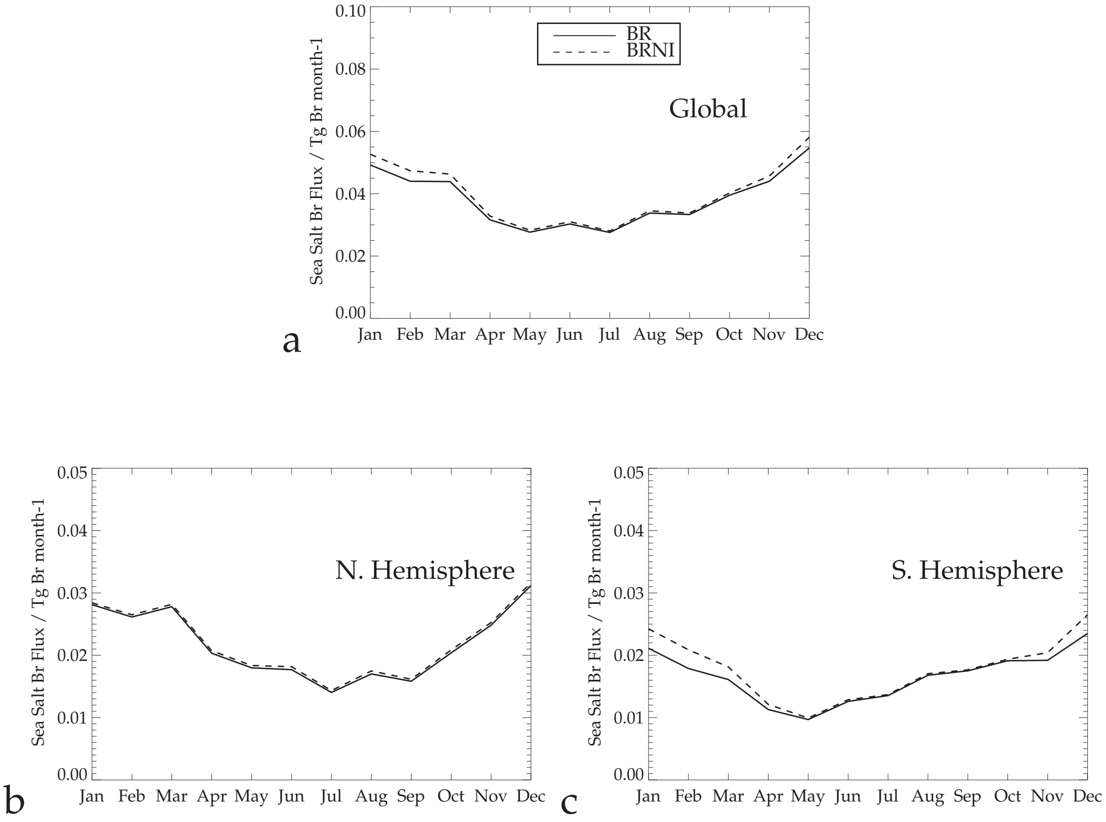

Figure 4.26: Annual cycle of Br emissions from sea salt (Tg Br month^{-1}) for (a) Global, (b) Northern Hemisphere and (c) Southern Hemisphere in model runs **BR** and **BRNI**.

Figure 4.26 provides clear evidence that emissions of DMS could play a role in controlling the source of bromine from sea salt aerosols during the SH summer. The DMS-SO_2-sea salt-BrO feedback could have important implications for understanding how CCN number concentrations will respond to possible future increases in DMS. Charlson *et al.* (1987) first suggested global warming may lead to increased oceanic productivity and a larger DMS flux. They also suggested this may represent a negative climate forcing, as higher emissions would lead to higher CCN number concentrations and subsequently increased cloud albedo and cloud lifetime through the 1st and 2nd aerosol indirect effects. The future response in DMS remains uncertain but if emissions of DMS were to increase, the resulting change in CCN is an important question. A recent study by Woodhouse *et al.* (2010) attempted to quantify the response in CCN to increases in DMS and found the sensitivity to be low. However, a key limitation of that study was the use of prescribed oxidants, which does not allow for any possible chemical feedbacks. Also oxidation by BrO was not accounted for. Given that the DMS lifetime and hence transport to the free troposphere is controlled by the availability of oxidants, ignoring any chemical feedbacks in the system may hold implications for conclusions drawn about the response in CCN.

The coupled chemistry-aerosol-bromine model developed as part of this work provides a more detailed tool for assessing the response in CCN to changes in DMS as coupled DMS-HO_x-NO_x-bromine feedbacks can be accounted for. The response in CCN to an increased DMS flux of 45% is now investigated.

The globally averaged DMS lifetime increased by 0.18 days (11%) between run **NOBR** and run **NOBRNI** compared to 0.04 days (6%) increase between runs **BR** and run **BRNI**, hence the DMS-SO_2-sea salt-BrO feedback acts to reduce the sensitivity of the DMS lifetime to increases in the DMS flux. Also the annual mean percent contribution of BrO to the DMS sink increased to 39% in run **BRNI**. Higher fractional oxidation by BrO will inhibit new particle formation by favouring the formation of DMSO. To examine the response in CCN number concentrations due to an increased DMS source, the monthly mean zonally averaged increase in CCN number concentrations in runs **BR** and **BRNI** is compared to **NOBR** and **NOBRNI** in Figure 4.27.

CCN number concentrations increase in both the **BRNI** and **NOBRNI** simulations relative to the **BR** and **NOBR** runs in response to the increased DMS source. The largest increase in CCN is simulated in the 30-40°S latitude band because of high DMS emissions in this region. The simulated change in the CCN number concentration is lower in the **BR** simulations. This suggests that the increased Br_2 source from sea salt driven by increased aerosol acidification from DMS sourced SO_2 acts to suppress the response in CCN number concentrations to increases in the DMS flux. The same response is evident throughout the different latitude bands in the SH as shown in Figure 4.27. The sensitivity of CCN number concentrations to a higher DMS flux is reduced by between 27 and 42% when bromine chemistry is included (Table 4.5).

The is an important finding as it suggests oxidant feedbacks driven by increases in DMS emissions are important for future changes in CCN number concentrations. This is the first study to show that coupled DMS-halogen driven oxidant feedbacks may be important in future responses in CCN. The suppression in CCN response can be attributed to two factors: Firstly due to the increased importance of the addition pathway in DMS oxidation and secondly due to a decrease in the DMS lifetime and subsequently less transport to the free troposphere.

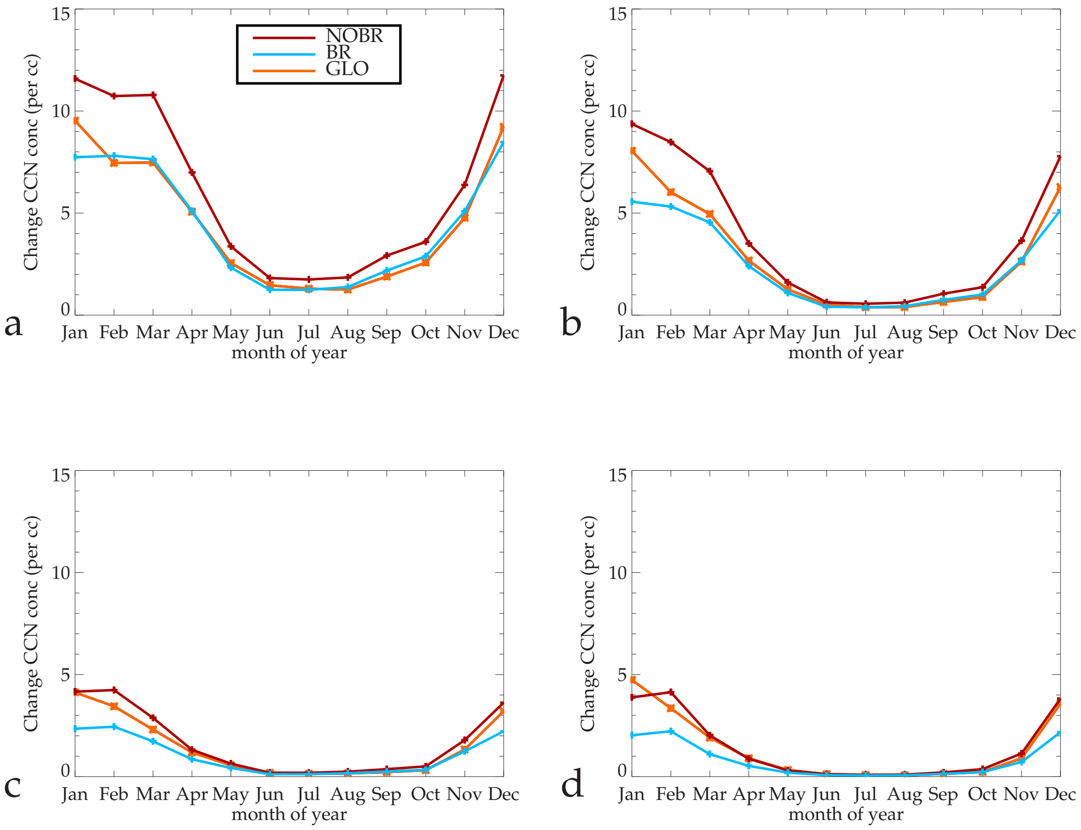

Figure 4.27: Absolute change in zonally averaged CCN number concentrations (cm^{-3}) between simulations **NOBR** and **NOBRNI** and between **BR** and **BRNI**. Results shown as seasonal cycle in four latitude bands (a) 30-40°S, (b) 40-50°S, (c) 50-60°S and (d) 60-70°S. For comparison absolute change between runs **GLO** and **GLONI** is also shown.

For comparison with the Woodhouse *et al.* (2010) study Figure 4.27 also shows the response in CCN to the higher DMS flux in the **GLO** model presented in the Chapter 3. The response in CCN to the increased DMS flux in the **BR** model is generally lower than that in the **GLO** model, suggesting the DMS-SO_2-sea salt BrO feedback may result in a lower sensitivity of CCN to increases in DMS than suggested by Woodhouse *et al.* (2010).

Table 4.5: Changes in bromine budgets, DMS emissions and CCN number concentrations for December 2004 in the **BR** and **NOBR** simulations

	NOBRNI-NOBR	**BRNI-BR**	change
Br sea salt emissions (Tg Br month^{-1})			
Global		0.0025 (6.3%)	
Northern Hemisphere		0.0004 (1.6%)	
Southern Hemisphere		0.0021 (13.1%)	
DMS			
DMS Burden change (Tg S)	0.032	0.015	-53%
DMS lifetime change (days)	0.18	0.04	-78%
CCN (cm^{-3})			
Zmean change CCN 30-40S	11.7	8.5	-27%
Zmean change CCN 40-50S	7.8	5.1	-35%
Zmean change CCN 50-60S	3.6	2.2	-39%
Zmean change CCN 60-70S	3.8	2.2	-42%

4.9 Discussion and Conclusions

This chapter presented results from the first global simulations of the impact of bromine chemistry on DMS oxidation and marine aerosol formation in the remote marine boundary layer. The model reproduces 65% of the observed daytime monthly mean BrO at the Cape Verde Atmospheric Observatory (CVAO) in the tropical East Atlantic Ocean **BR** mean = 1.56 pptv, obs mean = 2.42 pptv). Model comparison with troposphere column BrO observations from the GOME satellite show the model predicts higher troposphere column BrO than the observations. The low sensitivity of the GOME instrument in the boundary layer over low albedo surfaces (e.g. Ocean) may explain some of this overestimation.

The simulated bromine fields provide a large sink for ozone compared to a simulation without bromine chemistry. Zonally averaged ozone concentrations decrease by greater than 6% outside the tropics in December with the largest reductions in the SH high latitudes (>24%). The global tropospheric ozone burden decreases by 26 Tg O_3 (7.8%) in the bromine simulation. The main bromine loss pathways for ozone are HO_2 + BrO (130 Tg O_3 yr^{-1}) and $BrONO_2$ + aerosol (18 Tg O_3 yr^{-1}). Bromine chemistry also results in large decreases in NO_x throughout the lower troposphere in December (>20%) with the largest NO_x reductions simulated in the NH between 60°-70°N, attributable to heterogenous uptake of $BrONO_2$ on aerosol. HO_x concentrations decrease by 2-8% throughout most of the troposphere with larger decreases in December in the NH (32-40%).

However, global mean OH is not signficantly affected decreasing by only 0.5% in the bromine simulation. Comparison with the observed daytime ozone loss at CVAO show the introduction of bromine chemistry slightly increases the modelled daytime ozone loss compared to a simulation without bromine chemistry but both simulations significantly underestimate the observed loss.

The model simulations suggest BrO contributes 36% of the annual mean DMS oxidation sink, which is greater than that of NO_3. The highest contribution is simulated over the SH oceans ($\geq$ 50%). The introduction of bromine chemistry also reduces the DMS lifetime and burden by 42%. As a result zonally averaged CCN number concentrations decrease by 10 to 25% over the Southern Hemisphere (SH) oceans during the summer months. When only CCN formation attributable to DMS emissions is accounted for the reduction in CCN is 23 to 43%.

In addition, the model simulations suggest emissions of Br_2 from sea salt in the SH oceans are linked to the DMS source. Using an alternative DMS source parameterisation which gives a 45% larger DMS flux, enhanced the sea salt bromine source by between 11 and 17% in the SH summer. This oxidant feedback increases the DMS oxidation sink and suppresses the increase in the DMS lifetime to increases in the DMS flux. Higher fractional DMS oxidation by BrO also reduces the yield of SO_2 formation and subsequently new particle formation. The DMS-SO_2-SS-BrO feedback ultimately acts to suppress the increase in CCN formation due to increases in the DMS flux and may be important for future changes in CCN over the SH oceans. These results are sufficient to suggest a coupled oxidant treatment of bromine chemistry should be included in all future modelling studies of the marine sulfur cycle and aerosol formation.

It is important to note this work is subject to a number of important limitations that should be improved in future studies. There is large uncertainty in the DMS source and this must be better constrained in global modelling simulations if oxidant-aerosol-feedbacks and subsequent CCN changes are to be determined. The DMS oxidation scheme used in this study is simple, better treatment of DMS oxidation and its products could be achieved by implementing a more detailed scheme that includes a higher number of reactions and treating more intermediate species in the oxidation chain. In particular, the introduction of bromine chemistry increases the importance of the DMS addition pathway and a more detailed treatment of DMSO to account for uptake to aerosol should be implemented. Parameterised DMS schemes such as Pham *et al.* (1995) are suitable for studying DMS sinks but the fate of DMS reaction products such as SO_2 and DMSO is not represented as well (Lucas & Prinn, 2005). In future work improving the DMS oxidation scheme to better capture the yields of SO_2, DMSO, MSA and H_2SO_4 should be a priority. The assumed uniform distribution of clouds in horizontal and vertical space in TOMCAT represents an important limitation of this study and likely has some impact on photchemistry in the model. Implementing a more realistic treatment of clouds in TOMCAT is key to improving future model studies. Further measurements of bromide depletions in sea salt aerosol and BrO mixing ratios in the SH are also required to fully understand the importance of reactive bromine chemistry in the remote marine SH. Observations of BrO in particular are currently very sparse in the SH and ground based observations in this region are required. The treatment of the HBr + HOBr heterogeneous reactions could also be improved. The current method does not adequately represent the diurnal behaviour of HOBr because HBr is limiting in the recycling process. In addition, this work shows the use of prescribed oxidants for studying future responses in CCN represents a key limitation in such studies. The oxidant feedbacks discussed in this study would not be captured by prescribed oxidant studies.

In future studies two further uncertainties should be addressed that are not accounted for in this work. Firstly, Sievering *et al.* (2004) identified that biogenic alkalinity in sea salt, associated with Ca enhancement, increases sulfate production in sea salt aerosol by reaction with O_3. The strong pH dependence of this reaction (Chameides & Stelson, 1992), makes the alkalinity supply in the aerosol the limiting factor for sulfate formation. This study assumed sea salt alkalinity is equivalent to that of bulk seawater (Gurciullo *et al.*, 1999). Shipboard measurements in the western Pacific Ocean indicate sea salt aerosol may contain 1 to 2.5 times more alkalinity than that of bulk seaweater due to biogenic sources. This additional sea salt alkalinity could hold important implications for reactive bromine chemistry in the SH, by inhibiting sea salt acidification and reducing bromine release. Sievering *et al.* (2004) stated the additional sea salt alkalinity may further limit new particle production from DMS emissions by increasing heterogeneous loss of SO_2 to sea salt. However, the fractional loss of biogenic sulfur in the form of SO_2 in the remote marine atmosphere is controlled by the lifetime and oxidation pathways of DMS. The additional sea salt alkalinity, may actually suppress the DMS oxidation sink in the MBL and increase transport of DMS into the free troposphere, where SO_2 sinks are less efficient. However it is important to note the Sievering *et al.* (2004) observations have been questioned by subsequent modelling studies (Von Glasow & Crutzen, 2004a; Alexander *et al.*, 2005). A second key uncertainty is how organic surfactants on the surface of aerosol particles (Gill *et al.*, 1983) impact exchange processes between the gas and liquid phase. Organic surfactants form via either accumulation of dissolved organic matter (DOM) into the aerosol surface microlayer, gas bubble bursting at the surface or uptake of gas-phase compounds onto the aerosol. If the organic compounds form a film around the aerosol, mass transfer between the gas and liquid phase will be reduced. Smoydzin & von Glasow (2007) showed organic coatings have little impact on sea salt pH but gas-phase chlorine and bromine concentrations decreased. There remain large uncertainties in understanding how important organic surfactants are for surface exchange processes including the surfactant lifetime, density and composition (Smoydzin & von Glasow, 2007).

An outcome of the results presented in this chapter is the two uncertainties detailed above take on additional previously unstated importance as well as adding new complexity to the CLAW hypothesis (See also Von Glasow (2007)). This work suggests future changes in CCN driven by changes in DMS flux are linked to chemical feedbacks involving HO_x-NO_x and BrO. In a DMS - CCN only system as used in Woodhouse *et al.* (2010) the response in CCN to increases in DMS is estimated to be low. Accounting for chemical feedbacks between DMS-HO_x-NO_x-sea salt and BrO suggests the response in CCN is even lower, primarily explained by an increased bromine source driven by increased aerosol acidification from DMS sourced SO_2. However, the presence of biogenic alkalinity and organic surfactants in sea salt aerosol could reduce the efficiency of bromine release from sea salt aerosol. Furthermore, if DMS increases in response to higher productivity, one might expect biogenic alkalinity and organic surfactants in sea salt aerosol to also increase, suppressing any BrO oxidant feedback and favouring a higher CCN response to increases in DMS. Future work should evaluate the importance of both biogenic alkalinity and organic surfactants in the marine atmosphere.

Chapter 5

Iodine

5.1 Introduction

Emissions of organic iodine compounds from macroalgae and phytoplankton at the ocean surface provide a source of iodine compounds to the troposphere (Carpenter *et al.*, 1999, 2003). Iodine can provide a sink for ozone and perturb HO_x (Chameides & Davis, 1980) and NO_x partitioning (Davis *et al.*, 1996). The detection of iodine monoxide (IO) mixing ratios greater than 1 pptv in the marine boundary layer at Mace Head (Alicke *et al.*, 1999), Tenerife (Allan *et al.*, 2000) and Cape Verde Atmospheric Observatory (CVAO) (Read *et al.*, 2008) suggests that reactive iodine chemistry may be important for determining oxidising capacity in remote marine regions.

In Chapter 4 the model simulations which included a treatment of bromine chemistry were unable to reproduce the observed diurnal O_3 loss throughout the year at CVAO. This may suggest an additional sink for ozone not included in the model, such as IO, is important in the region. Using a box model Read *et al.* (2008) showed that daytime loss of O_3 at CVAO could only be reproduced when a treatment of iodine and bromine chemistry was included in their simulations.

Global modelling of iodine in the troposphere is challenging because of uncertainties in the sources and chemistry of iodine species. In addition there is only a very small number of observations of iodine compounds in the troposphere. This chapter is a first attempt at global iodine modelling and aims to investigate the likely distributions of organic and inorganic iodine species in the troposphere and their possible role in providing an additional sink for ozone in the remote marine boundary layer. Where necessary reasonable approximations are made and simple parameterisations developed in order to produce reasonable burdens of atmospheric iodine.

In this chapter the coupled bromine model described in Chapter 4 is extended to include an iodine chemistry scheme based on the THAMO model (Saiz-Lopez *et al.*, 2006). This is the first coupled chemistry and size-resolved aerosol microphysics model to include a treatment of bromine and iodine chemistry for studying halogen-oxidant-aerosol interactions in the troposphere. Section 5.2 describes the iodine scheme and emissions of organic and inorganic iodine species contained in the model. The predicted global distributions of inorganic iodine species in the model are discussed in Section 5.4. In Section 5.5 the iodine model is compared with observations of iodine compounds in the atmosphere. Finally, Section 5.6 addresses changes in O_3 due to emissions of organic iodine compounds.

5.2 Model Description and Experiments

The iodine scheme is based on that in the Tropospheric HAlogen Chemistry MOdel (THAMO) (Saiz-Lopez *et al.*, 2008). The scheme includes 6 organic and 12 inorganic iodine species shown in Table 5.1.

Table 5.1: Iodine species included in the model.

Inorganic	Organic
I	CH_3I
IO	CH_2I_2
HOI	C_3H_7I
HI	CH_2ICl
INO_2	CH_2IBr
$IONO_2$	C_2H_7I
I_2	
IBr	
OIO	
I_2O_2	

The reactions in the model iodine scheme are listed in Appendix A. Dry deposition velocities for HI and HOI, and values for determining an effective Henry's law coefficient required for wet removal of HI, HOI, and I_2, are taken are taken from Saiz-Lopez *et al.* (2008).

Four heterogeneous reactions are included in the iodine scheme: Uptake of HOI, HI, $IONO_2$ and INO_2, with γ values for each species taken from Saiz-Lopez *et al.* (2008) (γHI=0.1, γHOI=0.01,

γINO_2=0.01, $\gamma IONO_2$=0.01). Equation 3.7 is used to determine the rate of each heterogeneous reaction. The aerosol surface area is calculated from the aerosol size distribution for sea salt and sulfate in GLOMAP. All reactions are assumed to take place instantaneously on the surface of the aerosol.

$$IONO_{2(g)} + H_2O \longrightarrow 0.5I_{(g)} \tag{5.1}$$

$$INO_{2(g)} + H_2O \longrightarrow 0.5I_{(g)} \tag{5.2}$$

$$HI_{(g)} + H_2O \longrightarrow 0.5I_{(g)} \tag{5.3}$$

$$HOI_{(g)} + H_2O \longrightarrow 0.5I_{(g)} \tag{5.4}$$

Formation of higher iodine oxides is not considered in the scheme. The reaction of I_2O_2 with O_3 in the model is assumed to be a sink for I_y because higher I_2O_x species go on to form new condensation nuclei (CN). Note that this thesis does not aim to investigate the formation of CN from emissions of iodine compounds.

$$I_2O_2 + O_3 \longrightarrow \text{loss} \tag{5.5}$$

5.2.1 Organic Iodine Emissions

Emissions of organic iodine species in the model are constrained using observations from the Marine Aerosol Production (MAP) and Reactive Halogens in the Marine Boundary Layer Experiment (RHaMBLE) cruises. MAP took place in the North Atlantic during June and July 2006. The RHaMBLE cruise took place in the tropical North Atlantic during May and June, 2007. The flux estimates from these cruises are detailed in Jones *et al.* (2010).

As part of the model development a series of source experiments was performed at a model resolution of 5.6°×5.6° and compared with observations of CH_3I reported in Yokouchi *et al.* (2008). The source scenario that showed best agreement with CH_3I observations at the 8 remote stations in Yokouchi *et al.* (2008) is detailed below and was adopted for all subsequent model runs.

Monthly mean flux estimates for CH_3I in the model are separated into mid-latitude ocean (25°-60°) and tropical ocean (0°-25°) components. The source regions are separated because measurements of CH_3I in the mid-latitudes show a seasonal dependence related to sea surface temperature (Yokouchi *et al.*, 2001). In contrast, no seasonality in CH_3I is evident in the tropical oceans (Yokouchi *et al.*, 2001). In addition, in both the tropics and mid-latitudes areas of high productivity show enhanced organic CH_3I fluxes (Rasmussen *et al.*, 1982).

In order to calculate source estimates in the mid-latitude oceans, the flux observations from the MAP cruise detailed in Jones *et al.* (2010) are filtered by removing all CH_3I fluxes less than 20 nmol m^{-2} day^{-1}. The mean value of the remaining observations is assumed to be representative of a summertime high productivity location.

The calculated flux value is then corrected to account for seasonality in the the sea surface temperature (SST) and oceanic productivity. The SST correction factor is determined using monthly mean SST values on a $1^\circ\times1^\circ$ grid using Equation 5.6. The SST data (NOAA ERSST V3) is provided by the NOAA/OAR/ESRL PSD
(http://www.esrl.noaa.gov/psd/data/gridded/data.noaa.ersst.html).

$$\mathrm{SST_{corr}} = (\mathrm{SST} - \mathrm{SST_{min}})/(\mathrm{SST_{max}} - \mathrm{SST_{min}}) \tag{5.6}$$

Where SST_{max} is the maximum SST in the grid box during the year and SST_{min} is the minimum. If SST_{corr} is less than 0.1 a value of 0.1 is used.

To account for the dependence of the CH_3I flux on productivity an oceanic chlorophyll-a (Chl-a) concentration field at $1^\circ\times1^\circ$ horizontal resolution is taken from Arnold *et al.* (2009), which is based on observations from the SeaWiFS satellite instrument
(http://oceancolor.gsfc.nasa.gov/SeaWiFS). The Chl-a field is assumed to provide a measure of the productivity in the mixed layer between 0 to 6 mg m^{-3}. Figure 5.1 shows the Chl-a field in January and July; highest Chl-a values are observed in the summer and throughout most of the open oceans Chl-a values are less than 1 mg m^{-3}. The final monthly mean CH_3I flux is calculated from Equation 5.7. It is assumed the mean flux value from the data is representative of the maximum SST (i.e. SST = SST_{max}) and a Chl-a concentration of 1.0 mg m^{-3}. The MAP cruise cruise took place in August in a region of high productivity in the North Atlantic Ocean, which justifies these two assumptions.

$$\mathrm{CH_3I_{flux}} = \mathrm{FLUX_{obs}} \times \mathrm{SST_{corr}} \times \mathrm{Chl-a} \tag{5.7}$$

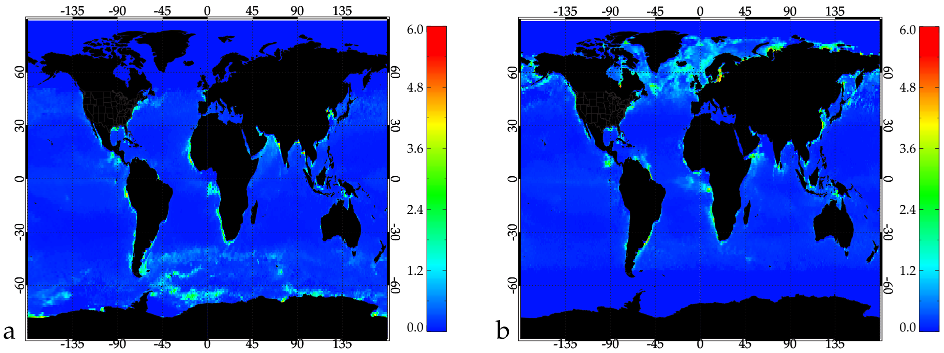

Figure 5.1: Ocean mixed layer Chl-a concentration field (mg m^{-3}) in (a) January and (b) July. Taken from (Arnold *et al.*, 2009) using data from the SeaWiFS satellite instrument (http://oceancolor.gsfc.nasa.gov/SeaWiFS).

In the tropics no seasonality in the CH_3I concentrations is observed at San Cristobal Island (Yokouchi *et al.*, 2008). In initial TOMCAT tests assuming a ubiquitous CH_3I flux over the tropical oceans as in Mahajan *et al.* (2010) resulted in an overestimation of CH_3I mixing ratios at San Cristobal by a factor 2. Also, simply assuming an iodocarbon source driven by Chl-a concentrations underestimated the observed CH_3I mixing ratios given the low Chl-a concentrations over large parts of the tropical oceans (see Figure 5.1). In order to account for this, in the tropical oceans a background oceanic CH_3I flux is also calculated. The background ocean flux was calculated by filtering the RHaMBLE cruise CH_3I measured fluxes to remove all values above 30 nmol cm^2 day^{-1} and taking the median of the remaining values. The productivity enhanced ocean flux was calculated using the CH_3I flux used in Mahajan *et al.* (2010) from the RHaMBLE cruise and correcting for productivity using Equation 5.7, assuming SST_{corr} = 1.0. The final iodocarbon flux value used in the model is calculated as the larger of the background flux and productivity enhanced flux value, not the sum of the two. The estimated CH_3I fluxes using the developed methodology in January and July are shown in Figure 5.2

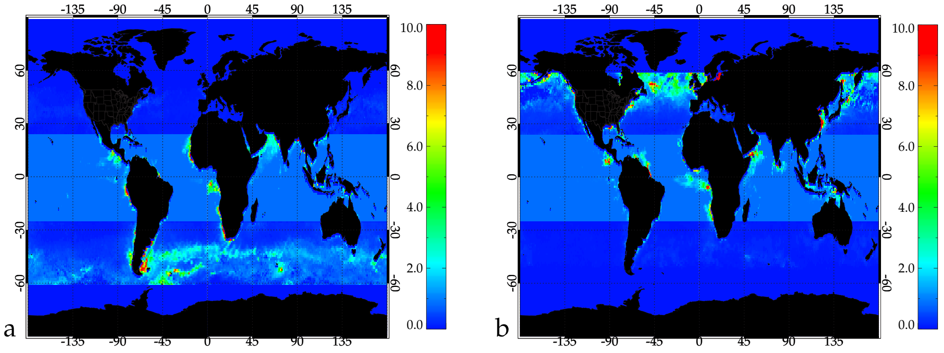

Figure 5.2: Calculated CH_3I flux (molecules cm^{-2} s^{-1}) in the model for (a) January and (b) July.

The methodology for CH_3I was applied to all organic iodine species in this work. The source fluxes for all species are constrained by the CH_3I flux measurements. Where the data is filtered to remove high or low CH_3I flux values, the co-located measurements for other species are also removed. Clearly this assumption is not ideal given that fluxes of CH_2ICl, for example, do not correlate well with CH_3I fluxes (Kurihara *et al.*, 2010), reflecting the different oceanic production mechanisms of the two species. However, not all the iodocarbons have extensive observational datasets and, given the extreme sparsity and variability of iodocarbon flux measurements, constraining emissions estimates for a global modelling study is difficult. No land-based fluxes of iodocarbons are accounted for in this study.

The assumed flux estimates for the 6 organic iodine species for each source component and region are detailed in Table 5.2. Table 5.3 shows the total flux for each organic iodine compound in the model compared to previous studies source estimates of organic iodine compounds. The simulated global organic iodine fluxes are underestimated compared to the estimate of Jones *et al.* (2010) by 0.12 Tg I yr^{-1}. This is due to an underprediction of the fluxes of CH_3I and CH_2ICl in the model, the two largest source gases in Jones *et al.* (2010). An explanation for the underestimate is the use of Chl-a field as a measure of productivity in determining the global organic iodine fluxes. Chl-a is directly a measure of ocean color, however quality satellite datasets that provide a better estimate of productivity are not yet available.

Table 5.2: Organic halogen species fluxes (nmol m^{-2} day^{-1}) in simulations **I** and **IORG**.

Species	Mid-Latitude Flux	Tropical Ocean Background Flux	Tropical Ocean Chl-a Flux
CH_3I	75.21	12.48	48.5
CH_2I_2	10.45	10.01	13.0
CH_2ICl	6.05	15.16	16.2
CH_2IBr	6.59	5.93	10.9
CH_2H_5I	0.5	3.23	4.1
C_3H_7I	1.49	0.82	0.9

Table 5.3: Global emissions of organic iodine (Tg I yr^{-1}) in the coupled model derived for this work and estimated fluxes from Law & Sturges (2006) and Jones *et al.* (2010)

Species	Simulated Flux	**LS06** Flux	**J10** Flux
CH_3I	0.223	0.09 - 0.45	0.30
CH_2I_2	0.105		0.11
C_3H_7I	0.008		<0.01
CH_2ICl	0.115	0.095	0.17
CH_2IBr	0.053		0.05
C_2H_5I	0.023		0.02
Total	**0.528**		**0.65**

LS06=Law & Sturges (2006), **J10**=Jones *et al.* (2010).

5.2.2 Inorganic Iodine Emissions

The inorganic iodine source flux in simulation **I** (see Section 5.3 for description of model runs) is based on the work of Garland & Curtis (1981). Garland & Curtis (1981) first suggested the deposition and subsequent reaction of O_3 with IO_3^- at the sea surface results in a flux of I_2 to the atmosphere. More recently a number laboratory studies have also shown organic halogen compounds can be formed by the oxidation halogen anions by chlorophyll or aromatic carbonyl compounds (Reeser *et al.*, 2009; Jammoul *et al.*, 2009). However, these mechanisms are complex and remain largely uncertain. In this study it is assumed the I_2 flux is equal to 0.05% of the O_3 deposition flux to the sea surface. The flux is limited to the daytime following Mahajan *et al.* (2010) who showed reproducing the IO diurnal variation required an active inorganic iodine flux in the daytime.

A fixed ozone deposition velocity of 0.05 cm s^{-1} is assumed over the oceans. This assumption is not ideal given that in reality the ozone deposition velocity depends on the sea surface temperature (Johnson & Davis, 2006), wind speed (Fairall *et al.*, 2007) and the availability of IO_3^- and Dissolved Organic Matter (DOM) in surface sea water (Garland *et al.*, 1980; Clifford *et al.*, 2008). However, an interactive trace gas deposition scheme is not currently available in TOMCAT and a more detailed treatment is beyond the scope of this study.

Preliminary simulations showed the model is highly sensitive to the assumed magnitude and spatial extent of the inorganic iodine flux. This clearly demonstrates the large uncertainties in the source mechanisms involved not just in terms of ozone deposition velocities but also the composition of surface seawater and availability of reactants. In simulation **I** the inorganic iodine flux is restricted to the tropical North Atlantic between 5° and 20°N and 25° and 45°W.

5.3 Model Experiments

In this chapter, four model simulations are presented. **NOI**, **I**, **IORG** and **NOBRI**. Simulation **NOI** is the same as simulation **BR** in Chapter 4. Simulation **I** includes organic and inorganic emissions of iodine compounds. Simulation **IORG** includes only emissions of organic iodine compounds and simulation **NOBRI** does not include any emissions of iodine or bromine species.

5.4 Evaluation of the Iodine Model - Global Distributions

The predicted global distributions of inorganic and organic iodine compounds in simulation **IORG** are now discussed. The monthly mean surface and zonally averaged CH_3I mixing ratio in January and July is shown in Figure 5.3. Largest CH_3I mixing ratios are simulated at mid-high latitudes in the summer hemisphere close to areas of high productivity, consistent with the strong source dependence of CH_3I on Chl-a and SST in the model. There is little seasonality in CH_3I in the tropics with predicted mixing ratios greater than 0.4 pptv throughout the year. In the zonal mean plots CH_3I mixing ratios greater than 0.3 pptv are predicted throughout the free troposphere in the mid-high latitude hemisphere winter even in the absence of a significant source. In the summer CH_3I mixing ratios decrease rapidly with altitude. This is because CH_3I has a much longer lifetime in the winter than the summer, resulting in higher CH_3I mixing ratios in the free troposphere in the winter.

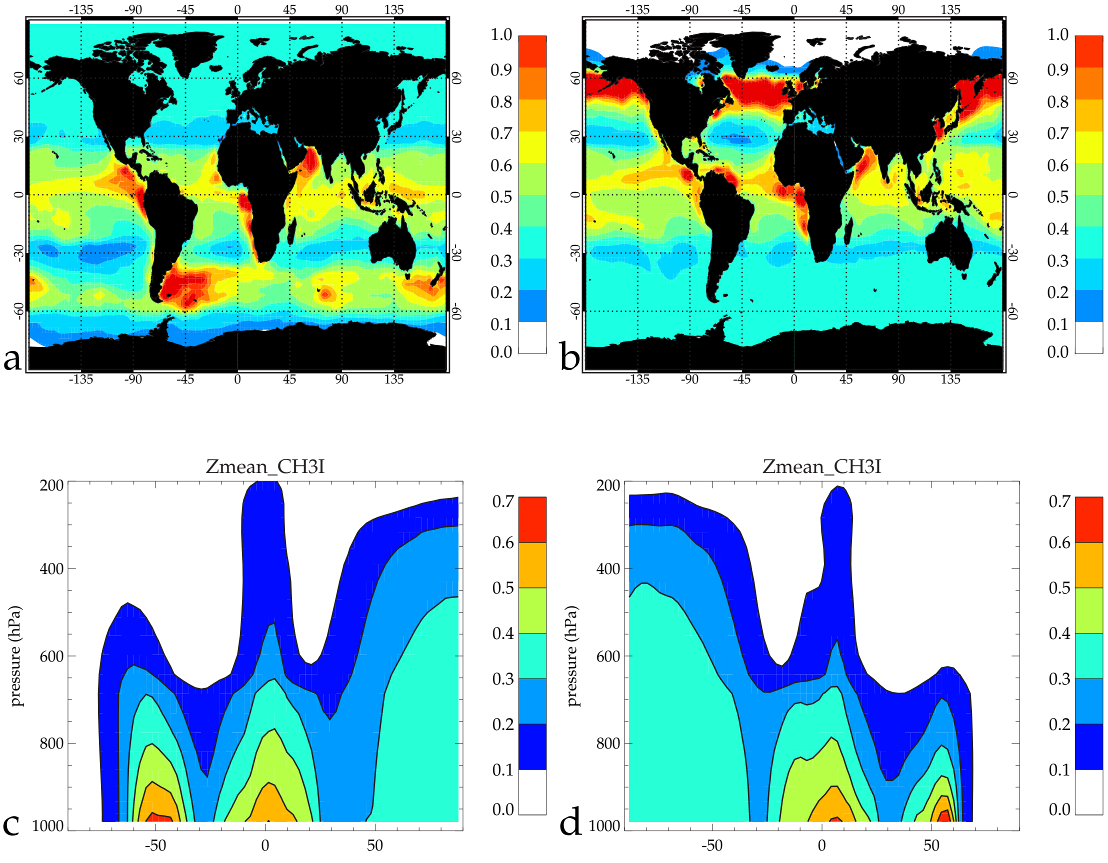

Figure 5.3: Surface and zonally averaged monthly mean CH_3I mixing ratio (pptv) in simulation IORG during (a) and (c) January, (b) and (d) July.

The zonal mean distributions of CH_2ICl, C_2H_5I and CH_2I_2 in January and July are shown in Figure 5.4. These species have a smaller source in the model than CH_3I (see Table 5.3) and a shorter lifetime than CH_3I (See Table 2.2). To better show the distributions of these species the plot scale in Figure 5.4 is different to that in Figure 5.3. All three species are predicted to have mixing ratios less than 0.02 pptv outside the tropics. C_2H_5I has the longest lifetime of the three species (∼4 days), which explains its transport to the mid free troposphere even though it has the smallest source in the model. CH_2I_2 has the shortest lifetime of the three species (minutes) hence it is not transported far above the surface. CH_2IBr and C_3H_7I are not shown because neither compound is predicted to be present with mixing ratios above 0.02 pptv.

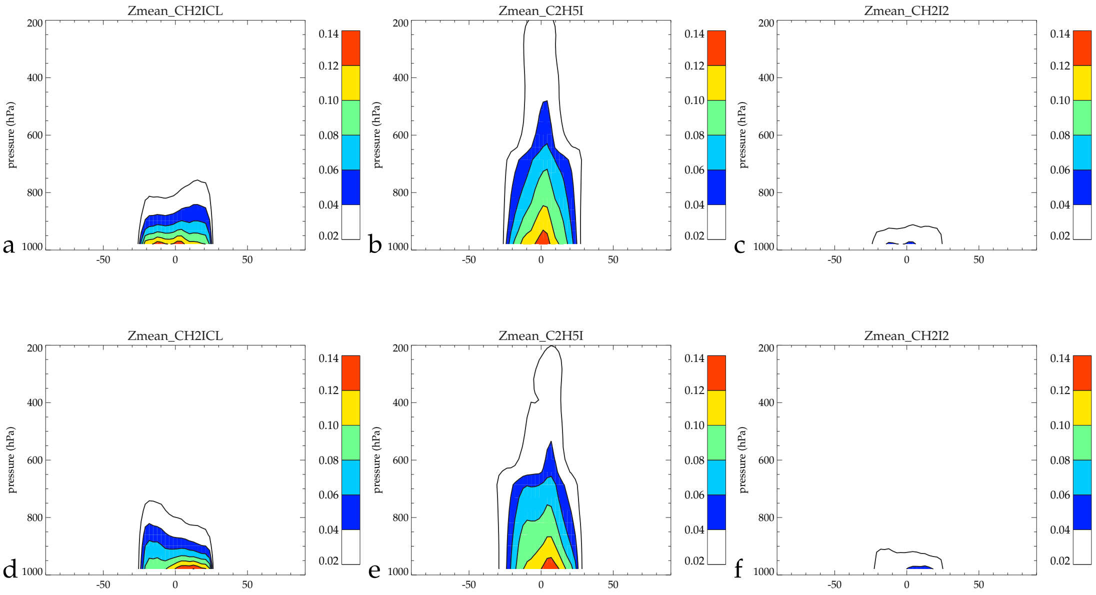

Figure 5.4: Zonally averaged monthly mean organic iodine mixing ratio (pptv) during (a), (b) and (c) January and (d), (e) and (f) July for (a) and (d) CH_2ICl, (b) and (e) C_2H_5I and (c) and (f) CH_2I_2.

Total inorganic iodine (I_y) is calculated as the sum of all inorganic iodine species ($I_y = I + 2\times I_2 + IO + OIO + HOI + HI + INO_2 + IONO_2 + IBr + 2\times I_2O_2$). Figure 5.5 shows monthly mean surface I_y during January, April, July and October in simulation **IORG**. The largest I_y mixing ratios are simulated in the tropics consistent with the large organic sources of iodine. I_y mixing ratios at mid and high latitudes are larger in the summer hemisphere, suggesting the large organic iodine fluxes driven by summertime peaks in oceanic productivity and sea surface temperature dominate over increased rates of photochemical loss.

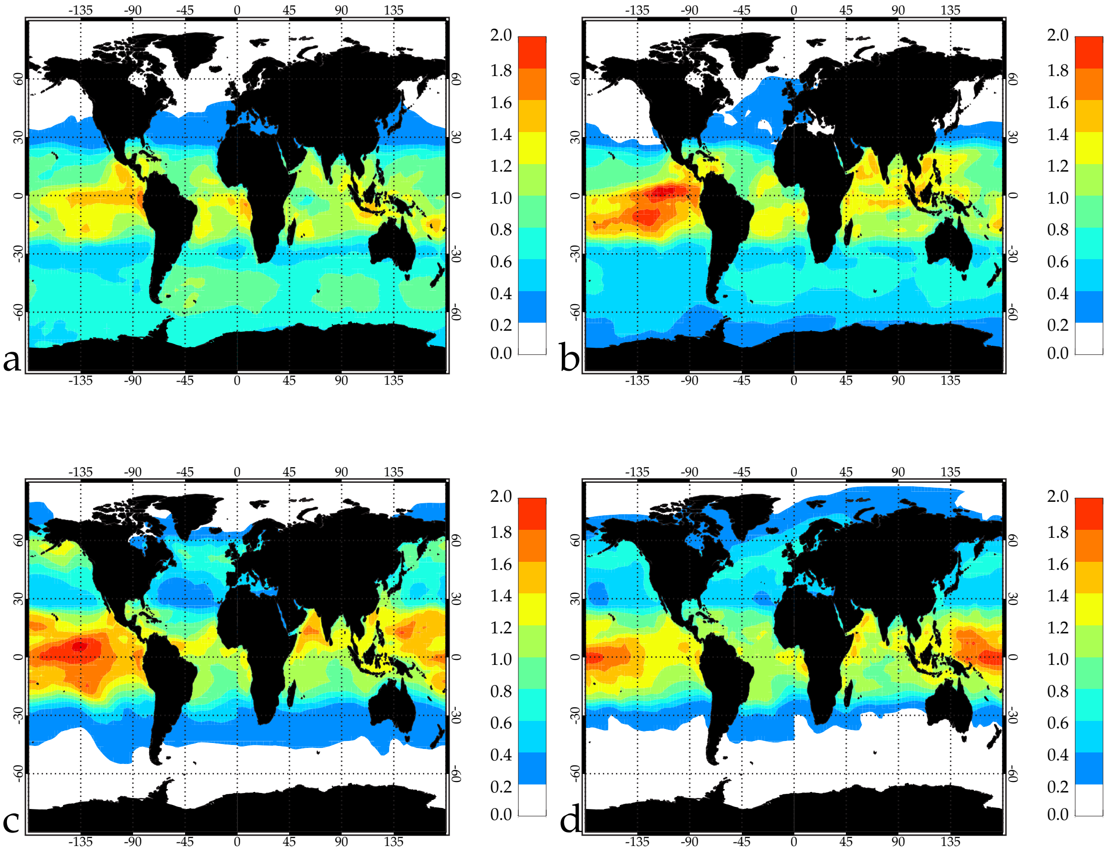

Figure 5.5: Surface monthly averaged total inorganic iodine (I_y) mixing ratio (pptv) in simulation IORG during (a) January, (b) April, (c) July and (d) October.

The zonally averaged monthly mean I_y in January, April, July and October in simulation **IORG** is shown in Figure 5.6. The simulations show up to 0.75 pptv I_y reaching the tropical upper troposphere. Very little I_y (< 0.25 pptv) is simulated in the winter hemisphere, consistent with small winter sources of organic iodine.

Figures 5.7 and 5.8 shows the 24-hour mean inorganic iodine partitioning in January and July in simulation **IORG**. HOI represents the largest fraction of I_y (30-50%) throughout most of the tropical troposphere. IO is predicted to be 0-20% of total I_y. At high latitudes in the NH summer IO contributes >20% I_y. Perhaps suprisingly, I contributes the largest fraction of I_y in the high latitude southern hemisphere (SH) summer. This may be explained by the low bond dissociation energy of IO (240 kJmol^{-1}) which rapidly dissociates in the 24 hour sunlight to form I + O. The higher I fraction in the SH winter than the northern hemisphere (NH) winter can be explained by lower HO_2 and O_3 concentrations in the SH and by the strong negative temperature dependence of the O_3 + I reaction, which is slower in the colder temperatures of the SH. In contrast in the NH high latitude summer HOI is the dominant fraction because HO_2 is higher in the NH high latitudes

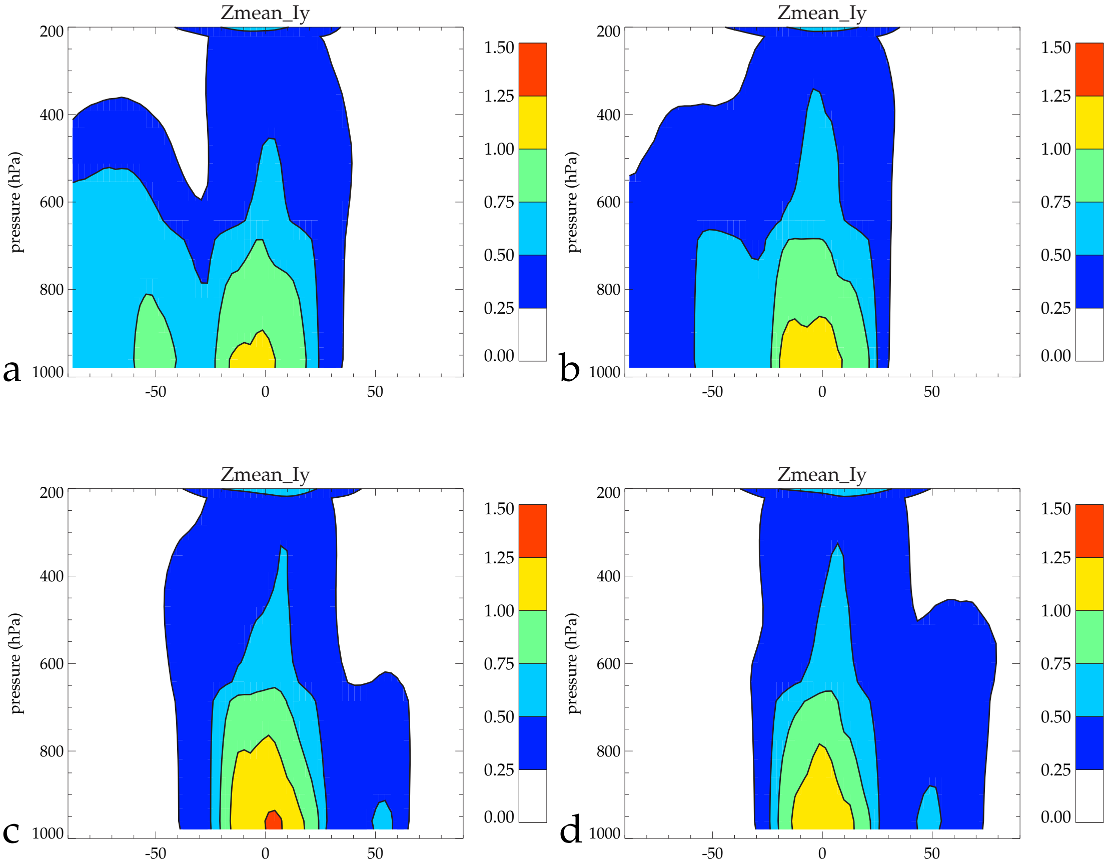

Figure 5.6: Zonally averaged monthly mean total inorganic iodine (I_y) mixing ratio (pptv) in simulation IORG during (a) January, (b) April, (c) July and (d) October.

than the SH high latitudes at this time. NO_2 is predicted to be an important fraction of I_y in the NH winter between 30° and 60°N (30-50%) due to high NO_x emissions in the region. Throughout the rest of the troposphere INO_2 is generally 10-30% of I_y. $IONO_2$ and IBr are more important components of I_y in the winter. The larger fraction of IBr in the NH winter than in the SH summer may be explained by the higher aerosol surface areas in the NH that cycle HOI, INO_2, $IONO_2$ and HI to IBr, which has a long lifetime in the absence of sunlight. I_2O_2, OIO, HI and I_2 all contribute only a small fraction of I_y ($<10\%$) and are not shown in Figures 5.7 and 5.8. The low fraction of I_y present as IO suggests observations of IO could be a poor constraint on total I_y and hence emissions fluxes of iodine.

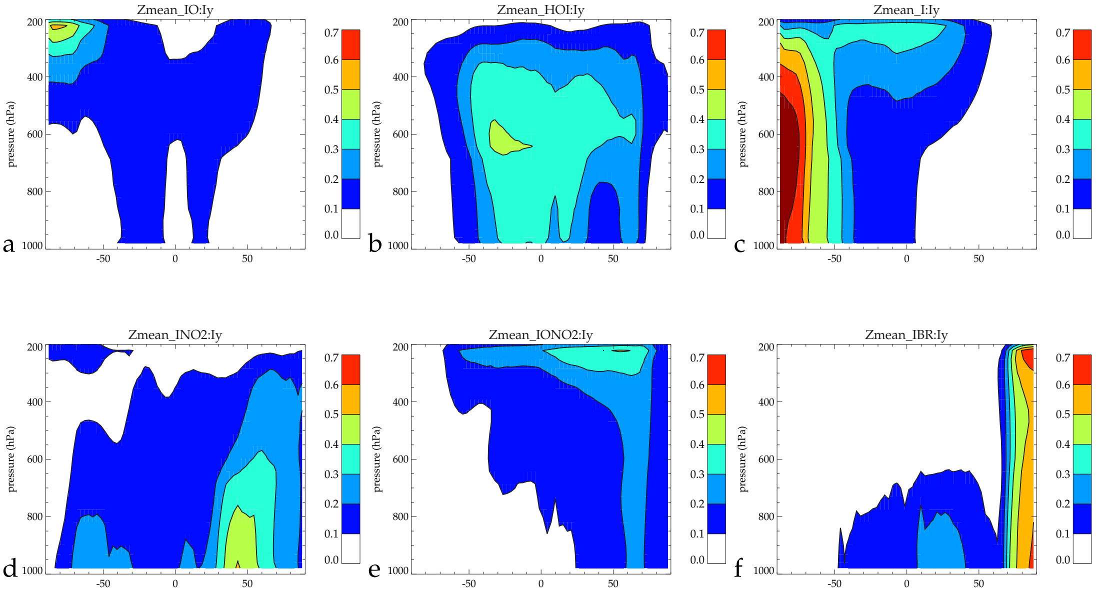

Figure 5.7: Zonally averaged monthly mean inorganic iodine partitioning during January. Plots are for (a) IO:I_y, (b) HOI:I_y, (c) I:I_y, (d) INO_2:I_y, (e) $IONO_2$:I_y and (f) IBr:I_y.

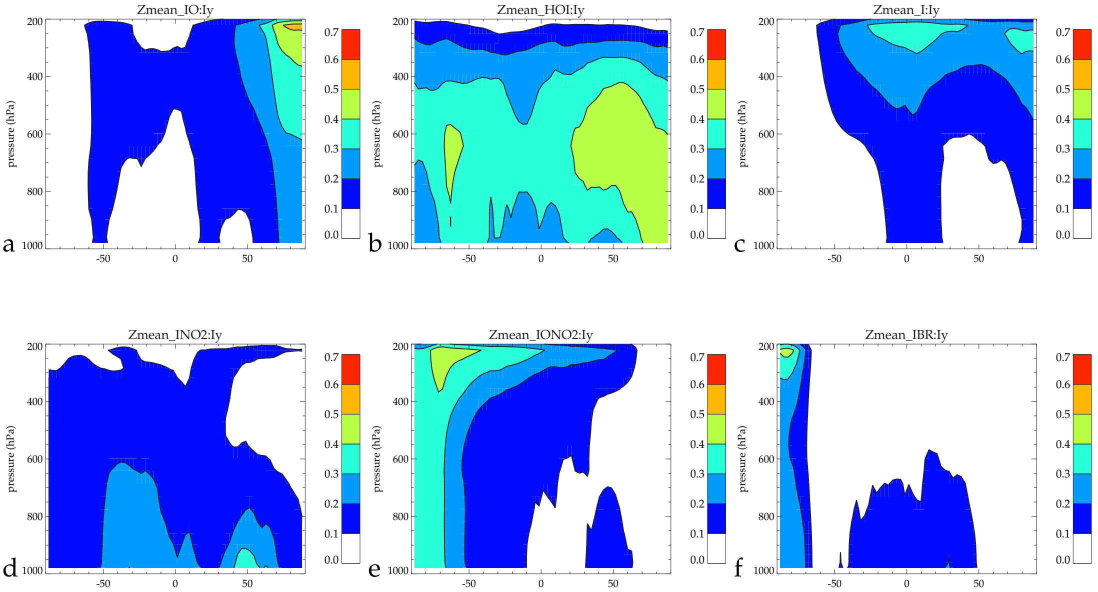

Figure 5.8: As Figure 5.7 but for July. Plots are for (a) IO:I_y, (b) HOI:I_y, (c) I:I_y, (d) INO_2:I_y, (e) $IONO_2$:I_y and (f) IBr:I_y.

Figures 5.9 and 5.10 shows the 24-hour mean surface inorganic iodine partitioning in January and July in simulation **IORG**. IO represents 10-20% of I_y at the surface throughout the tropical open oceans (Figures 5.9a and 5.10a). A smaller fraction of I_y partitions to IO in the North Atlantic Ocean in Decembe r and July due high shipping NO_x emissions that favour formation of INO_2 (Figures 5.9d and 5.10d). The dominant form of I_y at the surface during both January and December is HOI which represents more than 30% of I_y overlarge areas of the oceans (Figures 5.9b and 5.10b). I represents the dominant form of I_y at high latitudes in the SH during December (Figure 5.9c). $IONO_2$ is an important I_y species (20-30%) in the SH high latitudes during the winter (Figure 5.10e). $IONO_2$ represents a smaller fraction of I_y during the NH winter (Figure 5.9e), instead I_y partitions to IBr (Figure 5.9f). The favourable partitioning of I_y to IBr in the NH winter is explained by higher levels of Bromine in the NH winter than the SH winter. (See Section 4.3 for discussion).

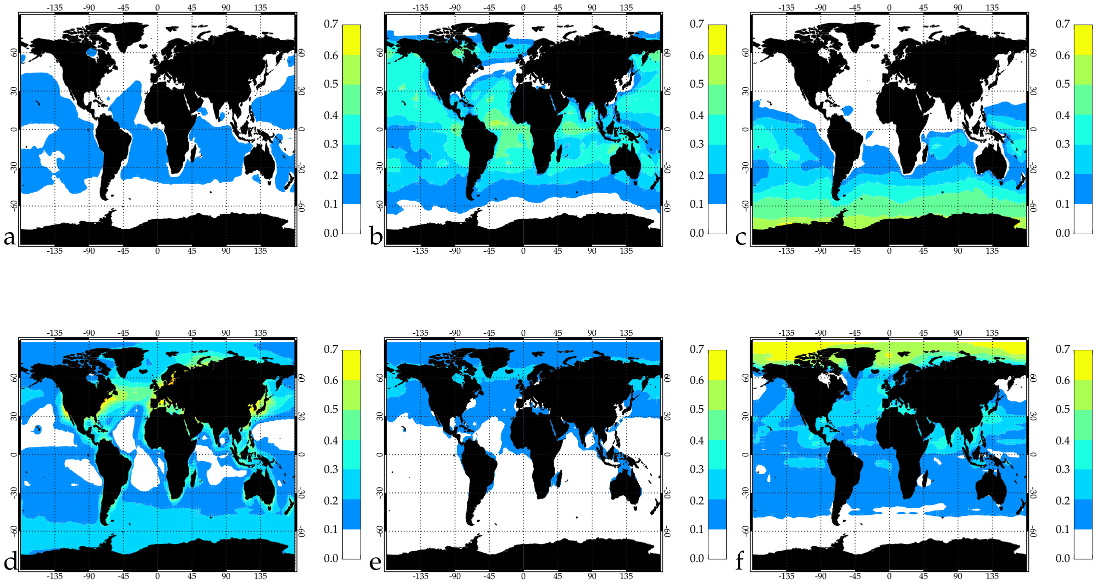
a
b
c
d
e
f
-135 -90 -45 0 45 90 135
60 30 0 -30 -60
0.7 0.6 0.5 0.4 0.3 0.2 0.1 0.0

Figure 5.9: Surface monthly mean inorganic iodine partitioning during January. Plots are for (a) $IO:I_y$, (b) $HOI:I_y$, (c) $I:I_y$, (d) $INO_2:I_y$, (e) $IONO_2:I_y$ and (f) $IBr:I_y$.

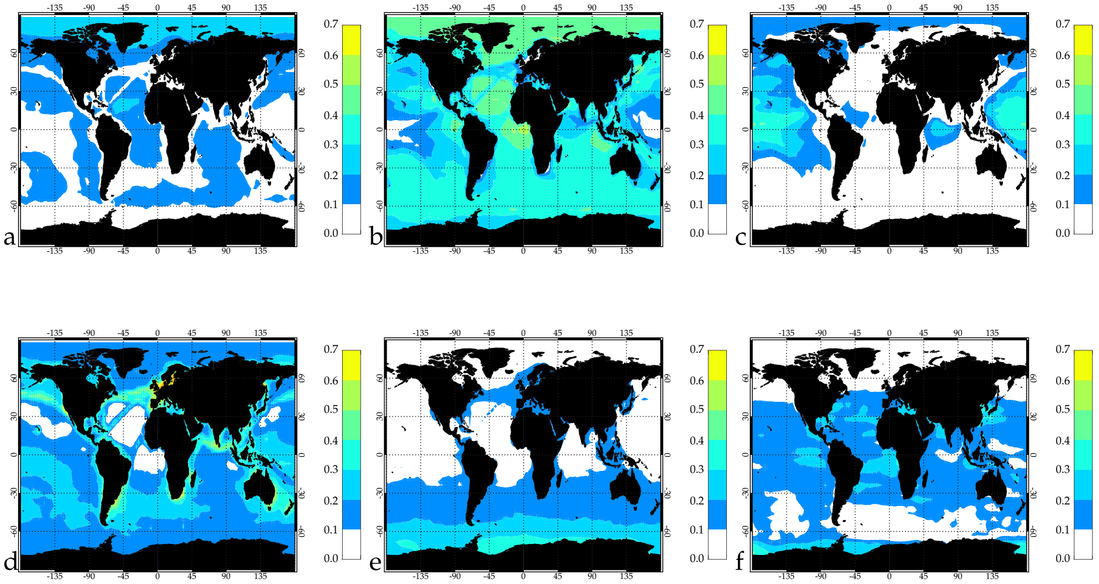
a
b
c
d
e
f
-135 -90 -45 0 45 90 135
60 30 0 -30 -60
0.7 0.6 0.5 0.4 0.3 0.2 0.1 0.0

Figure 5.10: As Figure 5.9 but for July. Plots are for (a) $IO:I_y$, (b) $HOI:I_y$, (c) $I:I_y$, (d) $INO_2:I_y$, (e) $IONO_2:I_y$ and (f) $IBr:I_y$.

Figures 5.11 and 5.12 shows the 24-hour mean surface inorganic iodine mixing ratios in January and July of the 6 main inorganic iodine species in simulation **IORG**. Surface IO mixing ratios are predicted to 0.1-0.2 pptv over the tropical oceans during December and July (Figures 5.11a and 5.12a). Clearly the model underpredicts the observed daytime IO levels of 1.0-2.0 pptv at Cape Verde (Read *et al.*, 2008). HOI mixing ratios greater than 0.1 pptv are simulated in the tropcial and NH oceans (Figures 5.11b and 5.12b). Maximum HOI mixing ratios of 0.5 pptv are predicted in the Western Tropical Pacific Ocean and Western Tropical Atlantic Ocean during Decmember and July. Simulation **IORG** predicts I mixing ratios between and 0.3 and 0.7 pptv in a large region of the Pacific Ocean during December and July (Figures 5.11c and 5.12c). INO_2 (Figures 5.11d and 5.12d) is simulated at higher mixing ratios than $IONO_2$ (Figures 5.11e and 5.12e) in simulation **IORG**. Over large areas of the Pacific Ocean INO_2 mixing ratios are greater than 0.2 pptv. Finally IBr mixing ratios of 0.1-0.4 pptv are simulated throughout the tropical oceans in December and July (See Figures 5.11f and 5.12f).

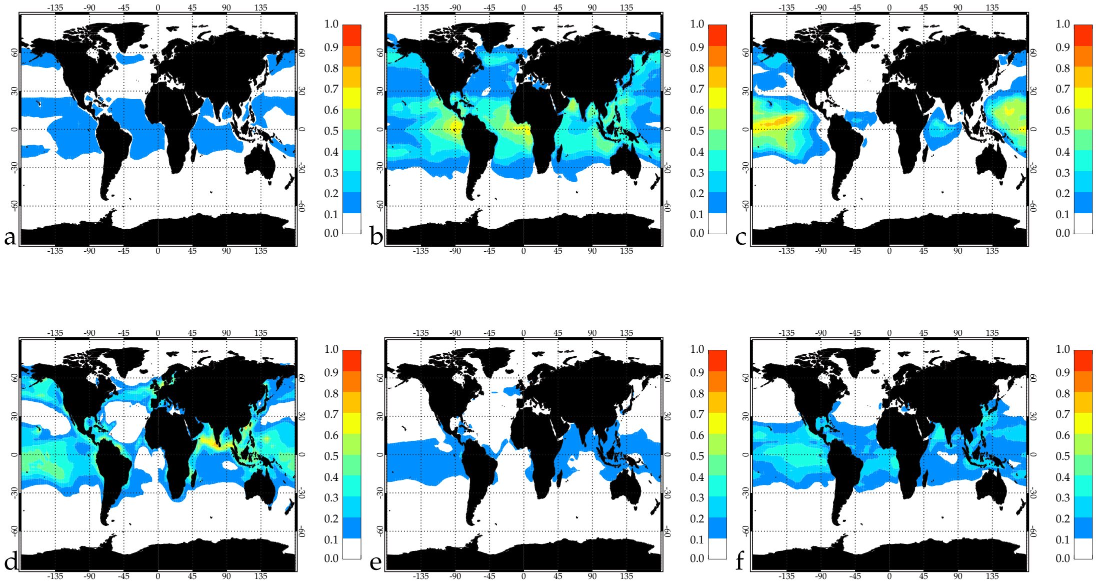
a
b
c
d
e
f
-135 -90 -45 0 45 90 135
60 30 0 -30 -60
1.0 0.9 0.8 0.7 0.6 0.5 0.4 0.3 0.2 0.1 0.0

Figure 5.11: Surface monthly mean inorganic iodine mixing ratios during January. Plots are for (a) IO, (b) HOI, (c) I, (d) INO_2, (e) $IONO_2$ and (f) IBr.

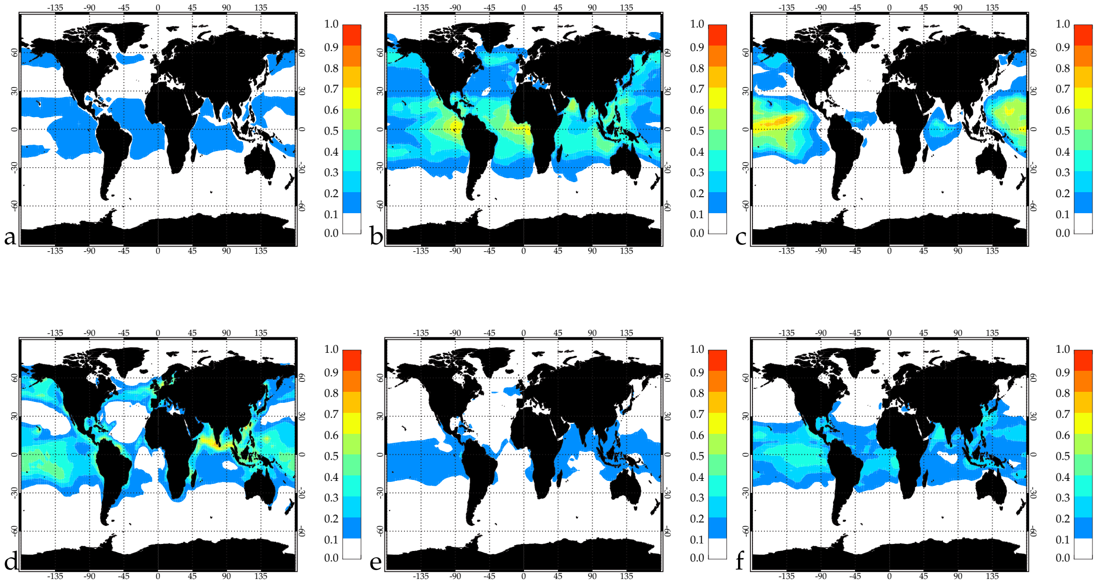
a
b
c
d
e
f
-135 -90 -45 0 45 90 135
60 30 0 -30 -60
1.0 0.9 0.8 0.7 0.6 0.5 0.4 0.3 0.2 0.1 0.0

Figure 5.12: As Figure 5.11 but for July. Plots are for (a) IO, (b) HOI, (c) I, (d) INO_2, (e) $IONO_2$ and (f) IBr.

Figures 5.13 and 5.14 shows the 24-hour mean surface inorganic iodine mixing ratios in January and July of the 6 main inorganic iodine species in simulation **IORG**. Simulated monthly average IO mixing ratios are below 0.1 pptv everywhere with the exception of the tropical boundary layer where 0.1-0.2 pptv is simulated (Figures 5.13a and 5.14a). Simulated zonally averaged HOI mixing ratios are between 0.2 and 0.4 pptv throughout the tropics during December and July (Figures 5.13b and 5.14b). In the high latitude SH in December I mixing ratios between 0.3 and 0.5 pptv are simulated (Figure 5.13c).

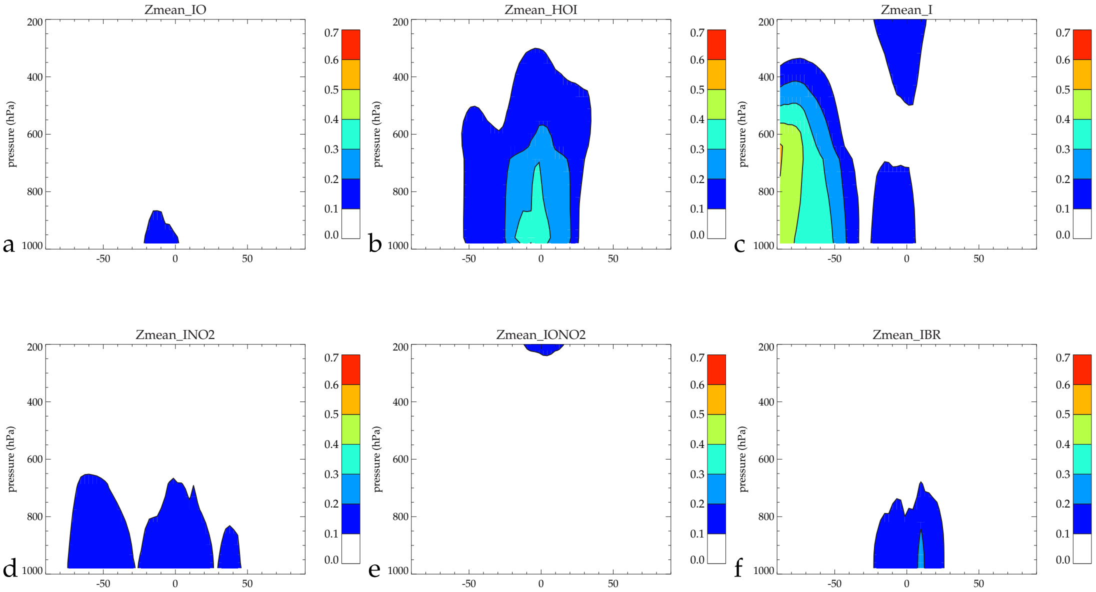

Figure 5.13: Zonally averaged monthly mean inorganic iodine mixing ratios during January. Plots are for (a) IO, (b) HOI, (c) I, (d) INO_2, (e) $IONO_2$ and (f) IBr.

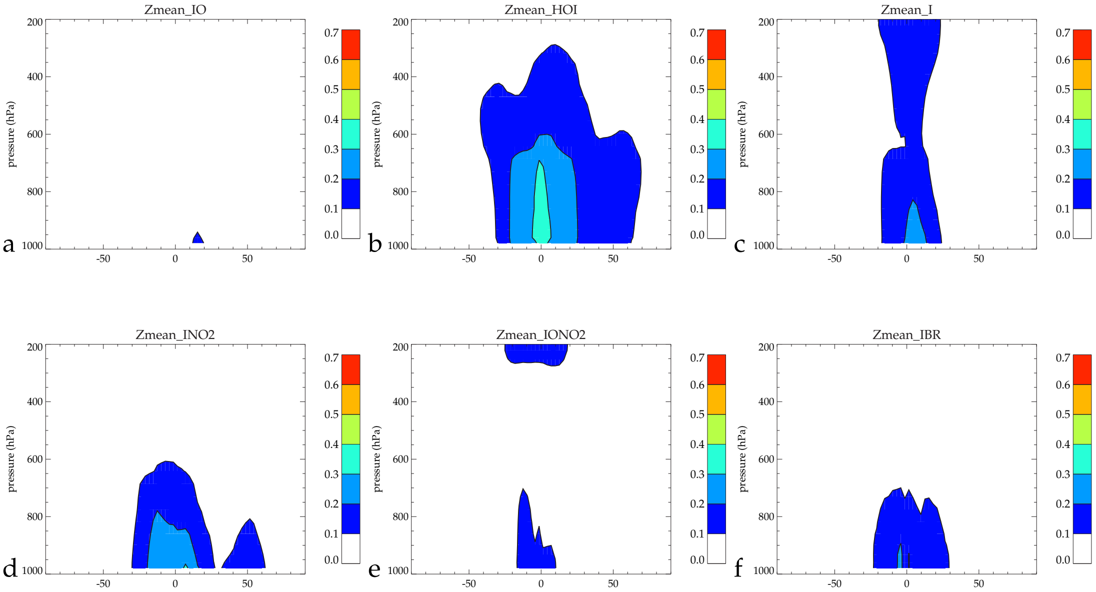

Figure 5.14: As Figure 5.13 but for July. Plots are for (a) IO, (b) HOI, (c) I, (d) INO_2, (e) $IONO_2$ and (f) IBr.

5.5 Evaluation of the Iodine Model - Comparisons with Observations

This section provides a more focused comparison with observations of CH_3I and IO. Comparisons with other iodine species are not shown because of sparse availability of observations.

Emission estimates of CH_3I in the new model are now validated using atmospheric observations detailed in Yokouchi *et al.* (2008). Figure 5.15 shows the monthly mean simulated CH_3I in run **IORG** and measurements of CH_3I during each month at 8 observation stations.

At the high latitude stations (Alert and Syowa), CH_3I mixing ratios are low throughout the year (<0.7pptv). These stations show a large seasonal amplitude driven by seasonality in sources and sinks. Maximum CH_3I mixing ratios are observed in the winter hemisphere when photochemical loss is very slow. This suggests the source of CH_3I at these sites during the winter is transport from mid-latitudes (Yokouchi *et al.*, 2008). Simulation **IORG** captures the amplitude of the seasonal variation at these stations but shows that CH_3I builds up and falls a few months earlier than shown by the observations, suggesting some uncertainty in the CH_3I source in the mid-latitude spring and autumn.

At mid-latitude stations (Cape Grim, Cape Ochiishi, Happo and Tsukuka) the summertime maximum in CH_3I suggests that the large sources dominate over the increased photochemical loss. Higher emissions of CH_3I in the summer are driven by seasonal maximum in SST (Yokouchi *et al.*, 2008) and oceanic productivity (Rasmussen *et al.*, 1982). Simulation **IORG** compares well with observations at most of the mid-latitude sites. The very high CH_3I mixing ratios observed at Tsukuba might reflect terrestrial sources (e.g. rice fields) (Yokouchi *et al.*, 2008) that are not included in the model. Similarly, at Cape Ochiishi the high CH_3I mixing ratios may reflect transport of inland-sourced air masses (Yokouchi *et al.*, 2008).

In the tropics, there is little seasonality in CH_3I due to low variability in the sources and sinks. At San Cristobal simulation **IORG** slightly underestimates the observed CH_3I in the spring.

The overall comparison of the modelled CH_3I and observed CH_3I shows the model does a fine job. At stations where there is a large difference in observed and modelled CH_3I (e.g. Tsubuka) the difference can be explained by terrestrial-based sources not included in the model.

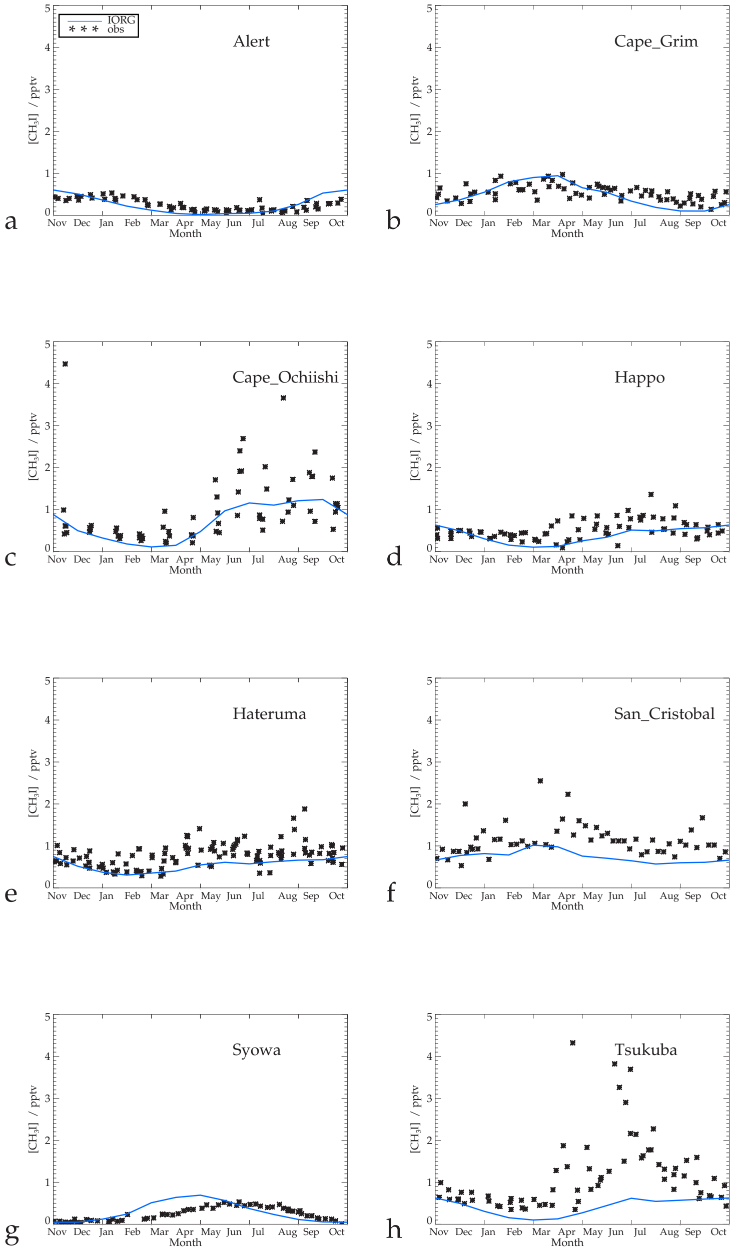

Figure 5.15: Monthly mean modelled CH_3I (pptv) in run **IORG** compared to flask sampling observations of CH_3I (not monthly mean) at 8 remote measurement stations. (a) Alert [82.5°N, 62.5°W], (b) Cape Grim [40.4°S, 144.6°E], (c) Cape Ochiishi [43.2°N, 145.5°E], (d) Happo Ridge [36.7°N, 137.8°E], (e) Hateruma Island [24.1°N, 123.8°E], (f) San Cristobal [1.0°S, 89.4°W], (g) Syowa [68.5°S, 41.3°E] and (h) Tsukuba [36.0°N, 140.1°E]. Observations taken from Yokouchi *et al.* (2008).

The observed and simulated monthly mean daytime and maximum IO at CVAO are shown in Figure 5.16. The observations show 1 to 2 pptv dayime IO with no clear seasonal variation. Due to the fairly coarse model resolution (2.8° in horizontal), the simulation **I** was highly sensitive to the inorganic iodine flux in the CVAO region, probably because of the site's close proximity to the west coast of Africa. Also, the transport of air masses containing higher levels of ozone associated with emissions of NO_x from biomass burning over Africa during December and January may drive a large localised inorganic iodine flux. The crude assumption of a simple linear dependence of the inorganic iodine flux proportional to ozone deposition does not take into consideration any limitations in other reactants controlling the flux. For this reason, simulation **I** includes an inorganic source of iodine to the west of CVAO in the mid-tropical North Atlantic Ocean. The modelled IO from run **I** shown in Figure 5.16 is for a location within this restricted source zone, [16.85°N, 36.87°W] in a different grid box to the West of CVAO. Figure 5.16 shows emissions of organic iodine compounds can explain roughly 0.1 pptv of daytime IO at CVAO. Mahajan *et al.* (2010) used a column model to argue the organic iodine fluxes observed in the vicinity of CVAO during the RHaMBLE cruise detailed in Jones *et al.* (2010) could explain up to 0.5 pptv of daytime IO. This suggests that although CH_3I mixing ratios compare well, other source gases may not be adequately represented by the methodology used for emissions of CH_3I. When the additional inorganic source of iodine is included in simulation **I** the modelled daytime mean IO increases to 0.4 pptv. The modelled daytime IO better reproduces the observations when an inorganic flux of iodine is included. Given current observed organic iodine fluxes it is unlikely that organic iodine fluxes alone can explain IO mixing ratios larger than 1 pptv as observed at CVAO. An alternative explanation for the low IO at CVAO may be that the sinks in the model are too high. Iodine chemistry remains uncertain, the kinetics and mechanisms by which inorganic iodine compounds form new particles, removing iodine from the gas phase is also subject to ongoing debate.

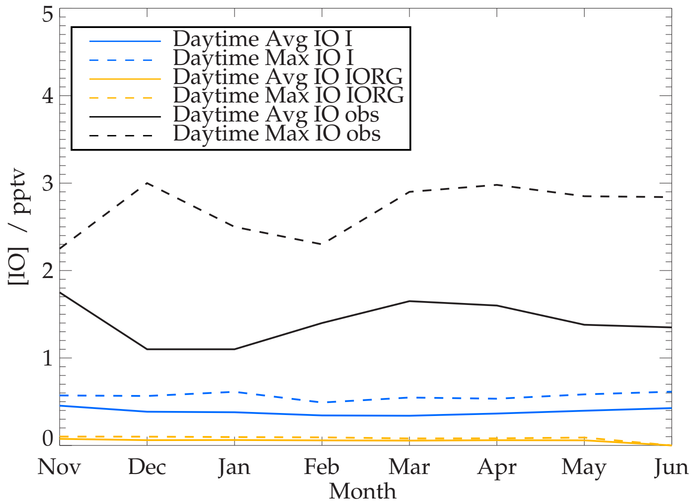

Figure 5.16: Monthly mean and maximum observed and modelled IO mixing ratios (pptv) in runs **IORG** and **I** in the tropical North Atlantic Ocean [16.85°N, 26.87°W]. Observations taken from Read *et al.* (2008).

5.6 Impact of Iodine on Daytime Ozone Loss

In Chapter 4 it was shown that model simulations including bromine chemistry were unable to reproduce the observed daytime ozone loss at CVAO. Emissions of iodine compounds may represent an important additional daytime ozone sink in the remote marine atmosphere as discussed by Read *et al.* (2008), hence their impact on ozone at CVAO in the updated TOMCAT model is worth investigating. Figure 5.17 shows the simulated monthly mean diurnal ozone loss in simulations **NOBRI**, **NOI** and **IORG** at CVAO from November 2006 to June 2007. The introduction of iodine chemistry increases the simulated daytime ozone loss from an average of 0.96 ppbv day $^{-1}$ in simulation **NOI** to 1.47 ppbv day $^{-1}$ in simulation **IORG** improving the agreement with observations.

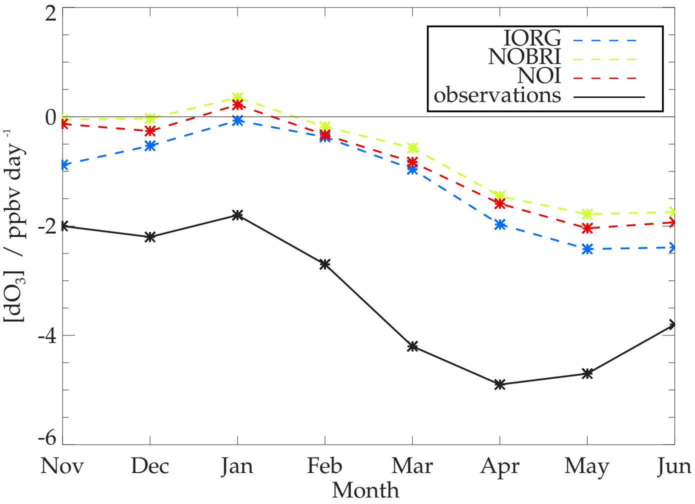

Figure 5.17: Monthly mean observed and modelled daytime ozone loss (ppbv day^{-1}) in runs **IORG**, **NOBRI** and **NOI** at Cape Verde Atmospheric Observatory [16.85°N, 24.87°W]. Observations taken from (Read *et al.*, 2008).

The 0.51 ppbv day^{-1} (53%) increase in daytime ozone loss in simulation **IORG** compared to **NOI** shows the potential for low levels of IO ($\sim$0.1 pptv) to provide a sink for ozone. It is important to note this additonal ozone sink may not be simply due to IO alone but may also be attributable to iodine chemistry amplifying the effect of bromine chemistry by speeding-up the reformation of atomic bromine through the reactions 5.8 and 5.9.

$$IO + BrO \longrightarrow IBr + O_2 \tag{5.8}$$

$$IBr + hv \longrightarrow I + Br \tag{5.9}$$

Read *et al.* (2008) estimates IO and BrO together contribute between 1.0 and 2.0 ppbv day^{-1} of ozone loss. Figure 5.17 shows BrO and IO contribute beween 0.3 and 1.0 ppbv day^{-1}. Clearly, the underestimate in daytime IO mixing ratios provides an important explanation for the underprediction.

Figure 5.17 shows the inclusion of iodine and bromine chemistry results in larger modelled daytime ozone loss at CVAO which improves agreement with observations. However, the observed daytime ozone loss at CVAO is still under predicted in simulation **IORG**by 1.82ppbv day^{-1}. This under prediction can be explained by an overestimate in the NO mixing ratio (see Figure 4.15) in the region in the model which inhibits photochemical ozone destruction and also an underestimate in daytime IO (Figure 5.16). In Figure 5.16 it was shown the modelled IO agrees better with observations when an inorganic source of iodine is considered, as in simulation **I**. In order to address the effect of the higher IO, the simulated daytime ozone loss is now compared at a location west of CVAO in the tropical North Atlantic Ocean [16.85°N, 36.87°W]. This location may provide a more conclusive test to get the model's capability for capturing the observed daytime ozone loss because modelled NO concentrations are lower than at CVAO and compares better with observations there (Figure 5.18).

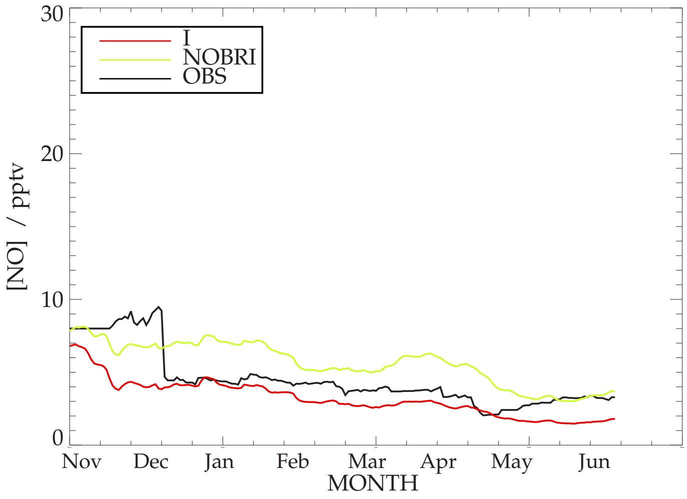

Figure 5.18: Observed and modelled daytime NO mixing ratios taken as an average over a 30-day period in runs **I** and **NOBRI** in the tropical North Atlantic Ocean [16.85°N, 36.87°W]. Observations are for CVAO [16.85°N, 24.87°W] and taken from (Lee *et al.*, 2009b).

Figure 5.19 shows the simulated monthly mean daytime ozone loss in simulations **NOBRI**, **IORG** and **I** in the tropical North Atlantic Ocean from November 2006 to June 2007. The modelled daytime ozone loss is compared against the observations from CVAO because that site is thought to be representative of the background tropical Atlantic Ocean. The lower NO mixing ratios at this location in the model compared to CVAO result in larger average daytime ozone loss in simulation **NOBRI** (1.44 ppbv day^{-1}), but still under predicts the observed average daytime ozone loss by 1.85 ppbv day^{-1} during the observation period. The inclusion of bromine and iodine chemistry increases daytime ozone loss at this location and improves the comparison with the observations. In simulation **IORG** an average daytime ozone loss of 2.14 ppbv day^{-1} is predicted. The additional ∼0.3 pptv IO in simulation **I** increases the average daytime ozone loss to 2.35 ppbv day^{-1} compared to simulation **IORG**. From November to January all the observed daytime O_3 loss is

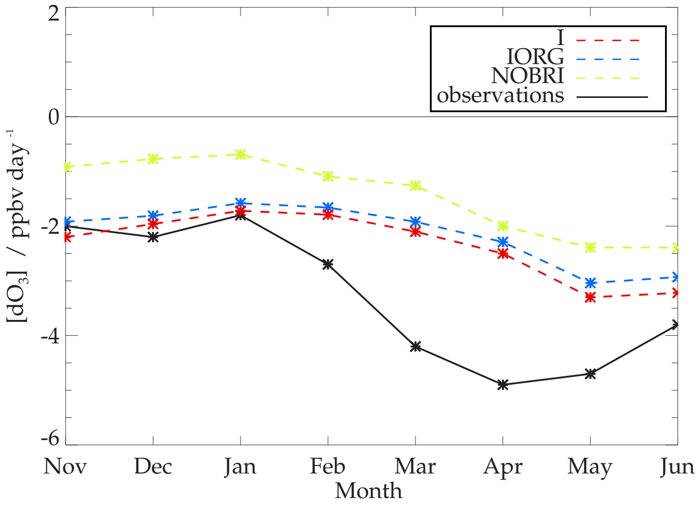

Figure 5.19: Monthly mean observed and modelled daytime ozone loss (ppbv day^{-1}) in runs **IORG** and **I** in the tropical North Atlantic Ocean [16.85°N, 36.87°W]. Observations are for CVAO [16.85°N, 24.87°W] and taken from (Read *et al.*, 2008).

reproduced by simulations **IORG** and **I** (Figure 5.19). Given that daytime mixing ratios of IO are underestimated in the model during this period (Figure 5.16) it is likely that the balance of ozone loss due to the different cycles is probably not correct. The lower NO mixing ratio in simulation **I** suggests that photochemical ozone loss is likely to be too high.

The mean daytime observed and simulated halogen oxide (XO) mixing ratios and their absolute contribution to the daytime ozone loss in this modelling study compared to the box model in Read *et al.* (2008) are shown in Figure 5.20. The total XO contribution to daytime ozone loss in TOMCAT is calculated as the difference in daytime ozone loss between simulations **I** and **NOBRI**.

The TOMCAT XO mixing ratio and ozone loss is taken from the tropical North Atlantic site rather than CVAO. Modelled BrO mixing ratios compare well with the observations (See Figure 4.6) but IO is underestimated by $\sim$ 1.0 pptv (see figure 5.16). The predicted ozone loss due to XO in simulation **I** is underestimated compares to the box model in Read *et al.* (2008) from November to January ($\sim$1.96 ppbv day^{-1}) even though IO mixing ratios are under predicted. This can be explained by the decrease in NO between simulations **NOBRI** and **I** (Figure 5.18) which results in enhanced photochemical ozone loss in simulation **I** during this period. The potential for XO to provide a sink for NO_x has previously been reported in Keene *et al.* (2009) who showed the inclusion of halogens significantly reduces daytime NO_x and NO mixing ratios. From February to June the modelled contribution of XO to daytime ozone loss in simulation **I** is lower than predicted by the box model in Read *et al.* (2008), which is likely to be explained by the underestimate in IO during these months (Figure 5.16).

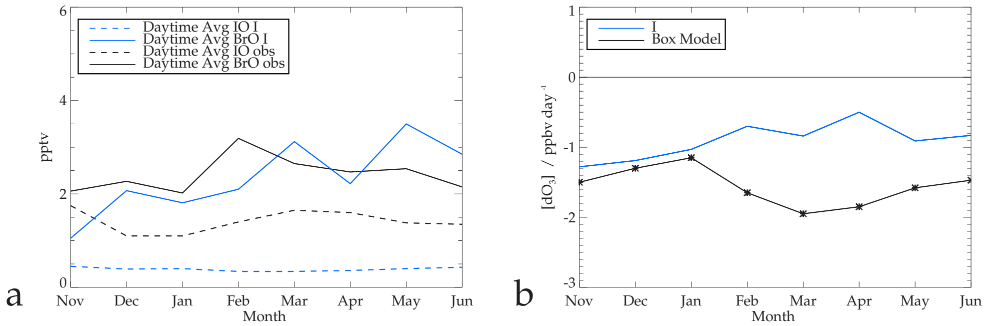

Figure 5.20: (a) Monthly mean observed and modelled daytime BrO and IO mixing ratios in simulation **I**. Observations are for CVAO [16.85°N, 24.87°W] and taken from (Read *et al.*, 2008). (b) Monthly mean modelled daytime ozone loss due to XO (ppbv day^{-1}) in simulation **I** in the tropical North Atlantic Ocean [16.85°N, 36.87°W] compared to that predicted by the box model in Read *et al.* (2008).

5.7 Impact of Iodine on Global Ozone Budgets

The potential for iodine species to impact tropospheric ozone has been reported by previous studies (Chameides & Davis, 1980). In this section the changes to the global ozone budgets between the **NOI** and **IORG** simulations are presented and discussed. Figure 5.21 shows the percentage change in monthly mean surface ozone between simulations **NOI** and **IORG** in January, April, July and October. In the tropics between 15°N and 15°S surface ozone is simulated to decrease by between 0.25 and 4.0% during all months. The western and central Pacific Ocean shows the largest

% decrease in O_3. At mid-high latitudes in the SH ozone mixing ratios decrease by between 0 and 3% in the winter but in the summer show a smaller decrease. The seasonal pattern in O_3 loss is consistent with the emissions of organic iodine species whcih show a summer maximum. Figure 5.21 shows monthly mean ozone mixing ratios around CVAO show a 0.24 - 1% change. It is important to note that the predicted IO in simulation **IORG** is over 1.0 pptv lower than observations in the tropical East Atlantic Ocean (See Figure 5.16). Figure 5.22 shows the percentage change in zonally averged monthly mean ozone between simulations **NOI** and **IORG** in January, April, July and October. A similar pattern is shown in the zonal mean plots to the surface plots. Ozone decreases by between 0.25 and 3.0%. The largest decreases in O_3 are simulated in the SH during the summer (2-3%). The decrease in ozone is smaller in NH throughout the year.

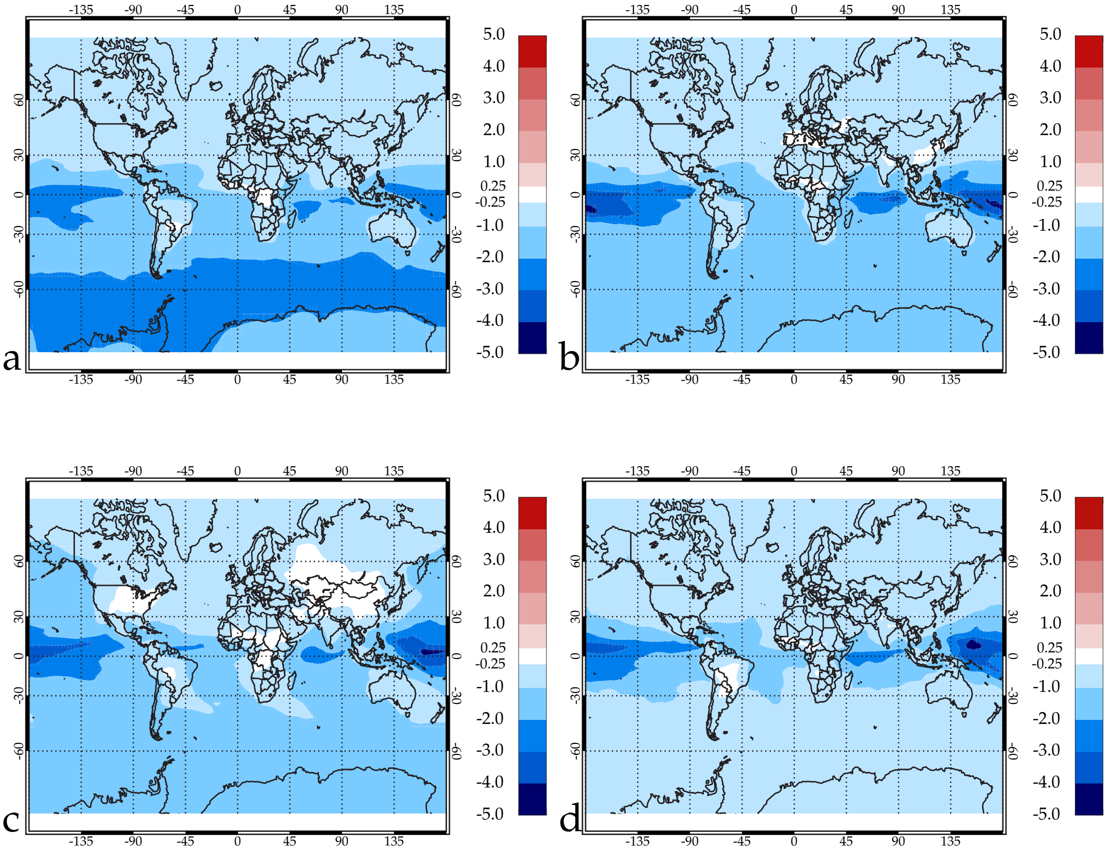

Figure 5.21: Surface percentage change in monthly mean ozone between runs **NOI** and **IORG** during (a) January, (b) April, (c) July and (d) October.

To better understand the changes in the ozone between the **NOI** and **IORG** simulations, Table 5.4 shows the ozone budgets for the two simulations compared to previous published studies. The results are for an annual simulation for 2007 and not 2004 as reported in the Chapter 4.

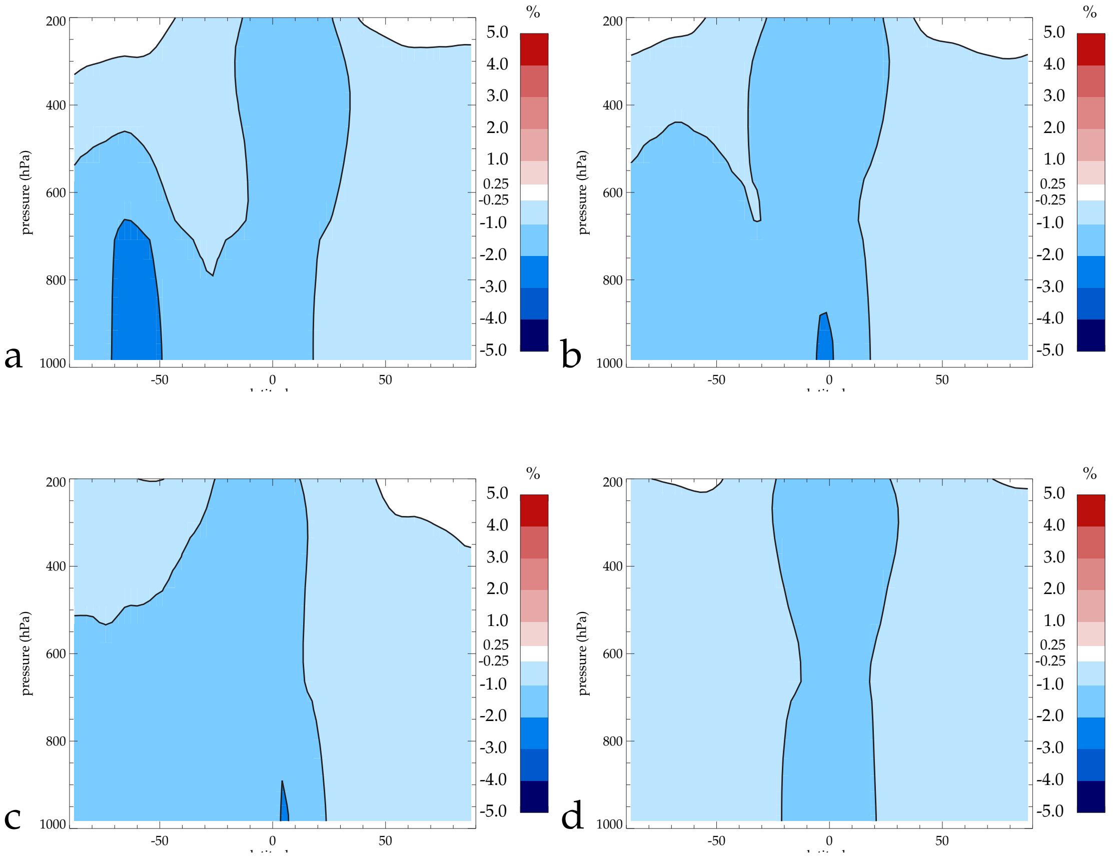

Figure 5.22: Zonally averaged percentage change in monthlymean ozone between runs **NOI** and **IORG** during (a) January, (b) April, (c) July and (d) October.

The use of different years explains why the ozone burden reported in simulation **NOI** here is 318 Tg O_3 compared to 315 Tg O_3 for simulation **BR** in Chapter 4. The simulations show the introduction of iodine chemistry in simulation **IORG** decreases the ozone burden compared to the **NOI** simulation by 3 Tg O_3 (1.0%). Simulation **IORG** shows the main pathway for ozone loss is the reaction of I_2O_2 with O_3 (142 Tg O_3 yr^{-1}), followed by IO + HO_2 (46 Tg O_3 yr^{-1}). The total iodine and bromine sink for ozone is 381 Tg O_3 yr^{-1} in simulation **IORG**. The introduction of iodine chemistry results in a decrease in the lifetime of ozone in the troposphere from 23.8 days in simulation **IORG** to 22.9 days in simulation **IORG**.

Table 5.4: Ozone burdens and budgets in the **NOI**, **IORG** simulations and previous published studies.

	NOI	**IORG**	**S04**	**S06**
Ozone Burden (Tg O_3)	318	315	273	340 ±40
Ozone Chemical Sources (Tg O_3 yr^{-1})				
NO + HO_2	3169	3171	3393	
NO + CH_3O_2	797	801	876	
NO + Other	404	406	706	
Total Chemical Sources	4370	4378	4975	5060±570
Ozone Stratosphere flux (Tg O_3 yr^{-1})	NA	NA	395	520±200
Ozone Chemical Sinks (Tg O_3 yr^{-1})				
O^1D + H_2O	1492	1476	2355	
O_3 + HO_2	1006	991	1224	
Other	731	727	841	
BrO + HO_2	143	142		
$BrONO_2$ + Aerosol	20	20		
BrO + Other	27	27		
Total Bromine sinks	190	189		
IO + HO_2		46		
O_3 + I_2O_2		142		
IO + Other		4		
Total Iodine sinks		192		
Total Br + I sinks	190	381		
Total Chemical Sinks	3419	3575	4421	4560±720
Dry Deposition (Tg O_3 yr^{-1})	1451	1441	949	1010±220
Ozone Lifetime (days)	23.8	22.9	18.6	22.3±2.0

S04=Stevenson *et al.* (2004), **S06**=Stevenson *et al.* (2006)

5.8 Conclusions

This chapter presented results from a coupled size-resolved aerosol and chemistry model with a description of bromine and iodine chemistry. These results are the first attempts at global tropospheric iodine modelling and the work included significant development of the model chemistry scheme and parameterisation of emissions. Flux estimates for iodocarbon emissions are in agreement with emission estimates determined from observations. The model compares well with methyl iodide measurements at 8 remote stations, capturing the seasonality in the observations.

Simulated iodine distributions show high I_y in the tropics throughout the year, consistent with a large organic iodine source. High I_y mixing ratios are also predicted in the summer, due to large sources of organic iodine compounds associated with peak oceanic productivity and sea surface temperatures. The model predicts HOI is the dominant fraction of inorganic iodine in most of the troposphere (30-50%). IO represents only 0-20% of I_y and IBr and $IONO_2$ contribute the largest fraction in the high latitude winter. In the high latitude southern hemisphere summer the dominant fraction of I_y is I. This is explained by lower ozone and HO_2 mixing ratios and lower temperatures in the SH. The low ratio of IO to I_y shows the lack of constraint of I_y chemistry provided by current observations.

A comparison with measurements of the mean observed daytime IO at the Cape Verde Atmospheric Observatory (CVAO) shows the model is unable to reproduce the observations when only organic iodine compound emission fluxes are included (IO $\sim$0.1 pptv). This suggests an additional source of reactive iodine species is required to explain the observations of daytime IO. When an inorganic source of iodine was included assumed to be 0.05% of the ozone dry deposition flux to the ocean surface the modelled daytime IO in the tropical North Atlantic Ocean increased to 0.4 pptv, however this still underestimates the observed IO at CVAO by 1.0 pptv.. This inorganic iodine flux had to be constrained to the tropical North Atlantic Ocean as the model was sensitive to the location and magnitude of the inorganic flux suggesting uncertainties in the precise mechanism controlling the flux.

The introduction of iodine and bromine chemistry improved the agreement between modelled and observed daytime ozone loss at CVAO. In simulations without halogen chemistry the model predicted 1.44 ppbv day^{-1} daytime ozone loss compared to the observed loss of 3.29 ppbv day^{-1}. The inclusion of iodine and bromine chemistry increased the modelled daytime ozone loss to 2.35 ppbv day^{-1}. The results from this chapter suggest reactive halogen chemistry is important for controlling daytime ozone loss over the remote marine ocean. However, there remain large uncertainties in the sources and chemistry of iodine compounds in the atmosphere which must be better understood in order to fully understand and quantify the importance of iodine chemistry in the troposphere.

Globally the introduction of organic iodine emissions decrease the global ozone burden by 3.0 Tg O_3 (1.0%) from 318 Tg O_3 to 315 Tg O_3. The global ozone field decreases in the tropics by 0.25-4.0%. At mid and high latitudes in the SH ozone decreases by between 1.0 and 3.0% with the largest decreases simulated during the summer. The simulations show the main iodine sink for ozone is the reaction of I_2O_2 with O_3 and subsequent loss to aerosol. HO_2 + IO is the second most important ozone loss pathway.

The results from this chapter suggest reactive halogen chemistry is important for controlling daytime ozone loss over the remote marine ocean. Simulated IO mixing ratios are underestimated in the model and this represents an important source of uncertainty in underestanding these results. Furthermore, there remain large uncertainties in the sources and chemistry of iodine compounds in the atmosphere which must be better understood in order to fully understand and quantify the importance of iodine chemistry in the troposphere. The source parameterizations used in this work require significant future developement to better capture the processes. A key limitation of the work presented in this chapter is the assumption that the SeaWiFs satellite instrument provides a measure of oceanic productivity. This instrument actually provides a measure of ocean colour. When a better indicator of productivity with global coverage becomes available this metric should be used. Furthermore a number of iodine source processes remain poorly understood and are the subject of ongoing laboratory research. Finally, more obsverations of iodine species, both organic and inorganic are required to test simulated distributions of iodine species.

Chapter 6

Conclusions

In this thesis a size-resolved aerosol microphysics module (GLOMAP) has been coupled to a detailed 3-D Eulerian offline chemical transport model (TOMCAT). The newly developed coupled model has also been extended to include a bromine and iodine chemistry scheme. The new coupled model therefore simulates interactions between halogens, oxidants and aerosol in the troposphere.

The model developed in this work is one of the first global coupled chemical and size-resolved aerosol models to include a description of halogen chemistry. This has allowed an investigation of how emissions of bromine and iodine species impact oxidising capacity and aerosol formation in the remote marine atmosphere and potential feedbacks within this system. Such studies have not been possible with previous models.

6.1 Summary of Results

The major findings of this work are now summarised with reference to the aims of this thesis in Section 1.3.

1. The GLOMAP aerosol microphysics model (Spracklen *et al.*, 2005a) has been coupled to the TOMCAT CTM (Chipperfield, 2006) to allow for interactions between sulfur chemistry, aerosol and oxidants.

(a) The coupled model captures spatial and temporal variations is DMS, SO_2 and ${SO_4}^{2-}$ in agreement with previous modelling studies. Improved comparisons with observations are predicted by the coupled model for DMS, SO_2 and ${SO_4}^{2-}$ at some stations but not all.

(b) In the northern hemisphere (NH) winter cloud condensation nuclei (CCN) number concentrations increase by 12-36% in the coupled model. This is due to increased oxidant limitation in the NH winter which acts to re-distribute sulfate mass from existing accumulation mode particles to growth of Aitken mode particles, resulting in an increased number of smaller CCN.

(c) In the coupled model DMS represents an important sink for NO_3 over the remote ocean. Over the main continental industrial regions large depletions in H_2O_2 are simulated during the NH winter because of high SO_2 emissions as previously reported by Roelofs *et al.* (1998).

(d) The reaction of N_2O_5 + H_2O on aerosol and cloud droplets provides an important sink for NO_x. Zonally averaged NO_x mixing ratios decrease by >40% during winter in the NH. Smaller decreases in NO_x (20-40%) in the SH winter are simulated because of lower available aerosol surface area. The reduction in NO_x impacts on the production of ozone, decreasing ozone mixing ratios by up to 9-12% in the NH winter. The simulated ozone loss in the NH winter is lower than that predicted by Dentener & Crutzen (1993) but in agreement with Tie *et al.* (2001).

2. A bromine chemistry scheme has been implemented in the model and used to investigate the impact on oxidising capacity and aerosol formation in the troposphere.

(a) Simulated bromine fields and Br_y speciation are in agreement with the previous global modelling study of Yang *et al.* (2005). Maximum Br_y is simulated in the North Atlantic in winter.

(b) Modelled BrO captures 65% of the daytime mean observed BrO at the surface at the Cape Verde Atmospheric Observatory (CVAO) in the tropical East Atlantic Ocean. However, modelled daytime ozone loss at CVAO is significantly underestimated compared to observations.

(c) Bromine chemistry results in a 24% decrease in ozone in the southern hemisphere (SH) summer. Large decreases in zonally averaged NO_x (>80%) and HO_x (32-40%) mixing ratios are simulated in the NH winter in regions with high aerosol loading.

(d) BrO is a globally significant oxidant for DMS contributing 36% of the total DMS sink. NO_3 contributes 19% and OH 45%. Inclusion of BrO reduces the DMS lifetime and burden by 42%.

(e) The inclusion of bromine chemistry results in a decrease in zonally averaged CCN number concentrations of 10-25% over the SH oceans during the summer months. When only CCN formation attributable to DMS emissions is accounted for the reduction in CCN is 27-42%.

(f) The response in CCN to increases in DMS is controlled by chemical feedbacks involving HO_x, NO_x, sea salt and BrO. A reactive bromine chemistry feedback involving enhanced uptake of DMS-sourced SO_2 onto sea salt acts to suppress the response in CCN to increases in DMS by favouring the growth of existing aerosol over formation of new aerosol particles.

(g) The global tropospheric ozone burden decreases by 26 Tg O_3 (7.8%) in the bromine simulation. The main bromine loss pathways for ozone are HO_2 + BrO (130 Tg O_3 yr^{-1}) and $BrONO_2$ + aerosol (18 Tg O_3 yr^{-1}).

3. An iodine chemistry scheme has been included and its impact on oxidising capacity and aerosol formation investigated.

(a) Modelled CH_3I concentrations reproduce the magnitude and seasonality shown by observations.

(b) The simulated IO:I_y ratio is less than 20% and shows the lack of constraint of I_y chemistry provided by current observations.

(c) Modelled IO at CVAO is underestimated compared to observations when only emissions of organic iodine fluxes are included, in agreement with Mahajan *et al.* (2010). If an inorganic flux of I_2 is included (as 0.05% of the ozone deposited to the ocean surface) a daytime IO mixing ratio of 0.4 pptv is simulated.

(d) The inclusion of iodine chemistry results in larger simulated daytime ozone loss in the tropical North Atlantic Ocean and improves the agreement with observations at CVAO.

(e) The global tropospheric ozone burden decreases by 3.0 Tg O_3 (1.0%) in the organic iodine emissions simulation. The main iodine loss pathways for ozone are I_2O_2 + O_3 (142 Tg O_3 yr^{-1}) and HO_2 + IO (46 Tg O_3 yr^{-1}).

6.2 Synthesis

This work has demonstrated the importance of the interactive treatment of oxidants in models for controlling aerosol formation in the troposphere. Oxidant depletions driven by DMS-NO_x-HO_x-O_x interactions in the coupled model result in an increased DMS burden and lifetime compared to the uncoupled model. Large increases in SO_2 during the NH winter are simulated over SO_2 source regions such as East Asia, North America and Europe in the coupled model. This is due to depletions in H_2O_2, the primary SO_2 oxidant. The changes in DMS and SO_2 oxidation impact the formation of sulfate aerosol and (CCN) number concentrations. Zonally averaged CCN number concentrations increase by 3-36% as the increased oxidant limitation in the coupled model acts to re-distribute sulfate mass from existing accumulation mode particles to growth of Aitken mode particles, resulting in an increased number of smaller CCN.

The first simulations of the heterogeneous reaction of N_2O_5 + H_2O on aerosol and cloud droplets in TOMCAT show this reaction is an important sink for NO_x in the wintertime. Higher fractional loss is simulated in the NH (>40%) than the SH (20-40%) because of higher aerosol loadings in the north and conditions favourable to N_2O_5 formation. Ozone mixing ratios decrease by 9-12% in the NH winter in response to the enhanced NO_x sink.

The impact of bromine chemistry on oxidising capacity, DMS oxidation and marine aerosol formation has been examined. The model captures the magnitude and spatial distribution of observed troposphere column BrO as observed by satellites. Also, 65% of the observed monthly mean daytime BrO at the Cape Verde Atmosphereic Observatory is predicted throughout the period from November to June. During the spring months the model predicts 85% of the observed daytime BrO. Emissions of bromine species are found to strongly perturb oxidising capacity by providing a sink for ozone, HO_x and NO_x. The global tropospheric ozone burden decreases by 26 Tg O_3 (7.8%) in the bromine simulation. The main bromine loss pathways for ozone are HO_2 + BrO (130 Tg O_3 yr^{-1}) and $BrONO_2$ + aerosol (18 Tg O_3 yr^{-1}). BrO is also found to contribute a significant fraction of global DMS oxidation (36%) with the largest contribution over the SH oceans (>50%). The large contribution of BrO to DMS oxidation reduces CCN number concentrations in the SH summer because the oxidation products favour growth of existing aerosol over formation of new aerosol. Furthermore, this work has identified a possible DMS-sea salt-oxidant feedback in the remote marine atmosphere that may control the response of CCN to increases in DMS. Higher DMS emissions increase acidification of sea salt aerosol and subsequently result in a higher source of Br_2 from sea salt in the SH summer. This feedback acts to increase the fractional oxidation of DMS by BrO and suppress the response in CCN to increases in DMS.

This work has also presented the first attempt at global modelling of iodine in the troposphere. The modelled seasonality of methyl iodide compares well with surface observations. Simulated distributions and speciations of I_y show HOI to be the largest component of I_y (30-50%) in the troposphere with IO representing 0-20% of I_y. Modelled IO is underestimated compared to observations at CVAO in the tropical East Atlantic when only organic iodocarbon fluxes are included suggesting an inorganic source is also required. This work also shows the inclusion of bromine and iodine chemistry results in larger simulated daytime ozone loss in the tropical North Atlantic Ocean and improves the comparison with observations from the CVAO, suggesting BrO and IO are an important sink for ozone in this region. The global tropospheric ozone burden decreases by 2 Tg O_3 (0.6%) in the organic iodine emissions simulation. The main iodine loss pathways for ozone are I_2O_2 + O_3 (158 Tg O_3 yr^{-1}) and HO_2 + IO (46 Tg O_3 yr^{-1}).

6.3 Implications for Future Work

This work has identified feedbacks between emissions of DMS, oxidants and the source of bromine from sea salt, which are important for controlling marine aerosol formation in the SH. These results emphasise the need for an improved observation network of seawater and atmosphere DMS concentrations. A wider network for measuring BrO concentrations and sea salt bromide depletions is required to improve our understanding of reactive bromine chemistry. There also remains potential for improvement in aerosol phase cycling and treatment of bromine release from sea salt. The importance of biologically enhanced sea salt alkalinity Sievering *et al.* (2004) and organic coatings (Gill *et al.*, 1983) on the surface of sea salt for impacting bromine release and SO_2 oxidation should be further investigated. A key uncertainty surrounding DMS for laboratory studies to address is the oxidation pathways of DMS, particulary if DMSO can form SO_2. Also, this work suggests model simulations that use prescribed oxidant fields to drive aerosol formation are incapable of capturing these feedbacks. A coupled oxidant treatment of bromine chemistry should be included in all future modelling studies of the marine sulfur cycle as this impacts aerosol formation and aerosol-climate interactions.

The first global simulations of iodine chemistry in the troposphere underestimate IO over the tropical Atlantic Ocean compared to observations when only organic iodine sources are accounted for, suggesting an additional inorganic source of iodine may be missing. A crude treatment of inorganic iodine emissions improved simulated IO compared to observations. However, the precise mechanism controlling this inorganic iodine source remains highly uncertain and must be better understood for the importance of reactive iodine chemistry and its impact on oxidising capacity to be better quantified.

Important limitations of this work are the use of fixed cloud fields in horizontal and vertical space in TOMCAT throughout the year. This assumption is an over simplification and is likely to impact photochemistry and the models ability to represent chemical processes. The DMS oxidation scheme used in this study is simple, better treatment of DMS oxidation and its products could be achieved by implementing a more detailed scheme that includes a higher number of reactions and treating more intermediate species in the oxidation chain. In particular, the introduction of bromine chemistry increases the importance of the DMS addition pathway and a more detailed treatment of DMSO to account for uptake to aerosol should be implemented. The treatment of the HBr + HOBr heterogeneous reactions could also be improved. The current method does not adequately represent the diurnal behaviour of HOBr according to detailed box modelling studies because HBr is limiting in the recycling process. Also, the use of the SeaWiFs satellite instrument observations of ocean colour used as an indicator of oceanic productivity is an assumption that can be improved. When a better indicator of oceanic productivity becomes available from satellite this metric should be used.

Appendix A

List of Reactions in the Coupled TOMCAT-GLOMAP Bromine and Iodine Model

Table A.1: Chemical Species in the TOMCAT CTM

Category	Species
Shorter	O_x (= O_3 + O(^3P) + O(^1D)), H_2O_2
lived species	NO_x (= NO + NO_2), NO_3, N_2O_5,
	HNO_3, HO_2NO_2, HONO,
	PAN, PPAN, $MeONO_2$,
	HCHO, MeOOH, MeCHO, Me_2CO,
	C_2H_6, EtOOH, EtCHO, C_3H_8, n-PrOOH, i-PrOOH,
	C_5H_8, C_2H_4, C_2H_2, ISOOH, ISON, MACR,
	MACROOH, MPAN, HACET, MGLY, NALD, HCOOH,
	$MeCO_3H$, $MeCO_2H$, MeOH,
	SO_2, H_2SO_4, DMSO, MSA, H_2S,
	Br_x (= Br_2 + BrO),
	HBr, HOBr, Br, $BrNO_3$, $BrNO_2$
Steady-state	OH, HO_2, MeO_2, EtO_2,
	$MeCO_3$, $EtCO_3$, n-PrOO, i-PrOO,
	$MeCOCH_2OO$, $MeCOCH_2OOH$,
	ISO_2, $MACRO_2$
Source gases	CH_4, CO
	DMS, COS, CS_2,
	CH_3Br, $CHBr_3$, CH_2Br_2,
	CH_2BrCl, $CHBr_2Cl$, $CHBrCl_2$,
Fixed	O_2, N_2, H_2, CO_2
Analyses	H_2O
Stratosphere tracers	OS, O(^{1}D)S, O(^{3}P)S, O_3S, NO_XS, HNO_3S, NO_YS

Me=CH_3, Et=C_2H_5, Pr= C_3H_7

Table A.2: CTM Gas-Phase Bimolecular Reactions

Reaction	Reactants	Products	Rate (cm^3 $molecule^{-1}$ s^{-1})	Reference
1	HO_2 + NO	→ OH + NO_2	k=3.60x10^{-12} exp(270/T)	IUPACC [2006]
2	HO_2 + NO_3	→ OH + NO_2	k=4.00x10^{-12} exp(0.0/T)	IUPACC [2006]
3	HO_2 + O_3	→ OH + O_2	see [1]	IUPACC [2006]
4	HO_2 + HO_2	→ H_2O_2	k=2.20x10^{-13} exp(600/T)	IUPACC [2006]
5	HO_2 + MeOO	→ MeOOH	k=3.80x10^{-13} exp(780/T)	IUPACC [2006]
6	HO_2 + MeOO	→ HCHO	k=3.80x10^{-13} exp(780/T)	IUPACC [2006]
7	HO_2 + EtOO	→ EtOOH	k=3.80x10^{-13} exp(900/T)	IUPACC [2006]
8	HO_2 + $MeCO_3$	→ $MeCO_3H$	k=2.08x10^{-13} exp(980/T)	IUPACC [2006]
9	HO_2 + $MeCO_3$	→ $MeCO_2H$ + O_3	k=1.04x10^{-13} exp(980/T)	IUPACC [2006]
10	HO_2 + $MeCO_3$	→ OH + MeOO	k=2.08x10^{-13} exp(980/T)	IUPACC [2006]
11	HO_2 + n-PrOO	→ n-PrOOH	k=1.51x10^{-13} exp(1300/T)	MCM
12	HO_2 + i-PrOO	→ i-PrOOH	k=1.51x10^{-13} exp(1300/T)	MCM
13	HO_2 + $EtCO_3$	→ O_2 + $EtCO_3H$	k=3.05x10^{-13} exp(1040/T)	MCM
14	HO_2 + $EtCO_3$	→ O_3 + $EtCO_2H$	k=1.25x10^{-13} exp(1040/T)	MCM
15	HO_2 + $MeCOCH_2OO$	→ $MeCOCH_2OOH$	k=1.36x10^{-13} exp(1250/T)	MCM
16	MeOO + NO	→ HO_2 + HCHO + NO_2	k=2.95x10^{-12} exp(285/T)	IUPACC [2006]
17	MeOO + NO	→ $MeONO_2$	k=2.95x10^{-15} exp(285/T)	IUPACC [2006]
18	MeOO + NO_3	→ HO_2 + HCHO + NO_2	k=1.30x10^{-12} exp(0.0/T)	IUPACC [2006]
19	MeOO + MeOO	→ MeOH + HCHO	k=1.03x10^{-13} exp(365/T)	IUPACC [2006]
20	MeOO + MeOO	→ $2HO_2$ + 2HCHO	k=1.03x10^{-13} exp(365/T)	IUPACC [2006]
21	MeOO + $MeCO_3$	→ HO_2 + HCHO + MeOO	k=1.80x10^{-12} exp(500/T)	IUPACC [2006]
22	MeOO + $MeCO_3$	→ $MeCO_2H$ + HCHO	k=2.00x10^{-13} exp(500/T)	IUPACC [2006]
23	EtOO + NO	→ MeCHO + HO_2 + NO_2	k=2.60x10^{-12} exp(380/T)	IUPACC [2006]
24	EtOO + NO_3	→ MeCHO + HO_2 + NO_2	k=2.30x10^{-12} exp(0.0/T)	IUPACC [2006]
25	EtOO + $MeCO_3$	→ MeCHO + HO_2 + MeOO	k=4.40x10^{-13} exp(1070/T)	IUPACC [2006]
26	$MeCO_3$ + NO	→ MeOO + CO_2 + NO_2	k=7.50x10^{-12} exp(290/T)	IUPACC [2006]
27	$MeCO_3$ + NO_3	→ MeOO + CO_2 + NO_2	k=4.00x10^{-12} exp(0.0/T)	MCM

Continued on next page

Table A.2 – continued from previous page

Reaction	Reactants	Products	Rate (cm^3 $molecule^{-1}$ s^{-1})	Reference
28	n-PrOO + NO	→ EtCHO + HO_2 + NO_2	$k=2.90x10^{-12}$ exp(350/T)	IUPACC [2006]
29	n-PrOO + NO_3	→ EtCHO + HO_2 + NO_2	$k=2.50x10^{-12}$ exp(0.0/T)	MCM
30	i-PrOO + NO	→ Me_2CO + HO_2 + NO_2	$k=2.70x10^{-12}$ exp(360/T)	IUPACC [2006]
31	i-PrOO + NO_3	→ Me_2CO + HO_2 + NO_2	$k=2.50x10^{-12}$ exp(0.0/T)	MCM
32	$EtCO_3$ + NO	→ EtOO + CO_2 + NO_2	$k=6.70x10^{-12}$ exp(340/T)	IUPACC [2006]
33	$EtCO_3$ + NO_3	→ EtOO + CO_2 + NO_2	$k=4.00x10^{-12}$ exp(0.0/T)	MCM
34	$MeCOCH_2OO$ + NO	→ $MeCO_3$ + HCHO + NO_2	$k=2.80x10^{-12}$ exp(300/T)	Tyndall et al., []
35	$MeCOCH_2OO$ + NO_3	→ $MeCO_3$ + HCHO + NO_2	$k=2.50x10^{-12}$ exp(0.0/T)	MCM
36	NO + NO_3	→ NO_2 + NO_2	$k=1.80x10^{-11}$ exp(110/T)	IUPACC [2006]
37	NO + O_3	→ NO_2	$k=1.40x10^{-12}$ exp(-1310/T)	IUPACC [2006]
38	NO_2 + O_3	→ NO_3	$k=1.40x10^{-13}$ exp(-2470/T)	IUPACC [2006]
39	NO^3 + HCHO	→ $HONO_2$ + HO_2 + CO	$k=2.00x10^{-12}$ exp(-2440/T)	IUPACC [2006]
40	NO^3 + MeCHO	→ $HONO_2$ + $MeCO_3$	$k=1.40x10^{-12}$ exp(-1860/T)	IUPACC [2006]
41	NO^3 + EtCHO	→ $HONO_2$ + $EtCO_3$	$k=3.46x10^{-12}$ exp(-1862/T)	MCM
42	NO^3 + Me_2CO	→ $HONO_2$ + $MeCOCH_2OO$	$k=3.00x10^{-17}$ exp(0.0/T)	IUPACC [2006]
43	$O(^3P)$ + O_3	→ O_2 + O_2	$k=8.00x10^{-12}$ exp(-2060/T)	IUPACC [2006]
44	$O(^1D)$ + CH_4	→ OH + MeOO	$k=1.05x10^{-10}$ exp(0.0/T)	IUPACC [2006]
45	$O(^1D)$ + CH_4	→ HCHO + H_2	$k=7.50x10^{-12}$ exp(0.0/T)	IUPACC [2006]
46	$O(^1D)$ + CH_4	→ HCHO + HO_2 + HO_2	$k=3.45x10^{-11}$ exp(0.0/T)	IUPACC [2006]
47	$O(^1D)$ + H_2O	→ OH + OH	$k=2.20x10^{-10}$ exp(0.0/T)	IUPACC [2006]
48	$O(^1D)$ + N_2	→ $O(^3P)$ + N_2	$k=2.10x10^{-11}$ exp(115/T)	Ravishinkara et al.[2002]
49	$O(^1D)$ + O_2	→ $O(^3P)$ + O_2	$k=3.20x10^{-11}$ exp(67/T)	IUPACC [2006]
50	OH + CH_4	→ H2O + MeOO	$k=1.85x10^{-12}$ exp(-1690/T)	IUPACC [2006]
51	OH + C_2H_6	→ H_2O + EtOO	$k=6.90x10^{-12}$ exp(-1000/T)	IUPACC [2006]
52	OH + C_3H_8	→ n-PrOO + H_2O	$k=7.60x10^{-12}$ exp(-585/T)	IUPACC [2006]
53	OH + C_3H_8	→ i-PrOO + H_2O	$k=7.60x10^{-12}$ exp(-585/T)	IUPACC [2006]
54	OH + CO	→ HO_2	$k=1.44x10^{-13}$ exp(0.0/T)	IUPACC [2006]
55	OH + EtCHO	→ H_2O + $EtCO_3$	$k=5.10x10^{-12}$ exp(405/T)	IUPACC [2006]

Continued on next page

Table A.2 – continued from previous page

Reaction	Reactants	Products	Rate (cm^3 molecule^{-1} s^{-1})	Reference
56	OH + EtOOH	→ H_2O + MeCHO + OH	k=8.01x10^{-12} exp(0.0/T)	MCM
57	OH + EtOOH	→ H_2O + EtOO	k=1.90x10^{-12} exp(190/T)	MCM
58	OH + H_2	→ H_2O + HO_2	k=7.70x10^{-12} exp(-2100/T)	IUPACC [2006]
59	OH + H_2O_2	→ H_2O + HO_2	k=2.90x10^{-12} exp(-160/T)	IUPACC [2006]
60	OH + HCHO	→ H_2O + HO_2 + CO	k=5.40x10^{-12} exp(135/T)	IUPACC [2006]
61	OH + HO_2	→ H_2O	k=4.80x10^{-11} exp(250/T)	IUPACC [2006]
62	OH + HO_2NO_2	→ H_2O + NO_2	k=1.90x10^{-12} exp(270/T)	IUPACC [2006]
63	OH + $HONO_2$	→ H_2O + NO_3	k=1.50x10^{-13} exp(0.0/T)	IUPACC [2006]
64	OH + HONO	→ H_2O + NO_2	k=2.50x10^{-12} exp(260/T)	IUPACC [2006]
65	OH + MeOOH	→ H_2O + HCHO + OH	k=1.02x10^{-12} exp(190/T)	IUPACC [2006]
66	OH + MeOOH	→ H_2 + MeOO	k=1.89x10^{-12} exp(190/T)	IUPACC [2006]
67	OH + $MeONO_2$	→ HCHO + NO_2 + H_2O	k=4.00x10^{-13} exp(-845/T)	IUPACC [2006]
68	OH + Me_2CO	→ H_2O + $MeCOCH_2OO$	k=8.80x10^{-12} exp(-1320/T)	IUPACC [2006]
69	OH + $MeCOCH_2OOH$	→ H_2O + $MeCOCH_2OO$	k=1.90x10^{-12} exp(190/T)	MCM
70	OH + $MeCOCH_2OOH$	→ H_2O + MGLY	k=8.39x10^{-12} exp(0.0/T)	MCM
71	OH + MeCHO	→ H_2O + $MeCO_3$	k=4.40x10^{-12} exp(365/T)	IUPACC [2006]
72	OH + NO_3	→ HO_2 + NO_2	k=2.00x10^{-11} exp(0.0/T)	IUPACC [2006]
73	OH + O_3	→ HO_2 + O_2	k=1.70x10^{-12} exp(-940/T)	IUPACC [2006]
74	OH + OH	→ H_2O + O(3P)	k=6.31x10^{-14} exp(945/T)	IUPACC [2006]
75	OH + PAN	→ HCHO + NO_2 + H_2O	k=3.00x10^{-14} exp(0.0/T)	IUPACC [2006]
76	OH + PPAN	→ MeCHO + NO_2 + H_2O	k=1.27x10^{-12} exp(0.0/T)	MCM
77	OH + n-PrOOH	→ n-PrOO + H_2O	k=1.90x10^{-12} exp(190/T)	MCM
78	OH + n-PrOOH	→ EtCHO + H_2O + OH	k=1.10x10^{-11} exp(0.0/T)	MCM
79	OH + i-PrOOH	→ i-PrOO + H_2O	k=1.90x10^{-12} exp(190/T)	MCM
80	OH + i-PrOOH	→ Me_2CO + OH	k=1.66x10^{-11} exp(0.0/T)	MCM
81	O(3P) + NO_2	→ NO + O_2	k=5.50x10^{-12} exp(188/T)	IUPACC [2006]
82	OH + C_5H_8	→ ISO_2	k=2.70x10^{-11} exp(390/T)	IUPACC [2006]
83	O_3 + C_5H_8	→ MACR + HCHO + $MACRO_2$ + $MeCO_3$	k=3.33x10^{-15} exp(-1995/T)	IUPACC [2006]

Continued on next page

Table A.2 – continued from previous page

Reaction	Reactants	Products	Rate (cm^3 $molecule^{-1}$ s^{-1})	Reference
		1.950 1.740 0.300 0.300		
84	O_3 + C_5H_8	→ MeOO + HCOOH + CO + H_2O_2	k=3.33x10^{-15} exp(-1995/T)	
	+	0.240 0.840 0.420 0.270		
85	O_3 C_5H_8	→ HO_2 + OH	k=3.33x10^{-15} exp(-1995/T)	
		0.750 0.750		
86	NO_3 + C_5H_8	→ ISON	k=3.15x10^{-12} exp(-450/T)	IUPACC [2006]
87	NO + ISO_2	→ NO_2 + MACR + HCHO + HO_2	k=2.43x10^{-12} exp(360/T)	MCM v3.1/MIM
88	NO + ISO_2	→ ISON	k=1.12x10^{-13} exp(360/T)	
89	HO_2 + ISO_2	→ ISOOH	k=2.05x10^{-13} exp(1300/T)	MCM v3.1/MIM
90	ISO_2 + ISO_2	→ MACR + MACR + HCHO + HO_2	k=2.00x10^{-12} exp(0.0/T)	MIM
91	OH + ISOOH	→ MACR + OH	k=1.00x10^{-10} exp(0.0/T)	MIM
92	OH + ISON	→ HACET + NALD	k=1.30x10^{-11} exp(0.0/T)	MIM
93	OH + MACR	→ $MACRO_2$	k=1.30x10^{-12} exp(610/T)	IUPACC [2006]
94	OH + MACR	→ $MACRO_2$	k=4.00x10^{-12} exp(380/T)	IUPACC [2006]
95	O_3 + MACR	→ MGLY + HCOOH + HO_2 + CO	k=2.13x10^{-16} exp(-1520/T)	IUPACC [2006]
		1.800 0.900 0.640 0.440		
96	O_3 + MACR	→ OH + $MeCO_3$	k=2.13x10^{-16} exp(-1520/T)	
		0.380 0.200		
97	O_3 + MACR	→ MGLY + HCOOH + HO_2 + CO	k=3.50x10^{-16} exp(-2100/T)	IUPACC [2006]
		1.800 0.900 0.640 0.440		
98	O_3 + MACR	→ OH + $MeCO_3$	k=3.50x10^{-16} exp(-2100/T)	
		0.380 0.200		
99	NO + $MACRO_2$	→ NO_2 + $MeCO_3$ + HACET + CO	k=1.27x10^{-12} exp(360/T)	MCM v3.1/MIM
		2.000 0.500 0.500 0.500		
100	NO + $MACRO_2$	→ MGLY + HCHO + HO_2	k=1.27x10^{-12} exp(360/T)	
		1.000 1.500 1.500		
101	HO_2 + $MACRO_2$	→ MACROOH	k=1.82x10^{-11} exp(1300/T)	MCM v3.1/MIM
102	$MACRO_2$ + $MACRO_2$	→ HACET + MGLY + HCHO + CO	k=1.00x10^{-12} exp(0.0/T)	MCM v3.1/MIM

Continued on next page

Table A.2 – continued from previous page

Reaction	Reactants	Products	Rate (cm^3 molecule^{-1} s^{-1})	Reference
		2.000 2.000 1.000 1.000		
103	$MACRO_2$ + $MACRO_2$	→ HO_2	k=1.00x10^{-12} exp(0.0/T)	
		2.000		
104	OH + MPAN	→ HACET + NO_2	k=2.90x10^{-11} exp(0.0/T)	IUPACC [2006]
105	OH + MACROOH	→ $MACRO_2$	k=3.00x10^{-11} exp(0.0/T)	MIM
106	OH + HACET	→ MGLY + HO_2	k=3.00x10^{-12} exp(0.0/T)	IUPACC [2006]/MIM
107	OH + MGLY	→ $MeCO_3$ + CO	k=1.50x10^{-11} exp(0.0/T)	IUPACC [2006]/MIM
108	NO_3 + MGLY	→ $MeCO_3$ + CO + $HONO_2$	k=3.46x10^{-12} exp(-1860/T)	MCM v3.1
109	OH + NALD	→ HCHO + CO + NO_2	k=4.40x10^{-12} exp(365/T)	IUPACC [2006]/MIM
110	OH + $MeCO_3H$	→ $MeCO_3$	k=3.70x10^{-12} exp(0.0/T)	MCM v3.1
111	OH + $MeCO_2H$	→ MeOO	k=4.00x10^{-13} exp(200/T)	JPL [2003]
112	OH + HCOOH	→ HO_2	k=4.50x10^{-13} exp(0.0/T)	IUPACC [2006]
113	MeOH + OH	→ HCHO + HO_2	k=3.10x10^{-12} exp(360/T)	Jacobson Book
114	OH + C_2H_4	→ OH	k=1.00x10^{-12} exp(0.0/T)	MPC2
115	OH + C_2H_2	→ OH	k=1.00x10^{-12} exp(0.0/T)	MPC2
116	HO_2 + O_3S	→ HO_2 + O_2	k=2.03x10^{-16} exp(693/T)	IUPACC [2006]
117	OH + O_3S	→ OH + O_2	k=1.70x10^{-12} exp(-940/T)	IUPACC [2006]
118	O(1D)S + H_2O	→ H_2O	k=2.20x10^{-10} exp(0.0/T)	IUPACC [2006]
119	O(1D)S + N_2	→ O(3P)S + N_2	k=2.10x10^{-11} exp(115/T)	Ravishinkara et al.,[2002]
120	O(1D)S + O_2	→ O(3P)S + O_2	k=3.20x10^{-11} exp(67/T)	IUPACC [2006]
121	DMS + OH	→ SO_2 + MeOO + HCHO	k=9.60x10^{-12} exp(-240/T)	Pham et al [1995]
122	DMS + OH	→ SO_2 + DMSO + HO_2 + MeOO	see [2]	IUPAC[2006]
		0.6 0.4 0.4 0.6		
123	DMSO + OH	→ SO_2 + MeOO	k=5.80x10^{-11} exp(0.0/T)	Pham et al [1995]
124	DMSO + OH	→ SO_2 + MSA + MeOO	k=5.80x10^{-11} exp(0.0/T)	Pham et al [1995]
		0.6 0.4 0.6		
125	DMS + NO_3	→ SO_2 + $HONO_2$ + MeOO + HCHO	k=1.90x10^{-13} exp(500/T)	Pham et al [1995]
126	CS_2 + OH	→ SO_2 + COS + OH	k=8.80x10^{-16} exp(2300/T)	Pham et al [1995]

Continued on next page

Table A.2 – continued from previous page

Reaction	Reactants	Products	Rate (cm^3 molecule^{-1} s^{-1})	Reference
127	H_2S + OH	→ SO_2 + OH	k=6.00x10^{-12} exp(-75/T)	Pham et al [1995]
128	COS + OH	→ SO_2 + OH	k=1.10x10^{-13} exp(-1200/T)	Pham et al [1995]
129	Br + O_3	→ BrO + O_2	k=1.70x10^{-11} exp(-800/T)	IUPAC[2006]
130	BrO + HO_2	→ HOBr + O_2	k=4.50x10^{-12} exp(500/T)	IUPAC[2006]
131	Br + HO_2	→ HBr + O_2	k=7.70x10^{-12} exp(-450/T)	IUPAC[2006]
132	HBr + OH	→ Br + H_2O	k=6.70x10^{-12} exp(155/T)	IUPAC[2006]
133	BrO + BrO	→ Br + Br + O_2	k=2.70x10^{-12} exp(0.0/T)	IUPAC[2006]
134	BrO + BrO	→ Br_2 + O_2	k=2.90x10^{-14} exp(840/T)	IUPAC[2006]
135	BrO + NO	→ Br + NO_2	k=8.70x10^{-12} exp(260/T)	IUPAC[2006]
136	Br + $BrNO_3$	→ Br_2 + NO_3	k=4.90x10^{-11} exp(0.0/T)	Orlando and Tyndall [1996]
137	Br_2 + OH	→ HOBr + Br	k=1.90x10^{-11} exp(240/T)	IUPAC[2006]
138	BrO + OH	→ Br + HO_2	k=1.80x10^{-11} exp(250/T)	IUPAC[2006]
139	Br + NO_3	→ BrO + NO_2	k=1.60x10^{-11} exp(0.0/T)	IUPAC[2006]
140	Br + HCHO	→ HBr + HO_2 + CO	k=7.70x10^{-12} exp(-580/T)	IUPAC[2006]
141	Br + MeCHO	→ HBr + $MeCO_3$	k=1.80x10^{-11} exp(-460/T)	IUPAC[2006]
142	Br + EtCHO	→ HBr + $EtCO_3$	k=9.70x10^{-12} exp(0.0/T)	Michalowski et al [2000]
143	BrO + MeOO	→ HOBr + HCHO	k=4.30x10^{-12} exp(0.0/T)	IUPAC[2006]
144	BrO + MeOO	→ Br + HCHO + HO_2	k=1.40x10^{-12} exp(0.0/T)	IUPAC[2006]
145	BrO + $MeCO_3$	→ Br + MeOO	k=1.70x10^{-12} exp(0.0/T)	Michalowski et al [2000]
146	$CHBr_3$ + OH	→ Br + Br + Br	k=1.35x10^{-12} exp(-600/T)	JPL[2006]
147	CH_3Br + OH	→ Br	k=1.70x10^{-12} exp(-1215/T)	IUPAC[2006]
148	CH_2Br_2 + OH	→ Br + Br	k=1.50x10^{-12} exp(-775/T)	IUPAC[2006]
149	$CHBr_2Cl$ + OH	→ Br + Br	k=1.50x10^{-12} exp(-775/T)	Estimated see [3]
150	$CHBrCl_2$ + OH	→ Br	k=1.50x10^{-12} exp(-775/T)	Estimated see [3]
151	CH_2BrCl + OH	→ Br	k=2.40x10^{-12} exp(-920/T)	IUPAC[2006]
152	BrO + DMS	→ DMSO + Br	k=1.50x10^{-14} exp(1000/T)	IUPAC[2006]
153	I + HO_2	→ HI + O_2	k=1.50x10^{-11} exp(-1090/T)	IUPAC [2007]
154	I + O_3	→ IO + O_2	k=2.10x10^{-11} exp(-830/T)	IUPAC [2007]

Continued on next page

Table A.2 – continued from previous page

Reaction	Reactants	Products	Rate (cm^3 $molecule^{-1}$ s^{-1})	Reference
155	I + BrO	→ IO + Br	k=$1.20x10^{-11}$ exp(0.0/T)	JPL [2006]
156	I + NO_3	→ IO + NO_2	k=$1.00x10^{-10}$ exp(0.0/T)	Dillon et al [2008]
157	I + $IONO_2$	→ I_2 + NO_3	k=$5.50x10^{-11}$ exp(0.0/T)	Kaltsoyannis and Plane [2008]
158	IO + HO_2	→ HOI + O_2	k=$1.40x10^{-11}$ exp(540/T)	IUPAC[2007]
159	IO + NO	→ I + NO_2	k=$9.10x10^{-12}$ exp(240/T)	JPL [2006]
160	IO + IO	→ I + OIO + I_2O_2	k=$5.40x10^{-11}$ exp(180/T)	IUPAC[2007]
		0.3 0.3 0.7		
161	IO + O(3P)	→ I + O_2	k=$1.20x10^{-10}$ exp(0.0/T)	JPL [2006]
162	IO + OH	→ I + HO_2	k=$1.00x10^{-10}$ exp(0.0/T)	
163	IO + BrO	→ Br + OIO	k=$4.36x10^{-12}$ exp(-760/T)	JPL [2006]
164	IO + BrO	→ Br + I + O_2	k=$2.01x10^{-12}$ exp(-760/T)	JPL [2006]
165	IO + BrO	→ IBr + O_2	k=$0.36x10^{-12}$ exp(-760/T)	JPL [2006]
166	IO + NO_3	→ OIO + NO_2	k=$9.00x10^{-12}$ exp(0.0/T)	Dillon et al [2008]
167	IO + O_3	→ OIO + O_2	k=$2.00x10^{-16}$ exp(0.0/T)	IUPAC[2007]
168	IO + O_3	→ I + O_2 O_2	k=$1.00x10^{-15}$ exp(0.0/T)	IUPAC[2007]
169	IO + OIO	→ loss	k=$0.50x10^{-10}$ exp(0.0/T)	Gomez Martin et al [2007]
170	OIO + OIO	→ loss	k=$1.50x10^{-10}$ exp(0.0/T)	Gomez Martin et al [2007]
171	OIO + NO	→ IO + NO_2	k=$1.10x10^{-12}$ exp(542/T)	Plane et al [2006]
172	OIO + OH	→ HOI + O_2	k=$6.00x10^{-12}$ exp(0.0/T)	Plane et al [2006]
173	I_2 + O(3P)	→ IO + I	k=$1.40x10^{-10}$ exp(0.0/T)	JPL [2006]
174	I_2 + OH	→ HOI + I	k=$1.80x10^{-10}$ exp(0.0/T)	JPL [2006]
175	I_2 + O_3	→ IO + I + IO + OIO	k=$3.80x10^{-18}$ exp(0.0/T)	IUPAC[2007]
		0.5 0.5 0.5 0.5		
176	I_2 + NO_3	→ I + $IONO_2$	k=$1.50x10^{-12}$ exp(0.0/T)	Chambers et al [1992]
177	HI + OH	→ I + H_2O	k=$1.60x10^{-11}$ exp(440/T)	IUPAC[2007]
178	HOI + OH	→ IO + H_2O	k=$2.00x10^{-13}$ exp(0.0/T)	Chameides and Davis [1980]
179	INO_2 + INO_2	→ I_2 + NO_2 + NO_2	k=$2.90x10^{-11}$ exp(-2600/T)	JPL [2006]
180	CH_3I + OH	→ I	k=$4.30x10^{-12}$ exp(-1120/T)	IUPAC[2007]

Continued on next page

Table A.2 – continued from previous page

Reaction	Reactants	Products	Rate (cm^3 $molecule^{-1}$ s^{-1})	Reference
181	$I_2O_2 + O_3$	$\rightarrow O_2$	$k=6.00x10^{-13}$ exp(0.0/T)	Saunders and Plane [2005]

---

[1] Reaction (3) Rate, $k=2.03x10^{-16}$ $(T/300)^{4.57}$ exp(693/T)

[2] Reaction (122) Rate, $k=9.50x10^{-39}$ $[O_2]$exp(5270/T) /(1+$7.50x10^{-29}$ $[O_2]$exp(5610/T))

[3] Reactions (149) $CHBr_2Cl$ + OH and (150) $CHBrCl_2$ + OH are estimated to have same rate as (148) CH_2Br_2 + OH as in Yang et al [2005]

Table A.3: CTM Gas-Phase Termolecular and Thermal Decomposition Reactions

Reaction	Reactants	Products	Reaction Rates	Reference
1	$HO_2 + HO_2 + M$	$\rightarrow H_2O_2 + O_2$	see [1]	IUPACC [2006]
2	$HO_2 + NO_2 + M$	$\rightarrow HO_2NO_2 + M$	K_0=1.8x10^{-31}(T/300)$^{-3.2}$[N_2], k_∞=4.7x10^{-12} F_c=0.6	IUPACC [2006]
3	$HO_2NO_2 + M$	$\rightarrow HO_2 + NO_2$	K_0=4.1x10^{-5}exp(-10650/T)[N_2], k_∞=4.8x10^{15}exp(-11170/T) F_c=0.6	IUPACC [2006]
4	$MeCO_3 + NO_2 + M$	$\rightarrow$ PAN + M	K_0=2.7x10^{-28}(T/300)$^{-7.1}$[N_2], k_∞=1.2x10^{-11} F_c=0.3	IUPACC [2006]
5	PAN + M	$\rightarrow MeCO_3 + NO_2$	K_0=4.9x10^{-3}exp(-12100/T)[N_2], k_∞=5.4x10^{16}exp(-13830/T) F_c=0.3	IUPACC [2006]
6	$N_2O_5 + M$	$\rightarrow NO_2 + NO_3$	see [2]	IUPACC [2006]
7	$NO_2 + NO_3 + M$	$\rightarrow N_2O_5 + M$	K_0=3.6x10^{-30}(T/300)$^{-4.1}$[N_2], k_∞=1.9x10^{-12} F_c=0.35	IUPACC [2006]
8	$O(^3P) + O_2 + M$	$\rightarrow O_3 + M$	K_0=5.7x10^{-34}(T/300)$^{-2.6}$[N_2], k_∞=0.0x$10^{0.0}$ F_c=0.0	IUPACC [2006]
9	OH + NO + M	$\rightarrow$ HONO + M	K_0=7.4x10^{-31}(T/300)$^{-2.4}$[N_2], k_∞=3.3x10^{-11} F_c=1420	IUPACC [2006]
10	$OH + NO_2 + M$	$\rightarrow HONO_2 + M$	K_0=3.3x10^{-30}(T/300)$^{-3.0}$[N_2], k_∞=4.1x10^{-11} F_c=0.4	IUPACC [2006]
11	OH + OH + M	$\rightarrow H_2O_2 + M$	K_0=6.9x10^{-31}(T/300)$^{-0.8}$[N_2], k_∞=2.6x10^{-11} F_c=0.5	IUPACC [2006]
12	$EtCO_3 + NO_2 + M$	$\rightarrow$ PPAN + M	K_0=2.7x10^{-28}(T/300)$^{-7.1}$[N_2], k_∞=1.2x10^{-11} F_c=0.3	MCM
13	PPAN + M	$\rightarrow EtCO_3 + NO_2$	K_0=1.7x10^{-3}exp(11280/T)[N_2], k_∞=8.3x10^{16}exp(13940/T) F_c=0.36	IUPACC [2006]
14	$MACRO_2 + NO_2 + M$	$\rightarrow$ MPAN + M	K_0=2.7x10^{-28}exp(12100/T)[N_2], k_∞=1.2x10^{-11}exp(13830/T) F_c=0.3	
15	MPAN + M	$\rightarrow MACRO2 + NO_2$	K_0=4.9x10^{-3}(T/300)$^{0.0}$[N_2], k_∞=5.4x10^{16} F_c=0.3	
16	$O(3P)S + O_2 + M$	$\rightarrow O^3S + M$	K_0=5.7x10^{-34}(T/300)$^{-2.6}$[N_2], k_∞=0.0x$10^{0.0}$ F_c=0.0	IUPACC [2006]
17	$SO_2 + OH + M$	$\rightarrow H_2SO_4 + HO_2$	K_0=3.0x10^{-31}(T/300)$^{-3.3}$[N_2], k_∞=1.5x10^{-12} F_c=0.6	Pham et al [1995]
18	$BrO + NO_2 + M$	$\rightarrow BrNO_3 + M$	K_0=4.7x10^{-31}(T/300)$^{-3.1}$[N_2], k_∞=1.8x10^{-11} F_c=0.4	IUPAC[2006]
19	$Br + NO_2 + M$	$\rightarrow BrNO_2 + M$	K_0=4.2x10^{-31}(T/300)$^{-2.4}$[N_2], k_∞=2.7x10^{-11} F_c=0.55	IUPAC[2006]
20	$I + NO_2$	$\rightarrow INO_2 + M$	K_0=3.0x10^{-31}(T/300)$^{-1.0}$[N_2], k_∞=6.6x10^{-11} F_c=0.63	IUPAC[2006]
21	$IO + NO_2$	$\rightarrow IONO_2 + M$	K_0=7.7x10^{-31}(T/300)$^{-5.0}$[N_2], k_∞=1.6x10^{-11} F_c=0.40	IUPAC[2006]
22	$I_2O_2 + M$	$\rightarrow$ IO + IO	Rate assumed 0.04 s^{-1} at 290K	
23	$I_2O_2 + M$	$\rightarrow$ OIO + I	Rate assuemd 10.0 s^{-1} at 290K	

Rate constant k =([k_0[M]/(1 + k_0[M]/k_∞)] x $f_c^{\,n}$), where n = (1 + ($\log_{10}$(k_0[M]/k_∞))^2)$^{-1}$.

[1] Reaction (1), Rate k = (2.2x10^{-13}exp(600/T)+1.9x10^{-33}[N_2]exp(980/T))×(1+1.4x10^{-21})[H_2O]exp(2200/T))

[2] Reaction (6), K_0=1.3x10^{-3}(T/300)$^{-3.5}$exp(-11000/T)[N_2], k_∞=9.7x10^{14}(T/300)$^{-0.1}$exp(-11080/T) F_c=0.35

Table A.4: CTM Heterogeneous Reactions

Reaction	Reactants	Products
1	$BrNO_3$ + H_2O	→ HOBr + HNO_3
2	N_2O_5 + H_2O	→ HNO_3 + HNO_3
3	HOBr + HBr	→ Br_2 + H_2O
4	HI + H_2O	→ I 0.5
5	HOI + H_2O	→ I 0.5
6	INO_2 + H_2O	→ I 0.5
7	$IONO_2$ + H_2O	→ I 0.5

Table A.5: CTM Photolysis Reactions

Reaction	Reactants	Products	Reference
1	EtOOH + hν	→ MeCHO + HO_2 + OH	
2	H_2O_2 + hν	→ OH + OH	JPL [1992]
3a	HCHO + hν	→ HO_2 + HO_2 + CO	
3b	HCHO + hν	→ H_2 + CO	
5	HO_2NO_2 + hν	→ HO_2 + NO_2	
6	$HONO_2$ + hν	→ OH + NO_2	
7a	MeCHO + hν	→ MeOO + HO_2 + CO	Blitz et al., [2004]
7b	MeCHO + hν	→ CH4 + CO	Blitz et al., [2004]
9	MeOOH + hν	→ HO_2 + HCHO + OH	JPL [1990]
10	N_2O_5 + hν	→ NO_3 + NO_2	
11	NO_2 + hν	→ NO + O(3P)	JPL [1992]
12a	NO_3 + hν	→ NO + O_2	Johnston [1996]
12b	NO_3 + hν	→ NO_2 + $O(^3P)$	Johnston [1996]
14	O_2 + hν	→ $2O(^3P)$	Yoshino et al., [1988]
15a	O_3 + hν	→ O_2 + $O(^1D)$	
15b	O_3 + hν	→ O_2 + $O(^3P)$	
17	PAN + hν	→ $MeCO_3$ + NO_2	IUPACC [1999]
18	HONO + hν	→ OH + NO	JPL [1992]
19	EtCHO + hν	→ EtOO + HO_2 + CO	IUPACC [2002]
20	Me_2CO + hν	→ $MeCO_3$ + MeOO	IUPACC [1999]
21	n-PrOOH + hν	→ EtCHO + HO_2 + OH	
22	i-PrOOH + hν	→ Me_2CO + HO_2 + OH	
23	$MeCOCH_2OOH$ + hν	→ $MeCO_3$ + HCHO + OH	
24	PPAN + hν	→ $EtCO_3$ + NO_2	
25	$MeONO_2$ + hν	→ HO_2 + HCHO + NO_2	
26	ISOOH + hν	→ OH + MACR + HCHO + HO_2	
27	ISON + hν	→ NO_2 + MACR + HCHO + HO_2	IUPACC [2002]

Continued on next page

Table A.5 – continued from previous page

Reaction	Reactants	Products	Reference
28	MACR + hν	→ $MeCO_3$ + HCHO + CO + HO_2	IUPACC [2002]
29	MPAN + hν	→ $MACRO_2$ + NO_2 +	
30a	MACROOH + hν	→ OH + HO_2 + OH + HO_2	
31b	MACROOH + hν	→ HACET + CO + MGLY + HCHO	
32	HACET + hν	→ $MeCO_3$ + HCHO + HO_2 +	
33	MGLY + hν	→ $MeCO_3$ + CO + HO_2 +	IUPACC [2002]
34	NALD + hν	→ HCHO + CO + NO_2 + HO_2	
35	$MeCO_3H$ + hν	→ MeOO + OH	Orlando and Tundall [2003]
36a	O_3S + hν	→ O_2 + O(1D)S	
36b	O_3S + hν	→ O_2 + O(3P)S	
38	BrO + hν	→ Br + O(3P)	JPL [1992]
39	HOBr + hν	→ Br + OH	JPL [2000]
40a	$BrONO_2$ + hν	→ BrO + NO_2	JPL [1997]
41b	$BrONO_2$ + hν	→ Br + NO_3	
42	$BrNO_2$ + hν	→ Br + NO_2	
43	Br_2 + hν	→ Br + Br	
44	$CHBr_3$ + hν	→ Br + Br + Br	
45	$CHBr_2Cl$ + hν	→ Br + Br	
46	$CHBrCl_2$ + hν	→ Br	
47	I_2 + hν	→ I + I	JPL [2006]
48	IO + hν	→ I + O	Harwood et al., [2006]
49	OIO + hν	→ I + O_2	Cox et al., [1999]
50	HOI + hν	→ I + OH	Rowley et al., [1999]
51	$IONO_2$ + hν	→ I + NO_3	IUPAC [2000]
52	INO_2 + hν	→ I + NO_2	JPL [2006]
53	INO_2 + hν	→ IO + NO	JPL [2006]
54	CH_3I + hν	→ I	JPL [2006]
55	CH_2ICl + hν	→ I	JPL [2006]

Continued on next page

Table A.5 – continued from previous page

Reaction	Reactants	Products	Reference
56	$CH_2IBr + h\nu$	$\rightarrow I + Br$	JPL [2006]
57	$CH_2I_2 + h\nu$	$\rightarrow I + I$	JPL [2006]
58	$C_2H_5I + h\nu$	$\rightarrow I$	JPL [2006]
59	$C_3H_7I + h\nu$	$\rightarrow I$	JPL [2006]
61	$IBr + h\nu$	$\rightarrow I + Br$	JPL [2006]

References

Evaluated Kinetic Data International Union of Pure and Applied Chemistry (IUPAC) (2006) *http://www.iupac-kineti.ch.cam.ac.uk/index.html*

Chemical Kinetics and Photochemical Data for Use in Atmospheric Studies, Jet Propulsion Laboratory (JPL) (2006) *http://jpldataeval.jpl.nasa.gov/download.html*

Master Chemical Mechanism (MCM), Leeds, UK *http://mcm.leeds.ac.uk/MCM/roots.htt*

Michalowski, B., J. Francisco, S. Li, A. Barrie, J. Bottleenheim and P. Shepson (2000) A computer model study of multiphase chemistry in the Arctic boundary layer during polar sunrise, *J. Geophys. Res., 105,* 15,131-15,145.

Orlando, J. and G. Tyndall (1996), Rate coefficients for the decomposition of $BrONO_2$ and the heat of formation of $BrONO_2$, *J. Phys. Chem., 100*, 19398-19405.

Pham, M., J. Muller, G. Brasseur, C. Granier and G. Megie (1995), A three-dimensional study of the tropospheric sulfur cycle, *J. Geophys. Res., 100*, 26,061-26,092

References

ADAMS, P.J. & SEINFELD, J.H. (2002). Predicting global aerosol size distributions in general circulation models. *Journal Of Geophysical Research-Atmospheres*, **107**.

AHRENS, C.D. (1999). *Ahrens, C. D.*. Brooks/Cole.

ALDENER, M., BROWN, S.S., STARK, H., WILLIAMS, E.J., LERNER, B.M., KUSTER, W.C., GOLDAN, P.D., QUINN, P.K., BATES, T.S., FEHSENFELD, F.C. & RAVISHANKARA, A.R. (2006). Reactivity and loss mechanisms of NO3 and N2O5 in a polluted marine environment: Results from in situ measurements during New England Air Quality Study 2002. *Journal Of Geophysical Research-Atmospheres*, **111**, D23S73.

ALEXANDER, B., PARK, R.J., JACOB, D.J., LI, Q.B., YANTOSCA, R.M., SAVARINO, J., LEE, C.C.W. & THIEMENS, M.H. (2005). Sulfate formation in sea-salt aerosols: Constraints from oxygen isotopes. *Jour. Geophys. Res.-Atmos.*, **110**, D10307.

ALICKE, B., HEBESTREIT, K., STUTZ, J. & PLATT, U. (1999). Iodine oxide in the marine boundary layer. *Nature*, **397**, 572–573.

ALLAN, B.J., MCFIGGANS, G., PLANE, J.M.C. & COE, H. (2000). Observations of iodine monoxide in the remote marine boundary layer. *Journal Of Geophysical Research-Atmospheres*, **105**, 14363–14369.

ANDREAE, M.O. & CRUTZEN, P.J. (1997). Atmospheric aerosols: Biogeochemical sources and role in atmospheric chemistry. *Science*, **276**, 1052–1058.

ANDREAE, M.O. & MERLET, P. (2001). Emission of trace gases and aerosols from biomass burning. *Global Biogeochemical Cycles*, **15**, 955–966.

ANDREAS, E.L., EDSON, J.B., MONAHAN, E.C., ROUAULT, M.P. & SMITH, S.D. (1995). The Spray Contribution To Net Evaporation From The Sea - A Review Of Recent Progress. *Boundary-Layer Meteorology*, **72**, 3–52.

ANDRES, R.J. & KASGNOC, A.D. (1998). A time-averaged inventory of subaerial volcanic sulfur emissions. *Journal Of Geophysical Research-Atmospheres*, **103**, 25251–25261.

ARNOLD, S.R., CHIPPERFIELD, M.P. & BLITZ, M.A. (2005). A three-dimensional model study of the effect of new temperature-dependent quantum yields for acetone photolysis. *Journal Of Geophysical Research-Atmospheres*, **110**.

ARNOLD, S.R., SPRACKLEN, D.V., WILLIAMS, J., YASSAA, N., SCIARE, J., BONSANG, B., GROS, V., PEEKEN, I., LEWIS, A.C., ALVAIN, S. & MOULIN, C. (2009). Evaluation of the global oceanic isoprene source and its impacts on marine organic carbon aerosol. *Atmospheric Chemistry And Physics*, **9**, 1253–1262.

ATKINSON, R. (2000). Atmospheric chemistry of VOCs and NOx. *Atmospheric Environment*, **34**, 2063–2101.

AYERS, G.P. & GILLETT, R.W. (2000). DMS and its oxidation products in the remote marine atmosphere: implications for climate and atmospheric chemistry. *Journal of Sea Research*, **43**, 275–286.

AYERS, G.P. & GRAS, J.L. (1991). Seasonal Relationship Between Cloud Condensation Nuclei And Aerosol Methanesulfonate In Marine Air. *Nature*, **353**, 834–835.

AYERS, G.P., IVEY, J.P. & GILLETT, R.W. (1991). Coherence Between Seasonal Cycles Of Dimethyl Sulfide, Methanesulfonate And Sulfate In Marine Air. *Nature*, **349**, 404–406.

AYERS, G.P., GILLETT, R.W., CAINEY, J.M. & DICK, A.L. (1999). Chloride and bromide loss from sea-salt particles in southern ocean air. *Journal Of Atmospheric Chemistry*, **33**, 299–319.

BARNES, I., BASTIAN, V., BECKER, K.H. & OVERATH, R.D. (1991). Kinetic-Studies Of The Reactions Of Io, Bro, And Clo With Dimethylsulfide. *International Journal Of Chemical Kinetics*, **23**, 579–591.

BARNES, I., HJORTH, J. & MIHALOPOULOS, N. (2006). Dimethyl sulfide and dimethyl sulfoxide and their oxidation in the atmosphere. *Chemical Reviews*, **106**, 940–975.

BARTH, M.C., RASCH, P.J., KIEHL, J.T., BENKOVITZ, C.M. & SCHWARTZ, S.E. (2000). Sulfur chemistry in the National Center for Atmospheric Research Community Climate Model: Description, evaluation, features, and sensitivity to aqueous chemistry. *Journal Of Geophysical Research-Atmospheres*, **105**, 1387–1415.

BEHNKE, W., SCHEER, V. & ZETSCH, C. (1994). Production of BrONO2, Br2 and ClNO2 from the reaction between sea spray aerosol and N2O5. *Journal of Aerosol Science*, **25**, S277–S278.

BELL, N., KOCH, D. & SHINDELL, D.T. (2005). Impacts of chemistry-aerosol coupling on tropospheric ozone and sulfate simulations in a general circulation model. *Journal Of Geophysical Research-Atmospheres*, **110**, D14305.

BERGLEN, T.F., BERNTSEN, T.K., ISAKSEN, I.S.A. & SUNDET, J.K. (2004). A global model of the coupled sulfur/oxidant chemistry in the troposphere: The sulfur cycle. *Journal Of Geophysical Research-Atmospheres*, **109**, D19310.

BEY, I., JACOB, D.J., YANTOSCA, R.M., LOGAN, J.A., FIELD, B.D., FIORE, A.M., LI, Q.B., LIU, H.G.Y., MICKLEY, L.J. & SCHULTZ, M.G. (2001). Global modeling of tropospheric chemistry with assimilated meteorology: Model description and evaluation. *Journal Of Geophysical Research-Atmospheres*, **106**, 23073–23095.

BLANCHARD, D.C. & WOODCOCK, A.H. (1980). The production, concentration and verticla distribution of the sea-salt aerosol. *Ann. N. Y. Acad. Sci.*, **338**, 330–347.

BLOSS, W.J., LEE, J.D., JOHNSON, G.P., SOMMARIVA, R., HEARD, D.E., SAIZ-LOPEZ, A., PLANE, J.M.C., MCFIGGANS, G., COE, H., FLYNN, M., WILLIAMS, P., RICKARD, A.R. & FLEMING, Z.L. (2005). Impact of halogen monoxide chemistry upon boundary layer OH and HO2 concentrations at a coastal site. *Geophysical Research Letters*, **32**, L06814.

BOBROWSKI, N., HONNINGER, G., GALLE, B. & PLATT, U. (2003). Detection of bromine monoxide in a volcanic plume. *Nature*, **423**, 273–276.

BOUCHER, O., MOULIN, C., BELVISO, S., AUMONT, O., BOPP, L., COSME, E., VON KUHLMANN, R., LAWRENCE, M.G., PHAM, M., REDDY, M.S., SCIARE, J. & VENKATARAMAN, C. (2003). DMS atmospheric concentrations and sulphate aerosol indirect radiative forcing: a sensitivity study to the DMS source representation and oxidation. *Atmospheric Chemistry And Physics*, **3**, 49–65.

BREIDER, T.J., CHIPPERFIELD, M.P., RICHARDS, N.A.D., CARSLAW, K.S., MANN, G.W. & SPRACKLEN, D.V. (2010). Impact of BrO on dimethylsulfide in the remote marine boundary layer. *Geophysical Research Letters*, **37**, L02807.

BURROWS, J.P., WEBER, M., BUCHWITZ, M., ROZANOV, V., LADSTATTER-WEISSENMAYER, A., RICHTER, A., DEBEEK, R., HOOGEN, R., BRAMSTEDT, K., EICHMANN, K.U. & EISINGER, M. (1999). The global ozone monitoring experiment (GOME): Mission concept and first scientific results. *Journal Of The Atmospheric Sciences*, **56**, 151–175.

BUTLER, J.H., KING, D.B., LOBERT, J.M., MONTZKA, S.A., YVON-LEWIS, S.A., HALL, B.D., WARWICK, N.J., MONDEEL, D.J., AYDIN, M. & ELKINS, J.W. (2007). Oceanic distributions and emissions of short-lived halocarbons. *Global Biogeochemical Cycles*, **21**.

BUTLER, J.N. (1982). *Carbon Dioxide Equilibria and their Applications*. Addison-Wesley.

CARPENTER, L.J. (2003). Iodine in the marine boundary layer. *Chemical Reviews*, **103**, 4953–4962.

CARPENTER, L.J., MONKS, P.S., BANDY, B.J., PENKETT, S.A., GALBALLY, I.E. & MEYER, C.P. (1997). A study of peroxy radicals and ozone photochemistry at coastal sites in the northern and southern hemispheres. *Journal Of Geophysical Research-Atmospheres*, **102**, 25417–25427.

CARPENTER, L.J., STURGES, W.T., PENKETT, S.A., LISS, P.S., ALICKE, B., HEBESTREIT, K. & PLATT, U. (1999). Short-lived alkyl iodides and bromides at Mace Head, Ireland: Links to biogenic sources and halogen oxide production. *Journal Of Geophysical Research-Atmospheres*, **104**, 1679–1689.

CARPENTER, L.J., LISS, P.S. & PENKETT, S.A. (2003). Marine organohalogens in the atmosphere over the Atlantic and Southern Oceans. *Journal Of Geophysical Research-Atmospheres*, **108**, 4256.

CARVER, G., BROWN, P. & WILD, O. (1997). The ASAD atmsopheric chemistry integration package and chemical reaction database. *Computer Physics Communications*, **105**, 197–215.

CHAMEIDES, W. & WALKER, J.C.G. (1973). Photochemical Theory Of Tropospheric Ozone. *Journal Of Geophysical Research*, **78**, 8751–8760.

CHAMEIDES, W.L. (1984). The Photochemistry Of A Remote Marine Stratiform Cloud. *Journal Of Geophysical Research-Atmospheres*, **89**, 4739–4755.

CHAMEIDES, W.L. & DAVIS, D.D. (1980). Iodine: Its potential role in tropospheric photochemistry. *J. Geophys. Res.*, **85**, 7383–7398.

CHAMEIDES, W.L. & STELSON, A.W. (1992). Aqueous-Phase Chemical Processes In Deliquescent Sea-Salt Aerosols - A Mechanism That Couples The Atmospheric Cycles Of S And Sea Salt. *Journal Of Geophysical Research-Atmospheres*, **97**, 20565–20580.

CHARLSON, R.J., LOVELOCK, J.E., ANDRAE, M.O. & WARREN, S.G. (1987). Oceanic Phytoplankton, Atmospheric Sulfur, Cloud Albedo And Climate. *Nature*, **326**, 655–661.

CHARLSON, R.J., SCHWARTZ, S.E., HALES, J.M., CESS, R.D., COAKLEY, J.A., HANSEN, J.E. & HOFMANN, D.J. (1992). Climate Forcing By Anthropogenic Aerosols. *Science*, **255**, 423–430.

CHEN, Y.H. & PRINN, R.G. (2006). Estimation of atmospheric methane emissions between 1996 and 2001 using a three-dimensional global chemical transport model. *Journal Of Geophysical Research-Atmospheres*, **111**, D10307.

CHIN, M., ROOD, R.B., LIN, S.J., MULLER, J.F. & THOMPSON, A.M. (2000). Atmospheric sulfur cycle simulated in the global model GOCART: Model description and global properties. *Journal Of Geophysical Research-Atmospheres*, **105**, 24671–24687.

CHIN, M.A., JACOB, D.J., GARDNER, G.M., FOREMANFOWLER, M.S., SPIRO, P.A. & SAVOIE, D.L. (1996). A global three-dimensional model of tropospheric sulfate. *Journal Of Geophysical Research-Atmospheres*, **101**, 18667–18690.

CHIPPERFIELD, M.P. (2006). New version of the TOMCAT/SLIMCAT off-line chemical transport model: Intercomparison of stratospheric tracer experiments. *Quarterly Journal Of The Royal Meteorological Society*, **132**, 1179–1203.

CLERBAUX, C. & CUNNOLD, D.M. (2006). Long-Lived Compounds, Chapter 1 in Scientific Assessment of Ozone Depletion, 2006. Tech. rep., Global Ozone Research and Monitoring Project- Report No. 50, 572 pp., WMO, Geneva, Switzerland.

CLIFFORD, D., DONALDSON, D.J., BRIGANTE, M., D'ANNA, B. & GEORGE, C. (2008). Reactive uptake of ozone by chlorophyll at aqueous surfaces. *Environmental Science & Technology*, **42**, 1138–1143.

COFALA, J., ARMANN, M., KLIMONT, Z. & SCHOPP, W. (2005). Scenarios of World Anthropogenic Emissions of SO2, NOx, and CO up to 2030. *Internal report of the transboundary Air Pollution Programme,International Institute for Applied Systems, Laxenberg, Austria.*

COVERT, D.S., KAPUSTIN, V.N., QUINN, P.K. & BATES, T.S. (1992). New Particle Formation In The Marine Boundary-Layer. *Journal Of Geophysical Research-Atmospheres*, **97**, 20581–20589.

CRUTZEN, P. (1973). Discussion Of Chemistry Of Some Minor Constituents In Stratosphere And Troposphere. *Pure And Applied Geophysics*, **106**, 1385–1399.

CURTIUS, J. (2006). Nucleation of atmospheric aerosol particles. *Comptes Rendus Physique*, **7**, 1027–1045.

DAVIES, J.A. & COX, R.A. (1998). Kinetics of the heterogeneous reaction of HNO3 with NaCl: Effect of water vapor. *Journal Of Physical Chemistry A*, **102**, 7631–7642.

DAVIS, D., CRAWFORD, J., LIU, S., MCKEEN, S., BANDY, A., THORNTON, D., ROWLAND, F. & BLAKE, D. (1996). Potential impact of iodine on tropospheric levels of ozone and other critical oxidants. *Journal Of Geophysical Research-Atmospheres*, **101**, 2135–2147.

DAVIS, D., CHEN, G., BANDY, A., THORNTON, D., EISELE, F., MAULDIN, L., TANNER, D., LENSCHOW, D., FUELBERG, H., HUEBERT, B., HEATH, J., CLARKE, A. & BLAKE, D. (1999). Dimethyl sulfide oxidation in the equatorial Pacific: Comparison of model simulations with field observations for DMS, SO2, H2SO4(g), MSA(g), MS, and NSS. *Journal Of Geophysical Research-Atmospheres*, **104**, 5765–5784.

De Bruyn, W.J., Dahl, E. & Saltzman, E.S. (2006). DMS and SO2 measurements in the tropical marine boundary layer. *Journal Of Atmospheric Chemistry*, **53**, 145–154.

Dentener, F., Kinne, S., Bond, T., Boucher, O., Cofala, J., Generoso, S., Ginoux, P., Gong, S., Hoelzemann, J.J., Ito, A., Marelli, L., Penner, J.E., Putaud, J.P., Textor, C., Schulz, M., van der Werf, G.R. & Wilson, J. (2006). Emissions of primary aerosol and precursor gases in the years 2000 and 1750 prescribed data-sets for AeroCom. *Atmospheric Chemistry And Physics*, **6**, 4321–4344.

Dentener, F.J. & Crutzen, P.J. (1993). Reaction Of N2o5 On Tropospheric Aerosols - Impact On The Global Distributions Of Nox, O3, And Oh. *Journal Of Geophysical Research-Atmospheres*, **98**, 7149–7163.

Easter, R.C. & Hales, J.M. (1983). Precipitation Scavenging, Dry Deposition and Resuspension. *Chapter Interpretation of the OSCAR data for reactive gas scavenging*, 649–662.

Easter, R.C., Ghan, S.J., Zhang, Y., Saylor, R.D., Chapman, E.G., Laulainen, N.S., Abdul-Razzak, H., Leung, L.R., Bian, X.D. & Zaveri, R.A. (2004). MIRAGE: Model description and evaluation of aerosols and trace gases. *Journal Of Geophysical Research-Atmospheres*, **109**.

Evans, M.J. & Jacob, D.J. (2005). Impact of new laboratory studies of N2O5 hydrolysis on global model budgets of tropospheric nitrogen oxides, ozone, and OH. *Geophysical Research Letters*, **32**.

Fairall, C.W., Helmig, D., Ganzeveld, L. & Hare, J. (2007). Water-side turbulence enhancement of ozone deposition to the ocean. *Atmospheric Chemistry And Physics*, **7**, 443–451.

Fickert, S., Adams, J.W. & Crowley, J.N. (1999). Activation of Br-2 and BrCl via uptake of HOBr onto aqueous salt solutions. *Journal Of Geophysical Research-Atmospheres*, **104**, 23719–23727.

Fitzenberger, R., Bosch, H., Camy-Peyret, C., Chipperfield, M.P., Harder, H., Platt, U., Sinnhuber, B.M., Wagner, T. & Pfeilsticker, K. (2000). First profile measurements of tropospheric BrO. *Geophysical Research Letters*, **27**, 2921–2924.

Fitzgerald, J.W. (1991). Marine Aerosols - A Review. *Atmospheric Environment Part A-General Topics*, **25**, 533–545.

Forster, P., Ramaswamy, V., Artaxo, P., Berntsen, T., Betts, R., Fahey, D.W., Haywood, J., Lean, J., Lowe, D.C., Myhre, G., Nganga, J., Prinn, G., R. amd Raga, Schulz, M. & Van Dorland, R. (2007). *Changes in Atmospheric Constituents and in Radiative Forcing. In: Climate Change 2007: The Physical Science Basis. Contribution of Working Group I to the Fourth Assessment Report of the Intergovernmental Panel on Climate Change. [Solomon, S., D. Qin, M. Manning, Z. Chen, M. Marquis, K.B. Averyt, M.Tignor and H.L. Miller (eds.)]*. Cambridge University Press, Cambridge, United Kingdom and New York, NY, USA.

Fuchs, N. & Sutugin, A. (1971). Topics in Current Aerosol Research, chap, Highly dispersed aerosols. *Pergemon*, 1–60.

Gabriel, R., von Glasow, R., Sander, R., Andreae, M.O. & Crutzen, P.J. (2002). Bromide content of sea-salt aerosol particles collected over the Indian Ocean during INDOEX 1999. *Journal Of Geophysical Research-Atmospheres*, **107**, 8032.

GALBALLY, I.E., BENTLEY, S.T. & MEYER, C.P. (2000). Mid-latitude marine boundary-layer ozone destruction at visible sunrise observed at Cape Grim, Tasmania, 41 degrees 5. *Geophysical Research Letters*, **27**, 3841–3844.

GANZEVELD, L., EERDEKENS, G., FEIG, G., FISCHER, H., HARDER, H., KONIGSTEDT, R., KUBISTIN, D., MARTINEZ, M., MEIXNER, F.X., SCHEEREN, H.A., SINHA, V., TARABORRELLI, D., WILLIAMS, J., DE ARELLANO, J.V.G. & LELIEVELD, J. (2008). Surface and boundary layer exchanges of volatile organic compounds, nitrogen oxides and ozone during the GABRIEL campaign. *Atmospheric Chemistry And Physics*, **8**, 6223–6243.

GARLAND, J.A. & CURTIS, H. (1981). Emission of Iodine from the sea surface in the presence of ozone. *Jour. Geophys Res*, **86**, 3183–3186.

GARLAND, J.A., ELZERMAN, A.W. & PENKETT, S.A. (1980). The Mechanism For Dry Deposition Of Ozone To Seawater Surfaces. *Journal Of Geophysical Research-Oceans And Atmospheres*, **85**, 7488–7492.

GIANNAKOPOULOS, G., CHIPPERFIELD, M., LAW, K., & PYLE, J. (1999). Validation and intercomparison of wet and dry deposition schemes using 210Pb in a global three-dimensional off-line chemical transport model. *Journal Of Geophysical Research-Atmospheres*, **104**, 23761–23784.

GILL, P.S., GRAEDEL, T.E. & WESCHLER, C.J. (1983). Organic Films On Atmospheric Aerosol-Particles, Fog Droplets, Cloud Droplets, Raindrops, And Snowflakes. *Reviews Of Geophysics*, **21**, 903–920.

GONG, S. (2003). A parameterization of sea-salt aerosol source function for sub- and super-micron particles. *Global Biogeochem. Cycles*, **17**, 1097–1103.

GRANIER, C., LAMARQUE, J.F., MIEVILLE, A., MULLER, J., OLIVIER, J., ORLANDO, J., PETERS, J., PETRON, G., TYNDALL, G. & WALLENS, S. (2005). POET, a database of surface emissions of ozone precursors., available on internet at http://www.aero.jussieu.fr/projet/ACCENT/POET.php, 2005.

GUELLE, W., SCHULZ, M., BALKANSKI, Y. & DENTENER, F. (2001). Influence of the source formulation on modeling the atmospheric global distribution of sea salt aerosol. *Journal Of Geophysical Research-Atmospheres*, **106**, 27509–27524.

GUENTHER, A., HEWITT, C.N., ERICKSON, D., FALL, R., GERON, C., GRAEDEL, T., HARLEY, P., KLINGER, L., LERDAU, M., MCKAY, W.A., PIERCE, T., SCHOLES, B., STEINBRECHER, R., TALLAMJAJU, R., TAYLOR, J. & ZIMMERMAN, P., N (1995). A Global-Model Of Natural Volatile Organic-Compound Emissions. *Journal Of Geophysical Research-Atmospheres*, **100**, 8873–8892.

GUIMBAUD, C., ARENS, F., GUTZWILLER, L., GAGGELER, H.W. & AMMANN, M. (2002). Uptake of HNO3 to deliquescent sea-salt particles: a study using the short-lived radioactive isotope tracer N-13. *Atmospheric Chemistry And Physics*, **2**, 249–257.

GURCIULLO, C., LERNER, B., SIEVERING, H. & PANDIS, S.N. (1999). Heterogeneous sulfate production in the remote marine environment: Cloud processing and sea-salt particle contributions. *Journal Of Geophysical Research-Atmospheres*, **104**, 21719–21731.

HALLQUIST, M., STEWART, D.J., STEPHENSON, S.K. & COX, R.A. (2003). Hydrolysis of N2O5 on sub-micron sulfate aerosols. *Physical Chemistry Chemical Physics*, **5**, 3453–3463.

HALMER, M.M., SCHMINCKE, H.U. & GRAF, H.F. (2002). The annual volcanic gas input into the atmosphere, in particular into the stratosphere: a global data set for the past 100 years. *Journal Of Volcanology And Geothermal Research*, **115**, 511–528.

HAYWOOD, J. & BOUCHER, O. (2000). Estimates of the direct and indirect radiative forcing due to tropospheric aerosols: A review. *Reviews Of Geophysics*, **38**, 513–543.

HENDRICK, F., VAN ROOZENDAEL, M., CHIPPERFIELD, M.P., DORF, M., GOUTAI, F., YANG, X., FAYT, C., HERMANS, C., PFEILSTICKER, K., POMMEREAU, J.P., PYLE, J.A., THEYS, N. & DE MAZIERE, M. (2007). Retrieval of stratospheric and tropospheric BrO profiles and columns using ground-based zenith-sky DOAS observations at Harestua, 60(o)N. *Atmos. Chem & Phys.*, **7**, 4869–4885.

HOBBS, P.V. (1993). *Aerosol-cloud-climate interactions*. Academic Press Inc.

HOFFMANN, M.R. & CALVERT, J.G. (1985). Chemical Transformation Modules for Eulerian Acid Deposition Models, Vol. 2, The Aqueous-Phase Chemistry, EPA/600/3-85/017. Tech. rep., U.S. Environmental protection Agency, Research Triangle Park, NC.

HOLTSLAG, A. & BOVILLE, B. (1993). Local versus nonlocal boundary layer diffusion in a global climate model. *Journal of Climate*, **6**, 1825–1842.

HOUGH, A.M. (1988). The calculation of photolysis rates for use in global modelling studies. *AERE Rep. R-13259*.

HOUGHTON, J., DING, D.J., Y. GRIGGS, NOGUER, M., VAN DER LINDEN, P.J., DAI, X., MASKELL, K. & JOHNSON, C.A. (2001). *IPCC, 2001: Climate Change 2001: The Scientific Basis. Contribution of Working Group I to the Third Assessment Report of the Intergovernmental Panel on Climate Change*. Cambridge University Press, Cambridge, United Kingdom and New York, NY, USA, 881 pp.

JACOB, D.J. (2000). Heterogeneous chemistry and tropospheric ozone. *Atmospheric Environment*, **34**, 2131–2159.

JACOB, D.J., HEIKES, B.G., FAN, S.M., LOGAN, J.A., MAUZERALL, D.L., BRADSHAW, J.D., SINGH, H.B., GREGORY, G.L., TALBOT, R.W., BLAKE, D.R. & SACHSE, G.W. (1996). Origin of ozone and NOx in the tropical troposphere: A photochemical analysis of aircraft observations over the South Atlantic basin. *Journal Of Geophysical Research-Atmospheres*, **101**, 24235–24250.

JACOBSON, M. (1997). Development and Application of a new air pollution modeling system. Part II: Aerosol module structure and design. *Atmospheric Environment*, **31A**, 131–144.

JAMMOUL, A., DUMAS, S., D'ANNA, B. & GEORGE, C. (2009). Photoinduced oxidation of sea salt halides by aromatic ketones: a source of halogenated radicals. *Atmospheric Chemistry And Physics*, **9**, 4229–4237.

JOCKEL, P., TOST, H., POZZER, A., BRUHL, C., BUCHHOLZ, J., GANZEVELD, L., HOOR, P., KERKWEG, A., LAWRENCE, M.G., SANDER, R., STEIL, B., STILLER, G., TANARHTE, M., TARABORRELLI, D., VAN AARDENNE, J. & LELIEVELD, J. (2006). The atmospheric chemistry general circulation model ECHAM5/MESSy1: consistent simulation of ozone from the surface to the mesosphere. *Atmospheric Chemistry And Physics*, **6**, 5067–5104.

JOHNSON, P.N. & DAVIS, R.A. (2006). Diffusivity of Ozone in water,. *J. Chem. and Eng. Data*, **41**, 1485–1487.

JONES, A., ROBERTS, D.L., WOODAGE, M.J. & JOHNSON, C.E. (2001). Indirect sulphate aerosol forcing in a climate model with an interactive sulphur cycle. *Journal Of Geophysical Research-Atmospheres*, **106**, 20293–20310.

JONES, C.E., HORNSBY, K.E., SOMMARIVA, R., DUNK, R.M., VON GLASOW, R., MCFIGGANS, G. & CARPENTER, L.J. (2010). Quantifying the contribution of marine organic gases to atmospheric iodine. *Geophys. Res. Letts.*, **37**.

JOURDAIN, B. & LEGRAND, M. (2001). Seasonal variations of atmospheric dimethylsulfide, dimethylsulfoxide, sulfur dioxide, methanesulfonate, and non-sea-salt sulfate aerosols at Dumont d'Urville (coastal Antarctica) (December 1998 to July 1999). *Journal Of Geophysical Research-Atmospheres*, **106**, 14391–14408.

KALESCHKE, L., RICHTER, A., BURROWS, J., AFE, O., HEYGSTER, G., NOTHOLT, J., RANKIN, A.M., ROSCOE, H.K., HOLLWEDEL, J., WAGNER, T. & JACOBI, H.W. (2004). Frost flowers on sea ice as a source of sea salt and their influence on tropospheric halogen chemistry. *Geophysical Research Letters*, **31**, L16114.

KANE, S.M., CALOZ, F. & LEU, M.T. (2001). Heterogeneous uptake of gaseous N2O5 by (NH4)(2)SO4, NH4HSO4, and H2SO4 aerosols. *Journal Of Physical Chemistry A*, **105**, 6465–6470.

KEENE, W.C. & GALLOWAY, J. (1986). Consideration Regarding Sources for Formic and Acetic Acids in the Troposphere. *J. Geophys. Res.*, **91**, 14466–14474.

KEENE, W.C. & SAVOIE, D.L. (1998). The pH of deliquesced sea-salt aerosol in polluted marine air. *Geophysical Research Letters*, **25**, 2181–2184.

KEENE, W.C., LONG, M.S., PSZENNY, A.A.P., SANDER, R., MABEN, J.R., WALL, A.J., O'HALLORAN, T.L., KERKWEG, A., FISCHER, E.V. & SCHREMS, O. (2009). Latitudinal variation in the multiphase chemical processing of inorganic halogens and related species over the eastern North and South Atlantic Oceans. *Atmospheric Chemistry And Physics*, **9**, 7361–7385.

KERKWEG, A., JOCKEL, P., POZZER, A., TOST, H., SANDER, R., SCHULZ, M., STIER, P., VIGNATI, E., WILSON, J. & LELIEVELD, J. (2008). Consistent simulation of bromine chemistry from the marine boundary layer to the stratosphere - Part 1: Model description, sea salt aerosols and pH. *Atmospheric Chemistry And Physics*, **8**, 5899–5917.

KETTLE, A. & ANDREAE, M. (2000). Flux of dimethylsulfide from the oceans: A comparison of updated data sets and flux models. *Journal Of Geophysical Research*, **105**, 26793–26808.

KOCH, D., JACOB, D., TEGEN, I., RIND, D. & CHIN, M. (1999). Tropospheric sulfur simulation and sulfate direct radiative forcing in the Goddard Institute for Space Studies general circulation model. *Journal Of Geophysical Research-Atmospheres*, **104**, 23799–23822.

KOELEMEIJER, R.B.A., STAMMES, P., HOVENIER, J.W. & DE HAAN, J.F. (2001). A fast method for retrieval of cloud parameters using oxygen A band measurements from the Global Ozone Monitoring Experiment. *Journal Of Geophysical Research-Atmospheres*, **106**, 3475–3490.

KOELEMEIJER, R.B.A., DE HAAN, J.F. & STAMMES, P. (2003). A database of spectral surface reflectivity in the range 335-772 nm derived from 5.5 years of GOME observations. *Journal Of Geophysical Research-Atmospheres*, **108**.

KORHONEN, H., CARSLAW, K.S., SPRACKLEN, D.V., MANN, G.W. & WOODHOUSE, M.T. (2008). Influence of oceanic dimethyl sulfide emissions on cloud condensation nuclei concentrations and seasonality over the remote Southern Hemisphere oceans: A global model study. *Journal Of Geophysical Research-Atmospheres*, **113**.

KRITZ, M. & RANCHER, J. (1980). Circulation of Na, Cl and Br in the tropical marine atmosphere. *Journal Of Geophysical Research*, **85**, 1633–1639.

KULMALA, M., LAAKSONEN, A. & PIRJOLA, L. (1998). Parameterizations for sulfuric acid/water nucleation rates. *Journal Of Geophysical Research-Atmospheres*, **103**, 8301–8307.

KULMALA, M., KORHONEN, P., LAAKSONEN, A., VIISANEN, Y., MCGRAW, R. & SEINFELD, J.H. (2000). Ternary nucleation of H2SO4, NH3 and H2O. *Nucleation And Atmospheric Aerosols 2000*, **534**, 111–114.

KURIHARA, M.K., KIMURA, M., IWAMOTO, Y., NARITA, Y., OOKI, A., EUM, Y.J., TSUDA, A., SUZUKI, K., TANI, Y., YOKOUCHI, Y., UEMATSU, M. & HASHIMOTO, S. (2010). Distributions of short-lived iodocarbons and biogenic trace gases in the open ocean and atmosphere in the western North Pacific. *Marine Chemistry*, **118**, 156–170.

LANGMANN, B., VARGHESE, S., MARMER, E., VIGNATI, E., WILSON, J., STIER, P. & O'DOWD, C. (2008). Aerosol distribution over Europe: a model evaluation study with detailed aerosol microphysics. *Atmospheric Chemistry And Physics*, **8**, 1591–1607.

LAW, K.S. & STURGES, W.T. (2006). Halogenated Very Short-Lived Substances, Chapter 2 in Scientific Assessment of Ozone Depletion, 2006. Tech. rep., Global Ozone Research and Monitoring Project- Report No. 50, 572 pp., WMO, Geneva, Switzerland.

LAW, K.S., PLANTEVIN, P.H., SHALLCROSS, D.E., ROGERS, H.L., PYLE, J.A., GROUHEL, C., THOURET, V. & MARENCO, A. (1998). Evaluation of modeled O-3 using Measurement of Ozone by Airbus In-Service Aircraft (MOZAIC) data. *Journal Of Geophysical Research-Atmospheres*, **103**, 25721–+.

LEE, J.D., MOLLER, S.J., READ, K.A., LEWIS, A.C., MENDES, L. & CARPENTER, L.J. (2009a). Year-round measurements of nitrogen oxides and ozone in the tropical North Atlantic marine boundary layer. *Journal Of Geophysical Research-Atmospheres*, **114**, D21302.

LEE, J.D., MCFIGGANS, G., ALLAN, J.D., BAKER, A.R., BALL, S.M., BENTON, A.K., CARPENTER, L.J., COMMANE, R., FINLEY, B.D., EVANS, M., FUENTES, E., FURNEAUX, K., GODDARD, A., GOOD, N., HAMILTON, J.F., HEARD, D.E., HERRMANN, H., HOLLINGSWORTH, A., HOPKINS, J.R., INGHAM, T., IRWIN, M., JONES, C.E., JONES, R.L., KEENE, W.C., LAWLER, M.J., LEHMANN, S., LEWIS, A.C., LONG, M.S., MAHAJAN, A., METHVEN, J., MOLLER, S.J., MULLER, K., MULLER, T., NIEDERMEIER, N., O'DOHERTY, S., OETJEN, H., PLANE, J.M.C., PSZENNY, A.A.P., READ, K.A., SAIZ-LOPEZ, A., SALTZMAN, E.S., SANDER, R., VON GLASOW, R., WHALLEY, L., WIEDENSOHLER, A. & YOUNG, D. (2010). Reactive Halogens in the Marine Boundary Layer (RHaMBLe): the tropical North Atlantic experiments. *Atmospheric Chemistry And Physics*, **10**, 1031–1055.

LEE, S.S., PENNER, J.E. & SALEEBY, S.M. (2009b). Aerosol effects on liquid-water path of thin stratocumulus clouds. *Journal Of Geophysical Research-Atmospheres*, **114**.

LESER, H., HONNINGER, G. & PLATT, U. (2003). MAX-DOAS measurements of BrO and NO2 in the marine boundary layer. *Geophysical Research Letters*, **30**, 1537.

LEVY, H. (1971). Normal Atmosphere - Large Radical And Formaldehyde Concentrations Predicted. *Science*, **173**, 141–&.

LIAO, H., ADAMS, P.J., CHUNG, S.H., SEINFELD, J.H., MICKLEY, L.J. & JACOB, D.J. (2003). Interactions between tropospheric chemistry and aerosols in a unified general circulation model. *Journal Of Geophysical Research-Atmospheres*, **108**.

LISS, P.S. & MERLIVAT, L. (1986). The Role of Air-Sea Exchange in Geochemical Cycling. *Air-Sea exchange rates - introduction and synthesis.*, 113–127.

LIU, S.C., TRAINER, M., FEHSENFELD, F.C., PARRISH, D.D., WILLIAMS, E.J., FAHEY, D.W., HUBLER, G. & MURPHY, P.C. (1987). Ozone Production In The Rural Troposphere And The Implications For Regional And Global Ozone Distributions. *Journal Of Geophysical Research-Atmospheres*, **92**, 4191–4207.

LIU, X.H., PENNER, J.E. & HERZOG, M. (2005). Global modeling of aerosol dynamics: Model description, evaluation, and interactions between sulfate and nonsulfate aerosols. *Journal Of Geophysical Research-Atmospheres*, **110**.

LOGAN, J.A., PRATHER, M.J., WOFSY, S.C. & MCCELROY, M.B. (1981). Tropospheric Chemistry - A Global Perspective. *Journal Of Geophysical Research-Oceans And Atmospheres*, **86**, 7210–7254.

LOHMANN, U., VON SALZEN, K., MCFARLANE, N., LEIGHTON, H.G. & FEICHTER, J. (1999). Tropospheric sulfur cycle in the Canadian general circulation model. *Journal Of Geophysical Research-Atmospheres*, **104**, 26833–26858.

LU, Z., STREETS, D.G., ZHANG, Q., WANG, S., CARMICHAEL, G.R., CHENG, Y.F., WEI, C., CHIN, M., DIEHL, T. & TAN, Q. (2010). Sulfur dioxide emissions in China and sulfur trends in East Asia since 2000. *Atmos. Chem. Phys.*, **10**, 6311–6331.

LUCAS, D.D. & PRINN, R.G. (2005). Sensitivities of gas-phase dimethylsulfide oxidation products to the assumed mechanisms in a chemical transport model. *Journal Of Geophysical Research-Atmospheres*, **110**, D21312.

MAHAJAN, A.S., PLANE, J.M.C., OETJEN, H., MENDES, L., SAUNDERS, R.W., SAIZ-LOPEZ, A., JONES, C.E., CARPENTER, L.J. & MCFIGGANS, G.B. (2010). Measurement and modelling of tropospheric reactive halogen species over the tropical Atlantic Ocean. *Atmospheric Chemistry And Physics*, **10**, 4611–4624.

MANKTELOW, P.T. (2008). *Understanding the complex fate of the sulfate aerosol*. Ph.D. thesis, University of Leeds.

MANKTELOW, P.T., MANN, G.W., CARSLAW, K.S., SPRACKLEN, D.V. & CHIPPERFIELD, M.P. (2007). Regional and global trends in sulfate aerosol since the 1980s. *Geophysical Research Letters*, **34**, L14803.

MANN, G., CARSLAW, K.S., SPRACKLEN, D.V., RIDLEY, D.A., MANKTELOW, P.M., CHIPPERFIELD, M.P., PICKERING, S.J. & JOHNSON, C.E. (2010). Description and Evaluation of GLOMAP-MODE: A modal global aerosol microphysics model fo the UKCA composition-climate model. *Prepared for Geosci. Model. Dev. Discuss.*

MARTENSSON, E.M., NILSSON, E.D., DE LEEUW, G., COHEN, L.H. & HANSSON, H.C. (2003). Laboratory simulations and parameterization of the primary marine aerosol production. *Journal Of Geophysical Research-Atmospheres*, **108**.

MARTI, J.J., WEBER, R.J., MCMURRY, P.H., EISELE, F., TANNER, D. & JEFFERSON, A. (1997). New particle formation at a remote continental site: Assessing the contributions of SO2 and organic precursors. *Journal Of Geophysical Research-Atmospheres*, **102**, 6331–6339.

MARTIN, R.V., JACOB, D.J., YANTOSCA, R.M., CHIN, M. & GINOUX, P. (2003). Global and regional decreases in tropospheric oxidants from photochemical effects of aerosols. *Journal Of Geophysical Research-Atmospheres*, **108**.

MARTINO, M., MILLS, G.P., WOELTJEN, J. & LISS, P.S. (2009). A new source of volatile organoiodine compounds in surface seawater. *Geophysical Research Letters*, **36**.

MATSUMOTO, J., IMAGAWA, K., IMAI, H., KOSUGI, N., IDEGUCHI, M., KATO, S. & KAJII, Y. (2006). Nocturnal sink of NOx via NO3 and N2O5 in the outflow from a source area in Japan. *Atmospheric Environment*, **40**, 6294–6302.

MCARDLE, J.V. & HOFFMANN, M.R. (1983). Kinetics And Mechanism Of The Oxidation Of Aquated Sulfur-Dioxide By Hydrogen-Peroxide At Low Ph. *Abstracts Of Papers Of The American Chemical Society*, **186**, 146–ENVR.

MCFIGGANS, G., COE, H., BURGESS, R., ALLAN, J., CUBISON, M., ALFARRA, M.R., SAUNDERS, R., SAIZ-LOPEZ, A., PLANE, J.M.C., WEVILL, D.J., CARPENTER, L.J., RICKARD, A.R. & MONKS, P.S. (2004). Direct evidence for coastal iodine particles from Laminaria macroalgae - linkage to emissions of molecular iodine. *Atmospheric Chemistry And Physics*, **4**, 701–713.

MINIKIN, A., LEGRAND, M., HALL, J., WAGENBACH, D., KLEEFELD, C., WOLFF, E., PASTEUR, E.C. & DUCROZ, F. (1998). Sulfur-containing species (sulfate and methanesulfonate) in coastal Antarctic aerosol and precipitation. *Journal Of Geophysical Research-Atmospheres*, **103**, 10975–10990.

MIRABEL, P. & KATZ, J.L. (1974). Binary Homogeneous Nucleation As A Mechanism For Formation Of Aerosols. *Journal Of Chemical Physics*, **60**, 1138–1144.

MONAHAN, E., SPIEL, D. & DAVIDSON, K. (1986). Oceanic Whitecaps, chap. A model of marine aerosol generation via whitecaps and wave disruption. *D. Reidel, Norwell, Mass*, 167–174.

MONKS, P.S. (2005). Gas-phase radical chemistry in the troposphere. *Chemical Society Reviews*, **34**, 376–395.

MONKS, P.S., CARPENTER, L.J., PENKETT, S.A., AYERS, G.P., GILLETT, R.W., GALBALLY, I.E. & MEYER, C.P. (1998). Fundamental ozone photochemistry in the remote marine boundary layer: The SOAPEX experiment, measurement and theory. *Atmospheric Environment*, **32**, 3647–3664.

MOXIM, W.J., LEVY, H. & KASIBHATLA, P.S. (1996). Simulated global tropospheric PAN: Its transport and impact on NOx. *Journal Of Geophysical Research-Atmospheres*, **101**, 12621–12638.

MOZURKEWICH, M. (1995). Mechanisms For The Release Of Halogens From Sea-Salt Particles By Free-Radical Reactions. *Journal Of Geophysical Research-Atmospheres*, **100**, 14199–14207.

NAGAO, I., MATSUMOTO, K. & TANAKA, H. (1999a). Characteristics of dimethylsulfide, ozone, aerosols, and cloud condensation nuclei in air masses over the northwestern Pacific Ocean. *Journal Of Geophysical Research-Atmospheres*, **104**, 11675–11693.

NAGAO, I., MATSUMOTO, K. & TANAKA, H. (1999b). Sunrise ozone destruction found in the sub-tropical marine boundary layer. *Geophysical Research Letters*, **26**, 3377–3380.

NEWBERG, J.T., MATTHEW, B.M. & ANASTASIO, C. (2005). Chloride and bromide depletions in sea-salt particles over the northeastern Pacific Ocean. *Journal Of Geophysical Research-Atmospheres*, **110**, D06209.

NGUYEN, B.C., MIHALPOULOS, N., PUTAUD, J.P., GAUDRY, A., GALLET, L., KEENE, W.C. & GALLOWAY, J.N. (1992). Covariations In Oceanic Dimethyl Sulfide, Its Oxidation-Products And Rain Acidity At Amsterdam Island In The Southern Indian-Ocean. *Journal Of Atmospheric Chemistry*, **15**, 39–53.

NIGHTINGALE, P.D., MALIN, G., LAW, C.S., WATSON, A.J., LISS, P.S., LIDDICOAT, M.I., BOUTIN, J. & UPSTILL-GODDARD, R.C. (2000). In situ evaluation of air-sea gas exchange paramaterizations using novel conservative and volatile tracers. *Globl Biogeochem. Cycles*, **14**, 373–388.

O'BRIEN, L.M., HARRIS, N.R.P., ROBINSON, A.D., GOSTLOW, B., WARWICK, N., YANG, X. & PYLE, J.A. (2009). Bromocarbons in the tropical marine boundary layer at the Cape Verde Observatory - measurements and modelling. *Atmospheric Chemistry And Physics*, **9**, 9083–9099.

O'DOWD, C.D., GEEVER, M. & HILL, M.K. (1998). New particle formation: Nucleation rates and spatial scales in the clean marine coastal environment. *Geophysical Research Letters*, **25**, 1661–1664.

O'DOWD, C.D., AALTO, P., HAMERI, K., KULMALA, M. & HOFFMANN, T. (2002a). Aerosol formation - Atmospheric particles from organic vapours. *Nature*, **416**, 497–498.

O'DOWD, C.D., JIMENEZ, J.L., BAHREINI, R., FLAGAN, R.C., SEINFELD, J.H., HAMERI, K., PIRJOLA, L., KULMALA, M., JENNINGS, S.G. & HOFFMANN, T. (2002b). Marine aerosol formation from biogenic iodine emissions. *Nature*, **417**, 632–636.

OSTHOFF, H.D., BATES, T.S., JOHNSON, J.E., KUSTER, W.C., GOLDAN, P., SOMMARIVA, R., WILLIAMS, E.J., LERNER, B.M., WARNEKE, C., DE GOUW, J.A., PETTERSSON, A., BAYNARD, T., MEAGHER, J.F., FEHSENFELD, F.C., RAVISHANKARA, A.R. & BROWN, S.S. (2009). Regional variation of the dimethyl sulfide oxidation mechanism in the summertime marine boundary layer in the Gulf of Maine. *Journal Of Geophysical Research-Atmospheres*, **114**.

PANDIS, S.N. & SEINFELD, J.H. (1989). Sensitivity Analysis Of A Chemical Mechanism For Aqueous-Phase Atmospheric Chemistry. *Journal Of Geophysical Research-Atmospheres*, **94**, 1105–1126.

PENKETT, S.A., MONKS, P.S., CARPENTER, L.J., CLEMITSHAW, K.C., AYERS, G.P., GILLETT, R.W., GALBALLY, I.E. & MEYER, C.P. (1997). Relationships between ozone photolysis rates and peroxy radical concentrations in clean marine air over the Southern Ocean. *Journal Of Geophysical Research-Atmospheres*, **102**, 12805–12817.

PHAM, M., MULLER, J.F., BRASSEUR, G.P., GRANIER, C. & MEGIE, G. (1995). A three-dimensional study of the tropospheric sulfur cycle. *Journal Of Geophysical Research-Atmospheres*, **100**, 26061–26092.

PIERCE, J.R. & ADAMS, P.J. (2006). Global evaluation of CCN formation by direct emission of sea salt and growth of ultrafine sea salt. *Journal Of Geophysical Research-Atmospheres*, **111**, D06203.

PLANE, J.M.C. & SAIZ-LOPEZ, A. (2006). *Analytical Techniques for Atmospheric Measurement*, chap. UV-Visible Differential Optical Absorption Spectroscopy (DOAS). Blackwell, Oxford.

PLATT, U. & JANSSEN, C. (1995). Observation and role of the free radicals NO3, ClO, BrO and IO in the troposphere. *Faraday Discussions*, 175–198.

PLATT, U. & LEBRAS, G. (1997). Influence of DMS on the O-X-NOY partitioning and the NOX distribution in the marine background atmosphere. *Geophysical Research Letters*, **24**, 1935–1938.

POZZOLI, L., BEY, I., RAST, S., SCHULTZ, M.G., STIER, P. & FEICHTER, J. (2008a). Trace gas and aerosol interactions in the fully coupled model of aerosol-chemistry-climate ECHAM5-HAMMOZ: 1. Model description and insights from the spring 2001 TRACE-P experiment. *Journal Of Geophysical Research-Atmospheres*, **113**.

POZZOLI, L., BEY, I., RAST, S., SCHULTZ, M.G., STIER, P. & FEICHTER, J. (2008b). Trace gas and aerosol interactions in the fully coupled model of aerosol-chemistry-climate ECHAM5-HAMMOZ: 2. Impact of heterogeneous chemistry on the global aerosol distributions. *Journal Of Geophysical Research-Atmospheres*, **113**, D07309.

PRATHER, M.J. (1986). Numerical Advection By Conservation Of 2nd-Order Moments. *Journal Of Geophysical Research-Atmospheres*, **91**, 6671–6681.

PRINGLE, K. (2006). *Aerosol - Cloud Interactions in a Global Model of Aerosol microphysics*. Ph.D. thesis, University of Leeds.

PSZENNY, A.A.P., MOLDANOV, J., KEENE, W.C., SANDER, R., MABEN, J.R., MARTINEZ, M., CRUTZEN, P.J., PERNER, D. & PRINN, R.G. (2004). Halogen cycling and aerosol pH in the Hawaiian marine boundary layer. *Atmospheric Chemistry And Physics*, **4**, 147–168.

QUACK, B. & WALLACE, D.W.R. (2003). Air-sea flux of bromoform: Controls, rates, and implications. *Global Biogeochemical Cycles*, **17**, 1023.

RASMUSSEN, R.A., KHALIL, M.A.K., GUNAWARDENA, R. & HOYT, S.D. (1982). Atmospheric Methyl Iodide. *J. Geophys. Res. - Atmos*, **87**, 3086 – 3090.

RAVISHANKARA, A.R. (1997). Heterogeneous and multiphase chemistry in the troposphere. *Science*, **276**, 1058–1065.

READ, K.A., LEWIS, A.C., BAUGUITTE, S., RANKIN, A.M., SALMON, R.A., WOLFF, E.W., SAIZ-LOPEZ, A., BLOSS, W.J., HEARD, D.E., LEE, J.D. & PLANE, J.M.C. (2008). DMS and MSA measurements in the Antarctic Boundary Layer: Impact of BrO on MSA production. *Atmospheric Chemistry And Physics*, **8**, 2985–2997.

REESER, D.I., JAMMOUL, A., CLIFFORD, D., BRIGANTE, M., D'ANNA, B., GEORGE, C. & DONALDSON, D.J. (2009). Photoenhanced Reaction of Ozone with Chlorophyll at the Seawater Surface. *Journal Of Physical Chemistry C*, **113**, 2071–2077.

ROELOFS, G.J., LELIEVELD, J. & GANZEVELD, L. (1998). Simulation of global sulfate distribution and the influence on effective cloud drop radii with a coupled photochemistry sulfur cycle model. *Tellus Series B-Chemical And Physical Meteorology*, **50**, 224–242.

ROSSOW, W.B. & SCHIFFER, R.A. (1999). Advances in understanding clouds from ISCCP. *Bulletin Of The American Meteorological Society*, **80**, 2261–2287.

SAIZ-LOPEZ, A. & PLANE, J.M.C. (2004). Novel iodine chemistry in the marine boundary layer. *Geophysical Research Letters*, **31**, L04112.

SAIZ-LOPEZ, A., PLANE, J.M.C. & SHILLITO, J.A. (2004). Bromine oxide in the mid-latitude marine boundary layer. *Geophysical Research Letters*, **31**, L03111.

SAIZ-LOPEZ, A., SHILLITO, J.A., COE, H. & PLANE, J.M.C. (2006). Measurements and modelling of I-2, IO, OIO, BrO and NO3 in the mid-latitude marine boundary layer. *Atmospheric Chemistry And Physics*, **6**, 1513–1528.

SAIZ-LOPEZ, A., CHANCE, K., LIU, X., KUROSU, T.P. & SANDER, S.P. (2007). First observations of iodine oxide from space. *Geophysical Research Letters*, **34**, L12812.

SAIZ-LOPEZ, A., PLANE, J.M.C., MAHAJAN, A.S., ANDERSON, P.S., BAUGUITTE, S.J.B., JONES, A.E., ROSCOE, H.K., SALMON, R.A., BLOSS, W.J., LEE, J.D. & HEARD, D.E. (2008). On the vertical distribution of boundary layer halogens over coastal Antarctica: implications for O-3, HOx, NOx and the Hg lifetime. *Atmospheric Chemistry And Physics*, **8**, 887–900.

SALOMAN, J., HODGES, J.C.F., FRIEDL, M., SCHAAF, C. & STRAHLER, A. (2004). Global land-water mask derived from MODIS Nadir BRDF-adjusted reflectances (NBAR) and the MODIS land cover algorithm. *Geoscience and Remote Sensing Symposium*.

SANDER, R., RUDICH, Y., VON GLASOW, R. & CRUTZEN, P.J. (1999). The role of BrNO3 in marine tropospheric chemistry: A model study. *Geophysical Research Letters*, **26**, 2857–2860.

SANDER, R., KEENE, W.C., PSZENNY, A.A.P., ARIMOTO, R., AYERS, G.P., BABOUKAS, E., CAINEY, J.M., CRUTZEN, P.J., DUCE, R.A., HONNINGER, G., HUEBERT, B.J., MAENHAUT, W., MIHALOPOULOS, N., TUREKIAN, V.C. & VAN DINGENEN, R. (2003). Inorganic bromine in the marine boundary layer: a critical review. *Atmospheric Chemistry And Physics*, **3**, 1301–1336.

SANDER, R., KERKWEG, A., JOCKEL, P. & LELIEVELD, J. (2005). Technical note: The new comprehensive atmospheric chemistry module MECCA. *Atmospheric Chemistry And Physics*, **5**, 445–450.

SAVOIE, D.I., PROSPERO, J.M., LARSEN, R.J., HUANG, F., IZAGUIRRE, M.A., HUANG, T., SNOWDON, T.H., CUSTALS, L. & SANDERSON, C.G. (1993). Nitrogen And Sulfur Species In Antarctic Aerosols At Mawson, Palmer Station, And Marsh (King George Island). *Journal Of Atmospheric Chemistry*, **17**, 95–122.

SCHAUFFLER, S.M., ATLAS, E.L., BLAKE, D.R., FLOCKE, F., LUEB, R.A., LEE-TAYLOR, J.M., STROUD, V. & TRAVNICEK, W. (1999). Distributions of brominated organic compounds in the troposphere and lower stratosphere. *Journal Of Geophysical Research-Atmospheres*, **104**, 21513–21535.

SCHMIDT, A., CARSLAW, K.S., MANN, G.W., WILSON, B.M., BREIDER, T.J., PICKERING, S.J. & THORDARSON, T. (2010). The impact of the 1783 - 1784 AD Laki eruption on global aerosol formation processes and cloud condensation nuclei. *Atmospheric Chemistry and Physics Discussions*, **10**, 3189–3228.

SCHMIDT, G.A., RUEDY, R., HANSEN, J.E., ALEINOV, I., BELL, N., BAUER, M., BAUER, S., CAIRNS, B., CANUTO, V., CHENG, Y., DEL GENIO, A., FALUVEGI, G., FRIEND, A.D., HALL, T.M., HU, Y.Y., KELLEY, M., KIANG, N.Y., KOCH, D., LACIS, A.A., LERNER, J., LO, K.K., MILLER, R.L., NAZARENKO, L., OINAS, V., PERLWITZ, J., PERLWITZ, J., RIND, D., ROMANOU, A., RUSSELL, G.L., SATO, M., SHINDELL, D.T., STONE, P.H., SUN, S., TAUSNEV, N., THRESHER, D. & YAO, M.S. (2006). Present-day atmospheric simulations using GISS ModelE: Comparison to in situ, satellite, and reanalysis data. *Journal Of Climate*, **19**, 153–192.

SCHOFIELD, R., KREHER, K., CONNOR, B.J., JOHNSTON, P.V., THOMAS, A., SHOOTER, D., CHIPPERFIELD, M.P., RODGERS, C.D. & MOUNT, G.H. (2004). Retrieved tropospheric and stratospheric BrO columns over Lauder, New Zealand. *Journal Of Geophysical Research-Atmospheres*, **109**, D14304.

SCHWARZ, S. (1986). Mass-transport considerations pertinent to aqueous phase reactions of gases in liquid-water clouds. *Chemistry of Multiphase Atmospheric Systems*, 415–471.

SCIARE, J., BABOUKAS, E., KANAKIDOU, M., KRISCHKE, U., BELVISO, S., BARDOUKI, H. & MIHALOPOULOS, N. (2000a). Spatial and temporal variability of atmospheric sulfur-containing gases and particles during the Albatross campaign. *Journal Of Geophysical Research-Atmospheres*, **105**, 14433–14448.

SCIARE, J., KANAKIDOU, M. & MIHALOPOULOS, N. (2000b). Diurnal and seasonal variation of atmospheric dimethylsulfoxide at Amsterdam Island in the southern Indian Ocean. *Journal Of Geophysical Research-Atmospheres*, **105**, 17257–17265.

SCIARE, J., BABOUKAS, E. & MIHALOPOULOS, N. (2001). Short-term variability of atmospheric DMS and its oxidation products at Amsterdam Island during summer time. *Journal Of Atmospheric Chemistry*, **39**, 281–302.

SEINFELD, J.H. (1999). Atmospheric chemistry, aerosols, and climate: global coupling. *Air Pollution Vii*, **6**, 679–684.

SEINFELD, J.H. & PANDIS, S.N. (1998). *Atmospheric Chemistry and Physics*. Wiley, New York, Chichester, Weinheim.

SEKHON, R.S. & SRIVASTA, R. (1971). Doppler Radar Observations Of Drop-Size Distributions In A Thunderstorm. *Journal Of The Atmospheric Sciences*, **28**, 983–&.

SHINDELL, D.T., GRENFELL, J.L., RIND, D., GREWE, V. & PRICE, C. (2001). Chemistry-climate interactions in the Goddard Institute for Space Studies general circulation model 1. Tropospheric chemistry model description and evaluation. *Journal Of Geophysical Research-Atmospheres*, **106**, 8047–8075.

SIEVERING, H., BOATMAN, J., GORMAN, E., KIM, Y., ANDERSON, L., ENNIS, G., LURIA, M. & PANDIS, S. (1992). Removal Of Sulfur From The Marine Boundary-Layer By Ozone Oxidation In Sea-Salt Aerosols. *Nature*, **360**, 571–573k.

SIEVERING, H., CAINEY, J., HARVEY, M., MCGREGOR, J., NICHOL, S. & QUINN, P. (2004). Aerosol non-sea-salt sulfate in the remote marine boundary layer under clear-sky and normal cloudiness conditions: Ocean-derived biogenic alkalinity enhances sea-salt sulfate production by ozone oxidation. *Journal Of Geophysical Research-Atmospheres*, **109**.

SLINN, W.G.N. (1982). Predictions for particle deposition to vegetative surfaces. *Atmospheric Environment*, **16**, 1785–1794.

SMITH, M. & HARRISON, N. (1998). The sea spray generation function. *Journal of Aerosol Science*, **29**, S189–S190.

SMOYDZIN, L. & VON GLASOW, R. (2007). Do organic surface films on sea salt aerosols influence atmospheric chemistry? a model study. *Atmospheric Chemistry And Physics*, **7**, 5555–5567.

SONG, C. & CARMICHAEL, G. (2001). A three dimensional modeling investigation of the evolution processesof dust and sea-salt particles in east Asia. *Journal Of Geophysical Research*, **106**, 18131–18154.

SONG, C.H. & CARMICHAEL, G.R. (1999). The aging process of naturally emitted aerosol (sea-salt and mineral aerosol) during long range transport. *Atmospheric Environment*, **33**, 2203–2218.

SORTEBERG, A. & HOV, O. (1996). Two parametrizations of the dry deposition exchange for SO2 and NH3 in a numerical model. *Atmospheric Environment*, **30**, 1823–1840.

SPRACKLEN, D.V., PRINGLE, K.J., CARSLAW, K.S., CHIPPERFIELD, M.P. & MANN, G.W. (2005a). A global off-line model of size-resolved aerosol microphysics: I. Model development and prediction of aerosol properties. *Atmospheric Chemistry And Physics*, **5**, 2227–2252.

SPRACKLEN, D.V., PRINGLE, K.J., CARSLAW, K.S., CHIPPERFIELD, M.P. & MANN, G.W. (2005b). A global off-line model of size-resolved aerosol microphysics: II. Identification of key uncertainties. *Atmospheric Chemistry And Physics*, **5**, 3233–3250.

STARK, H., BROWN, S.S., GOLDAN, P.D., ALDENER, M., KUSTER, W.C., JAKOUBEK, R., FEHSENFELD, F.C., MEAGHER, J., BATES, T.S. & RAVISHANKARA, A.R. (2007). Influence of nitrate radical on the oxidation of dimethyl sulfide in a polluted marine environment. *Journal Of Geophysical Research-Atmospheres*, **112**, D10S10.

STAUDT, A.C., JACOB, D.J., RAVETTA, F., LOGAN, J.A., BACHIOCHI, D., KRISHNAMURTI, T.N., SANDHOLM, S., RIDLEY, B., SINGH, H.B. & TALBOT, B. (2003). Sources and chemistry of nitrogen oxides over the tropical Pacific. *Journal Of Geophysical Research-Atmospheres*, **108**.

STEVENSON, D.S., DOHERTY, R.M., SANDERSON, M.G., COLLINS, W.J., JOHNSON, C.E. & DERWENT, R.G. (2004). Radiative forcing from aircraft NOx emissions: Mechanisms and seasonal dependence. *Journal Of Geophysical Research-Atmospheres*, **109**.

STEVENSON, D.S., DENTENER, F.J., SCHULTZ, M.G., ELLINGSEN, K., VAN NOIJE, T.P.C., WILD, O., ZENG, G., AMANN, M., ATHERTON, C.S., BELL, N., BERGMANN, D.J., BEY, I., BUTLER, T., COFALA, J., COLLINS, W.J., DERWENT, R.G., DOHERTY, R.M., DREVET, J., ESKES, H.J., FIORE, A.M., GAUSS, M., HAUGLUSTAINE, D.A., HOROWITZ, L.W., ISAKSEN, I.S.A., KROL, M.C., LAMARQUE, J.F., LAWRENCE, M.G., MONTANARO, V., MULLER, J.F., PITARI, G., PRATHER, M.J., PYLE, J.A., RAST, S., RODRIGUEZ, J.M., SANDERSON, M.G., SAVAGE, N.H., SHINDELL, D.T., STRAHAN, S.E., SUDO, K. & SZOPA, S. (2006). Multimodel ensemble simulations of present-day and near-future tropospheric ozone. *Journal Of Geophysical Research-Atmospheres*, **111**.

STIER, P., FEICHTER, J., KINNE, S., KLOSTER, S., VIGNATI, E., WILSON, J., GANZEVELD, L., TEGEN, I., WERNER, M., BALKANSKI, Y., SCHULZ, M., BOUCHER, O., MINIKIN, A. & PETZOLD, A. (2005). The aerosol-climate model ECHAM5-HAM. *Atmospheric Chemistry And Physics*, **5**, 1125–1156.

STUTZ, J., ACKERMANN, R., FAST, J.D. & BARRIE, L. (2002). Atmospheric reactive chlorine and bromine at the Great Salt Lake, Utah. *Geophys. Res. Letts.*, **29**, 1380.

TEXTOR, C., SCHULZ, M., GUIBERT, S., KINNE, S., BALKANSKI, Y., BAUER, S., BERNTSEN, T., BERGLEN, T., BOUCHER, O., CHIN, M., DENTENER, F., DIEHL, T., EASTER, R., FEICHTER, H., FILLMORE, D., GHAN, S., GINOUX, P., GONG, S., KRISTJANSSON, J.E., KROL, M., LAUER, A., LAMARQUE, J.F., LIU, X., MONTANARO, V., MYHRE, G., PENNER, J., PITARI, G., REDDY, S., SELAND, O., STIER, P., TAKEMURA, T. & TIE, X. (2006). Analysis and quantification of the diversities of aerosol life cycles within AeroCom. *Atmospheric Chemistry And Physics*, **6**, 1777–1813.

THEYS, N., VAN ROOZENDAEL, M., HENDRICK, F., FAYT, C., HERMANS, C., BARAY, J.L., GOUTAIL, F., POMMEREAU, J.P. & DE MAZIERE, M. (2007). Retrieval of stratospheric and tropospheric BrO columns from multi-axis DOAS measurements at Reunion Island (21 degrees S, 56 degrees E). *Atmospheric Chemistry And Physics*, **7**, 4733–4749.

THEYS, N., VAN ROOZENDAEL, M., ERRERA, Q., HENDRICK, F., DAERDEN, F., CHABRILLAT, S., DORF, M., PFEILSTICKER, K., ROZANOV, A., LOTZ, W., BURROWS, J.P., LAMBERT, J.C., GOUTAIL, F., ROSCOE, H.K. & DE MAZIERE, M. (2009). A global stratospheric bromine monoxide climatology based on the BASCOE chemical transport model. *Atmospheric Chemistry And Physics*, **9**, 831–848.

THOMAS, M.A., SUNTHARALINGAM, P., POZZOLI, L., RAST, S., DEVASTHALE, A., KLOSTER, S., FEICHTER, J. & LENTON, T.M. (2010). Quantification of DMS aerosol-cloud-climate interactions using the ECHAM5-HAMMOZ model in a current climate scenario. *Atmospheric Chemistry And Physics*, **10**, 7425–7438.

TIE, X., BRASSEUR, G., EMMONS, L., HOROWITZ, L. & KINNISON, D. (2001). Effects of aerosols on tropospheric oxidants: A global model study. *Journal Of Geophysical Research-Atmospheres*, **106**, 22931–22964.

TIEDTKE, M. (1989). A Comprehensive Mass Flux Scheme For Cumulus Parameterization In Large-Scale Models. *Monthly Weather Review*, **117**, 1779–1800.

TOUMI, R. (1994). BrO As A Sink For Dimethylsulfide In The Marine Atmosphere. *Geophysical Research Letters*, **21**, 117–120.

TREVENA, A.J., JONES, G.B., WRIGHT, S.W. & VAN DEN ENDEN, R.L. (2000). Profiles of DMSP, algal pigments, nutrients and salinity in pack ice from eastern Antarctica. *Journal Of Sea Research*, **43**, 265–273.

TRUESDALE, V.W., LUTHER, G.W. & CANOSAMAS, C. (1995). Molecular-Iodine Reduction In Seawater - An Improved Rate-Equation Considering Organic-Compounds. *Marine Chemistry*, **48**, 143–150.

TWOMEY, S. (1974). Pollution And Planetary Albedo. *Atmospheric Environment*, **8**, 1251–1256.

VAN DER WERF, G.R., RANDERSON, J.T., COLLATZ, G.J. & GIGLIO, L. (2003). Carbon emissions from fires in tropical and subtropical ecosystems. *Global Change Biology*, **9**, 547–562.

VAN ROOZENDAEL, M., WAGNER, T., RICHTER, A., PUNDT, I., ARLANDER, D.W., BURROWS, J.P., CHIPPERFIELD, M., FAYT, C., JOHNSTON, P.V., LAMBERT, J.C., KREHER, K., PFEILSTICKER, K., PLATT, U., POMMEREAU, J.P., SINNHUBER, B.M., TORNKVIST, K.K. & WITTROCK, F. (2002). Intercomparison of BrO measurements from ERS-2 GOME, ground-based and balloon platforms. *Remote Sensing Of Trace Constituents In The Lower Stratosphere, Troposphere And The Earth'S Surface: Global Observations, Air Pollution And The Atmospheric Correction*, **29**, 1661–1666.

VIGNATI, E., WILSON, J. & STIER, P. (2004). M7: An efficient size-resolved aerosol microphysics module for large-scale aerosol transport models,. *Journal Of Geophysical Research-Atmospheres*, **109**, 485.

VOGT, R., CRUTZEN, P.J. & SANDER, R. (1996). A mechanism for halogen release from sea-salt aerosol in the remote marine boundary layer. *Nature*, **383**, 327–330.

VON GLASOW, R. (2007). A look at the CLAW hypothesis from an atmospheric chemistry point of view. *Environmental Chemistry*, **4**, 379–381.

VON GLASOW, R. & CRUTZEN, P.J. (2004a). Model study of multiphase DMS oxidation with a focus on halogens. *Atmospheric Chemistry And Physics*, **4**, 589–608.

VON GLASOW, R., SANDER, R., BOTT, A. & CRUTZEN, P.J. (2002). Modeling halogen chemistry in the marine boundary layer - 1. Cloud-free MBL. *Journal Of Geophysical Research-Atmospheres*, **107**, 4341.

VON GLASOW, R., VON KUHLMANN, R., LAWRENCE, M.G., PLATT, U. & CRUTZEN, P.J. (2004b). Impact of reactive bromine chemistry in the troposphere. *Atmospheric Chemistry And Physics*, **4**, 2481–2497.

VREKOUSSIS, M., KANAKIDOU, M., MIHALOPOULOS, N., CRUTZEN, P.J., LELIEVELD, J., PERNER, D., BERRESHEIM, H. & BABOUKAS, E. (2004). Role of the NO3 radicals in oxidation processes in the eastern Mediterranean troposphere during the MINOS campaign. *Atmospheric Chemistry And Physics*, **4**, 169–182.

VREKOUSSIS, M., MIHALOPOULOS, N., GERASOPOULOS, E., KANAKIDOU, M., CRUTZEN, P.J. & LELIEVELD, J. (2007). Two-years of NO3 radical observations in the boundary layer over the Eastern Mediterranean. *Atmospheric Chemistry And Physics*, **7**, 315–327.

Wagner, T. & Platt, U. (1998). Satellite mapping of enhanced BrO concentrations in the troposphere. *Nature*, **395**, 486–490.

Wagner, T., Leue, C., Wenig, M., Pfeilsticker, K. & Platt, U. (2001). Spatial and temporal distribution of enhanced boundary layer BrO concentrations measured by the GOME instrument aboard ERS-2. *Journal Of Geophysical Research-Atmospheres*, **106**, 24225–24235.

Wang, Y.H., Logan, J.A. & Jacob, D.J. (1998). Global simulation of tropospheric O-3-NOx-hydrocarbon chemistry 2. Model evaluation and global ozone budget. *Journal Of Geophysical Research-Atmospheres*, **103**, 10727–10755.

Warwick, N.J., Pyle, J.A., Carver, G.D., Yang, X., Savage, N.H., O'Connor, F.M. & Cox, R.A. (2006). Global modeling of biogenic bromocarbons. *Journal Of Geophysical Research-Atmospheres*, **111**.

Watanabe, K., Nojiri, Y. & Kariya, S. (2005). Measurements of ozone concentrations on a commercial vessel in the marine boundary layer over the northern North Pacific Ocean. *Journal Of Geophysical Research-Atmospheres*, **110**, D11310.

Wayne, R.P. (2000). *Chemistry of Atmopsheres*. Oxford.

Whalley, L.K., Furneaux, K.L., Goddard, A., Lee, J.D., Mahajan, A., Oetjen, H., Read, K.A., Kaaden, N., Carpenter, L.J., Lewis, A.C., Plane, J.M.C., Saltzman, E.S., Wiedensohler, A. & Heard, D.E. (2010). The chemistry of OH and HO2 radicals in the boundary layer over the tropical Atlantic Ocean. *Atmospheric Chemistry And Physics*, **10**, 1555–1576.

Woodcock, A.H. (1953). Salt Nuclei In Marine Air As A Function Of Altitude And Wind Force. *Journal Of Meteorology*, **10**, 362–371.

Woodhouse, M.T., Carslaw, K.S., Mann, G.W., Vallina, S.M., Vogt, M., Halloran, P.R. & Boucher, O. (2010). Low Sensitivity of cloud condensation nuclei to changes in the sea-air flux of dimethyl-sulphide. *Atmos. Chem. Phys.*, **10**, 7545 – 7559.

Yang, X., Cox, R.A., Warwick, N.J., Pyle, J.A., Carver, G.D., O'Connor, F.M. & Savage, N.H. (2005). Tropospheric bromine chemistry and its impacts on ozone: A model study. *Journal Of Geophysical Research-Atmospheres*, **110**, D23311.

Yang, X., Pyle, J.A. & Cox, R.A. (2008). Sea salt aerosol production and bromine release: Role of snow on sea ice. *Geophysical Research Letters*, **35**.

Yang, X., Pyle, J.A., Cox, R.A., Theys, N. & Van Roozendael, M. (2010). Snow-sourced bromine and its implications for polar tropospheric ozone. *Atmospheric Chemistry And Physics*, **10**, 7763–7773.

Yokouchi, Y., Nojiri, Y., Barrie, L.A., Toom-Sauntry, D. & Fujinuma, Y. (2001). Atmospheric methyl iodide: High correlation with surface seawater temperature and its implications on the sea-to-air flux. *Journal Of Geophysical Research-Atmospheres*, **106**, 12661–12668.

Yokouchi, Y., Osada, K., Wada, M., Hasebe, F., Agama, M., Murakami, R., Mukai, H., Nojiri, Y., Inuzuka, Y., Toom-Sauntry, D. & Fraser, P. (2008). Global distribution and seasonal concentration change of methyl iodide in the atmosphere. *Journal Of Geophysical Research-Atmospheres*, **113**.

YOON, Y.J. & BRIMBLECOMBE, P. (2002). Modelling the contribution of sea salt and dimethyl sulfide derived aerosol to marine CCN. *Atmospheric Chemistry And Physics*, **2**, 17–30.

YVON, S.A. & SALTZMAN, E.S. (1996). Atmospheric sulfur cycling in the tropical Pacific marine boundary layer (12 degrees S,135 degrees W): A comparison of field data and model results .2. Sulfur dioxide. *Journal Of Geophysical Research-Atmospheres*, **101**, 6911–6918.

YVON, S.A., PLANE, J.M.C., NIEN, C.F., COOPER, D.J. & SALTZMAN, E.S. (1996a). Interaction between nitrogen and sulfur cycles in the polluted marine boundary layer. *Journal Of Geophysical Research-Atmospheres*, **101**, 1379–1386.

YVON, S.A., SALTZMAN, E.S., COOPER, D.J., BATES, T.S. & THOMPSON, A.M. (1996b). Atmospheric sulfur cycling in the tropical Pacific marine boundary layer (12 degrees S,135 degrees W): A comparison of field data and model results .1. Dimethylsulfide. *Journal Of Geophysical Research-Atmospheres*, **101**, 6899–6909.

ZHANG, L., GONG, J., S. ANDPADRO & BARRIE, L. (2001). A size-segregated particle dry deposition scheme for an atmospheric aerosol module. *Atmospheric Environment*, **35**, 549–560.